RSC Applied Polymers

REVIEW

View Article Online
View Journal | View Issue

Cite this: *RSC Appl. Polym.*, 2026, **4**, 120

Recent advances in hollow and core–shell intrinsically conducting polymers for applications in electromagnetic interference shielding/microwave absorption, removal of metal ions/dyes and supercapacitors

Suneel Kumar Srivastava

In recent years, considerable attention has been paid to hollow micro–nano-structured intrinsically conducting polymers (ICPs), like polyaniline, polypyrrole, polythiophene and poly(3,4-ethylenedioxythiophene). The availability of the shells and inner voids in the hollow ICP accounts for their tunable physical/chemical properties, offers low density, a high surface area, reduced length for both mass and charge transport, and offers promising applications in environmental remediation and energy. In view of this, the present review article is focused on the synthesis methods used in the fabrication of hollow intrinsically conducting polymers by means of hard and soft template approaches including template-free methods, synthesis of double-shelled hollow spheres of ICP, hollow ICP nanocomposites and core–shell structural materials of ICP. Subsequently, the review highlights the application of the hollow intrinsically conducting polymers, their nanocomposites and core–shell structured materials for applications in electromagnetic interference shielding/microwave absorption, removal of heavy metal ions and different dyes from wastewater, and as efficient electrode materials in supercapacitors. Finally, the review ends with a summary and future perspective on hollow-structured and core–shell conducting polymers and their applications in the above fields of application.

Received 24th July 2025,
Accepted 4th November 2025

DOI: 10.1039/d5lp00230c

rsc.li/rscapplpolym

1. Introduction

Intrinsically conducting polymers (ICPs), comprising polyaniline (PANI), polypyrrole (PPy), polythiophene (PT), and poly(3,4-ethylenedioxythiophene) (PEDOT), are considered a special class of polymers due to their light weight, ease of fabrication, good environmental stability, low cost, high mechanical flexibility, and good biocompatibility.[1] Fig. 1 (inset) shows the schematic chemical structures of different monomers of all these ICPs.[2] They exhibit tunable surface area, electrical conductivity, optical properties, unique redox tenability, and high electrochemical response.[3] As a result, ICPs find their applications in various advanced fields, such as sensing,[4] solar cell rechargeable,[5] battery,[6] supercapacitor,[7] bioelectronic applications,[8] electromagnetic interference shielding and microwave absorption,[9] healthcare monitoring,[10] photocatalysis and opportunities for artificial intelligence,[11] biomedical applications,[12] drug delivery,[13] removal of water pollutants.[14,15]

The physical properties of PANI, PPy, PTH and PEDOT are influenced by their morphology.[16] In this regard, PANI, compared with other ICPs, has been studied extensively for various reasons to date considering different morphologies, such as granular structure,[17] nanoparticles,[17] spongy,[18] dendrite,[19] nanoneddles,[20] nanocables,[21] nanotubes,[21,22] nanofiber,[23] nanowire,[24] nanobelts,[25] nanorods,[26] nanostick,[27] nanoflakes,[28] microspheres,[29] nanocapsules,[30] flower-like nanosheet clusters,[31] coral-like,[32] honeycomb,[33] worm-like interlinked structures,[34] tetragonal star like,[35] nanospheres[36] *etc.* Polypyrrole, polythiophene and PEDOT also exist in many of these morphologies. It is well established that manipulation of the morphology can lead to enhancement of the physicochemical properties and the performance of conducting polymers.[37,38] In this regard, 'hollow structure' ICPs with void space inside a distinct shell and dimensions in the micrometer-/nanometer range have been receiving a considerable amount of attention in recent years.[39–50] The synthesis of such hollow materials with a single or double shells of various compositions and morphologies has been reported following hard-templating, soft-templating and template-free methods.[49]

Hollow structures can be of different shapes, as schematically illustrated in Fig. 2.[41] From this perspective, hollow

Department of Chemistry, Indian Institute of Technology, Kharagpur-721302, India. E-mail: suneel@chem.iitkgp.ac.in, suneelchemkgp@gmail.com

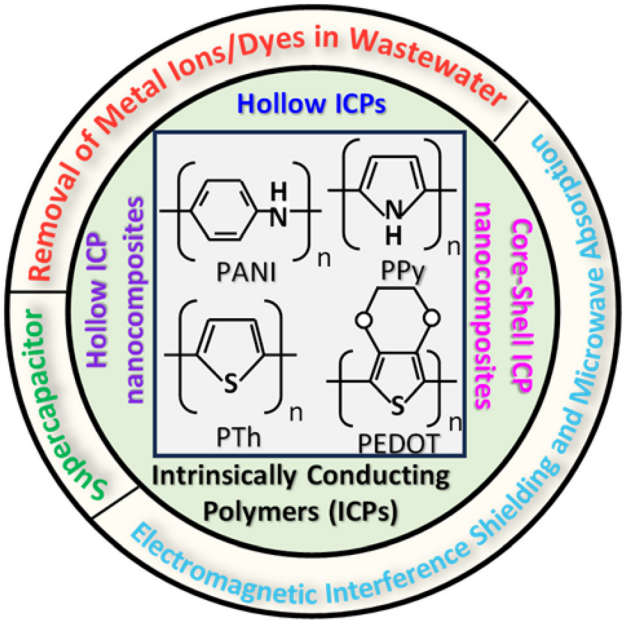

Fig. 1 Hollow and core–shell intrinsically conducting polymers (ICPs) and their applications (Inset: structures of common ICPs.[2] Reproduced with permission from Elsevier).

spheres are considered to be more advantageous than their corresponding solid counterparts due to the presence of a large fraction of empty space inside and intact shell(s).[50] The interior geometry, surface functionality, high specific surface area, and high conductivity, as well as the controllable chemical and physical properties of the hollow ICP nanostructures make them the most promising candidates in several of the applications stated earlier.[6,51] In addition, much attention has also been paid to nanotubes, characterized by their unique hollow tubular structure.[52] Furthermore, the introduction of nanomaterial(s) into these conducting polymers can introduce unique properties such as high surface area, high electrical conductivity and other features that could enhance their performance in multifaceted applications.[49–53]

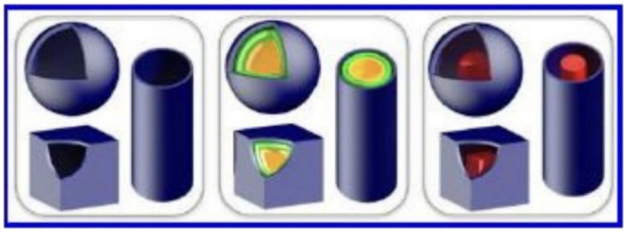

Fig. 2 Schematic illustration showing various hollow structures: (left) hollow spheres/boxes/tubes; (middle) multi-shelled hollow spheres/boxes/tubes; (right) yolk–shell, cube-in-box, and wire-in-tube structures.[41] Reproduced with permission from ACS.

The microwave (MW) radiation emitted from various electrical and electronic devices adversely degrades their performance[9,54] and is very harmful to human health.[55] Therefore, electromagnetic interference (EMI) shielding and microwave absorption materials are essentially needed for mitigating such electromagnetic pollution.[56–59] In this context, hollow conducting polymers combined with fillers (such as magnetic nanoparticles) can also facilitate enhanced EMI shielding and microwave absorption due to the dielectric loss owing to the intrinsic conductivity from the polymer and magnetic loss arising from the magnetic filler, respectively. The unique hollow morphology of conducting polymers with increased surface area prevents secondary electromagnetic pollution due to reflection. Furthermore, the presence of multiple internal reflections and the trapping of EM waves contribute to their excellent performance in EMI shielding and microwave absorption. It may be noted that hollow ICPs can interact with EM waves and convert the energy of the microwaves into heat and dissipate it.[9] In addition, hollow PANI and PPy have been extensively studied as adsorbents in the removal of heavy metals and dyes in water.[60–64] The excellent adsorption performance of hollow conducting polymers in the removal of metals and dyes is ascribed to their large specific surface area and its tunable surface properties. The available functional binding sites in the conducting polymers readily interact with pollutants through various mechanisms, accounting for their effectiveness as adsorbents. Recently, hollow ICPs have also been used in supercapacitor applications due to their low cost and properties.[7] It may be noted that the unique hollow spherical morphology of ICPs accounts for their larger surface area, significantly lower density, and high loading capacity, and shorter ion diffusion paths facilitate achieving high-power density, fast charge and discharge rates, and long cycle life.[65] In addition, hollow conducting polymers also improve cycling stability by allowing for controlled volume changes during redox reactions.[53]

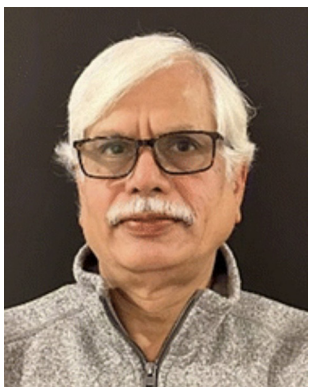

Suneel Kumar Srivastava

Suneel Kumar Srivastava received his Ph.D. degree from the Indian Institute of Technology, Kharagpur, in 1984. He is a former Professor in the Department of Chemistry of the same Institute, serving from 1986 to 2021. Dr Srivastava carried out his post-doctoral work as a DAAD Fellow in the Technical University, Karlsruhe (1988–89, 2002, 2006), University of Siegen (1994, 1999), Technical University, Munchen (2009), Leibniz Institute of Polymer Research, Dresden (2013), Germany, and University of Nantes, France (2003, 2007). His research interests are in the field of nondimensional nanomaterials for their application in the fields of energy, environment and polymer nanocomposites. Dr Srivastava has guided 23 Ph.D. students, published more than 200 research papers in refereed journals, contributed to 20 chapters in books and edited 2 books.

In recent years, core–shell-structured materials formed by the judicious tuning of the core as well as the shell(s) have received considerable attention due to their applications in a variety of fields.[66–68] In this regard, core–shell materials exhibiting enhanced magnetic and dielectric loss have the ability to perform well in electromagnetic interference shielding and microwave absorption.[67,69] In addition, impedance matching in the core–shell materials creates numerous interfaces for multiple reflections and facilitates attenuation of microwaves due to multiple reflections.[9] Core–shell materials formed by combining a functional conducting polymer shell with a stable core are also receiving more attention as adsorbents for the removal of pollutants in water.[68] The choice is mainly guided by the unique properties of both the core and the shell in achieving high adsorption capacity, separation efficiency, and reusability compared with conductive polymers exhibiting low solubility, limited active sites, poor mechanical strength, and separation difficulties. Most importantly, a magnetic core can facilitate the complete separation of the core–shell adsorbents from water by applying an additional magnetic field.[70,71] The core–shell approach has also been used in fabricating ICP-based electrode materials with excellent electrochemical performance in supercapacitor applications.[7] This attractive choice is motivated by the synergistic combination of the core and shell materials leading to a high specific surface area for abundant reaction sites, mechanical stability, good electrical conductivity for fast charge transfer, faster diffusion kinetics, high specific capacitance, and longer cyclability.[72,73]

In view of this, several review articles have appeared in recent years on intrinsically conducting polymers focused on the electromagnetic interference shielding and microwave absorption,[2,9,54,74–80] removal of heavy metal ions[60–64,81–85] and organic dyes[60–64,86–91] in wastewater, and supercapacitors,[7,65,72,73,92–98] and several others are also referred to in subsequent sections. However, considering the rapid developments, there exists a lack of a comprehensive review highlighting the novel contribution of hollow and core–shell intrinsically conducting polymers with their applications in mitigating electronic/environmental pollution and their applications in energy storage.

Motivated by this, the present review aims to highlight the novel contribution made by intrinsically conducting polymers in this regard by focusing exclusively on hollow and core–shell morphologies across three distinct application fields (EMI shielding, adsorption, supercapacitors). Accordingly, the present article is focused on the preparation of hollow intrinsically conducting polymers (PANI, PPy, PTP, PEDOT) and core–shell materials comprising ICP through different approaches. This is followed by their applications in electromagnetic interference shielding/microwave absorption, removal of heavy metal ions/dyes in water, and supercapacitors (Fig. 1). Finally, the review article ends with a future perspective and summary. Overall, the fabrication of the unique hollow and core–shell morphology of important intrinsically conducting polymers and the role they play in the multifaceted applications reviewed in this article clearly complements the existing literature.

2. Intrinsically conducting polymers

Considerable interest has been aroused in intrinsically conducting polymers (ICPs) during the past decades due to their many advantages, such as easy modification, chemical diversity, corrosion resistance, morphology, tunable conductivity and applications.[99–101] The different properties of these polymers are related to the conjugated chains with alternating single and double bonds and the delocalized π-electrons.[96] The conducting polymers have been doped by different methods in order to achieve high conductivities.[101–104] In general, conductivity increases with increasing doping level and becomes saturated at high doping levels for most of the conducting polymers.[105] The doping is introduced in ICPs through the backbone of the polymer chain by neutral dopants (I_2, Br_2, AsF_2, H_2SO_4, $FeCl_3$ *etc.*), ionic dopants ($LiClO_4$, $FeClO_4$, CF_3SO_3Na, $BuNClO_4$ *etc.*), organic dopants (CF_3COOH, CF_3SO_3Na *etc.*) and polymeric dopants such as poly(styrene sulphonic acid), poly(vinyl sulphonic acid), and poly(acrylic acid).[106,107]

The electrical properties of conducting polymers are modified by p- and n-type doping.[105] The delocalization of the charge carriers over the polymer chain accounts for their electronic conductivity.[102] Generally, the negatively charged carriers in n-doping are not as stable as positively charged ones. This makes p-type doping more attractive in academic research as well as for all practical application purposes.[102,108,109] Fig. 3(a) describes the electronic and chemical structures of polythiophene as a representative conducting polymer subjected to p-type doping and n-type doping.[102] The electronic bands and chemical structures illustrating undoped, polaron, bipolaron and fully doped states of polypyrrole are also described in Fig. 3(b).[102]

3. Synthesis of intrinsically conducting polymers

3.1 Chemical methods

3.1.1 Polyaniline. Polyaniline is one of the most common intrinsically conducting polymers and is prepared typically by a chemical oxidation method using aniline monomer in an acidic medium (HCl or H_2SO_4) in the presence of oxidants, such as $FeCl_3$, $(NH_4)_2S_2O_8$, and H_2O_2 KIO_3.[110–112] The formation of polyaniline is indicated by the observed change in the colour of the reaction medium. The acidic condition has a vital influence on the yield and conductivity of the PANI and appropriate for subsequent doping.[113] According to Armes and Miller,[114] the yield and conductivity of the polyaniline in the chemical synthesis depend on the initial oxidant/monomer mole ratio. Investigations have also reported the influence of polymerization temperature on the molecular weight, crystallinity, and electrical conductivity of polyaniline.[115] Fig. 4 describes the chemical polymerization mechanism of polyaniline in the acidic medium.[99] Generally, chemical polymeriz-

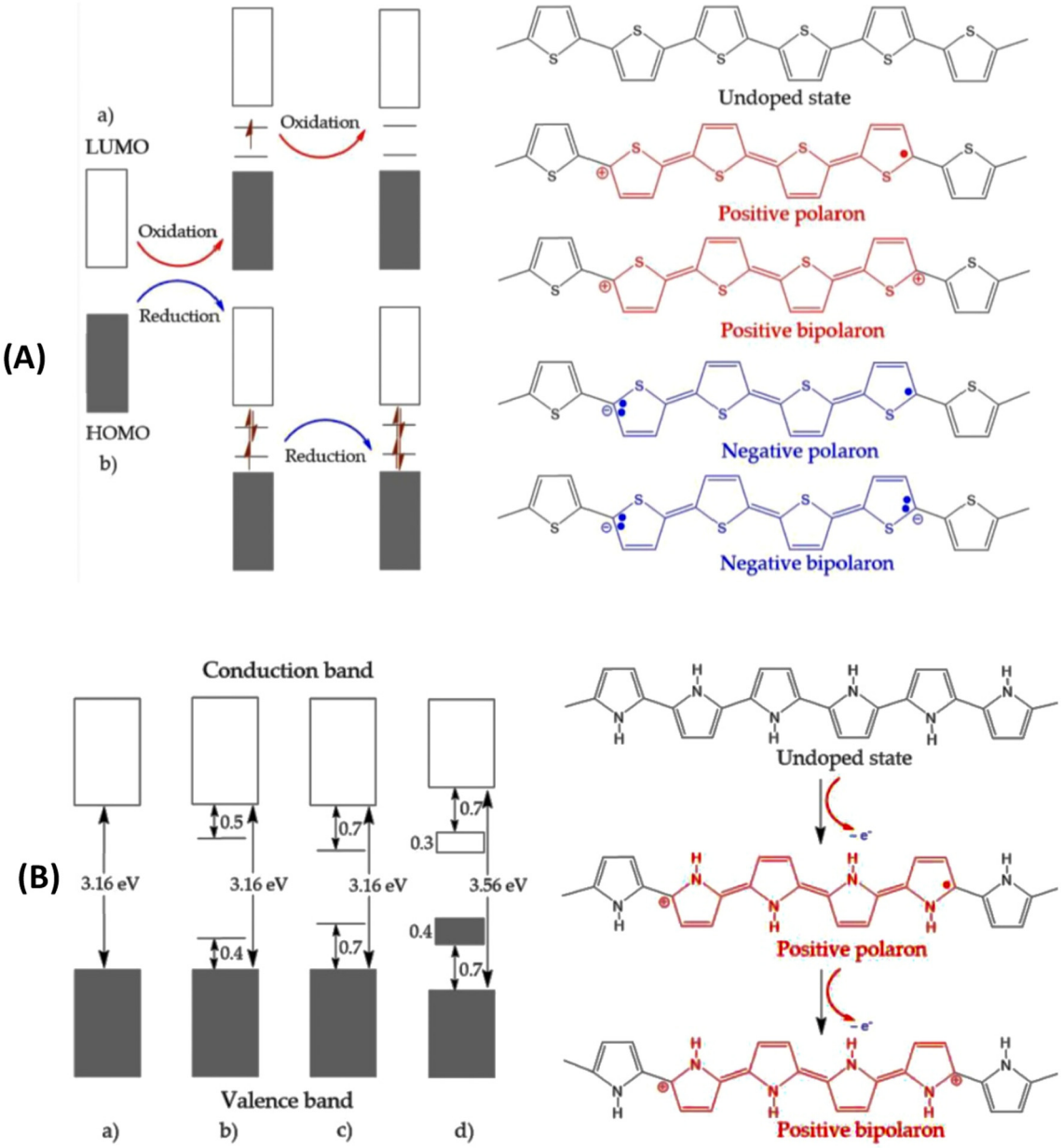

Fig. 3 (A) The electronic band and chemical structures of polythiophene (PTh) with (a) p-type doping and (b) n-type doping, and (B) electronic bands and chemical structures illustrating (a) undoped; (b) polaron; (c) bipolaron; and (d) fully doped states of polypyrrole.[102] Reproduced with permission from MDPI.

ation of aniline is carried out at 0 to 5 °C irrespective of the solvent, oxidant and surfactant used.[116–118] The details on the synthesis of polyaniline and its properties have also been recently reviewed.[119]

3.1.2 Polypyrrole. Polypyrrole was initially created as a black powdery material by the chemical oxidation of a pyrrole monomer in the presence of hydrogen peroxide.[120] However, processability, morphology, conductivity and environmental stability are some key issues that need to be addressed for the wide application range of chemically prepared PPy.[121–123] Polypyrrole has been prepared by combining anionic surfactants (sodium dodecyl benzene sulfonate, sodium alkyl naphthalenesulfonate, sodium alkylsulfonate) and $Fe_2(SO_4)_3$ (oxidant), exhibiting high conductivity and superior environmental stability[124] Further studies have also shown the enhanced conductivity and environmental stability of polypyrrole chemically prepared in the presence of an aqueous solution containing $Fe_2(SO_4)_3$ (oxidant), sulfonic surfactant and a phenol derivative.[125] The chemical oxidative polymerization of the pyrrole monomer is usually reported at room temperature in aqueous solution.[126]

The mechanism of pyrrole monomer polymerization has also received a considerable amount of attention.[127–131] The most widely accepted polymerization mechanism of PPy is dis-

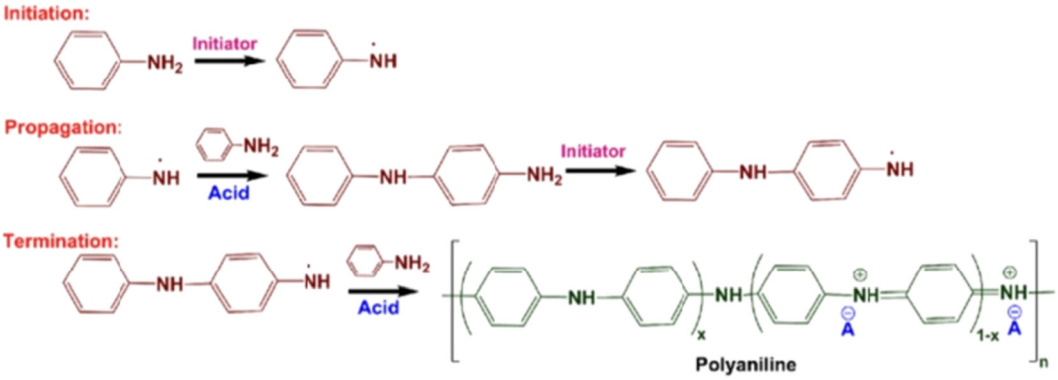

Fig. 4 Chemical polymerization mechanisms of polyaniline. Chemical polymerization of polyaniline is carried out in acidic medium by using a common initiator such as ammonium persulfate and potassium persulfate.[99] Reproduced with permission from ACS.

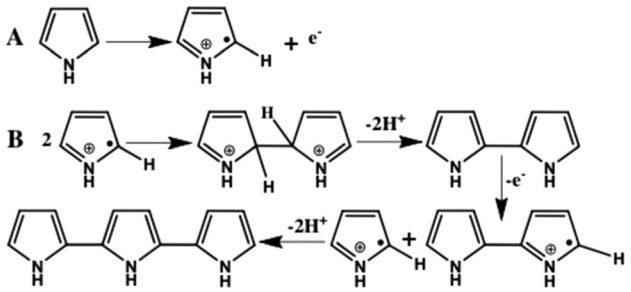

Fig. 5 The oxidation of a pyrrole monomer (A) and formation of dimer and trimer of pyrrole (B).[128] Reproduced with permission from Elsevier.

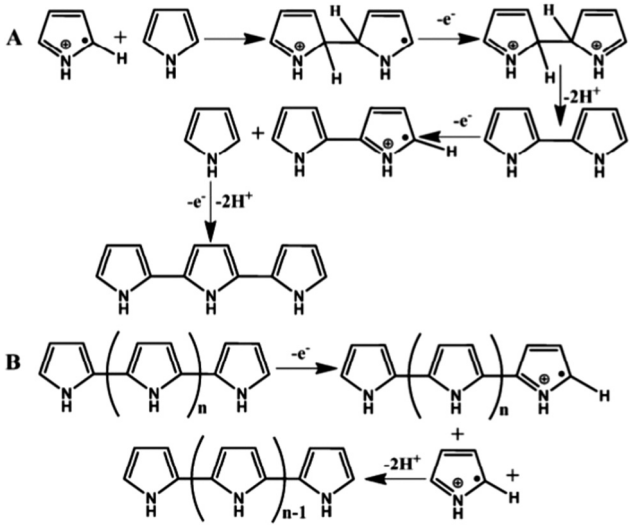

Fig. 6 The formation of dimer and trimer of pyrrole (A) and further formation of the PPy (B).[128] Reproduced with permission from Elsevier.

played in Fig. 5.[127,128] The oxidation of a pyrrole monomer yields a radical cation of the monomer in the initiation step (Fig. 5A). Coupling of the two generated radical cations then deprotonation produces a bipyrrole.[130] This bipyrrole in the propagation step is oxidized again and couples with another oxidized segment in the propagation step Fig. 5(B). Further continuation of the re-oxidation, coupling, and deprotonation ultimately leads to the formation of polypyrrole.

Another chemical oxidative polymerization mechanism has also been proposed. According to this, the radical cation in the propagation step of this mechanism reacts with a neutral monomer.[131] The dimer formed in this manner is oxidized to a dimeric radical cation that subsequently attacks another neutral monomer to form a trimer (Fig. 6(A)),[128] and polymer chains grow by the repeated process to ultimately form polypyrrole. Recently, Tan and Ghandi[127] observed that a commonly used mechanism (Fig. 5B) for the polymerization of pyrrole is not well suited for the formation of PPy in aqueous medium. Instead, the polymerization mechanism of polypyrrole follows a different mechanism, as schematically shown in Fig. 6.[128]

3.1.3 Polythiophene. Polythiophene and its derivatives have been receiving much attention due to their wide range of applications in electronic devices.[132] The formation of polythiophene can be achieved *via* the chemical oxidative polymerization of thiophene monomer using an oxidizing agent.[133,134] The most commonly accepted mechanism involves the formation of radical cations as a result of the oxidative polymerization of the thiophene monomer. The synthesis of different water-soluble polythiophenes has been reviewed for their multifunctional applications.[135]

3.1.4 Poly(3,4-ethylenedioxythiophene). Poly(3,4-ethylenedioxythiophene) (PEDOT) exhibits high conductivity, good physical and chemical stability and facilitates easy doping and solution processing, making it most appropriate in several advanced applications.[136–138] It can be prepared by the oxidative chemical polymerization of EDOT monomers in the presence of oxidants, such as $FeCl_3$, $Ce(SO_4)_2$ and $(NH_4)_2Ce(NO_3)_6$,[139,140] and oxidative chemical vapour deposition.[141,142] Ha *et al.*[143] studied the effect of the processing parameters that influence the oxidative polymerization of 3,4-ethylenedioxythiophene (EDOT) and a methanol-substituted derivative in maximizing the conductivity of the polymer. Ali *et al.*[144]

studied the effects of iron(III) *p*-toluenesulfonate hexahydrate oxidant on the growth of conductive PEDOT nanofilms prepared by vapor phase polymerization.

3.2 Electrodeposition methods

The electrodeposition method has been proved to be a versatile route for growing conducting polymers on a substrate for small-scale synthesis within a short reaction time under mild reaction conditions.[145] This technique is simple, rapid, cost effective and ensures good control of the micro/nanostructured polymer morphology, achieved with accurate process control, compared with other techniques.[146–153] The process is usually performed using a constant current or voltage approach, typically in a three-electrode (reference, working, and counter) cell containing the electrolyte and the monomer solution. The monomer of the conducting polymer undergoes electrochemical polymerization and is subsequently deposited on the surface of the substrate (Ti,[147] Mg,[149] Pt,[150] stainless steel,[150] carbon cloth,[151] glassy C,[152] indium tin oxide,[153] graphite sheet[154] *etc*). The effect of counter ions on the physical properties of polypyrrole electrochemically deposited on a Pt electrode has been reported.[155] The codeposition method has also been reported, similar to electrode coating, by dissolving the insulating polymer (host) in the electrolyte solution that also contains the monomer of the conductive polymer.[156]

Fig. 7 describes the electrochemical polymerization mechanisms of polyaniline carried out in the electrolyte solution of aniline and acid through application of a potential difference between the working and counter electrodes.[99]

3.3 Other methods

In addition, several other preparative methods for conducting polymers have been used, such as photopolymerization,[157] radio-frequency plasma polymerization,[158] organometallic cross-coupling reaction[159] and vacuum vapour phase polymerization.[160,161]

The properties of the conducting polymers are influenced by oxidant, monomer molar ratio, type of oxidizing agent, pH, polymerization temperature, time, concentration, electrolyte concentration, and degree of doping.[162–165] The electrical conductivity of most conducting polymers increases with dopant concentration and becomes saturated at a high doping level.[104] Temperature is another parameter playing a significant role in the synthesis of ICPs. The selection of solvent is also an important factor. Generally, the polymerization of PANI and PPy is reported using solvents like water, MeOH, THF, DMF, DMSO acetonitrile, propylene carbonate and sea water.[41,166–168] However, aqueous medium as a solvent is most desirable due to its relatively low cost, ease of handling and nontoxicity.

4. Synthesis of hollow and core–shell ICPs

The synthesis of hollow polymeric micro/nanospheres and micro/nanotubes of ICPs have been receiving much attention in recent years due to their promising applications in electromagnetic interference shielding and microwave absorption, environmental remediation and energy storage devices. In view of this, ICPs exhibiting multifaceted types of hollow morphology, such as hollow micro/nanospheres and micro/nanotubes, have been achieved through different approaches. These include direct and template-directed synthesis, the core–shell approach, self-assembly and electrospinning, and are described below.

4.1 Hard template method for single-shell hollow ICPs

Recently, template-assisted synthesis has attracted much attention in the fabrication of materials of well-defined morphology in terms of shape and size ranging from nanometer to micrometer range.[169–172] In this regard, template-assisted methods are considered as one of most accepted approaches for the synthesis of hollow-structured intrinsically conducting polymer materials. These templates can be classified into two types, namely hard and soft templates, based on the difference in their structure (Fig. 8(a)).[173] Hard templates are rigid structures in contrast to the soft templates characterized by flexible structures, with each approach guided by its own advantages and disadvantages.[174] The synthesis of materials using different types of templates is schematically shown in Fig. 8(b).[175]

However, the main challenge in the preparation of hollow morphology, such as spheres, using template methods lies in

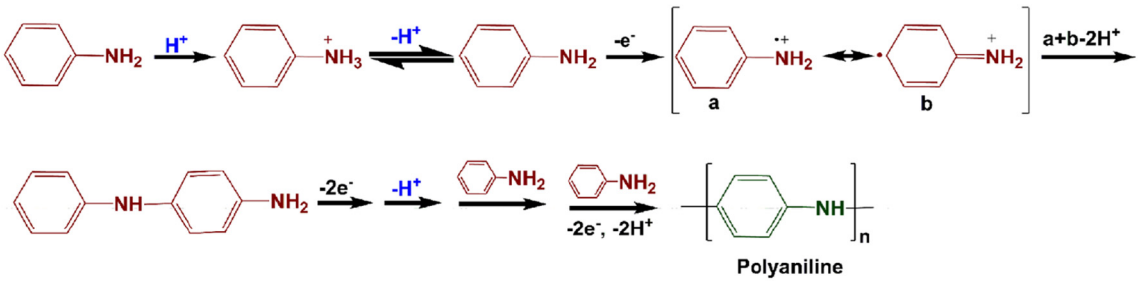

Fig. 7 Electrochemical polarization mechanism of polyaniline (electro-polymerization is carried out in the electrolyte solution of aniline and acid through applying a potential difference between the working and counter electrode).[99] Reproduced with permission from ACS.

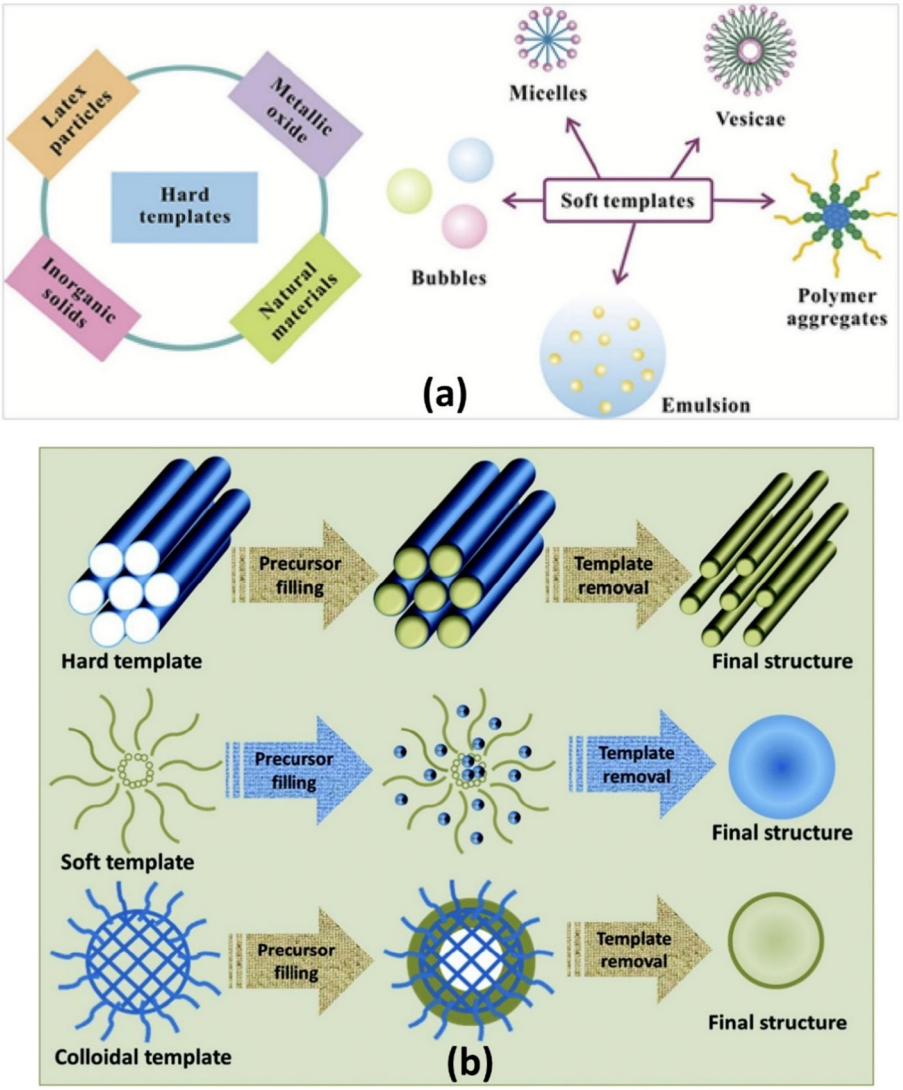

Fig. 8 (a) Representative materials that can be used as templates.[173] Reproduced with permission from Elsevier, and (b) schematic representation of the synthesis of materials using different types of templates.[175] Reproduced with permission from RSC.

the availability of suitable templates of definite size/shape, surface property, and production availability, and their subsequent removal through chemical or thermal means as an additional step to produce a void space.[176] In this regard, the hard template has great advantages, such as adjustable pore structure and morphology; nevertheless, the hard template method also has disadvantages.[171] It usually requires a core surface modification to ensure successful coating of shell substances.[173] Hollow structures can also be prepared by a soft template method as a viable option.[175,176] Although the hard template has high reproducibility and stability, its separation may be troublesome and may damage the structure of the desired materials with hollow morphology.[171] On the other hand, with the soft template it is easier to prepare nanomaterials of various sizes and shape due to the simplicity of the process involved, and its easy removal than the hard template.[171] In addition, soft templates are sensitive to solution environments (pH, solvents, ionic strength *etc.*), thereby limiting the application of the soft-core template processes.[177] The hollow morphology achieved by the hard template procedure is guided by its adjustable pore structure and morphology. As a result, several hollow nanostructures can be fabricated considering the availability of the wide range of such hard templates.[178]

4.1.1 Aluminium oxide. Anodized aluminium oxide (AAO) exhibits regular porous channels and can be prepared by subjecting aluminium to electrochemical oxidation in acidic solutions.[179] The pore diameter of the AAO can be adjusted by controlling the parameters of the anodization process, such as temperature, concentration, current density *etc.*[180] AAO is used as a template to synthesize 1-D nanostructures due to its several advantages, such as commercial availability, high chemical stability, uniform pore size, and its removal following established methods. Xiong *et al.*[181] used AAO for the syn-

thesis of highly ordered polyaniline nanotube arrays by *in situ* polymerization. The electrochemical polymerization method has been used in the preparation of doped and de-doped nanotubes and nanowires of polypyrrole, polyaniline, and poly (3,4-ethylenedioxythiophene) using Al_2O_3 nanoporous templates.[182] In another study, polypyrrole nano-tubule arrays were prepared by the electrochemical alternating current (ac) polymerization method using AAO membranes as the template.[183]

Cheng *et al.*[184] prepared highly uniform and ordered polypyrrole nanotube arrays with the help of porous anodic aluminium oxide following chemical oxidation polymerization for 2 hours. Functional polypyrrole nanotubes have been fabricated using the anodized aluminium oxide membrane as template in liquid phase polymerization conditions.[185] In another method, Jang *et al.*[186] adopted one-step vapour deposition polymerization to synthesize a highly uniform surface and tuneable wall thickness in polypyrrole nanotubes using anodic aluminium oxide template membranes soaked in ferric chloride aqueous solution.

Quasi-polyaniline hollow nanotubes (outer dia: 230 nm) were prepared by a dipping method based on the highly ordered porous anodic alumina membrane.[187] Poly(3, 4-ethylenedioxythiophene) tosylate film was grown in confined anodized aluminium oxide (nanopores) transferred onto cleaned ITO glass substrates following the chemical polymerization of the mixture comprising the solution of EDOT, iron(III)-tosylate in butanol and pyridine.[188] Liu *et al.*[189] electrochemically synthesized PEDOT nanotube arrays in the cylindrical pores of an alumina template membrane using acetonitrile solution of 20 mM EDOT.

4.1.2 Mesoporous silica. Mesoporous silica has attracted attention in various applications due to its high specific area, good hydrophobicity, low cytotoxicity, large pore volume and tunable pore size.[171,190] Mesoporous silica has also been used as a template in the preparation of intrinsically conducting polymers, like PANI and PPy with hollow structures. The process involves coating silica particles with PANI (PPy) followed by the expulsion of the silica template (core) by etching it in NaOH or HF to leave behind a hollow PANI (PPy) shell, respectively.

Fu *et al.*[191] initially prepared silica nanoparticles with surface-grafted polymer of 4-vinylaniline (SiO_2-*g*-PVAn) according to the scheme displayed in Fig. 9(a). Subsequent surface oxidative graft copolymerization of aniline using the aniline moieties of PVAn and deprotonation followed by exposure to HF produced hollow nanospheres of P(VAn-*graft*-PANI) (thickness of shell: ~15–40 nm, core void dia: ~25 nm). A mesoporous polyaniline hollow nanosphere with average diameter and thickness of 330 nm shell 78 nm, respectively, has been prepared using SiO_2@resorcinol-formaldehyde/SiO_2 as substrate followed by *in situ* polymerization of aniline on its surface and subsequent expulsion of the silica shell by dispersing it in HF at room temperature.[192] Li *et al.*[193] prepared Pt/PPy hollow hybrid microspheres by using NH_2-functionized SiO_2 as template decorated with H_2PtCl_6, Fig. 9(b). In another study, SiO_2/polymethacrylic acid (PMAA) microspheres were used as templates to synthesize hollow polypyrrole microspheres (Fig. 9(c)).[194]

4.1.3 Organic polymers and other inorganic materials

4.1.3.1 Hollow polyaniline. Among several hard templates, polystyrene microspheres have attracted much attention in synthesizing spherically shaped particles, spherical core–shell and hollow structures.[195–199] Bai *et al.*[200] prepared colloidal hollow spheres of conducting polymers (PANI and PPy) by using sulfonated polystyrene beads as a templating agent. In another study, hollow PANI and PPy microspheres were prepared by oxidative chemical oxidation of the respective monomers using sulfonated polystyrene microspheres as template (size: 2.2–3.4 μm).[201] Niu *et al.*[202] prepared PANI capsules and hollow PANI spheres with controlled shell thickness and cavity size using sulfonated polystyrene as a template. Sulfonated polystyrene particles have been used as template to synthesize hollow polyaniline[203] and polypyrrole[204] by emulsion polymerization of the individual monomers in acid solution and ammonium persulphate (oxidant). Saraf *et al.*[205] prepared hollow microspheres of PANI doped with styrene sulfonic acid (size: 0.5–1 μm) through a chemical route by maintaining the dopant : monomer : oxidant ratio as 1 : 1 : 1.

Mangeney *et al.*[206] used polystyrene latex particles (dia: 1.33 μm) to prepare PPy-coated PS latex polystyrene bearing surface-protonated *N*-propyl amino functional groups in aqueous solution by copolymerization of pyrrole and *N*-aminated pyrrole (pyrrole-NH_2) using $FeCl_3$. Furthermore, the fabricated (PS-PPyNH_2) particles were subsequently decorated with citrate-stabilized gold nanoparticles, as shown in Fig. 9(d). Uniform polyaniline thin shells and hollow capsules were fabricated using polyelectrolyte-coated microspheres as templates.[207] Monodisperse hollow polyaniline nanospheres with controlled surface smoothness were synthesized by *in situ* polymerization of aniline monomers adsorbed on a carboxyl-functionalized polystyrene surface.[208] In another study, Sung *et al.*[209] synthesized submicron-size hollow PANI dicarboxylate salt to study the influences of alkyl chain length, functional group and stable dispersion on its electrorheological performance.

Polyaniline/Au composite hollow spheres were successfully synthesized using polystyrene/sulfonated polystyrene as the templates.[210] The thickness of the PANI shell can be well controlled by adjusting the amount of aniline monomer. Fig. 10 (a–d) shows the morphology of PANI (A: SEM; C: TEM) and PANI/Au (B: SEM; D: TEM) composite hollow spheres under specified preparative conditions. The possible formation of hollow PANI spheres and its Au composites are presented in Fig. 11. Gao *et al.*[211] fabricated hollow polyaniline microspheres in the presence of Cu rings as template using $H_4SiW_{12}O_{40}$ and ammonium persulfate as dopant and oxidant, respectively. Zhang and Liu[212] synthesized hollow polyaniline nanoparticles *via* the chemical oxidative polymerization of aniline using γ-Fe_2O_3 nanoparticles as the reactive templates in the presence of hydrochloric acid. Their studies have shown that reacting temperature played a vital role in the formation

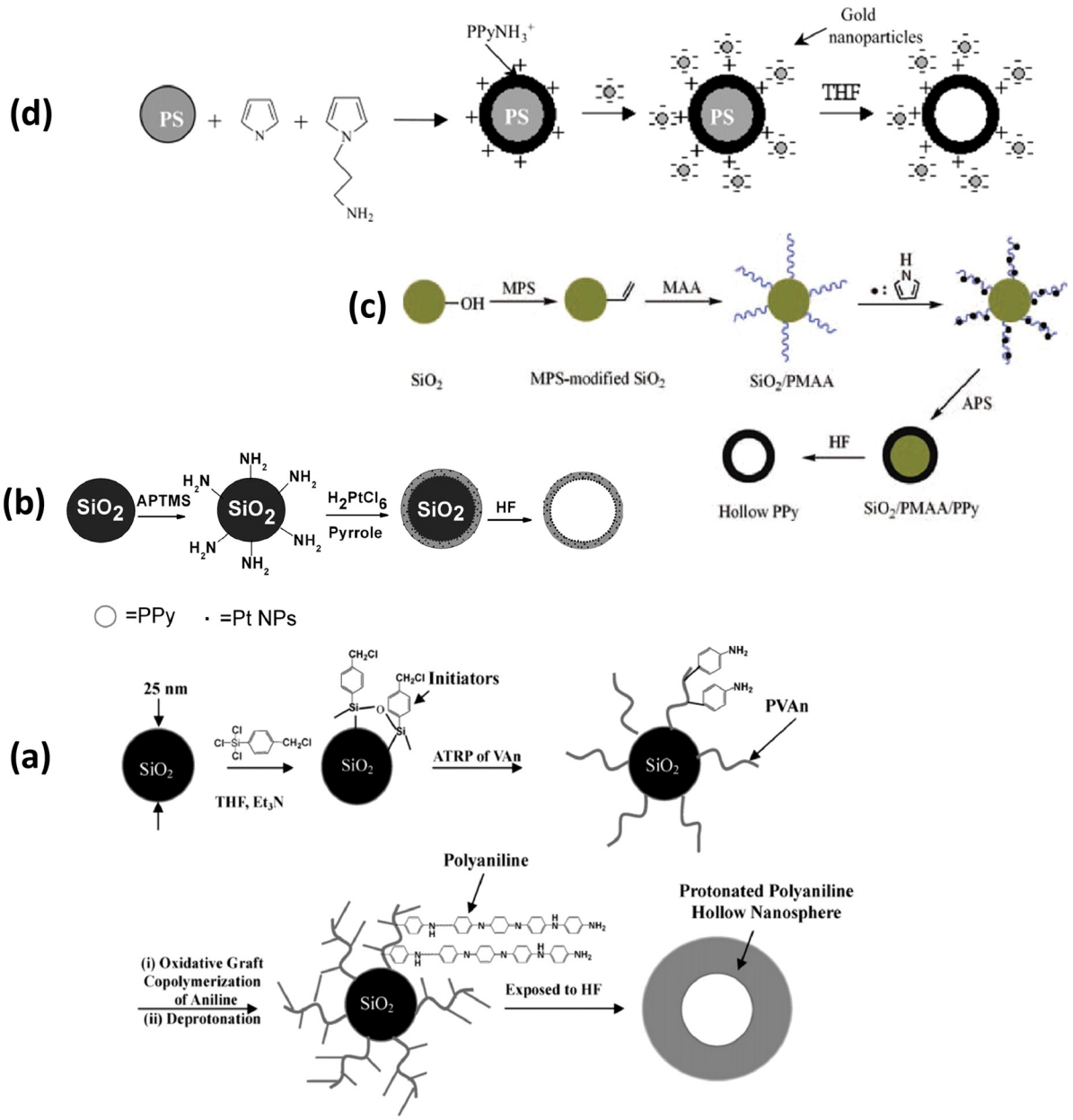

Fig. 9 (a) Preparation of conductive poly(4-vinylaniline-*graft*-polyaniline), or P(VAn-*g*-PANI), hollow nanospheres *via* surface-initiated atom transfer radical polymerization (ATRP) and oxidative graft copolymerization.[191] Reproduced with permission from ACS. (b) The illustration of the formation of Pt/PPy hollow spheres.[193] Reproduced with permission from Wiley. (c) Formation of SiO_2/PMAA/PPy nanocomposite and PPy hollow spheres.[194] Reproduced with permission from Wiley. (d) Schematic representation of the assembly of negatively charged gold nanoparticles on the surface of positively charged core–shell polypyrrole–polystyrene latex particles bearing surface-protonated *N*-propylamino groups.[206] Reproduced with permission from ACS.

of the hollow nanoparticles. Halloysite was used as a hard template to prepare polyaniline–polypyrrole binary composite nanotubes.[213] Gao and coworkers[214] demonstrated the fabrication of polyaniline nanotubes using the inner eggshell membrane as a template. Their investigations revealed the key role played by the pore size of the template in the formation of polyaniline nanotubes.

Zhu *et al.*[215] reported the double surfactant-layer of polyvinylpyrroldine (PVP) and sodium dodecyl sulfate (SDS)-assisted oxidative polymerization using monodisperse metal oxides (CuO, Fe_2O_3, In_2O_3) as templates (Fig. 12(a)). Following this, hollow PANI nanocapsules were prepared by dissolving metal oxides in acid solution. The method has also been used to prepare nanocomposites of CuO/PANI, Fe_2O_3/PANI, In_2O_3/PANI and Fe_2O_3/Si O_2/PANI. Further investigations revealed the formation of well-controlled core/shell metal oxides/PANI nanocomposites and PANI capsules. Hollow octahedral PANI nanocapsules have been fabricated using Cu_2O (octahedral) as

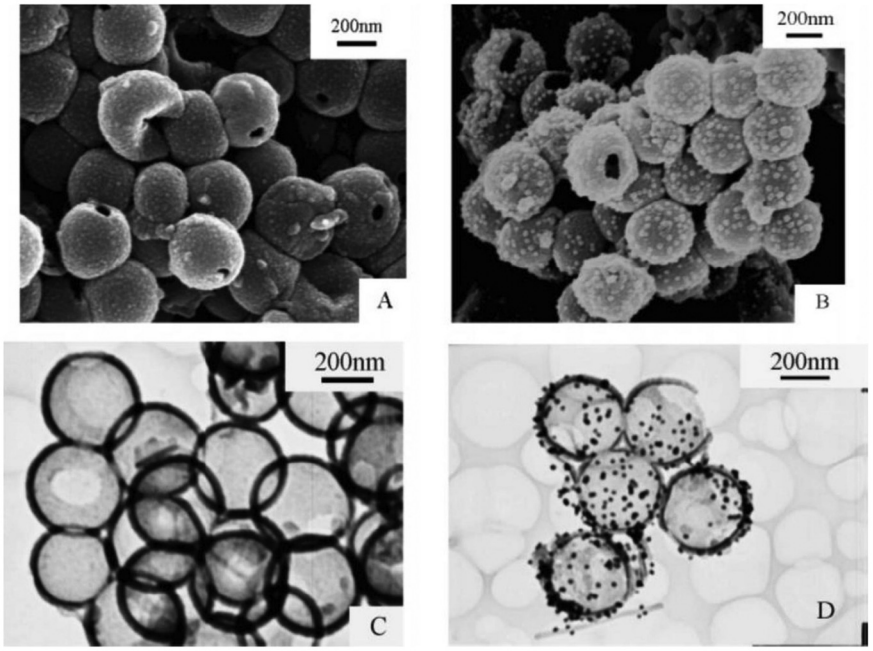

Fig. 10 SEM and TEM images of PANI (A: SEM; C: TEM) and PANI/Au (B: SEM; D: TEM) composite hollow spheres (Synthetic conditions: aniline, 1 mmol, APS, 1 mmol, concentration of PANI in the Au colloid, 1.0 mg mL^{-1}).[210] Reproduced with permission from ACS.

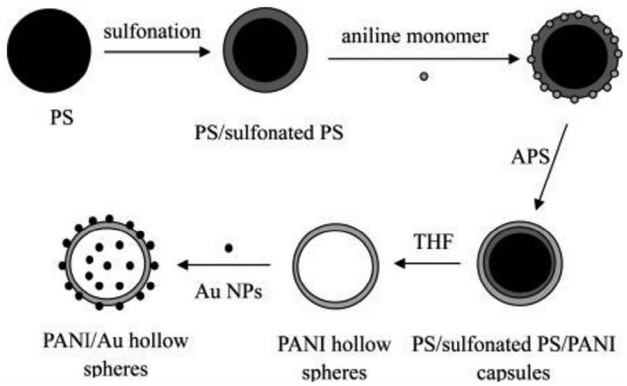

Fig. 11 Scheme of the preparation of PANI and PANI/Au hollow spheres.[210] Reproduced with permission from ACS.

template in the presence of H_3PO_4.[216,217] It may be noted that the removal of the Cu_2O template is not required, compared with other conventional methods, due to its reaction with ammonium persulfate (oxidant) to form a soluble Cu^{2+} salt during the process of the polymerization. The synthesis of nanorings and flat hollow capsules of polyaniline was also reported *via* the chemical oxidative polymerization of aniline using $VOPO_4$ $2H_2O$ nanoplates acting as oxidant and sacrificial template.[218]

4.1.3.2 Hollow polypyrrole. The most common synthetic approach for the fabrication of the hollow polypyrrole microsphere was followed by a core (polystyrene, PS)/shell (polypyrrole) approach. This involved the *in situ* chemical oxidative copolymerization of the pyrrole monomer on the surface of a sulfonated PS microsphere followed by the extraction of the PS cores in a suitable solvent like tetrahydrofuran.[219–224] Zhang *et al.*[225] prepared polypyrrole-polystyrene (PPy-PS) hybrid hollow spheres by oxidative polymerization of pyrrole $FeCl_3$ $6H_2O$ in an emulsion of PS latex, as shown in Fig. 12(b). It was suggested that the formation of PPy-PS hybrid hollow spheres could be induced by capillary forces that exist among the PPy nanoparticles (granular) deposited on the surfaces of PS latex at the start of the reaction. Hollow polypyrrole microcapsules (dia: 527 nm, shell thickness: 20 nm) have been reported, by the cosolvent approach using a polystyrene core as a template.[226] Marinakos *et al.*[227] used Au nanoparticles as templates in synthesizing nanometer-sized hollow PPy nanocapsules. Mesoporous hollow polypyrrole spheres have been fabricated by a chemical polymerization method using silica spheres as hard templates.[228] Su *et al.*[229] reported the synthesis of polypyrrole hollow nanospheres using poly(methyl methacrylate) nanospheres as templates. Chang *et al.*[230] carried out *in situ* polymerization of pyrrole in the presence of polystyrene (PS) latex particles. Subsequent removal of the core (PS) resulted in the formation of hollow spherical polypyrrole balls.

According to Qu and Shi,[231] the direct electrochemical oxidation of pyrrole in an aqueous solution of poly(styrene sulfonic acid) resulted in microstructures with hollow interiors comprising microspheres, microcrocks, microbowls, and micropumpkins. A stepwise electropolymerization process has been adopted in producing the nanostructured arrays of hollow polypyrrole with a conical shape.[232] The pores of nanoporous polycarbonate membrane were used as templates to chemically synthesize polypyrrole nanotubules.[233] Kros

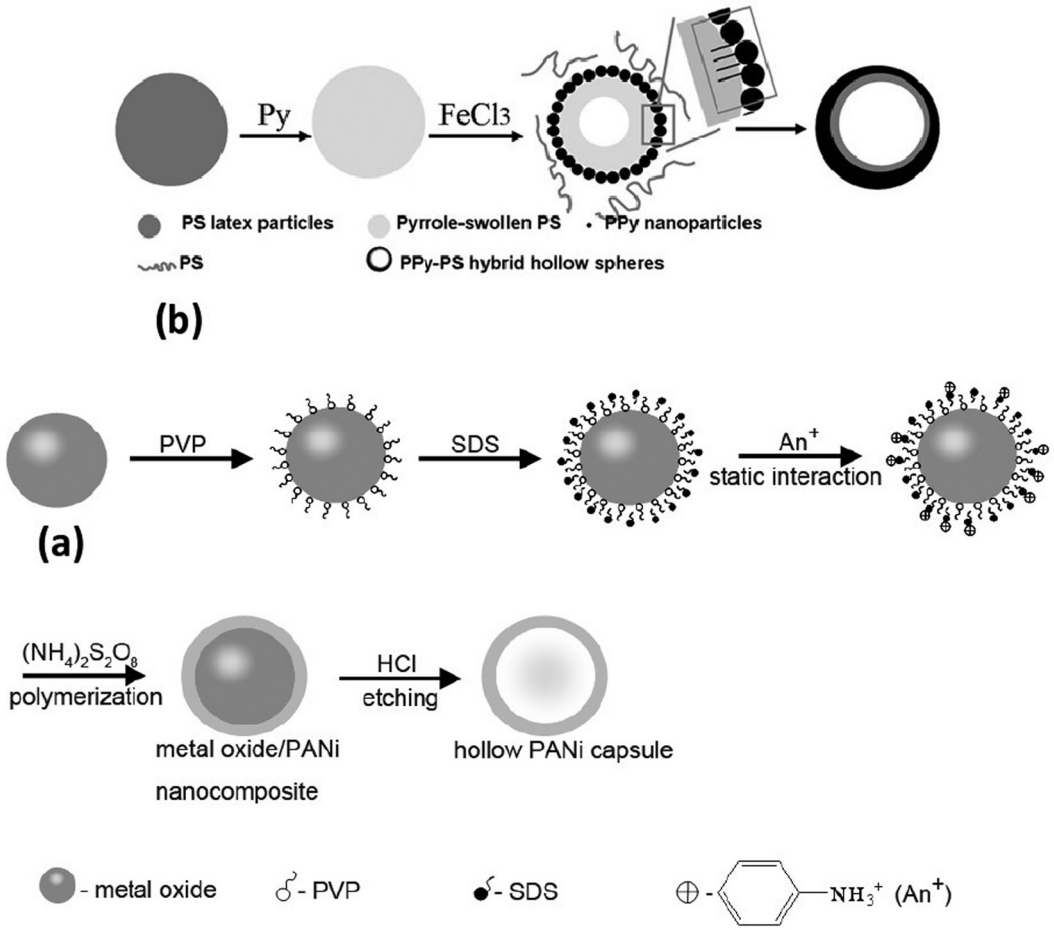

Fig. 12 (a) Schematic illustration for the formation of well-controlled core/shell metal oxides/PANi nanocomposites and PANi capsules.[215] Reproduced with permission from IOP. (b) The fabrication process of PPy-PS hybrid hollow spheres.[225] Reproduced with permission from Elsevier.

et al.[234] carried out the polymerization of monomers (*e.g.*, pyrrole, thiophenes) inside the pores of track-etched polymeric membranes. The hollow tubules formed in this manner exhibited relatively enhanced electrical properties compared with their respective bulk analogues. In another work, a ZSM-5 molecular sieve was used as a template to synthesize hollow pyrrole–platinum complex spheres following the chemical polymerization of pyrrole with potassium hexachloroplatinate(IV) as oxidant.[235] Dubal *et al.*[236] synthesized polypyrrole nanotubes using MnO_2 as a sacrificial template in the presence of pyrrole 1 M HCl and $K_2Cr_2O_7$. Hollow nanotubes of polypyrrole have been prepared rapidly by chemical oxidative polymerization of pyrrole in the presence of V_2O_5 nanofibers (sacrificial template) and $FeCl_3$ as oxidant. This was followed by the removal of the template by dissolving it in aq. 1.0 M HCl.[237] In another study, MnO_2 powder was selected for a simultaneous dual role as oxidizing agent and sacrificial template in the chemical synthesis of hollow sea urchin-shaped polypyrrole.[238] In another study, polystyrene beads were used as the sacrifice template to prepare hollow polypyrrole nanoparticles.[239] Capsular PPy hollow nanofibers were fabricated by polymerizing pyrrole monomer on hollow V_2O_5 fibers (template) and subjected to acid etching to remove the V_2O_5 template.[240] In addition, Fe_3O_4@polypyrrole hollow capsules[241] and Fe_3O_4@PPy yolk/shell composites[242] were also prepared by a hard-template method.

4.1.3.3 Hollow poly(3,4 ethylenedioxythiophene) (PEDOT). Rehmen *et al.*[243] carried out vapor deposition of tosylate-doped PEDOT in fabricating hollow nanosphere coatings using polystyrene as template on carbon paper electrodes. In another study, PEDOT hollow nanospheres were successfully synthesized from SiO_2/PEDOT core/shell nanospheres by subjecting SiO_2 to chemical oxidative polymerization followed by etching of SiO_2 by hydrofluoric acid.[244] Luo *et al.*[245] coated functionalized PEDOT on a polystyrene core in aqueous solutions. The subsequent removal of this core by dissolving it in an appropriate organic solvent produced hollow PEDOT particles with single holes and PEDOT capsules. According to Zhang *et al.*,[246] PEDOT hollow spheres were fabricated using sulfonated polystyrene sphere template-assisted interfacial polymerization and introduced into the MXene film as an attractive flexible electrode for energy storage. ZnO microflower arrays have been used as a template to synthesize hollow microflower arrays of PEDOT with several two-dimensional

hollow nanopetals on each microflower.[247] Cheng *et al.*[248] electrodeposited poly(3,4-ethylenedioxythiophene) hollow microflower film onto a fluorine-doped tin oxide glass substrate using a film of ZnO microflowers as the template.

4.2 Soft template method and template-free approach for single-shelled ICPs

The choice of soft template and template free approach in synthesis of conducting polymers are guided by its multifaceted advantages such as the simplicity of the process, good repeatability and no requirement for its removal. This method is invariably used in the synthesis of conducting polymers nanotubes, hollow spheres and yolk–shell sphere-type materials.[173,249–253] In this regard, several structural directing agents are used, such as surfactants, block copolymers, amino acids, urea, methyl orange *etc*. The presence of these molecules aligns the monomers of the conducting polymers in solution and facilitates the overall polymerization process into the desired nanostructures like tubes or spheres by forming micelles or self-assembled structures around the monomers.

4.2.1 Hollow polyaniline. Zhang *et al.*[254] used a self-assembly method to synthesize PANI nanotubes (dia: 150–340 nm) in the presence of inorganic acids (*e.g.*, HCl, H_2SO_4, HBF_4, and H_3PO_4) as dopants with and without a surfactant. In the presence of a surfactant (sodium dodecylbenzenesulfonate and hexadecyltrimethylammonium bromide), the formation of the nanostructures took place due to the formation of micelles by anilinium cations and surfactant anions acted as templates, whereas in the absence of a surfactant the anilinium cation micelles formed were considered as templates. Further investigations indicated that the morphology, size, and electrical properties of the resulting nanostructures were guided by experimental conditions and dopant structure. The role played by the acidity profile in the nanotubular growth of polyaniline has been analysed to study its preparatory conditions by oxidizing aniline with ammonium peroxydisulfate in 0.4 M acetic acid.[255] These findings indicated that the neutral aniline molecules were oxidized to non-conducting aniline oligomers at pH > 3 and acted as templates for the subsequent growth of PANI nanotubes.

Han *et al.*[256] synthesized polyaniline nanotubes by the oxidative polymerization of aniline in dilute solution in the presence of cetyltrimethylammonium bromide. Self-assembled PANI nanotubes with a rectangular cross-sectional shape have been synthesized by *in situ* chemical oxidation polymerization in the presence of citric acid as the dopant.[257] In another study, Zhang *et al.*[258] prepared polyaniline nanotubes by a self-assembly process using carboxylic acids (propionic acid, lactic acid, succinic acid, malonic acid, tartaric acid, and citric acid) as dopants. They also investigated the effect of hydrogen bonding on the formation of nanotubes and aggregated dendrites of polyaniline. Highly crystalline polyaniline nanotubes and nanofibers have been synthesized in the presence of dicarboxylic acids (oxalic acid, malonic acid, succinic acid, glutaric acid, and adipic acid) (acting as dopants).[259] Zhang *et al.*[260] fabricated nanotubular polyaniline (self-assembled) following the chemically synthesized by ammonium persulfate oxidation of aniline in the presence of amino acid. The role played by the amino acids in this study is guided by their effect on the initial soft template for the growth of nanotubes based on the formation of micelles or oligomeric species during the initial stage of aniline oxidation. Rana *et al.*[261] used a soft template method to prepare PANI nanotubes of almost uniform diameter by selecting benzene 1,2,4,5-tetracarboxylic acid, acting simultaneously as dopant acid as well as structure-directing agent. Huang and Wan[262] investigated the influence of the molecular structure of sulfonic acids on the tubular morphology of the doped PANI. According to this, β-NSA-doped PANI exhibited tubular morphology by preparing it using an *in situ* doping polymerization method. Hollow PEDOT spheres (dia: 1.7–4.6 μm) were synthesized by aqueous chemical polymerization using self-assembled membrane of poly(3,4-ethylenedioxythiophene) doped with acetic acid at room temperature and ammonium persulfate as oxidant.[263]

Alternatively, synthesis of self-assembled polyaniline nanotubes has also been reported using itaconic acid,[264] camphor sulfonic acid,[265] polymeric acids: poly(4-styrenesulfonic acid), poly(acrylic acid), poly(methyl vinyl ether-alt-maleic acid),[266] malic acid, succinic acid, citric acid, and tartaric acid[267] as dopants. Mu *et al.*[268] reported the fabrication of self-assembled polyaniline nanotubes doped with D-tartaric acid for high-performance supercapacitor applications. Zhang and Wan[269] synthesized chiral polyaniline nanotubes following the self-assembly process using (1*R*)-(−)-10-camphorsulfonic acid (L-CSA) and (1*S*)-(+)-10-camphorsulfonic acid (D-CSA). It was noted that the formation yields and the size of the doped polyaniline nanotubes were guided by the molar ratio of CSA to aniline. Panigrahi and Srivastava[270] reported the synthesis of polyaniline hollow microspheres by the ultrasound-assisted emulsion polymerization technique using polystyrene microspheres as a template.

Zhang *et al.*[271] reported a self-assembly process for the syntheses of polyaniline nanotubes (dia:130–250 nm) doped with α-naphthalene sulfonic acid, β-naphthalene sulfonic acid, and 1,5-naphthalene disulfonic acid. According to Sun and Deng,[272] DL-tartaric acid played an important role as a dopant in determining the morphology of polyaniline prepared by interfacial oxidation polymerization of aniline using APS as the initiator. These findings led to the formation of spherical mushroom-like morphology and nanotubes of polyaniline corresponding to the DL-tartaric acid concentration of ~0.02 M and ~0.04 M, respectively.

Qiu *et al.*[273] synthesized polyaniline nanotubes (dia:100–300 nm, length: up to 2 μm) through a template-free polymerization using $(NH_4)_2S_2O_8$ as an oxidant and a protonic acid dopant (C_{60}-$(OSO_3H)_6$ or $PAMAM_{4.0}$ [naphthyl $(SO_3H)_2]_{24}$). The formation of oriented arrays of polyaniline nanotubes (60 to 150 nm in diameter) were also reported by hydrogen-bonding directionality in the presence of a crown ether derivative and ammonium persulfate in HCl solution.[274] Poly(2-acrylamido -2-methylpropane sulfonic acid) has been used as a

dopant as well as soft template for the synthesis of uniform hollow microspheres of PANI (dia: 410 nm, shell thickness: 72 nm) in aqueous solution following *in situ* polymerization of aniline in the presence of ammonium persulfate.[275] Huang *et al.*[276] reported a template-free method following inversed microemulsion polymerization in fabricating polyaniline hollow microspheres (outer dia: 4–6 mm, shell thickness: 150–250 nm) using β-naphthlene sulfoinic acid as dopant. Zhu *et al.*[277] prepared superhydrophobic rambutan-like hollow spheres of polyaniline by a self-assembly method in the presence of perfluorooctane sulfonic acid (dopant and soft template).

Zhang and Wan[278] reported transformation of self-assembled polyaniline from 1 D nanotubes (dia: ~109–150 nm) to hollow microspheres by changing the molar ratio of the dopant (salicylic acid) to monomer (aniline). The freeze-fracture electron microscopy studies revealed the role played by hollow spherical micelles comprising salicylic acid/aniline as templates in the formation of nanotubes/hollow spheres. The driving force in the self-assembly of hollow microspheres might be due to be the hydrogen bonding of the –OH group (salicylic acid) and amine group (polyaniline). Liang *et al.*[279] synthesized polypyrrole nanotube aerogels by using the weakly interconnected network of self-assembled nanotubes of lithocholic acid as a soft template.

Hollow nanospheres of methyl-substituted polyaniline[280] and poly(*m*-methylaniline)[281] microspheres were prepared through the self-assembly processes in the presence of ammonium persulfate. Tavandashti *et al.*[282] studied the transition of polyaniline from nanotubes to nanospheres following a soft template route, as schematically displayed in Fig. 13(a and b). According to this, the fabrication of polyaniline nanospheres was carried out *via* the oxidative polymerization of aniline in the presence of β-naphthalenesulfonic acid (β-NSA) as both surfactant and dopant, and ammonium persulfate as oxidant at 2–5 °C. Furthermore, control of the morphology of polyaniline was achieved by changing the reaction conditions. Ding *et al.*[283] prepared PANI nanotubes with diameters of 100–150 nm of single nanotubes by carrying out direct oxidation with APS in the absence of hard templates and acidic dopants. During this, the formation of the hollow spheres at the initial stage was accompanied by the micelles (soft template) formed by the aniline monomer in aqueous solution. Furthermore, investigations revealed a decrease in pH with

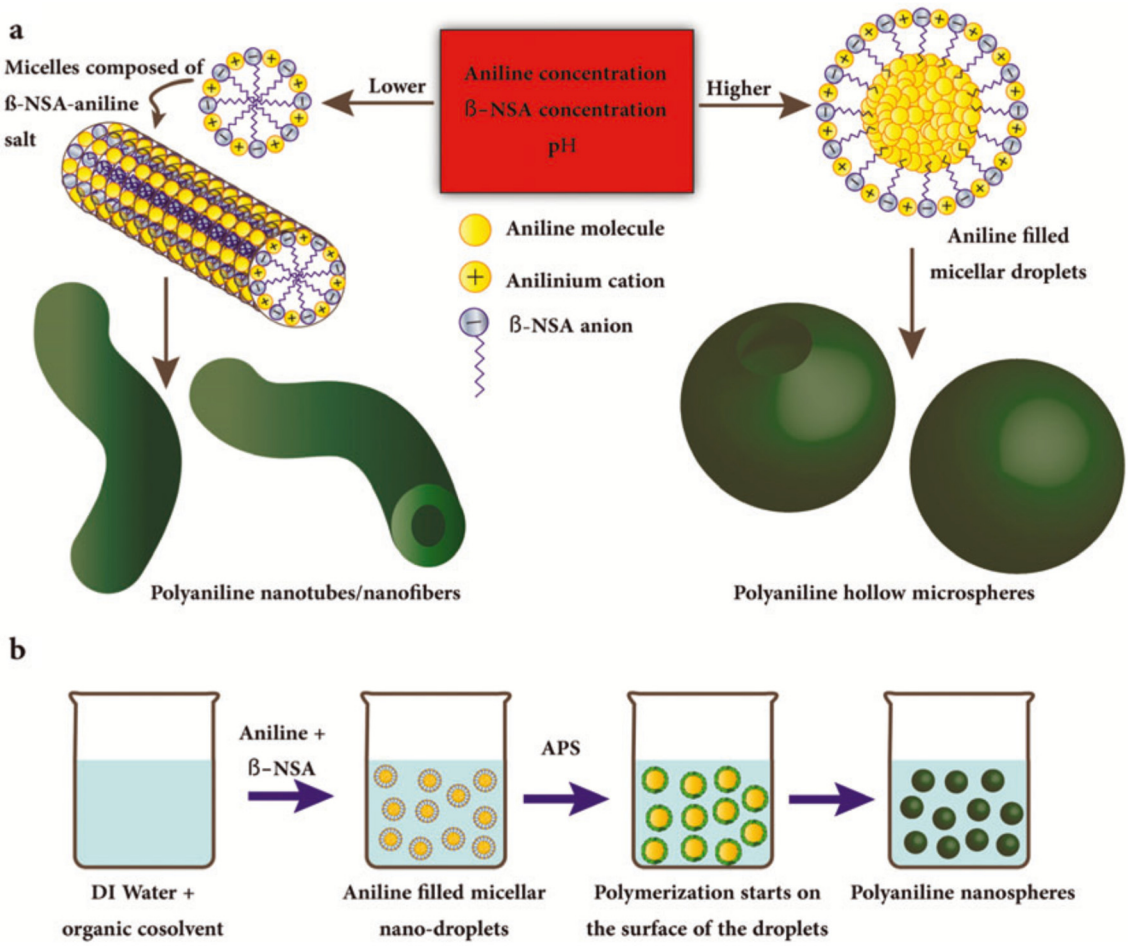

Fig. 13 The schematics of the formation mechanisms of (a) PANI nanotubes/nanofibres and hollow microspheres and (b) PANI nanospheres.[282] Reproduced with permission from Wiley.

increasing polymerization time resulted in a change in the morphology from hollow spheres to short and long tubes. Triton X-100 has been selected as a soft template to fabricate poly(aniline-copyrrole) hollow nanospheres *via* oxidative polymerization of aniline.[284] In a micelle-mediated phase transfer method, perfluorooctanoic acid/aniline acted as soft templates to form hollow nano/microspheres of polyaniline with mesoporous brain-like convex-fold shell structures.[285]

Vitamin C upon the addition of aniline monomer ([Vitamin C]/[Aniline] = 0.25) produced polyaniline nanotubes (dia.: 80–120 nm, length extending to several micrometers) *via* the oxidative polymerization method.[22] Ren and others[286] adopted a soft template method in the fabrication of a polyaniline microtube acidic solution using methyl orange as dopant in the presence of aniline monomer and ammonium peroxydisulfate. According to this, methyl orange is self-assembled into supramolecular aggregates and acts as templates in the formation of PANI microtubes. Urea has also been used as a soft template in the synthesis of polyaniline nanotubes by *in situ* chemical oxidative polymerization of aniline monomer.[287] Orellana and Roberts[288] used a simple approach for preparing polypyrrole microtubes without the need for a solution or substrate-based template. Wang *et al.*[289] synthesized polypyrrole nanotubes of ~50 nm diameter and a length extending to several micrometers using pyrrole, $FeCl_3{\cdot}6H_2O$, and methyl orange as monomer, initiator, and soft template, respectively.

A self-assembly method has been used to synthesize polyaniline nanotubes in the excess of $(NH_4)_2S_2O_8$ oxidant.[290] This could be ascribed to the formation of aniline dimer cation-radicals acting as effective surfactants. Zhang *et al.*[291] fabricated polyaniline hollow spheres with controllable size and shell thickness through the oxidation–reduction reaction-driven approach under hydrothermal conditions in the absence of any sacrificial templates and organic surfactants and using H_2O_2 and Fe^{3+} as oxidant and catalyst, respectively. Hollow polyaniline microsphere were also prepared by polymerization of aniline in aqueous medium using $K_3[Fe(CN)_6]$ as oxidant.[292] Wei and Wan[293] synthesized hollow microspheres of PANI (dia: 450–1370 nm) using aniline emulsion template doped with β-naphthalene sulfonic acid at −10 °C in the presence of ammonium persulfate acting as the oxidant. Investigations are also reported on the synthesis of PANI nanotubes, nanotubes with rectangular and circular cross-section hollow microspheres[294] and 3D hollow microspheres assembled from 1D PANI nanowires.[295]

Liu *et al.*[296] reported a template-free method to synthesize polyaniline film (thickness: 100 nm) embedded with PANI nanotubes without any surfactant or organic acid. Their studies revealed that oligomers with certain structures are responsible for the growth of the nanotubes. A micelle soft-template method was used in fabricating PANI nanotubes (external dia: 110 internal dia:, 10 nm, length: several μm) in the presence of oxalic acid as a dopant.[297] Tajima *et al.*[298] used nanobubble soft templates formed by ultrasonic irradiation in the synthesis of hollow polypyrrole spheres.

4.2.2 Hollow polypyrrole, polythiophene and PEDOT. In comparison with polyaniline, the fabrication of other hollow ICPs, especially polythiophene and polythiophene and PEDOT, has received less attention. Bhattarai *et al.*[299] employed a sacrificial template-based synthetic approach for fabricating polypyrrole hollow fibers by using sacrificial removal of electrospun polycaprolactone acting as a soft template. In another method, one-step *in situ* polymerization has been employed to synthesize azo-functionalized polypyrrole nanotubes in the presence of $FeCl_3$ and methyl orange.[300] In this, the formation of a fibrillar complex of $FeCl_3$ and methyl orange acts as reactive self-degrading template to facilitate the hollow nanotubular structure of PPy. Wang *et al.*[301] prepared micro/nanoscale highly electroactive PPy galvanostatically with a hollow 'horn'-like structure in a *p*-toluenesulfonate alkaline solution without any templates.

Xia *et al.*[302] used poly(vinylpyrr1olidone) (PVP) as a soft template in order to fabricate PEDOT exhibiting hollow spheres (size: 130–820 nm) *via* a self-assembly method. Bian *et al.*[303] used star-like unimolecular micelles as templates for the controlled syntheses of hollow nanostructures of polythiophene nanoparticles. A reverse emulsion polymerization was described using sodium bis(2-ethylhexyl) sulfosuccinate cylindrical micelles as the template at room temperature for the synthesis of PEDOT nanotubes (dia: 50–100 nm, length: 10–20 mm).[304] The synthesis of self-assembled 3D hierarchical PEDOT micro/nanostructures including hollow spheres and double-layer bowls was carried by a template-free method in the presence of perfluorosebacic acid as the dopant and $FeCl_3$ $6H_2O$ as the oxidant.[305] Ali *et al.*[306] synthesized PEDOT/Au hollow nanospheres by an *in situ* polymerization method comprising the ratio of EDOT and $HAuCl_4$ from 2 : 1 to 1 : 2. In another study, a surfactant-free Ouzo emulsion method was used to synthesize hollow or partially collapsed bowls of PEDOT using $FeCl_3{\cdot}6H_2O$, acetone, and toluene as oxidant, solvent, and anti-solvent, respectively (Fig. 14(a)).[307] This method has also been extended in successfully synthesizing PANI, PPy and PTh. Fig. 14(b–d) show the SEM images of PEDOT under different experimental conditions. Ni *et al.*[308] used the chemical polymerization of EDOT to synthesize hollow PEDOT microsphere in the presence of ammonium persulfate (oxidant) and PVP (micelles). Sui *et al.*[309] synthesized hollow microspheres of PEDOT (size: 0.5 to 10 μm) by the chemical oxidative polymerization of EDOT using ammonium persulfate in a catanionic surfactant solution comprising a mixture of cetyltrimethylammonium bromide and sodium dodecylbenzenesulfonate. Recently, Ge *et al.*[195] prepared honeycomb-shaped photothermal polypyrrole by electropolymerization.

4.3 Electrospinning method

Electrospinning is relatively inexpensive, simple and versatile method used in fabricating hollow (and core–shell) polymer fibers for a variety of applications.[310,311] The electrospun poly (amic acid) fiber membrane has been used as a template to fabricate hollow polyaniline nanofibers by *in situ* polymeriz-

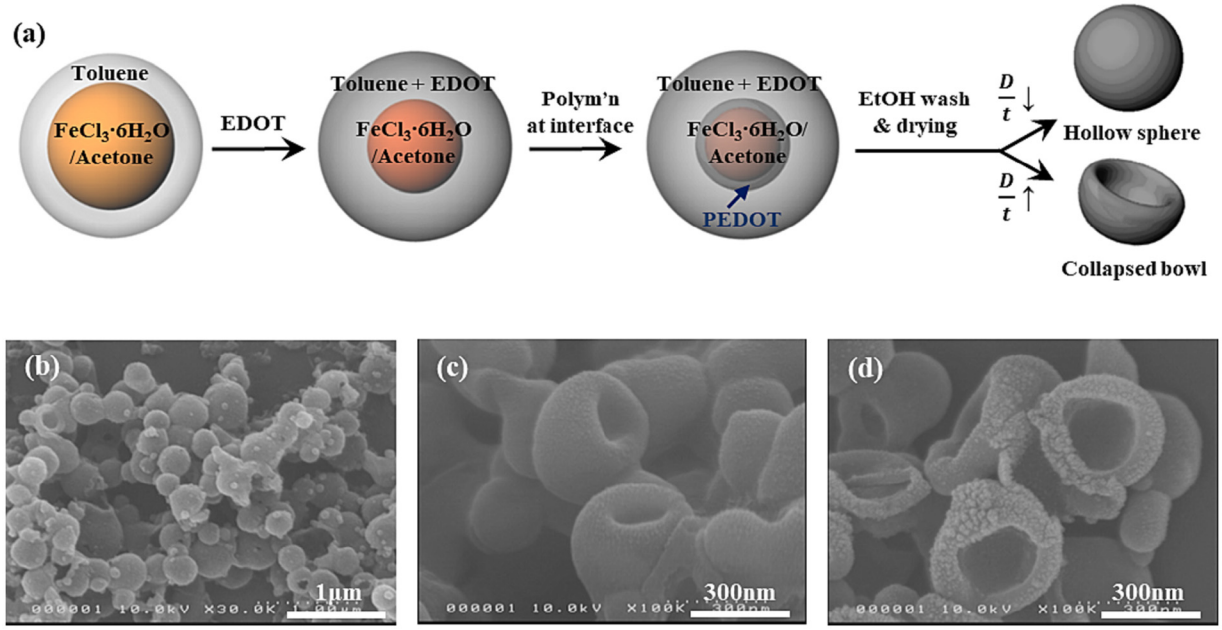

Fig. 14 (a) Schematic illustration for the oxidative chemical polymerization of PEDOT hollow spheres/bowls. (b–d) SEM images of the synthesized PEDOT nanostructures, (b) PEDOT nanoparticles before wash-removal of oxidant, (c) after the removal of oxidant by ethanol washing, and (d) collapsed hollow bowls after the washing and drying.[307] Reproduced with permission from Elsevier.

ation of aniline.[312] The formation of highly aligned PEDOT nano- and microscale fibers and tubes has been reported based on this technique and oxidative chemical polymerization.[313] The electrospinning preparation methods of several other hollow conducting polymers are described in subsequent sections under applications.

4.4 Synthesis of double-shelled hollow spheres of ICPs

In comparison with single-shell hollow spheres, hollow spheres with multi-shell structures receive extra advantages from inner structures.[314] The permeable shell and void space between each shell in the unique hollow structure accounts for interesting properties, such as a sequential absorbing/scattering characteristic, and the shortening of the diffusion distance for mass and charge transport for various applications. In this regard, very limited research has been reported on the preparation of intrinsically conducting polymers exhibiting the double-shell type of morphology. Bei and Xia[315] reported the synthesis of double-shelled polypyrrole hollow particles with a structure similar to that of a thermal bottle, using polystyrene hollow spheres (templates) containing a hole on the surface as templates. The choice of such template facilitated the diffusion of the monomer and acted as an initiator to form uniform PPy coatings on the inner and outer surfaces. Subsequently, selective removal of PS by dissolving in tetrahydrofuran (solvent) resulted in the formation of double-shelled polypyrrole hollow particles with a structure resembling that of a thermal bottle. Niu *et al.*[316] used iron oxide hollow microspheres as both the sacrificial template and initiator in acidic solution to prepare double-shelled polypyrrole hollow microspheres. According to Gu *et al.*,[317] MnO_2 nanorods selected as a self-sacrifice template formed double-shelled hollow polypyrrole nanotubes by *in situ* polymerization of the pyrrole monomer in the presence of hydrochloride acid and sodium p-styrene sulfonate.

4.5 Synthesis of hollow nanocomposites of ICPs and core–shell structures

Recently, hollow and core@shell composites have been receiving considerable attention due to their effective combination and interesting properties, with great promise for a broad range of applications in many fields.[67] In this regard, intrinsically conducting polymer-derived composites have gained significant recognition due to their unique properties, such as environmental stability, processability, and less corrosive nature with tunability.[72,73] In addition, such ICP-based binary and ternary core–shell nanocomposites offer advantages of their properties due to the combination of the core and the shell.[75] Core–shell nanostructured materials can be prepared by physical and chemical methods. However, the chemical synthesis of hollow and core–shell ICP nanostructures is better recognised compared with physical methods. This is mainly due to their greater versatility, precise control, and ability to use templates, unlike physical methods which invariably require complex equipment. In view of this, preparative methods for these hollow and core–shell ICP composites are described in the subsequent sections under their applications in the fields of electromagnetic interference shielding/microwave absorption, removal of metal ions/dyes and as supercapacitors.

Recently, electrodeposition has become a promising method for fabricating ICP-based core–shell materials as superior electrodes in supercapacitors, though its potential is

yet to be harnessed.[145,318] This is ascribed to the superior control over morphology, enhanced performance through binder-free synthesis, and improved interface between the polymer and substrate. Chen *et al.*[319] synthesized polypyrrole (binder free film) on carbon cloth by the electrodeposition method. Core–shell nanorod arrays with polyaniline were successfully electrodeposited into a mesoporous $NiCo_2O_4$ support.[320] Wu *et al.* reported[321] polypyrrole-coated low-crystallinity Fe_2O_3 supported on carbon cloth by a combination of chemical reduction and electrodeposition methods. The preparation of a free-standing graphene/polyaniline/MnO_2 ternary composite by sequential electrodeposition on carbon cloth as working electrodes was reported.[322] In another study, electrodeposition of PANI on the surface of GO/α-MnO_2 was used to prepare hierarchical GO/α-MnO_2/PANI composites.[323] This electrodeposition technique has also been used in fabricating $(CoCrFeMnNi)_3O_4$@CC-PPy,[324] $LaMnO_3$@CC-PPy,[325] and porous PPy/black phosphorus oxide composites electrodeposited on CNT.[326] In another approach, Fauzi *et al.*[327] used oxidative chemical vapor deposition to deposit a submicrometer-thick layer of PPy on the carbon fabric.

5. Application of hollow ICPs and their core–shell nanocomposites

5.1 Electromagnetic interference shielding and microwave absorption

In recent decades, the growing and extensive use of devices has contributed to electronic pollution due to electromagnetic interference, limiting their applications and also threatening human life (Fig. 15).[328] In this regard, the development of electromagnetic shielding and microwave-absorbing materials has recently been receiving considerable attention When an electromagnetic (EM) wave perforates through the shielding material, it involves primarily three processes, namely reflection, absorption, and multiple reflection.[2] The shielding performance of a material is expressed by term electromagnetic interference shielding effectiveness (EMI SE). The total EMI SE (SE_T) measures the ability of a material to block EM waves and is expressed in decibels (dB) as a function of the logarithm of the ratio of the power P, electric E, or magnetic H field intensities before and after EM attenuation, *i.e.*,

$$SE_T\,(dB) = 10\log\left(\frac{P_1}{P_2}\right) = 20\log\left(\frac{E_1}{E_T}\right) = 20\log\left(\frac{H_1}{H_T}\right) \quad (1)$$

where I and T represent the incident and transmitted components.[203,204]

Furthermore, SE_T is the sum of shielding efficiency originating from absorption (SE_A), reflection (SE_R) and multiple reflections (SE_M),[9] *i.e.*,

$$SE_T = SE_R + SE_A + SE_M \quad (2)$$

The factors affecting the shielding effectiveness include permeability, permittivity, skin depth and thickness, external physical properties, eddy current loss, magnetic loss, dielectric loss, size and morphology *etc.*[54] The impedance matching ratio, $|Z_M Z_0|$ (Z_{in}: input impedance, Z_0; free space impedance) is also another important factor that provides information about EM waves entering the shield. It may be noted that the reflection loss (R_L) of a shielding material is closely related to the input impedance (Z_{in}) and free space impedance (Z_0).

Fig. 15 Electromagnetic radiation hazards and application of EWAMs around daily life.[328] Reproduced with permission from Elsevier.

According to the transmission line theory, both Z_{in} and R_L are expressed as shown below.[9]

$$Z_{in} = Z_0\sqrt{\frac{\mu_r}{\varepsilon_r}}\tanh\left[i\frac{2\pi ft}{c}\sqrt{\varepsilon_r\mu_r}\right] \quad (3)$$

$$R_L = 20\log 10\left|\frac{Z_{in}-Z_0}{Z_{in}+Z_0}\right| \quad (4)$$

where t, ε_r and c represent thickness of the absorber relative dielectric permittivity and velocity of light in free space, respectively.

The methods commonly used to measure the electromagnetic shielding efficiency (also referred to as effectiveness) of a material can be based on the space transmission, shield box, shield room and coaxial transmission line approaches.[75]

In this regard, much interest has been focused recently on developing electromagnetic wave (EMW) shielding materials undergoing absorbing mechanisms.[9] This is because EMWs, following the reflection mechanism, produce secondary pollution due to their reflection to the environment. Accordingly, conductive polymers have been receiving considerable attention guided by their conductivity, light weight, corrosion resistance and processibility.[9] In this regard, the morphology of the intrinsically conducting polymer materials is considered a vital parameter in their functioning as EMW absorbers. This is ascribed to successive internal reflection (multiple internal reflections of incident EM waves).[204,329–333] Hollow microhemispheres like polypyrrole and carbon dielectric materials could act as promising high-performance microwave absorbers with strong reflection loss and wide absorption frequency bandwidth.[332]

According to the available literature, electromagnetic wave absorption materials have proved to be very effective at mitigating electromagnetic pollution and interference.[9] The choice of an ideal microwave absorber material is guided by light weight, good thermal stability, antioxidation capability, multi-interfaces, impedance matching, synergistic effects, strong absorption properties and wide bandwidth simultaneously.[54,333–335] In addition, other important features that affect the absorption of microwaves include complex permittivity/permeability, impudence matching and morphology of these materials.[9] In such studies, the choice of ICPs is guided by the low cost of synthesis and great environmental stability of hollow morphology, to account for the improved microwave absorbing properties. In addition, hollow ICP composites and ICP based core–shell materials have also been fabricated, integrating magnetic and dielectric losses to facilitate the absorption of EM waves.[334]

Among these, Fe_3O_4 has drawn a great deal of attention because of its low cost, easy synthesis, saturation magnetization value and high Curie temperature.[9] However, several drawbacks of Fe_3O_4, such as ease of oxidation, high density, dramatic decrease of permeability in the high-frequency range due to the Snoek's limit, weak interfacial compatibility and substrate dispersion difficulty need to be addressed.[9,334,335] In view of this, combining ICPs with magnetic materials could be more effective at enhancing the electromagnetic wave attenuation synergistically.[329] Furthermore, outstanding performance can also be achieved by combining dielectric and magnetic components together.[336] Accordingly, most studies are focused on Fe_3O_4 in the form of binary composites with ICP or its ternary nanocomposites involving ICPs and carbonaceous materials. It may be noted that the hollow structures of Fe_3O_4 nanospheres and PANI reduce the weight of the composites. In addition, they also extend the transmission path of microwaves as result of multiple reflection and scattering loss.

5.1.1 Hollow ICP micro-/nanospheres. Self-assembled 3D helical hollow superstructures of polyaniline (20 wt%) filled with epoxy (thickness: 2.0 mm) exhibited the lowest R_L value (−51.60 dB at 13.95 GHz) and the effective absorbing bandwidth (R_L < −10 dB) reached 5.12 GHz (12.03–17.15 GHz).[337] Wan *et al.*[332] fabricated hollow polypyrrole microhemispheres (HPMs) and hollow carbon microhemispheres (HCMs) by a sol–gel method using SiO_2 microspheres as the templates and investigated their microwave absorption properties. The studies have shown better microwave absorption properties in HCMs (reflection loss, R_L: −63.9 dB at 8.0 GHz, thickness: 5 mm) compared with the HPMs (R_L: −23.8 dB at 7.3 GHz, thickness: 4.2 mm) owing to the enhanced conductive loss and optimized impedance matching. It is anticipated that the multiple reflection/scattering derived from hollow hemispherical microstructures could account for such enhanced microwave absorption performance. Xu *et al.*[338] prepared hollow polypyrrole aerogel by modulating the proportion of hollow PPy nanofibers seeds and pyrrole. In their study, 8% paraffin-filled PPy sample (thickness: 2.69 mm) attained the minimum reflection loss value of −58.73 dB at 16.48 GHz and a wide effective absorption bandwidth of 7.28 GHz (thickness: 2.69 mm). Further studies revealed EMI shielding effectiveness of the composite loaded with 20 wt% of hollow PPy nanofiber aerogels in paraffin reaching 68.92 dB (thickness: 3.0 mm). Such performances have been explained considering the multireflection, interfacial polarization and formation of the conductive network.

Guo *et al.*[339] studied electromagnetic wave absorption of the hollow polypyrrole nanorods fabricated by using the self-assembly template that can be easily removed. These findings have shown that tuning the wall thickness facilitates control of the dielectric constant of HPPy. The variation of reflection loss with frequency in the range of 2–18 GHz with filler loading of 10 wt% indicated the minimum reflection of –54.94 dB with the largest effective absorption bandwidth of 7.36 GHz (thickness: 3.4 mm). The possible EMA mechanism of HPPy nanorods could be ascribed to impedance matching, multiple reflection, a good conductive network and enhancement of polarization loss. In another method, hollow or partially collapsed bowls of polyaniline, polypyrrole, polythiophene and poly(3,4-ethylenedioxythiophene) have successfully been synthesized by surfactant-free Ouzo emulsion.[307] Subsequently, the EMI shielding performance of the three samples PEDOT sphere/bowl film (thickness: 6.5 μm), composite film of

PEDOT hollow spheres/bowls film (thickness: 6.3 μm) with infiltrated PH1000 and pure PH1000 film (thickness: 6.2 μm) has been investigated in X-band (8–12 GHz). It was noted that EMI SE of the corresponding samples over the X-band follow the order: PEDOT hollow spheres/bowls film with infiltrated PH1000 (~75 dB) > PEDOT:PSS with infiltrated PH1000 film (~70 dB) > PEDOT hollow spheres/bowls film (very low). The low electrical conductivity of pure PEDOT hollow spheres/bowls film accounts for their inferior EMI performance. In contrast, the composite comprising the PEDOT hollow spheres/bowls film with infiltrated PH1000 exhibited enhanced EM absorption, as evident from the total EMI SE (SE_T), due to the larger contribution from the absorption compared with the reflection. Ni *et al.*[308] observed a maximum R_L of −24 dB at 15.9 GHz for a sample (thickness: 2 mm) of PEDOT hollow microspheres.

5.1.2 ICP micro-/nanotubes. Polyaniline microtubules prepared by a template-free method following doping (β-naphthelene sulfonic acid) and codoping (D-glucose) could find potential application as microwave-absorbing materials in the frequency range of 1–18 GHz.[340] Moučka *et al.*[341] used methyl orange as a soft template to synthesize polypyrrole nanotubes (dia: ~100–400 nm, length: in μm range) and investigated their application for electromagnetic interference shielding in the microwave region. EMI shielding studies of polypyrrole nanotubes and nanobelts (thickness: 2 mm) have displayed shielding of almost 80% of incident radiation in the C-band at very low loading of conductive filler in the silicone (5% w/w). PANI microtubes (dia: 3.0 μm, length: 12.0 μm) were successfully synthesized in the presence of toluene-*p*-sulfonic acid *via* a self-assembly process assisted by excess ammonium persulfate, and showed a reflection loss of about −15.5 dB (0–6000 MHz).[342] Yang *et al.*[343] synthesized nanorod-coated PANI hierarchical microtubes by a sodium dodecylsulfate/HCl (7.5 mM)-assisted oxidative polymerization method. Subsequent studies have shown that 50 wt% of the fabricated hierarchical 1D hollow structure with molten paraffin exhibited stronger absorption (−43.6 dB) and a wide absorption band of 5.84 GHz, smaller sample thickness (1.55 mm) and wider bandwidth (5.84 GHz). It was suggested that the 1D hierarchical, hollow structure, and conductivity (0.08 S cm^{-1}) account for this excellent performance by contributing to the enhanced permittivity, multiple resonances, strong attenuation capability, multiple scattering and EM radiation.

5.1.3 Binary nanocomposites of hollow ICPs. Panigrahi[203] and Srivastava synthesized polyaniline hollow microspheres (PnHM)/Ag nanocomposites by emulsion polymerization of aniline and Tollen's reagent as a source for Ag nanoparticles. The variation of SE *versus* frequency corresponding to the different thickness samples in S-and X band regions showed SE to be remarkably higher in PnHMAg (19.5 dB: 11.2 GHz) compared with PnHM (12 dB: 8.5 GHz). It is anticipated that the Ag nanoparticles present in PnHMAg act as interconnecting particles between the micro-sized PnHM in forming continuous linkages to account for the enhanced EMI shielding efficiency. In another study, they reported a novel approach for the trapping of microwave radiation in hollow polypyrrole microsphere through enhanced internal reflection.[204] In their work, the hollow polypyrrole (HPPY) was synthesized by the *in situ* chemical oxidative copolymerization of pyrrole (Py) using polystyrene as spherical template. In addition, HPPy/Ag nanocomposites were prepared using Tollen's reagent. SEM and TEM images of HPPy/Ag nanocomposites in Fig. 16(a and b) show the presence of Ag nanoparticles (<40 nm) on the surface of the HPPy shell. Further investigations showed significantly higher electromagnetic interference (EMI) shielding efficiency (SE) of HPPy (34.5–6 dB) compared with PPy (20–5 dB) in the frequency range of 0.5–8 GHz (Fig. 17(a)). EMI shielding efficiency was further enhanced to 59–23 in 10 wt% Ag-loaded HPPy/Ag-10. This was attributed to the EM wave trapping mechanism through enhanced internal reflection in HPPy/Ag, as displayed in Fig. 17(b).

Microwave absorption of milled carbon fiber (4 wt%) and hollow polyaniline spheres (1 wt%) impregnated in the epoxy matrix (thickness: 1.8 mm) exhibited maximum absorption (−49.3 dB) and the effective bandwidth of 1.7 GHz–10 dB in the X band region.[344] The observed reflection loss of EM waves in the given frequency range was attributed to the improve-

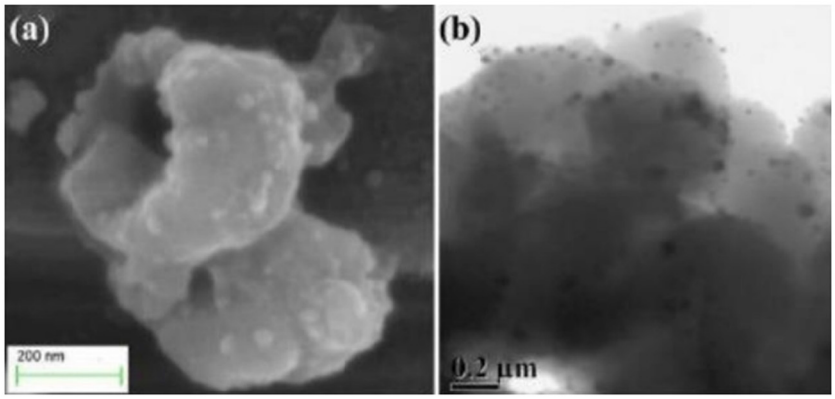

Fig. 16 (a) SEM image and (b) TEM image of HPPy/Ag-10.[204] Reproduced with permission from Nature Publication.

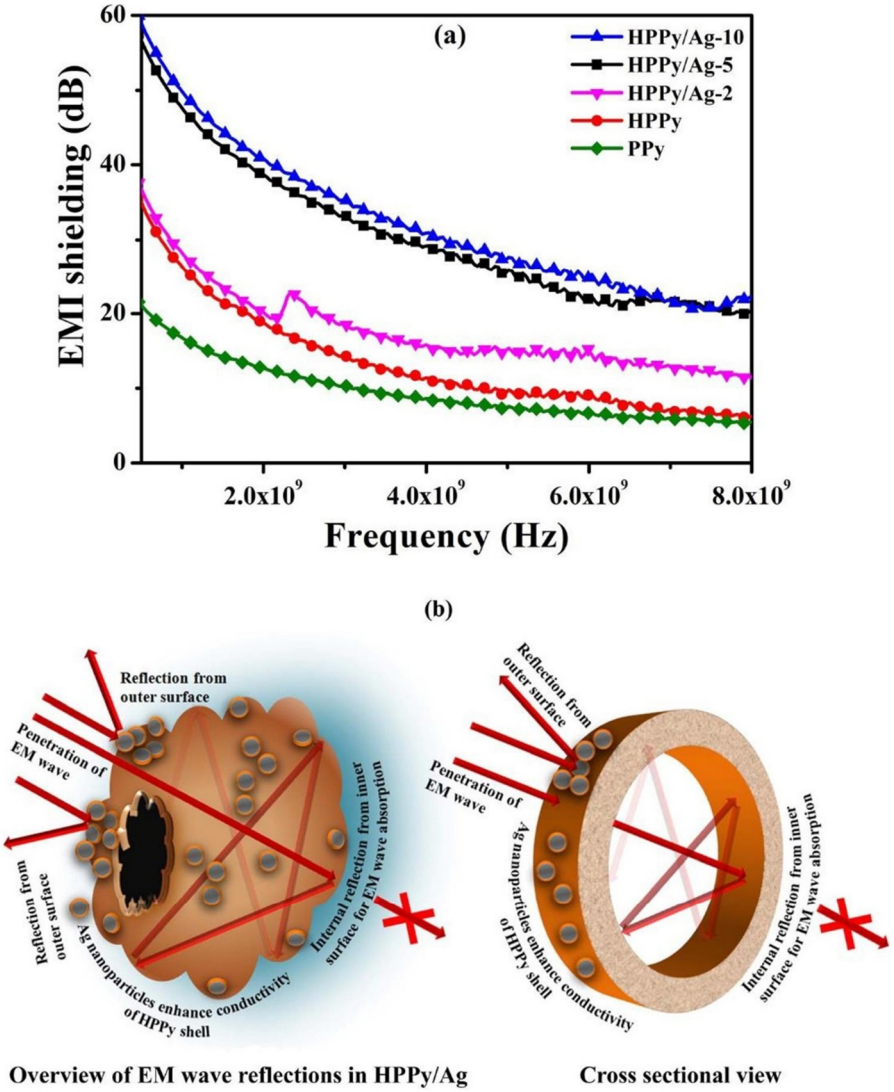

Fig. 17 (a) Variation of EMI shielding of PPy, HPPy, HPPy/Ag-2, HPPy/Ag-5, HPPy/Ag-10 with varying frequency at 0.5–8 GHz, and (b) trapping mechanism of EM wave through enhanced internal reflection in HPPy/Ag: An anticipated scheme.[204] Reproduced with permission from Nature Publication.

ment in impedance matching, multiple reflections and scattering of EM waves. According to Wang *et al.*,[345] hollow polyaniline-derived N/S co-doped carbon nanoflakes possessed R_L^{min} of −53.5 dB (10.2 GHz) and a corresponding effective absorption band of 4.5 GHz at 2.9 mm. This could be explained on the basis of conductivity loss, interfacial polarization relaxation and the impedance matching from the hollow structure synergistically, resulting in excellent microwave absorption performance.

Chu *et al.*[346] fabricated a well-designed structure of sandwich-like composite films based on hollow polyaniline and cellulose nanofiber (CNF) in the surface layers and MXene/CNF in the intermediate layer. This displayed an EMI SE of 35.3 dB for a proportion of MXene and PANI achieved at a lower filler loading compared with many others. It was suggested that the formation of such sandwich structure effectively reduced the reflection of the EM wave and made the absorption more dominant. Hollow polyaniline/Fe_3O_4 microsphere (7.33 wt%) composites showed the maximum reflection loss of −15.6 dB and maximum bandwidth of 8.0 GHz over −10 dB in the frequency range of 2–18 GHz.[347] Double-shelled hollow polypyrrole nanotubes were synthesized by using the reactive MnO_2 template.[317] They exhibited the optimal reflection loss of −50.4 dB and a wide EAB of 7.7 GHz in the presence of 5 wt% in a paraffin wax matrix. Such performance was ascribed to the synergistic effects of interfacial polarization and conduction loss.

5.1.4 Core@shell nanocomposites of ICPs

5.1.4.1 Binary core@shell nanocomposites. Guo *et al.*[348] observed maximum reflection loss (R_L^{max}) and EAB values of −52.01 dB and 2.72 GHz in the hollow core–shell-structured Fe_3O_4@Polypyrrole (Fe_3O_4: 60.0 wt%) synthesized by an *in situ*

polymerization method. Such performance was attributed to the synergistic effect on account of dielectric as well as magnetic losses. The broadband electromagnetic wave absorption properties of Fe_3O_4/PPy double-carbonized core–shell-like composites (thickness: 1.6 mm) exhibited R_L^{min} and EAB of −26 dB and 4.64 GHz, respectively.[349] The observed performance was ascribed to the synergistic effects of conductive loss, dielectric loss, magnetic loss, and multiple reflection loss. Tang *et al.*[350] synthesized Fe_3O_4@PPy with hollow core–shell structures by a solvothermal process followed by *in situ* polymerization. For this purpose, 170 μL, 180 μL, 190 μL of pyrrole were taken and the corresponding nanocomposites, referred to as FP-170, FP-180 and FP-190, acted as an efficient microwave absorber as indicated by their observed performance from a minimum reflection loss of −63.82 dB (4.55 mm), −84.92 dB (3.87 mm), and −71.25 dB (2.64 mm) at low frequencies, respectively. The maximum effective absorption bandwidth values of the corresponding composites were found to be 3.48 GHz (2.39 mm), 4.20 GHz, 2.38 mm and 4.96 GHz (2.16 mm). The excellent microwave absorption performance of hollow core–shell Fe_3O_4@PPy could be due to the good impedance matching, strong magnetic loss, including natural resonance and eddy current loss, excellent conductivity, defects and polar groups in h-Fe3O4 and PPy acting as polarization centers, the presence of abundant heterogeneous interfaces and interfacial polarization. Furthermore, the presence of the hollow structure of Fe_3O_4 in the nanocomposite contributed to the multiple reflection and scattering losses and also enhanced the impedance matching.

Promlok *et al.*[351] reported the formation of the hollow magnetic polyaniline by *in situ* polymerization in one pot for EMI applications. In another study, Fe_3O_4–polyelectrolyte modified polyaniline (Fe_3O_4–PE@PANI) was prepared by the self-assembly approach.[352] TEM imaging of the product clearly established the formation of hollow Fe_3O_4-Polyelectrolyte (PE) @PANI nanocomposites (average size ~500 nm), with Fe_3O_4 nanoparticles tightly and completely attached to the PANI hollow sphere surfaces. The 50 wt% of Fe_3O_4–PE@PANI loaded in paraffin exhibited a minimum reflection loss of −6.5 dB (14.3 GHz) and the frequency bandwidth (<−5 dB) from 12.5 to 15 GHz, and ascribed it to the impedance matching and dielectric/magnetic loss abilities. Hou *et al.*[353] prepared hollow-structure Fe_3O_4/PANI microspheres based on three steps, namely the preparation of Fe_3O_4 nanoparticles, hollow PANI microspheres and Fe_3O_4/PANI microspheres. Subsequently, they investigated the effects of the mass ratio of aniline/PS (template) on their EMW absorption properties. Fe_3O_4/PANI microspheres corresponding to the mass ratio of aniline/PS of 1 : 6 and thickness of 1.5 mm attained R_L^{min} of −24.3 dB, and the bandwidths below −10 dB corresponded to 4.64 GHz (11.04–15.68 GHz) for 2 mm thickness of the sample. It was suggested that dielectric loss, magnetic loss (2–7 GHz) and eddy current loss (7–18 Ghz) played important roles. In addition, hollow Fe_3O_4/PANI microspheres acted as a potential absorber in the absorption of microwaves due to strong destructive interference and eddy current loss. Hollow poly (aniline-*co*-pyrrole)–Fe_3O_4 (0.06 g) composite nanospheres were prepared *via* the oxidative polymerization of a mixture of aniline and pyrrole in the presence of a magnetic fluid.[354] The reflection loss calculations showed the best microwave-absorbing property between 0.5–10 GHz for the hollow poly(aniline-*co*-pyrrole) filled with 0.06 g of Fe_3O_4. These studies also revealed that both dielectric and magnetic loss significantly affect the efficiency of microwave absorption.

In another study, a Fe_3O_4/PANI[355] composite was fabricated with hollow Fe_3O_4 nanospheres and polyaniline nanotubes by the hydrothermal treatment and chemical oxidative polymerization, and its micro absorption properties were studied by varying the ratio of PANI and the loading amount of the composites in paraffin. These findings have shown remarkable performances (R_L^{min}: −55.03 dB, EAB: 4.88 GHz) for its thickness of 1.84 mm in the frequency range of 2–18 GHz. This excellent performance was attributed to the interfacial polarization loss, multiple reflection scattering loss and the synergistic effect of hollow Fe_3O_4 (magnetic) and 1D PANI (dielectric) material. Fe_3O_4 microsphere core (size: 300 nm)/PANI shell (thickness: 100 nm) synthesized by *in situ* polymerization reached R_L^{max} of −37.4 dB at 15.4 GHz.[356] Such enhanced microwave absorption properties arise due to the improved impedance, dielectric loss, interfacial loss and synergistic effect. Core–shell Fe_3O_4−PEDOT microspheres (EDOT)/(Fe_3O_4 molar ratio = 20) were also prepared by a two-step method in the presence of polyvinyl alcohol (stabilizer) and *p*-toluenesulfonic acid (dopant) (Fig. 18(a)).[357] TEM studies, displayed in Fig. 18(b) established Fe_3O_4 microspheres coated by PEDOT, and the thickness of the shell corresponded to 90 nm. The variation of reflection losses of Fe_3O_4/PEDOT with frequency in Fig. 18(c) showed excellent microwave absorbing property (R_L^{min}: –30 dB at 9.5 GHz, thickness: 4 mm) due to the impact of layer thickness, volume fraction and conductivity.

Fe_3O_4-polyaniline,[358] Fe_3O_4@Polypyrrole,[359,360] and $BaFe_{12}O_{19}$@PANIn[361] core–shell structured materials have also been studied for their electromagnetic wave absorption. Hosseini *et al.*[362] used a core–shell approach for fabricating polythiophene nanofiber coated on $MnFe_2O_4/Fe_3O_4$ through the combined co-precipitation and *in situ* polymerization methods. The micro absorption properties of the 1.5 mm nanocomposite showed minimum R_L of −21 dB (12 GHz) in the frequency range 8.0–12.0 GHz. $CoSe_2$@polythiophene[363] and rGO/$Ni_{0.5}Co_{0.5}Fe_2O_4$@PEDOT[364] core–shell composites were also synthesized and studied for their electromagnetic, microwave absorbing properties. Fe_3O_4 microspheres @PPy anchored on 3D graphene aerogel (GO to Fe_3O_4@Ppy wt ratio: 1 : 3) of 2.5 mm thickness reached a minimum reflection loss of −40.53 dB at 6.32 GHz and the effective bandwidth of 5.12 GHz (11.12–16.24 GHz).[365] Such enhanced microwave absorption properties of the ternary composite could be explained on the basis of abundant interfaces, enlarged dielectric properties, enhanced conductivity and synergistic effect.

Excellent microwave absorption performance has been shown by PANI decorated on prism-shaped hollow carbon (thickness: 2.5 mm) synthesized by *in situ* polymerization.[366] It showed the minimum reflection loss of −64.0 dB (11.1 GHz)

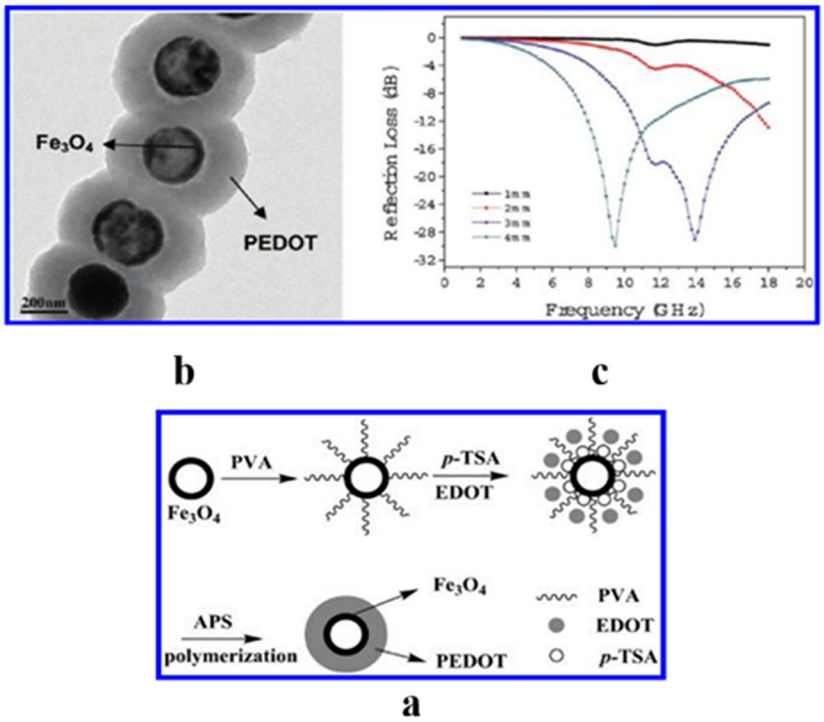

Fig. 18 (a) Formation mechanism of Fe_3O_4@PEDOT core–shell microspheres, (b) TEM images of Fe_3O_4@PEDOT core–shell microspheres prepared with (EDOT)/(Fe_3O_4) ratios: 20, and (c) reflection losses in different thickness of Fe_3O_4@PEDOT composites with (EDOT)/(Fe_3O_4) = 20.[357] Reproduced with permission from ACS.

and EAB corresponding to 5.0 GHz (9.5–14.5 GHz) attributed to high impedance matching, dielectric loss and geometric effect. Gai *et al.*[367] constructed PPy nanotubes@MoS_2 core–shell and observed the optimal R_L of −49.1 dB at 6.1 GHz and the widest bandwidth up to 6.4 GHz from 11.5 to 17.5 GHz (R_L < −10 dB) corresponding to its thickness of 2.5 mm. Such enhanced microwave absorption properties of PPy@MoS_2 composite were ascribed to the morphology, attenuation capacity and the impedance matching.

Tian *et al.*[368] fabricated PPy@PANI of tunable shell thickness (30–120 nm) by direct polymerization of aniline on the surface of PPy microspheres. The fabricated PPy@PANI composite showed a maximum reflection loss of −34.8 dB at 13.9 GHz and bandwidths exceeding −10 dB corresponding to 11.9–16.6 GHz (4.7 GHz). In another study, hollow $Zn_xFe_{3-x}O_4$@Polyaniline[369] core–shell composites acted as high-performance microwave absorbers with high reflection loss, respectively. *In situ* polymerized-grown polyaniline nanorod arrays on the surface of carbon (C@PANI) microspheres exhibited a waxberry-like shape.[370] Subsequently, their microwave absorption performance was evaluated and displayed considerable reflection loss (samples thickness: 2.2 mm), impedance matching ratio of samples and 3 D reflection loss with different thickness, as shown in Fig. 19(a, b and c), respectively. It was noted that C@PANI exhibited superior microwave absorption performance (sample thickness: 2.2 mm), R_L^{min}: −59.6 dB at 15.5 GHz, effective bandwidth for R_L < −10 dB: 5.4 GHz (12.6 to 18 GHz) compared with pure PANI and carbon microspheres. It was suggested that dielectric loss ability, synergistic effect and defects present in the C microspheres contributed to this high microwave absorption performance of C@PANI microspheres. In addition, relatively low electrical conductivity owing to the amorphous structure of C@PANI could be favourable in the impedance matching. The variation of 3 D reflection loss of C@PANI microspheres with the sample thickness in the range of 2–3 mm showed the shifting of the R_L^{min} peak from the high to low-frequency region. Based on the observations, the absorption mechanism of C@PANI microsphere has also been proposed. In another study, PANI shell fabricated on the surfaces of CNTs (CNT/aniline mass ratio = 1 : 2) acted as an excellent microwave absorber (R_L^{min}: ~41.5 dB at 9.5 GHz and EB for $R_L \leq -10$ dB: 5.1 GHz for 2 mm thickness) as a result of the microwave dissipation ability of CNTs and good impedance matching.[371]

Liu *et al.*[372] reported excellent microwave absorption performance (R_L^{max}: −38.1 dB at 11.6 GHz) in the frequency range of the X-band for the pyrrole as the shell on the core of carbon microspheres. The microwave absorption studies were made on core shell-type PEDOT (outer shell) nanocomposite with barium ferrite (center) synthesized by *in situ* emulsion polymerization in the frequency range of 12.4–18 GHz.[373] The subsequent findings on microwaves have shown its absorption value (SE_A) of 22.5 dB (>99% attenuation) owing to the higher dielectric and magnetic loss contributions. The effective electromagnetic shielding performance (EMI SE: 28.8 dB) has also been achieved in a core–shell heterostructure comprising poly-

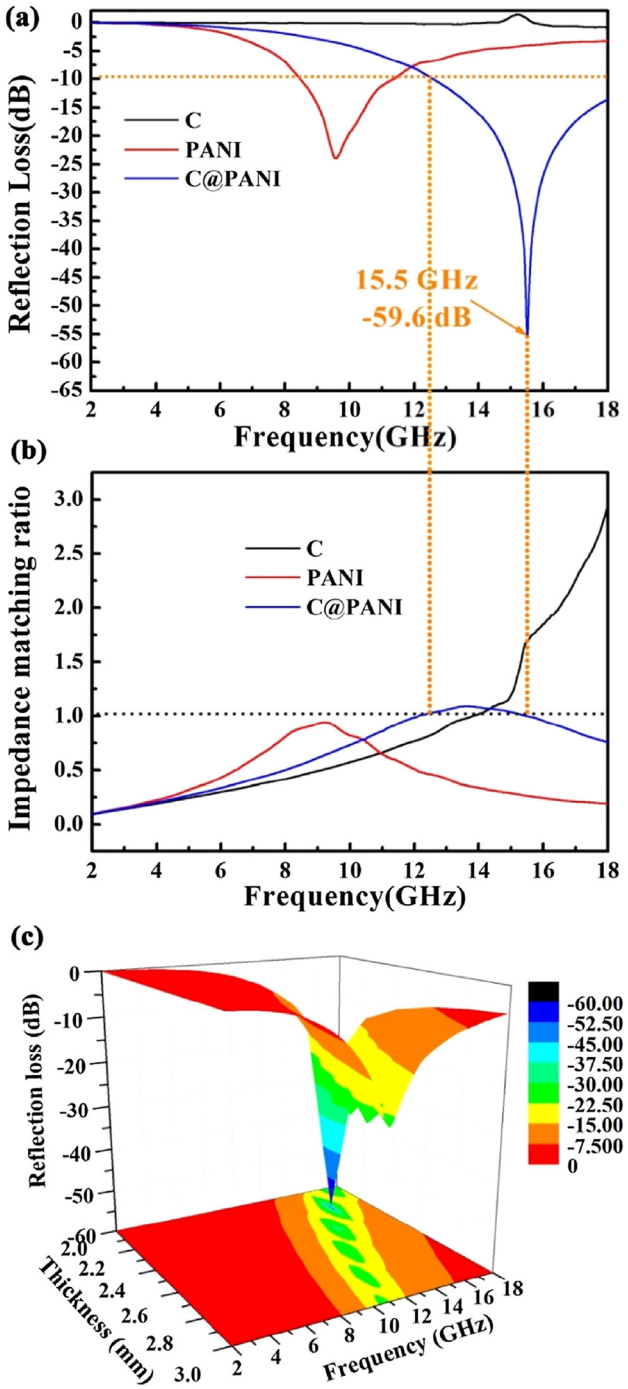

Fig. 19 (a) Reflection loss of samples with the thickness of 2.2 mm; (b) impedance matching ratio of samples; (c) three-dimensional reflection loss of C@PANI micro-spheres with different thickness.[370] Reproduced with permission from Elsevier.

aniline-coated bagasse fiber.[374] According to Saini *et al.*,[375] TEM studies established the coating of PANI deposited *via in situ* polymerization on the surface of individual MWCNT that contributed towards the absorption-dominated total shielding effectiveness (−27.5 to −39.2 dB) in the frequency range of (12.4–18.0 GHz). In another study, Polyaniline@Helical CNTs with dual chirality exhibited enhanced microwave absorption synergistically.[376]

5.1.4.2 Ternary and quaternary core@shell nanocomposites. Zhang *et al.*[377] used a spray-dry method to fabricate a ternary composite comprising hollow microspheres of PPy@Fe_3O_4/CNTs by combining the conductive PPy, strongly magnetic Fe_3O_4 and high-conductivity CNT components. It showed the maximum reflection loss of −51.8 dB (8.8 GHz) at the thickness of 2.38 mm. Such performance of PPy@Fe_3O_4/CNTs as an excellent microwave absorber was attributed to the dielectric, magnetic and conductive loss achieving synergistic absorption. Hollow polypyrrole/Ni/PVDF microspheres prepared by spray phase inversion acted as an efficient electromagnetic microwave absorber (R_L^{min}: −47.2 dB at 25.36 GHz) and (R_L^{min}: −39.8 dB at 31.30 GHz).[378] Further studies on the variation in the absorber thickness (1.0–3.5 mm) resulted in the tuning of the effective absorption bandwidth in the range of 18–40 GHz. PPy@FeCo@PPy nanotubes exhibited $R_L^{min}$of −50.5 dB and an EAB of 5.7 GHz at a thickness of 2.0 mm.[379] Excellent microwave absorption performance was also reported in the trilaminar composite comprising double-shell PPy@Air@MnO_2 nanotubes,[380] double-shell hollow poly(acrylonitrile) microspheres@polyaniline@Ag.[381] Ge *et al.*[382] prepared hollow-spherical composites of PANI/CoS/(carbon nanodots) CDS under the applied magnetic field of 0.5 T and observed strong electromagnetic wave absorbing characteristics (R_L^{max}: −24 dB at 14 GHz). According to this, magnetic field-induced ferromagnetic nanodomains of Co^{2+}clusters greatly enhance Maxwell–Wagner relaxation as well as ionic orientation polarization in the composite, leading to the dielectric loss. This in combination with magnetic loss contributed to EMW absorption of PANI/CoS/CDs-0.5T in the low-frequency range of 2–12.5 GHz.

Manna and Srivastava,[383] motivated by the role played by the dual interface in microwave absorption and shielding performance, reported the fabrication of Fe_3O_4@C@PANI according to the scheme in Fig. 20(a) by varying the aniline : Fe_3O_4@C as 9 : 1, 8 : 2, 7 : 3 with the aniline monomer under identical reaction conditions, and the products were designated as PFC-10, PFC-20 and PFC-30, respectively. HRTEM imaging of the trilaminar PFC-10 composite in Fig. 20(b) clearly shows the formation of the highest outermost thickness of nonmagnetic polyaniline shell (~30 nm) on Fe_3O_4@C corresponding to the aniline : Fe_3O_4@C ratio of 9 : 1. Further investigations revealed the decrease in complex permittivity and increase in complex permeability on encapsulation of Fe_3O_4@C by PANI due to impedance matching. Fig. 20(c) shows the highest shielding efficiency for the PFC-10 composite predominantly due to absorption (SE_A: ~47 dB) rather than reflection (SE_R: ~15 dB) in the frequency range of 2–8 GHz. Such findings in Fe_3O_4@C@PANI are unique owing to the dual interfaces compared with Fe_3O_4@C and Fe_3O_4/PANI due to their applicability limited to a discrete frequency. In addition, such remarkable EM wave attenuation in the Fe_3O_4@C by PANI trilaminar core@shell composite was also supported by impedance matching and dielectric and magnetic loss.

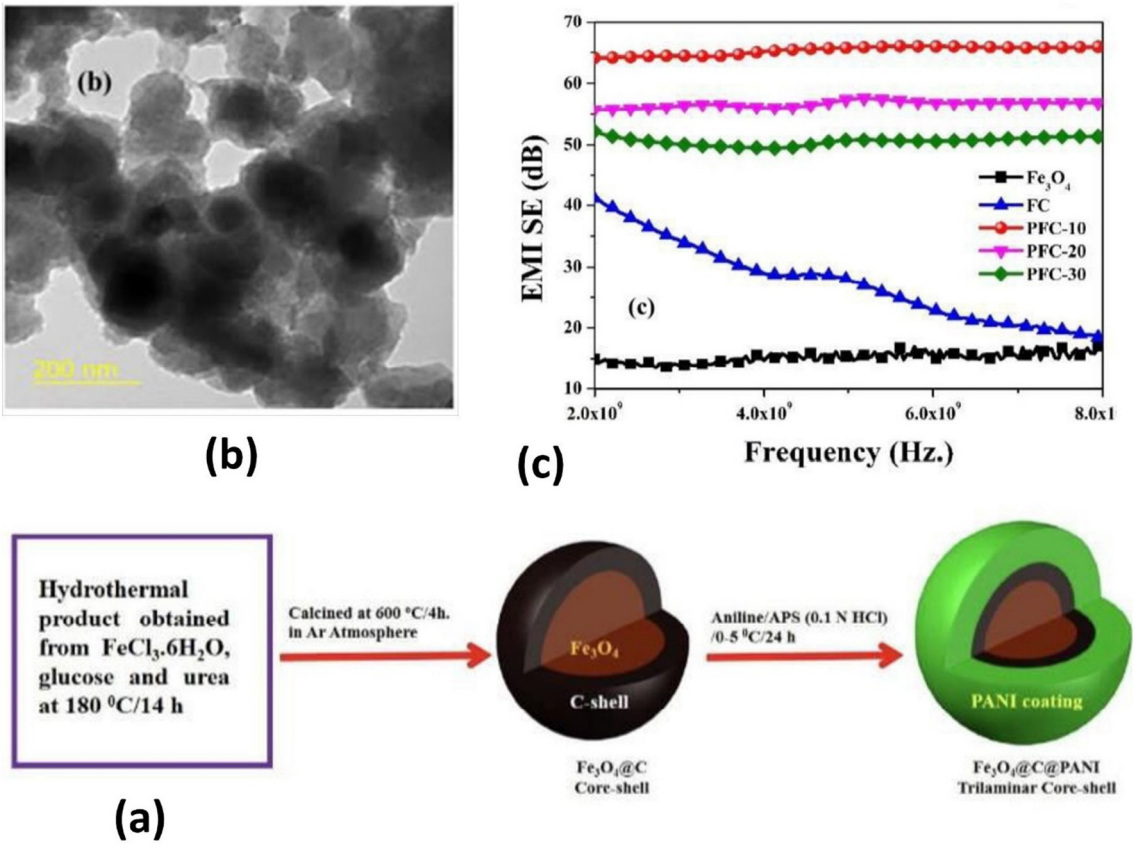

Fig. 20 (a) Schematic presentation of the fabrication of Fe_3O_4@C@PANI ternary composite (aniline : Fe_3O_4@C (FC) = 9 : 1, 8 : 2, 7 : 3 with aniline monomer under identical reaction conditions and procedure and designated as PFC-10, PFC-20 and PFC-30, respectively), (b) HRTEM images of PFC-10, and (c) frequency *vs.* EMISE of PFC composites.[383] Reproduced with permission from ACS.

Motivated by this, they extended their work on core@shell@shell-type Fe_3O_4@SiO_2@PPy, anticipating that the aggregation of Fe_3O_4 in the PPy matrix could be prevented by introducing SiO_2 as first shell (dielectric) between the interfaces of Fe_3O_4 and PPy in comparison to Fe_3O_4 alone.[384] Their findings indicated Fe_3O_4@SiO_2@PPy (Fe_3O_4@SiO_2/pyrrole wt/wt = 1 : 9) exhibited the highest total shielding efficiency (SE_T: ~32 dB) in the frequency range of 2–8 GHz (Fig. 21(a)) following reflection as the dominant shielding mechanism. This was attributed to role played by dual interfaces, poor impedance matching between the PPy (conducting)/SiO_2 (insulating) and high electrical conductivity of Fe_3O_4@SiO_2@PPy and interfacial polarization, and reflection/scattering of EM waves. These findings clearly established that switching of the dominating shielding mechanism from absorption to reflection could be achieved by tuning C@ PANI compared with SiO_2@PPy shells in Fe_3O_4@C@PANI and Fe_3O_4@SiO_2@PPy trilaminar composites, respectively (Fig. 21(b)). Such switching over of the shielding mechanism was also supported by the impedance mismatch and impedance matching in Fe_3O_4@SiO_2@PPy and Fe_3O_4@C@PANI.

Ji *et al.*[385] synthesized hollow γ-Fe_2O_3@PEDOT (FP) and γ-Fe_2O_3@SiO_2@PEDOT (FSP) core–shell nanocomposites. The corresponding SEM images of FSP and FP clearly established the removal of the SiO_2 layer from γ-Fe_2O_3@SiO_2@EDOT to form hollow γ-Fe_2O_3@PEDOT. Further investigations on the frequency (2–18 GHz) dependence of reflection loss revealed remarkable microwave absorption properties of hollow γ-Fe_2O_3@PEDOT (R_L^{min}: −44.7 dB: 12.9 GHz, EAB: 4.3 GHz in 10.8–15.1 GHz range) compared with the γ-Fe_2O_3@SiO_2@PEDOT (R_L^{min}: −21.3 dB: 14.1 GHz, EAB: 3.8 GHz: 12.6–16.4 GHz range) for thickness 2.0 mm. This was ascribed to the synergistic effect between the magnetic and dielectric components and the core–shell structure. Reports are also available on enhanced electromagnetic wave absorption of Co@Hollow carbon nanospheres @PANI[386] and FeNi@C@PANI.[387] Panigrahi and Srivastava[388] fabricated rubber (EPDM, NBR, and NR)@Polystyrene@Polyaniline blends and observed high shielding efficiency (>30 dB:1–8 GHz). Such high performance of rubber blends was attributed to the trapping of EM waves through enhanced internal reflection due to the typical core–shell morphology of PS@PANI. PPy nanotubes/NR/NBR[389] core–shell composites also displayed excellent electromagnetic wave absorption properties.

γ-Fe_2O_3/$(SiO_2)_2$−SO_3H/PPy composite (thickness: 2.0 mm) core/shell/shell microspheres displayed substantially improved microwave absorption properties (R_L^{max}: −43.1 dB) (15.1 GHz), EAB: 6.1 GHz (11.9–18.0 GHz) (Fig. 22(a)).[390] This was ascribed

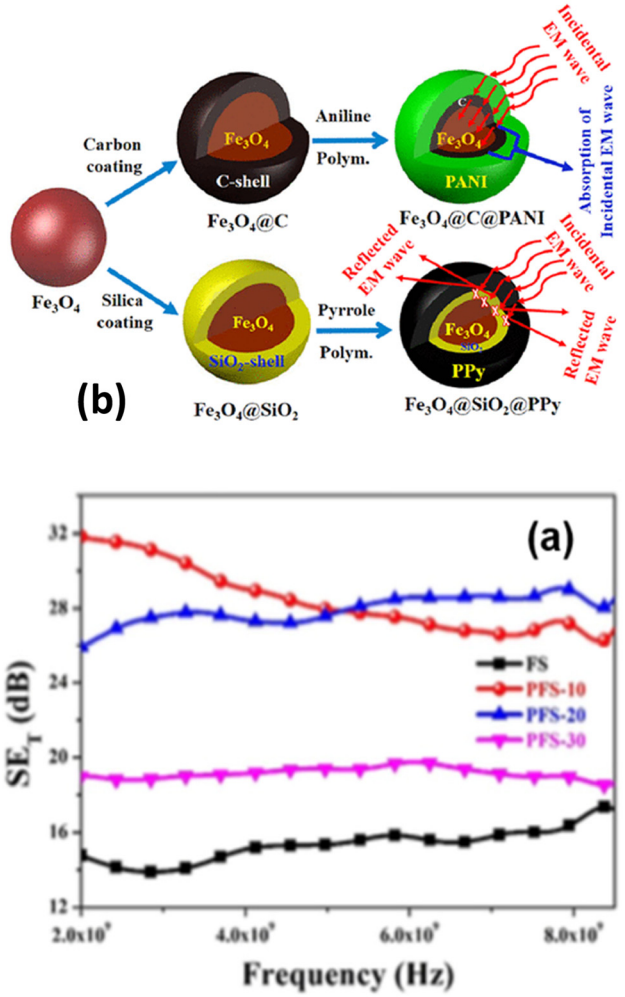

Fig. 21 (a) Plot of frequency *versus* SE_T of Fe_3O_4@SiO_2@PPy (PFS) nanocomposites (Pyrrole/Fe_3O_4@SiO_2 (PS) = 9 : 1, 8 : 2, and 7 : 3) with the aniline monomer under identical reaction conditions and procedures, and the samples were designated as (PFS-10, PFS-20, and PFS-30, respectively), and (b) tuning of shells in trilaminar Fe_3O_4@SiO_2@PPy and Fe_3O_4@C@PANI core@shell nanocomposites in controlling electromagnetic interference through switching of the shielding mechanism.[384] Reproduced with permission from ACS.

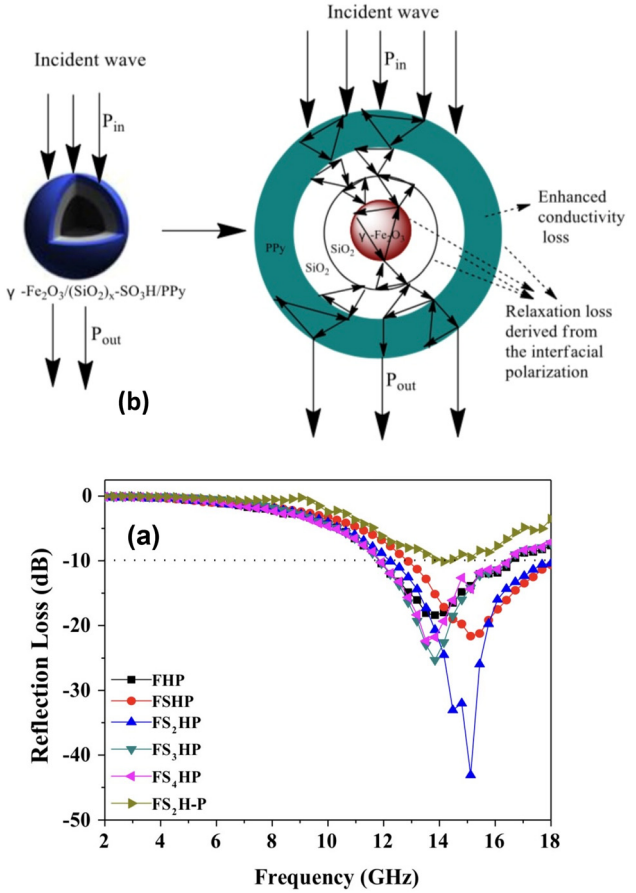

Fig. 22 (a) Variation of R_L of γ-Fe_2O_3/$(SiO_2)_x$–SO_3H/polypyrrole (referred to as FS_xHP, where x = 0,1,2,3,4) core/shell/shell microspheres and FS_2H-P (physical blend of FS_2H and PPy) with the frequency (d = 2 mm), and (b) physical model of the effects of core/shell/shell structures on the microwave absorption.[390] Reproduced with permission from Springer.

to impedance matching, unique core/shell/shell structures, synergistic interaction, dielectric loss (SiO_2 and PPy layers) and magnetic loss (γ-Fe_2O_3). A model has been proposed in Fig. 22(b) to account for the effects of core/shell/shell structures on microwave absorption. Core/shell/shell-structured Ni/C/PANI nanocapsules prepared by a two-step process involving modified arc-discharge and chemical polymerization exhibited an optimal R_L value of −9.3 dB at 6.2 GHz (thickness: 3 mm) with broad −5 dB (3.4–18 GHz) bandwidth.[391] Wang *et al.*[392] prepared hierarchical Fe_3O_4@Graphene@PANI following hydrothermal and *in situ* polymerization. The composite exhibited favourable microwave absorption properties, as evident from R_L^{max} of −43.7 dB (at 10.7 GHz) and the EAB <10 dB of 5.4 GHz (6.8–12.2 GHz) with a matching thickness of 3 mm. These findings were explained on the basis of impedance matching, enhanced interfacial polarization and orientation polarization.

Ding *et al.*[393] fabricated core@shell hierarchical cable-like TiO_2@Fe_3O_4@PPy (Thickness: 3.2 mm) and observed maximum reflection loss of −61.8 dB owing to the magnetic–dielectric synergy. CoNi@SiO_2@Polypyrrole nanocomposites displayed enhanced microwave absorbing capacity as evident from their minimum reflection loss of −34.19 dB at 9.59 GHz (thickness: 2.12 mm) and the EAB with R_L < −10 dB in the entire X-band.[394] In another study, core–shell SiC_{NWs}@MnO_2@PPy prepared through a multistep process showed the minimum reflection loss of −50.59 dB (matching thickness: 2.41 mm) and the effective absorption bandwidth of 6.64 GHz (matching thickness: 2.46 mm).[395] This excellent electromagnetic wave absorption performance was ascribed to the advantage of the interfacial polarization and dipole polarization displayed by core–shell SiCNWs@MnO_2@PPy. Several other ternary composites have also been reported as efficient microwave absorbers, such as Ni/PANI/RGO,[396] Fe_3O_4@PEDOT microspheres/RGO,[397] $NiCo_2O_4$ (hollow)@PPy nanofibers/RGO,[398] encapsula-

tion of γ-Fe_2O_3-decorated RGO in PANI core–shell tubes,[399] RGO/Fe_3O_4/PANI,[56] N-doped Graphene@PANI nanorod modified by Fe_3O_4 nanoclusters,[400] polyaniline/graphene oxide/Fe_3O_4,[401] magnetite nanoparticles decorated CNT/PANI,[402] PANI/CIP/Fe_3O_4,[403] and Fe_3O_4@SiO_2@PPy.[404] Shukla[405] prepared dual core–shell structured Fe_3O_4/C/PPy (Fe_3O_4/C : PPy:2 : 8 wt/wt) composites *via* a hydrothermal and chemical oxidative polymerization method and observed their absorption-dominated excellent EMI shielding efficiency (>28) dB in the range of 1 to 8.5 GHz (Fig. 23(a)). The probable mechanism in Fig. 23(b) shows the attenuation of electromagnetic waves by the trilaminar Fe_3O_4/C/PPy composite. It was also suggested that spin motion plays a decisive role in this performance. In addition, excellent electromagnetic absorption properties have also been reported in PANI@Natural graphite flakes (NGF)/MWCNT[406] and PEDOT/RGO/Co_3O_4.[407]

According to the available literature, a very limited amount of work has been reported on quaternary core–shell composites in general, or their applications in microwave absorption. In one such study quaternary MWCNT/CuO/Fe_3O_4/PANI nanocomposites following the weight ratio of CuO/Fe_3O_4/PANI to MWCNT in the 1 : 3, 1 : 4 and 1 : 5 showed minimum reflection losses −45.7, −85.4, and −87.4 dB, respectively.[408] The corresponding absorption bandwidths ($R_L \leq -10$ dB) of MWCNT/CuO/Fe_3O_4/PANI nanocomposites were found to be 6, 7.6, and 6 GHz. The higher value of loss constant (α) of MWCNT/CuO/Fe_3O_4/PANI nanocomposites indicated both magnetic and dielectric loss tangent playing key roles in influencing the microwave absorption efficiency.

Wang *et al.*[409] fabricated a 3D heterostructure of Graphene@Fe_3O_4@WO_3@PANI using a hydrothermal method and chemical oxidation polymerization and studied its performance in microwave absorption. In addition, the presence of WO_3 decreased permittivity, facilitating better impedance matching. The synthesized quaternary nanocomposite displayed a maximum R_L value (−46.7 dB) at 9.4 GHz and the maximum absorbing bandwidth exceeding −10 dB at 1.8 GHz (12.4 to 14.2 GHz) corresponding to the thickness of 4 mm and 1.5 mm, respectively. The EM wave absorption mechanism involved contributions originating from enhanced interfacial polarization, better impedance matching, multiple reflection, and a synergistic effect. In another study, Liu *et al.*[410] investigated the electromagnetic wave absorption properties of graphene (GN@Fe_3O_4@PANI) decorated with TiO_2 prepared by a hydrothermal method and *in situ* polymerization, as described in Fig. 24(a). The corresponding TEM image in Fig. 24(b and c) indicated TiO_2 nanosheets oriented perpendicular to GN@Fe_3O_4@PANI and TiO_2 nanosheets forming hierarchical structures. The EM wave absorption properties of graphene@Fe_3O_4@PANI@TiO_2 nanosheets loaded in 50 wt% paraffin are displayed in Fig. 24(d). According to this, GN@Fe_3O_4@PANI@TiO_2 nanosheets showed R_L^{max} of −41.8 dB at 14.4 GHz (thickness: 1.6 mm) and absorption bandwidth of $R_L < -10$ dB at ~3.5 GHz. The attenuation of EM waves was attributed to the interfacial polarization and improved impedance matching of the nanocomposites. Table 1 records the microwave absorbing properties of hollow ICPs, hollow ICP nanocomposites and ICP based core–shell nanocomposites.

5.2 Removal of heavy metals in water

Heavy metals have atomic weights between 63.5 and 200.6, and a specific gravity greater than 5.0.[411] These are considered as extremely important toxic environmental pollutants on their discharge from tanneries, fertilizers, mining, metal plating, batteries, pesticides, paper industries and many more, into lakes, rivers, and oceans or into open environments, endangering human life and other living systems owing to their toxicity. Some heavy metals such as Cu, Zn, Fe, Mn are essential for the working of the human metabolic system, but can lead to harmful effects when their concentrations are very

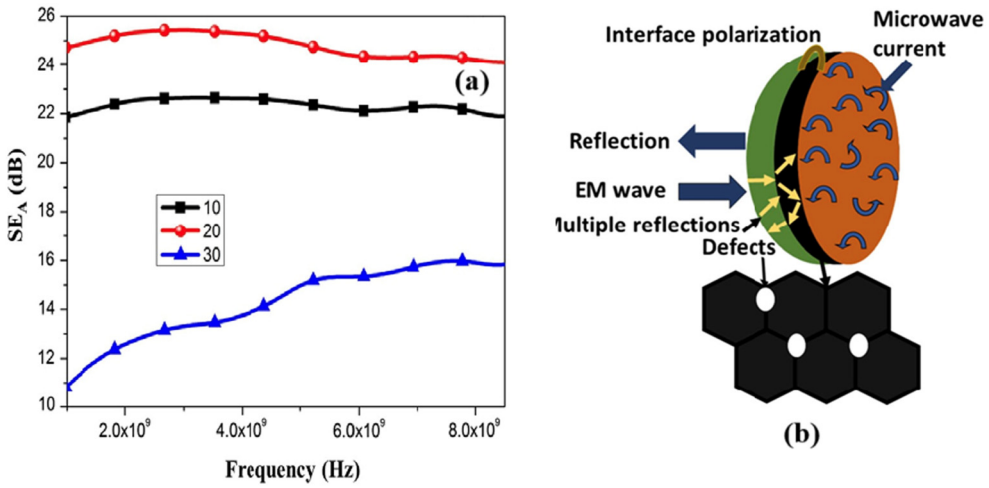

Fig. 23 (a) Plots of frequency *versus* SE_T Fe_3O_4/C/PPy core/shell composites with pyrrole: (Fe_3O_4/C = 9 : 1, 8 : 2,7 : 3) with pyrrole monomer under similar reaction situations, referred to as10, 20 and 30, respectively, and (b) schematic diagram of EMI attenuation mechanism.[405] Reproduced with permission from Springer.

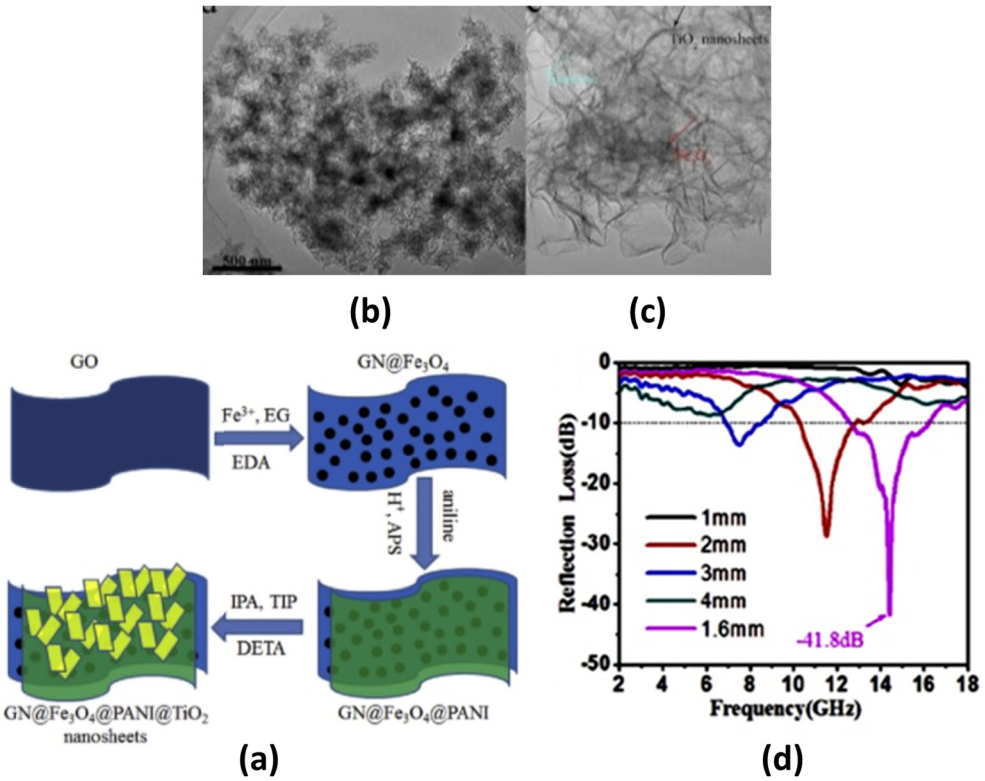

Fig. 24 (a) Schematic illustration of the fabrication of the GN@Fe_3O_4@PANI@TiO_2 nanosheets, (b and c) TEM images of graphene GN@Fe_3O_4@PANI@TiO_2 nanosheets, and (d) reflection loss curves of GN@Fe_3O_4@PANI@TiO_2 nanosheets.[410] Reproduced with permission from Elsevier.

high.[62] Table 2 highlights the sources as well as the health effects of heavy metals on human beings.[412]

In view of this, heavy metal ions can be removed from wastewaters/aqueous solution by using different adsorbents. Intrinsically conducting polymers, especially polyaniline and polypyrrole, have played an excellent role as adsorbents in the removal of different heavy metal ions from contaminated aqueous solutions.[81–85,413] This is ascribed to their several advantages, such as simple synthesis, excellent environmental stability, chemical versatility, biocompatibility, low cost, the presence of functional groups that facilitate their modification, and functionalization by doping and composite formation to favor the adsorption process by tuning their properties.[85,414] Furthermore, the hollow morphology of ICPs, especially polyaniline, can be effective for the adsorption of various pollutants such as heavy metals and dyes due to a large surface area. In addition, hollow ICP-based composites and core–shell nanomaterials have been reported as good adsorbents for removing heavy metal pollutants from wastewater due to their unique physical and chemical properties.

5.2.1 Chromium. Among all heavy metals, hexavalent chromium (Cr(VI)) is considered a serious hazard in water due to its high toxicity compared with Cr(III).[415] The source of Cr originates from the discharge coming out of chrome plating, textiles, leather tanning, metal finishing, and paint pigment industries into the water system. In this regard, a review related to the removal of Cr(VI) using hollow ICPs and core–shell (ICP) as adsorbents is given below.

5.2.1.1 Hollow ICPs. Recently, hollow spherical polyaniline synthesized using a poly(styrene-*co*-acrylic acid) sphere as the template showed high adsorption of Cr(VI), as evident from values of 601.3, 347.8 and 235 mg g^{-1} at pH corresponding to 1, 2, and 3, respectively.[416] Furthermore, the adsorption of Cr (VI) followed a pseudo second-order equation and Redlich–Peterson isotherm models, including excellent regeneration. According to Wu *et al.*,[417] hollow polyaniline micro/nanospheres (10 mg) achieved a maximum removal capacity of 127.88, 43.20 and 25.6 mg g^{-1} at the 1.2 mmol L^{-1} initial concentration of Cr(VI), corresponding to the solution pH of 3, 4 and 5, respectively. The kinetic studies fitted well with the second-order model, and the removal of Cr(VI) could be described by the Langmuir isotherm. 1D-polyaniline nanowire/tubes removed Cr(VI) rapidly and effectively from aqueous solution over a suitable pH range and the adsorbent could be easily regenerated for reuse.[418] A hollow tubular structure comprising the amino acid-doped polyaniline by *in situ* chemical polymerization method exhibited a removal capacity toward Cr(VI) (60.0 mg g^{-1}).[419] Li *et al.*[420] prepared bamboo-like polypyrrole nanotubes following the reactive-template vapor phase polymerization method using electrospun V_2O_5 nanofibers

Table 1 Microwave absorbing properties of hollow ICPs, hollow ICP nanocomposites and ICP based core–shell nanocomposites

Conducting polymer/nanocomposites	Method of preparation	Filling (wt%) in the matrix selected	Frequency range	Shielding performance (sample thickness)	Maximum bandwidth (<10 dB) (GHz)	Ref.
Hollow polyaniline/Ag	Emulsion polymerization	—	100 kHz–20 GH	SE_T: 19.5 dB	—	203
Hollow polypyrrole/Ag	*Via in situ* chemical oxidative copolymerization	—	100 kHz–20 GHz	SE_T: 34.5 dB	—	204
Fe_3O_4 (core: ~100 nm)/PPy (shell: ~70 nm)	*In situ* polymerization	50 wt% in paraffin	2–18 GHz	R_L^{min}: −22.4 dB at 12.9 GHz (thickness: 2.3 mm)	~5 GHz in the range of 4–18 GHz (thickness: 1.5–5.0 mm)	329
Fe_3O_4 microsphere@PANI	Two step oxi. polymerization	50 wt% in paraffin wax bn	2–16 GHz	R_L^{max}: −31.3 dB at 9.0 GHz (thickness: 3 mm)	4.0–18 GHz (thickness: 1.5 to 5.0 mm)	330
Graphene@Fe_3O_4@SiO_2@PANI	Dilute polymerization	25 wt% in paraffin wax	2–18 GHz	R_L^{max}: −40.7 dB at 12.5 GHz (thickness: 2.5 mm)	5.8 GHz (10.5–16.3 GHz)	331
3D helical hollow superstructure of PANI	Co-self-assembly process combined with emulsion droplets	20 wt% in paraffin	2–18 GHz	R_L^{min}: −51.60 dB at 13.95 GHz (thickness:2.0 mm)	5.12 GHz (12.03–17.15 GHz)	337
Hollow PPy nanofibers based self-assembled aerogel (seeds and Py proportion = 1 : 0.5)	Self-assembly	8% in paraffin	2–18 GHz	R_L^{min}: −58.73 dB at 16.48 GHz (thickness: 2.30 mm)	7.28 GHz (thickness: 2.69 mm)	338
Hollow PPy nanorods	*Via* self-assembly template sacrificial strategy	10 wt% in paraffin	2–18 GHz	R_L^{min}: −54.94 dB at 13.2 GHz (thickness: 3.4 mm)	7.36 GHz	339
PANI microtubes	*Via* a self-assembly process assisted by excess APS	—	0 to 6000 MHz.	R_L: −15.5 dB	—	342
PANI hierarchical microtubes	SDS/HCl (7.5 mM) assisted oxidative polymerization method	50% in paraffin	2–18 GHz	−43.6 dB: absorption (thickness: 1.55 mm)	5.84 GHz	343
Polyaniline 3D hollow spheres integrated milled carbon fibers (MCF)	PANI 3D hollow spheres are synthesized by removing the polystyrene (PS) core from PS/PANI composites	4 wt% MCF + 1 wt% PANI in epoxy	8–12 GHz	Max. absorption −49.3 dB (thickness: 1.8 mm)	1.7 GHz (thickness: 1.8 mm)	344
Polyaniline-mediated N and S co-doped carbon nanoflakes	*In situ* polymerization method and carbonization process with oxygen limitation	Paraffin wax (80 wt%) and samples (20 wt%)	2–18 GHz	R_L^{min}: −53.5 dB at 10.2 GHz (thickness: 2.9 mm)	4.5 GHz at 2.9 mm	345
Hollow PANI /CNF in the surface layers and MXene/CNF in the intermediate layer	Alternating vacuum-assisted filtration method	MXene: 8 wt% and Hollow PANI : 24 wt% in CNF matrix	8–12.4 GHz	EMI SE: 35.3 dB	—	346
Hollow Fe_3O_4 (7.33 wt%)@PANI (magnetic fluid: 15 ml)	Hollow PANI prepared by using PS microspheres as hard template and decorating Fe_3O_4 on its surface.	Paraffin filled with with a sample (loaded with 7.33 wt% Fe_3O_4) content of 75%	2–18 GHz	R_L^{max}: −15.6 dB	8.0 GHz	347
Fe_3O_4@PPy	*In situ* polymerization method	60 wt% of composites blended with paraffin wax	2–18 GHz	R_L^{max}: −52.01 dB in 25 wt% of paraffin wax loaded sample of 3.1 mm thickness	2.72 GHz (thickness: 3.1 mm)	348
Fe_3O_4/PPy double-carbonized core–shell-like composite	Rapid microwave assisted carbonization process	—	2–18 GHz	R_L^{min}: −26 dB at 16 GHz (thickness: 1.6 mm)	4.64 GHz (thickness: 1.6 mm)	349
Hollow core–shell Fe_3O_4@PPy	Solvothermal process, followed by *in situ* polymerization (aniline monomer: 170 μL)	50% of nanocomposite by wt in paraffin	2–18 GHz	R_L^{min}: −84.92 dB at 3.87 mm	4.20 GHz at 2.38 mm	350
Fe_3O_4–PE@PANI hollow sphere	Electrostatic self-assembly approach	50 wt% in paraffin	0.5–15 GHz	R_L^{min}: −6.5 dB at 14.3 GHz	Frequency bandwidth at less than −5 dB (12.5 to 15 GHz)	352

Table 1 *(Contd.)*

Conducting polymer/nanocomposites	Method of preparation	Filling (wt%) in the matrix selected	Frequency range	Shielding performance (sample thickness)	Maximum bandwidth (<10 dB) (GHz)	Ref.
Hollow structure Fe_3O_4/PANI microspheres (aniline : PS = 1 : 6)	Three-step synthesis 1.5 and 2.0 mm, the bandwidth below and 4.64 GHz (11.04–15.68 GHz)	50 wt% in paraffin	2–18 GHz	R_L^{min}: −24.3 dB at 18 GHz (thickness: 1.6 mm)	2.48 GHz (15.52–18 GHz) for 1.5 mm thickness, 4.64 GHz (11.04–15.68 GHz) for 2 thickness	353
Hollow poly(aniline-co-pyrrole)–(0.6 g Fe_3O_4)	Oxidized polymerization of aniline and pyrrole in the presence of Fe_3O_4 (0.06 g) using non-ionic surfactant as a template	50 wt% in paraffin	0.5–10 GHz	R_L^{min} : −3 dB at 9 GHz and 10 GHz (thickness: 2 mm)	—	354
Fe_3O_4/PANI (hollow 0D/1D)	Hydrothermal treatment and chemical oxidative polymerization	40% in wax	2–18 GHz	R_L^{min}: −55.03 dB (thickness: 1.84 mm)	4.88 GHz (thickness: 1.84 mm)	355
Fe_3O_4/polyaniline core/shell microspheres (PANI shell thickness: 100 nm)	*In situ* polymerization method	50 wt% in paraffin	1–18 GHz,	R_L^{max}: −37.4 dB at 15.4 GHz	—	356
Fe_3O_4-PEDOT microspheres (EDOT/Fe_3O_4 vol. fraction: 20%)	Two-step method	Paraffin wax	2–18 Ghz	R_L^{min}: ∼−30 dB at 9.5 GHz (thickness: 4 mm)	—	357
Core–shell Fe_3O_4–polyaniline	*In situ* polymerization of aniline in the presence of dodecyl benzenesulfonic acid	40% Fe_3O_4–polyaniline in paraffin wax	0.03–18 GHz	$R_L^{optimal}$: −35.1 dB at 16.7 GHz (thickness: 1.7 mm)	—	358
Core–shell Fe_3O_4@Polypyrrole	Process comprising etching (time: 5 min), polymerization and replication	50 wt% filler in paraffin	2–18 GHz	R_L^{max}: −41.9 dB (99.99%) at 13.3 GHz (thickness: 2.0 mm)	6.0 GHz (12.0–18.0 GHz).	359
Core–shell Fe_3O_4@Polypyrrole microspheres (pyrrole/Fe_3O_4 ratio = 20)	Chemical oxidative polymerization in the presence of polyvinyl alcohol and *p*-toluenesulfonic acid	50% filler in paraffin wax	2–18 GHz	R_L^{max}: −31.5 dB (99.99%) at 15.5 GHz (thickness: 2.5 mm)	5.2 GHz (12.8–18 GHz)	360
Core–shell structure $BaFe_{12}O_{19}$@PANI	30 vol% paraffin wax and 70 vol% powdered filler	*In situ* polymerization method (aniline: 400 μL)	2–18 GHz	R_L^{max}: −65.354 dB at 17.28 GHz (thickness: 1.47 mm.)	2.3 GHz	361
Polythiophene nanofibers coated on $MnFe_2O_4$/Fe_3O_4 (core–shell)	Co-precipitation and *in situ* polymerization	—	8.0–12.0 GHz	R_L^{min}: −21 dB at 12 GHz (thickness: 1.5 mm)	Whole X-band	362
$CoSe_2$@Polythiophene core–shell	Hydrothermal followed by *in situ* polymerization	10 wt% mixed with PVDF	2–18 GHz	R_L^{min}: −55.40 dB (thickness: 1.76 mm)	5.8 GHz (thickness: 1.76 mm)	363
rGO/$Ni_{0.5}Co_{0.5}Fe_2O_4$@PEDOT	*In situ* oxidative polymerization	—	12.4–18.0 GHz	SE_T: 38.79 dB	Broad absorption bandwidth	364
3D graphene-supported Fe_3O_4-coated by polypyrrole	One-step chemical reduction method (GO to Fe_3O_4@PPy) wt ratio = 1 : 3	Composites soaked into molten paraffin	2–18 GHz	R_L^{min}: −40.53 dB at 6.32 GHz (thickness:2.5 mm)	5.12 GHz (thickness: 2.5 mm)	365
Prism-shaped hollow carbon decorated with polyaniline	Carbonization and *in situ* polymerization	30 wt% filler in wax	2–18 GHz	R_L^{min}: −64.0 dB at 11.1 GHz (thickness: 2.5 mm)	5.0 GHz (9.5–14.5 GHz)	366
Core–shell PPy@MoS_2	Combining chemical oxidative polymerization and hydrothermal process	40 wt% filler in paraffin	2–18 GHz	$R_L^{optimal}$: −49.1 dB at 6.1 GHz (thickness: 2.5 mm)	6.4 GHz (11.5–17.5 GHz) at 2.5 mm	367
PPy@PANI	Polymerization of aniline on the surface of PPy microspheres	50 wt% filler in paraffin	2–18 GHz	R_L^{max}: −34.8 dB at 13.9 GHz (thickness: 2 mm)	4.7 GHz (11.9–16.6 GHz)	368
Hollow $Zn_xFe_{3-x}O_4$@Polyaniline	Solvothermal followed by *in situ* chemical oxidation polymerization ($Zn_xFe_{3-x}O_4$: aniline ratio = 0.5 : 1)	50 wt% filler in paraffin wax	2–18 GHz	R_L^{min}: −59.44 dB at 11.04 GHz (thickness: 2.31 mm)	4.65 GHz (13.35–18.0 GHz) for thickness of 1.72 mm.	369
Waxberry-like Carbon@Polyaniline microspheres	*Via* dilute polymerization	30 wt filler in paraffin wax	2–18 GHz	R_L^{min}: −59.6 dB at 15.5 GHz (thickness : 2.2 mm)	5.4 GHz (12.6 to 18 GHz) for thickness of 2.2 mm.	370
CNTs/polyaniline (shell)	Hybrid powders with wax at 10 wt% loading	*In situ* polymerization (mass ratio of CNTs/PANI:1 : 2)	2–18 GHz	R_L^{min}: −41.5 dB at 9.5 GHz (thicknesses: f 2 mm)	5.1 GHz at thicknss of 2.0 mm.	371

Table 1 *(Contd.)*

Conducting polymer/nanocomposites	Method of preparation	Filling (wt%) in the matrix selected	Frequency range	Shielding performance (sample thickness)	Maximum bandwidth (<10 dB) (GHz)	Ref.
PPy (shell)@Carbon microsphere (CMC)	*In situ* polymerization	40 wt% of composite corresponding to 0.6 g of CMC in paraffin wax	2–18 GHz.	R_L^{max}: −38.1 dB at 11.6 GHz (thickness: 3.00 mm)	11.17 to 12.26 GHz (thickness of 3.00 mm)	372
Core shell PEDOT/barium ferrite	*In situ* emulsion polymerization	—	12.4–18 GHz	SE_A: 22.5 dB at 15 GHz with minimal reflection loss of 2 dB	—	373
PANI-coated bagasse fiber (BF) core–shell heterostructure	One-step *in situ* polymerization of aniline in the dispersed system of BF	Mass ratio of BF/PANI to paraffin = 40 : 60	8.2–12.4 GHz	EMI SE: 28.8 dB (thickness: 0.4 mm)	—	374
Polyaniline-coated MWCNT	*In situ* polymerization	—	12.4–18.0 GHz	SE_T: −27.5 to −39.2 dB	—	375
Polyaniline@Helical-CNTs with dual chirality	*In situ* polymerization	Mass ratio of the samples to wax: 3 : 7	2–18 GHz.	R_L^{max}: −32.5 dB at 8.9 GHz (thickness: 3.7 mm)	5.1 GHz (from 7.1 to 11.2 GHz).	376
Hollow PPy microspheres@Fe_3O_4/CNTs	Spray-dry method	Mass ratio of powder with paraffin: 1 : 4	2–16 GHz	R_L^{max}: −51.8 dB at 8.8 GHz (thickness: 2.38 mm)	2.24 GHz (7.76 GHz to 10 GHz)	377
Hollow PPy/Ni/PVDF microspheres	Spray phase inversion method	Mixing samples with paraffin wax in a 1 : 8 wt ratio	18–40 GHz	R_L^{min}: −47.2 dB at 25.36 GHz and −39.8 dB at 31.30 GHz	18–40 GHz (thickness: 1.0–3.5 mm)	378
PPy@FeCo@PPy nanotubes	Combination of electroless plating and oxidative polymerization	Mass fraction of 15 wt% dispersed in the paraffin	2–18 GHz	R_L^{min}: −50.5 dB (thickness: 2.0 mm)	5.7 GHz (thickness: 2.0 mm)	379
1D double-shell PPy@Air@MnO_2 nanotubes	50 wt% in paraffin	Dispersion and self-assembly method	2–18 GHz	R_L^{max}: −52.49 dB at 8.88 GHz (thickness: 2.94 mm)	3.84 GHz (thickness: 2.94 mm)	380
Hollow-spherical composites of PANI/CoS/carbon nanodots (molar ratio of 3 : 1 : 1)	30 wt% in paraffin wax	*Via in situ* polymerization in the presence of magnetic field	2–18 GHz	R_L^{max}: −24 dB at 14 GHz under external applied field of 0.5 T (thickness: 3 mm)	1.92 GHz	382
Fe_3O_4@Carbon@PANI (Fe_3O_4@C: Aniline = 1 : 9 wt/wt)	Multiple steps	—	2–8 GHz	R_L: ∼33 dB SE_T: ∼65 dB	—	383
Fe_3O_4@SiO_2@PPy	Multistep	Mass ratio of products and paraffin = 3 : 7	2–18 GHz	SE_T: ∼32 dB (thickness: 1 mm)	—	384
γ-Fe_2O_3@PEDOT	Reaction of hydrofluoric acid and and γ-Fe_2O_3@SiO_2@PEDOT	Mass ratio of γ-Fe_2O_3@PEDOT and paraffin = 3 : 7	2–18 GHz	R_L^{min}: −44.7 dB at 12.9 GHz with a matching layer thickness of 2.0 mm	4.3 GHz (10.8–15.1 GHz)	385
Co@Hollow carbon nanospheres@Polyaniline	Mixed with paraffin in mass ratio of 1 : 2	Soft template, switching liquid phase transport and *in situ* polymerization method	2–18 GHz	R_L^{min}: −43.63 dB (matching thickness: 2.8 mm)	9.75 GHz (8–17.5 GHz) at a matched thickness of 2.8 mm	386
FeNi@C@Polyaniline	Combining the arc-discharge process and an *in situ* chemical oxidative polymerization reaction	FeNi@C@Polyaniline (40 wt%) mixed with paraffin	2–18 GHz	R_L^{min}: −49.2 dB at 16.6 GHz for a thickness of 1.3 mm	5 GHz (13–18 GHz) for the thickness of 1.4 mm	387
PS@PANI	Solution mixing	—	100 kHz–20 GHz	EMI SE: ∼32 dB at 8 GHz (thickness: 0.5 mm)	—	388
PPy nanotubes/NR/NBR (90/10)	5.24 wt% in paraffin	Mixing technology	8.2–12.4 GHz	R_L^{min}: −56.67 dB (thickness:2.9 mm)	3.7 GHz (thickness:2.9 mm)	389
γ-Fe_2O_3/$(SiO_2)_x$–SO_3H/polypyrrole core/shell/shell microspheres	Sol–gel process and an *in situ* polymerization	70% in paraffin wax	2–18 GHz	R_L^{max}: −43.1 dB (15.1 GHz), (thickness: 4 mm)	6.1 GHz (11.9–18.0 GHz)	390
Core/shell/shell-structured Ni/C/polyaniline	Modified arc discharge method and a chemical polymerization method	40 wt% in paraffin	2–18 GHz	$R_L^{optimal}$: −9.3 dB at 6.2 GHz (thickness: 3 mm)	5 dB (3.4–18 GHz)	391

Table 1 *(Contd.)*

Conducting polymer/nanocomposites	Method of preparation	Filling (wt%) in the matrix selected	Frequency range	Shielding performance (sample thickness)	Maximum bandwidth (<10 dB) (GHz)	Ref.
Fe_3O_4 microsphere@Graphene nanosheets@PANI nanorods	Hydrothermal and *in situ* polymerization methods	30% in paraffin	2–18 GHz	R_L^{max}: −43.7 dB at 10.7 GHz with a thickness of 3 mm	5.4 GHz (from 6.8 to 12.2 GHz)	392
TiO_2@Fe_3O_4@PPy	Sequential process of solvothermal treatment and polymerization	—	2–18 GHz	R_L^{max}: −61.8 dB (thickness: 3.2 mm)	6.0 GHz (X and Ku band) at 2.2 mm thickness	393
CoNi@SiO_2@PPy	Three-step reaction:	—	8.2 to 12.4 GHz	R_L^{min}: −34.19 dB at 9.59 GHz (thickness 2.12 mm)	Entire X-band (8.2–12.4 GHz)	394
SiC_{NWs}@MnO_2@PPy heterostructures	Chemical vapor deposition and two-step electrodeposition process	—	2–18 Ghz	R_L^{min}: −50.59 dB (Matching thickness: 2.41 mm)	6.64 GHz (matching thickness: 2.46 mm)	395
Ni/PANI/RGO	Hydrothermal followed by *in situ* polymerization	—	2–18 GHz	R_L^{max}: −51.3 dB at 4.9 GHz with 3.5 mm thickness	3.1 GHz (3.3 to 6.4 GHz)	396
Fe_3O_4@PEDOT microspheres/RGO	Multiple steps	50 wt% in paraffin	2.0–18.0 GHz	R_L^{max}: −48.8 dB at 9.12 GHz (matching thickness:2.9 mm)	4.32 GHz (matching thickness:2.9 mm)	397
Core–shell $NiCo_2O_4$@Polypyrrole nanofibers/RGO	50 wt% in paraffin	Combination of multiple steps	2.0–18.0 GHz	R_L^{min}: −61.20 dB at 14.26 GHz a (thickness:1.56 mm)	4.90 GHz at 1.57 mm	398
γ-Fe_2O_3 decorated RGO in PANI core–shell tubes	Aniline to Fe_2O_3-decorated rGO weight ratios = 1 : 3	Multiple steps	8.2–12.8 GHz	SE_T: ~51 dB) (thickness: 2.5 mm)	—	399
N-doped graphene@PANI nanorod arrays modified with Fe_3O_4	Hydrothermal reaction	25 wt% of the sample in paraffin	2–18 GHz	R_L^{max}: −40.8 dB at 14.8 GHz with thickness of 2.7 mm	5.1 GHz (10.4 to 15.5 GHz)	400
PANI/GO/Fe_3O_4	*In situ* polymerization	50% in paraffin wax	2–18 GHz	R_L^{max}: −53.5 dB at 7.5 GHz (thickness: 3.91 mm)	2.8 GHz (thickness: 3.91 mm)	401
PANI/carbonyl iron powder (CIP)/Fe_3O_4	Mechanical mixing PANI/CIP composite with PANI/Fe_3O_4 composite with mass ratio of 7 : 3	—	0.5–18 GHz	R_L^{max}: −48.3 dB at 9.6 GHz (thickness: 1.76 mm)	—	403
Fe_3O_4@SiO_2@PPy	Microemulsion polymerization method	Composites mixed paraffin with 15 wt%	2–18 Ghz	R_L^{min}: −40.9 dB at 6 GHz (thickness: 5 mm)	6.88 GHz (11.12–18 GHz)	404
Fe_3O_4/C/PPy (Fe_3O_4/C : PPy: 2 : 8 wt/wt)	Hydrothermal and chemical oxidative polymerization method	—	1–8.5 GHz	EMI SE: >28 dB (thickness: 0.8 mm)	—	405
PANI@Natural graphitic flakes (NGF)/MWCNT	*In situ* by ball milling	10 wt% of MWCNTs	12.4–18.0 GHz	EMI SE: −98 dB	—	406
PEDOT@RGO/Co_3O_4	Two-step method	50 wt% of paraffin	2–18 GHz	R_L^{max}: −51.1 dB (10.7 GHz) at thickness of 2.0 mm	3.1 GHz (9.4–12.5 GHz)	407
MWCNT/CuO/Fe_3O_4/PANI (wt ratios of CuO/Fe_3O_4/PANI to MWCNT = 1.5)	Step by-step approach	25% filler in paraffin	8.2–18 GHz	R_L^{min}: −87.4 dB (thickness: 3 mm)	6 GHz (12–18 GHz)	408
Graphene@Fe_3O_4@WO_3@PANI	Simple hydrothermal method and chemical oxidation polymerization	Composite blended with 70 wt% wax	2–18 GHz	R_L^{max}: −46.7 dB at 9.4 GHz (thickness: 4 mm)	1.8 GHz (12.4–14.2 GHz) at thickness of 1.5 mm	409
Graphene@Fe_3O_4@PANI@TiO_2	Hydrothermal method and *in situ* polymerization	50 wt% in paraffin	2–18 GHz	R_L^{max}: −41.8 dB at 14.4 GHz (thickness: 1.6 mm)	3.5 GHz	410

Table 2 Sources and health effects of heavy metals.[412] Reproduced with permission from IntechOpen

	Heavy metal	Sources	Health effects
Essential heavy metal	Zinc (Zn)	Oil refining plumbing, brass manufacturing	Gastrointestinal disorders, kidney and liver abnormal functioning
	Copper (Cu)	Copper polishing plating, printing	Abdominal disorders, metabolic activity abnormalities
	Iron (Fe)	High intake of iron supplements & oral consumption	Vomiting, diarrhea, abdominal pain, dehydration & lethargy
	Cobalt (Co)	Hip alloy replacement case	Haematological, cardiovascular hepatic, endocrine
Non essential heavy metal	Chromium (Cr)	Steel fabrication, electroplating textile	Lung disorders, (bronchitis, cancer), renal and reproductive system
	Lead (Pb)	Batteries, coal combustion, paint industry	Serious effects on mental health (Alzheimer's disease), nervous system
	Arsenic (As)	Atmospheric deposition, mining, pesticides	Highly effects dermal region (cancer), brain & cardiac problems
	Mercury (Hg)	Coal combustion, fish, mining, paint industry, paper industry, volcanic eruption	Sclerosis, blindness, Minamata disease, deafness, gastric problems, renal disorders
	Cadmium (Cd)	Plastic, fertilizers, pesticides	Osteo related problems, prostate cancer, lung diseases, renal issues

acting as templates as well as the oxidant. These findings indicated the maximum adsorption capacity of 9.281 mmol g^{-1} for Cr(VI) in aqueous solution, with the adsorption data fitting well with the Langmuir model and following pseudo-second-order kinetics (k: 0.0031 g $mmol^{-1}$ min^{-1}).

5.2.1.2 Binary core–shell composites. A polyaniline/polystyrene core–shell nanocomposite showed the ~95% removal of Cr(VI) corresponding to the initial concentration of Cr(VI), adsorbent dose, volume of the medium and pH of 100 mg L^{-1}, 250 mg, 50 mL and 2, respectively.[421] The maximum adsorption capacity (q_m) of PANI/PS for Cr(VI) was found to be 19 mg g^{-1}. The possible mechanism involved the complexation between Cr(VI) ions and the N atoms of the –N=C– groups through sharing of their lone pair of electrons. In addition, polyacrylonitrile/polyaniline core/shell nanofiber mat,[422] sulfonated poly(arylene ether nitrile)/polypyrrole core/shell nanofibrous mat,[423] Ag-P/Ppy core–shell composite,[424] polypyrrole-wrapped oxidized MWCNTs,[425] polyaniline-coated ethyl cellulose,[426] and polypyrrole-coated halloysite nanotube clay nanocomposite[427] have also been used as adsorbents in the efficient removal of toxic Cr(VI) from aqueous solution.

Fe_3O_4/PANI microspheres were fabricated through the interfacial polymerization and used as adsorbent in removing about 94% of Cr(VI) ions from water.[428] The adsorption isotherm followed the Langmuir isotherm mode (q_m: 200 mg g^{-1}), and pseudo-second-order kinetics. Fe_3O_4/PANI microspheres. In addition, Fe_3O_4/PANI has been evaluated for its regenerability and reusability to remove adsorbed Cr(VI) ions using NaOH aqueous solution. These studies have shown the adsorption capacity of Fe_3O_4/PANI microspheres retained 90% of the initial value after reusing five times. It may be interesting to mention that the regeneration of Fe_3O_4/PANI microspheres using hydrochloric acid is not possible as it degrades the polyaniline and dissolves the Fe_3O_4. In another study, Fe_3O_4/polypyrrole nanotubes prepared by a one-pot process exhibited a Cr(VI) adsorption capacity of ~451.45 mg g^{-1}.[429] This suggested that the adsorption process takes place due to ion exchange and chelation. Furthermore, the existence of $-NH^+$ on the Fe_3O_4/PPy nanotubes partially reduced Cr(VI) to Cr(III). Fe_3O_4/PPy nanotubes also retained about 90% of the initial removal efficiency after 5 adsorption/desorption cycles. According to this, adsorption of Cr(VI) on the Fe_3O_4/PPy nanotubes involved ion exchange and chelation. As a result, Cr(VI) was partially reduced to Cr(III) due to the existence of $-NH^+$ on the Fe_3O_4/PPy nanotubes.

In another study, Fe_3O_4-coated polypyrrole (initial concentration: 200 mg L^{-1}) showed 100% adsorption for 200 mg L^{-1} Cr(VI) aqueous solution corresponding to pH 2.[430] The proposed mechanism for the removal of Cr(VI) was guided by ion exchange and reduction on the surface of the nanocomposite. The kinetics studies indicated a pseudo-second-order rate model and Langmuir model predicted from the fitting of isotherm data. The maximum adsorption capacity of Polypyrrole/Fe_3O_4 magnetic nanocomposite increased from 169.4 to 243.9 mg g^{-1} corresponding to the temperature change from 25 °C to 45 °C, respectively. The possible mechanism was elucidated based on XPS studies. According to this, the possible mechanism for Cr(VI) removal by the PPy/Fe_3O_4 could be due to ion exchange and reduction on the surface. Several other adsorbents comprising magnetite arginine-functionalized polypyrrole,[431] magnetic particle-coated PPy and PANI,[432] polypyrrole-coated Fe_3O_4,[433] polypyrrole-modified natural corncob-core sponge,[434] polyaniline-coated protonic titanate nanobelt,[435] and MnO_2-coated polyaniline nanofibers[436] also successfully removed hexavalent chromium from water.

Du *et al.*[437] synthesized core–shell polypyrrole/hollow mesoporous SiO_2 particles by *in situ* polymerization to study the removal of Cr(VI) from aqueous solution that exhibited the maximum adsorption capacity of Cr(VI) of ~322 mg g^{-1} at 25 °C following the quasi-second-order kinetic model and the Langmuir isotherm model. In another study, deposition of PANI on the surface of ThO_2 has been validated by TEM analysis.[438] Further investigations revealed the adsorption of Cr(VI) on this core shell composite to be dependent on the solution pH. The kinetic model and adsorption process fitted well with the pseudo-second-order and Langmuir model (q_m: 141 mg g^{-1}). Polyacrylonitrile/polypyrrole core/shell nanofiber mat

exhibited high selectivity for Cr(VI) compared with the Ni(II) and Cu(II) ions in the solution.[439] The high removal efficiency of hexavalent chromium has also been reported on L-cystine-doped glucose carbon spheres (GCS)@PPy,[440] PANI@Nano hollow carbon spheres,[441] Polypyrrole@Attapulgite,[442] copper slag@polyaniline,[443] polyaniline@Ni(OH)$_2$,[444] PPy@MgFe$_2$O,[445] polypyrrole/graphene oxide,[446] and PANI@Almond shell biocomposite.[447]

5.2.1.3 Ternary core–shell composites. Dutta *et al.*[448] prepared polypyrrole–polyaniline-coated rice husk ash (termed PPy PANI@RHA) by *in situ* polymerization and used it in the removal of Cr(VI) from aqueous solution, and the corresponding findings are shown in Fig. 25(a–d). It revealed about 98% of Cr(VI) removal at room temperature (303 K) under optimum conditions (adsorbent dose: 0.8 g L^{-1}, adsorbate concentration: 50 mg L^{-1}, pH of ~2, contact time: 300 min). The adsorption studies indicated Elovich kinetics and the results are better described using the Freundlich isotherm model with a maximum adsorption capacity of 769.15 mg g^{-1}. The possible Cr(VI) adsorption mechanism by the PPy–PANI@ RHA adsorbent has been described in Fig. 26 on the basis of ion-exchange, strong electrostatic attraction and reduction of Cr(VI). Their findings also indicated the removal efficiency of Cr(VI) remains more or less unaltered in the presence of moderate concentrations of co-existing ions (Ca^{2+}, Na^{+}, Mg^{2+}, and Cl^{-}, NO^{3-}, PO_4^{3-}). The regenerated adsorbent subjected to adsorption of Cr(VI) for 5 desorption/adsorption cycles showed a removal efficiency of 94% and 80% in the first and second cycles, respectively.

In another study, the adsorption of Cr(VI) in aqueous solution on a polypyrrole-decorated graphene-silica (Graphene/SiO$_2$@Polypyrrole) composite exhibited the maximum adsorption capacity corresponding to 429.2 mg g^{-1} (298 K) at pH 2.[449] The adsorption of Cr(VI) on graphene/SiO$_2$@ polypyrrole fitted well with the pseudo-second-order kinetic and Langmuir isotherm model. The simultaneous removal of methyl orange and Cr(VI) from water has also been evaluated based on PPy@Magnetic chitosan adsorbent.[450] Da Rocha *et al.*[451] reported the formation of a layer of PPy chains on the PMMA/rice husk ash (RHA) fibers and observed a Cr(V) removal capacity q_e of 363.63 mg g^{-1} (after 150 min) at pH 2. In another study, core–shell PS/PANI-Fe$_3$O$_4$ adsorbent removed 100% Cr(VI) corresponding to pH: 2, adsorbent: 0.05 g, initial concentration of Cr(VI): 5 mg L^{-1}, total volume: 30 mL and 120 min, respectively.[452] The removal of hexavalent chromium from water has also been studied using a polyaniline/wood

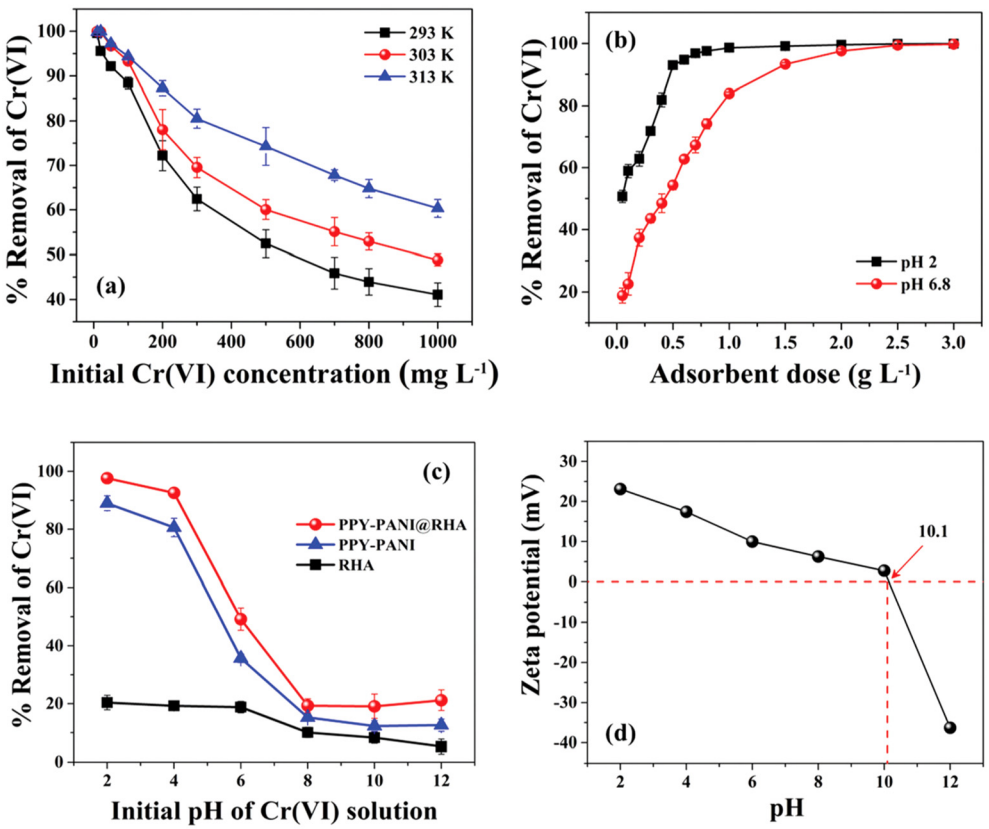

Fig. 25 (a) Effect of initial concentration of Cr(VI) at a different temperature (PPY PANI@RHA dose: 0.8 g L^{-1}; contact time: 300 min; agitation speed: 200 rpm; pH~2), (b) effect of adsorbent dose at pH 2 and without pH (~6.8) adjustment (initial Cr(VI) concentration: 50 mg L^{-1}; contact time: 300 min; agitation speed: 200 rpm; temperature: 303 K), (c) effect of initial solution pH on % removal of Cr(VI) by PPY–PANI@RHA, PPY–PANI and RHA adsorbents (Initial Cr(VI) concentration: 50 mg L^{-1}; contact time: 300 min; agitation speed: 200 rpm; temperature: 303 K), and (d) variation of zeta potential of PPY–PANI@RHA at different pH.[448] Reproduced with permission from RSC.

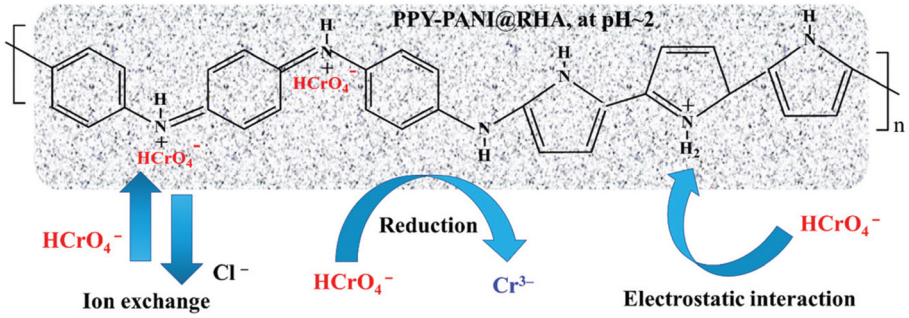

Fig. 26 Representation of possible Cr(VI) adsorption by PPY–PANI@RHA.[448] Reproduced with permission from RSC.

sawdust/polyethylene glycol composite.[453] Yao *et al.*[454] prepared Fe_3O_4@Polypyrrole nanospheres with a hierarchical porous structure anchored on graphene nanosheets and noted the excellent adsorption capability in Cr(VI) removal (q_m: ~348.4 mg g^{-1}) due to the synergic effect between graphene and Fe_3O_4@polypyrrole. The adsorption kinetics was explained on the basis of pseudo-second-order kinetics. In addition, the fabricated adsorbent was found to be stable and retained ~72.2% removal efficiency after six cycles.

The large specific surface area of γ-Fe_2O_3@Chitosan@PPy accounted for the maximum Cr(VI) adsorption capacity of 301.2 mg g^{-1}.[455] The magnetic nanocomposite removed 100% Cr(VI) in aqueous solution, and this was described as based on exchange and chelation as the dominant interaction mechanisms.

5.2.2 Lead. The source of lead pollution in water mainly comes from steel plants, battery factories, and several other industries. This can lead to serious health-related issues owing to its non-degradable characteristics and presence through bioaccumulation, even if present at a low level of concentration. In view of this, removal of Pb in water based on hollow ICPs and core–shell (ICP) as adsorbent is described as below.

5.2.2.1 Hollow ICPs. Han *et al.*[456] fabricated a hollow structure comprising PANI nanospheres with incontinuous multicavities by chemical polymerization using chloroaurate acid as oxidant and citric acid as dopant. Subsequently PANI nanospheres exhibiting incontinuous multicavities were formed by dissolving Au particles in excess saturated KI/I_2 solution. The adsorption capacity and adsorptivity values of PANI in the removal of Pb in water correspond to 1589 mg g^{-1} and 93%, respectively.

5.2.2.2 Binary and ternary core–shell composites. γ-Fe_2O_3 coated with proton acid doping polyaniline nanocomposites (γ-Fe_2O_3@PANI) showed high adsorption capacity for arsenic (V) removal in water (pH: 4 to 11), and this was explained based on the electrostatic interaction and hydrogen bonding.[457] Mehdinia *et al.*[458] investigated the effects of the transformation of core–shell Fe_3O_4@PPy to its rattle type (yolk shell) on removal of heavy metals Pb^{2+} and Cu^{2+} from water. PANI/TiO_2 adsorbent prepared by the chemical oxidative polymerization of aniline on the surface of TiO_2 hydrate showed adsorption capacities of Cr(VI) in water to be 394.43 mg g^{-1} with excellent reusability.[459] Furthermore, the adsorption of Cr(VI) oxyanions involved electrostatic attraction, hydrogen bonding and anion-π interactions.

Vatani and Eisazadeh[460] coated polythiophene on polystyrene and poly(vinyl chloride) to investigate the role they play as adsorbents in the removal of Pb(II) from aqueous solution. They observed the higher removal efficiency of PTh/PVC compared with PTh/PS nanocomposites under the optimum conditions (pH: 2, initial concentration of cations 100 mg^{-1}, equilibrium time: 30 min). Chen *et al.*[461] prepared a PTh/MnO_2 composite with MnO_2 as the core and PTh as the shell for the selective adsorption towards Pb^{2+}, Zn^{2+} and Cu^{2+} from industrial wastewater in the aqueous medium. These findings showed the adsorption capacities of Pb^{2+}, Zn^{2+} and Cu^{2+} (within 30 min) were found to be 82.10, 30.72 and 60.79 mg g^{-1}, respectively. These findings have been explained on the basis of a synergistic effect between PTh and MnO_2.

Binary composites have been prepared following the coating of polyaniline for their applications in the removal of Pb(II) ion in water. Fe_3O_4 particles coated with polyaniline showed the maximum lead adsorption capacity of Pb(II) as 114.9 mg g^{-1}.[462] Pb(II) ions were found to be almost completely removed under the optimum conditions (initial concentration of lead(II): 50 ppm, adsorbent dosage: 3 mg, pH: 9.3).

According to Shakhsari *et al.*,[463] $CoFe_2O_4$@PANI removed 98% of Pb at 25 °C from water under the optimum condition of initial concentration of metal ions (17 mg L^{-1}), adsorbent dose (1 g), pH (7) and time (120 minutes). The adsorption kinetics followed the quasi-first-order model, and data fitted well with the Freundlich isotherm. Polypyrrole-coated ZnO-NiO nanocomposites have also been investigated as adsorbents for enhanced removal of Pb(II) from aqueous solution and wastewater.[464] The possible mechanism of Pb(II) adsorption on the PPy/ZnO-NiO adsorbent has been explained based on ion exchange, electrostatic attraction, and the formation of metal complexes. The reusability and regeneration experiments after six adsorption–desorption cycles have shown a decrease in the adsorption and desorption of Pb(II) from 98.7% to 77.8% and 92% to 67%, respectively. Naphthalene sulfonic acid-doped polyaniline@Ni^0 composite (0.5 g L^{-1}) achieved 90.9% removal efficiency of Pb(II) ions in aqueous solution (pH: 5).[465] The findings based on the isotherm data

supported the Langmuir isotherm model, with maximum Pb(II) removal capacity of 414.6 mg g^{-1} at 25 °C. Fe_3O_4/polyaniline hollow microspheres have been fabricated and used as adsorbent in the uptake of Pb^{2+} from aqueous solution.[466] It followed the pseudo-second-order kinetics and adsorption data agreed well with the Langmuir isotherm.

Zare *et al.*[467] used a poly(aniline-*co*-3-aminobenzoic acid)-based magnetic core–shell nanocomposite and observed the maximum adsorption capacity of Pb(II) to be 138.31 mg g^{-1} in an aqueous solution. The findings were also found to be in agreement with the pseudo-first order and Freundlich isotherm. Pomegranate-like MnO_2@PANI using 0.1 mol L^{-1} of $KMnO_4$ has been successfully synthesized according to the procedure described in Fig. 27(a).[468] Subsequently, the variation of removal ratios (q) of Pb(II) ions with PANI nanoflowers (NF), commercial MnO_2, PANI spheres prepared with cavities and pomegranate-like MnO_2@PANI spheres as adsorbents has been studied, and the findings are displayed in Fig. 27(b and c). It is noted that respective removal ratios (q) values correspond to 36.1%, 54.9%, 71.2%, and 99.2%, respectively. MnO_2@PANI showed the maximum sorption capacity of 309.6 mg g^{-1}. Such excellent adsorbability of MnO_2@PANI spheres was ascribed to the presence of mesoporous structures of PANI spheres with more exposed adsorption sites towards Pb(II) ions. Alternatively, enhancing the sorption ability of Pb(II) ions could be ascribed to the interaction (chelation/physisorption) between MnO_2 and PANI contributing synergistically. The removal ratios of different heavy metal ions on PANI and PANI@MnO_2 as adsorbents were also tested for Ni(II), Cd(II), Cu(II), Zn(II) heavy metal ions. Subsequent findings revealed higher removal ratios of these heavy metals for the MnO_2@PANI hybrids compared with PANI nanospheres and also agreed well with the earlier results on Pb(II) ion adsorption. Chemically modified polythiophene with copper nanoparticles and polyvinylpyrolidine-sulfonic acid[469] and polypyrrole-iron oxide–seaweed[470] exhibited the adsorption capacity of lead from aqueous solution of 111 mg g^{-1} and 333.33 mg g^{-1}, respectively.

PANI/Jute fiber composites exhibited effective Cr(VI) and Cd(II) ion decontamination from water.[471] The core/shell like structure of the PTh/SiO_2 composite exhibited superior selectivity to separate and recycle Zn^{2+} among multiple ions (Pb^{2+}, Zn^{2+}, Cu^{2+}) in wastewater due to the synergistic effect.[472] Sun *et al.*[473] studied the adsorption of Cu(II), Pb(II) and Ni(II) on PANI@Aminopropyltriethoxysilane (APTS)-Fe_3O_4/Attapulgite composite and observed the maximum adsorption capacity of 189.03, 270.27 and 142.86 mg g^{-1}, respectively. The reusability performance of PANI@APTS-Fe_3O_4/Attapulgite after 5 times of use showed a slight decrease for all the heavy metals (Cu(II): 84% to 79%, Pb(II): 87% to 81%, Ni(II): 63% to 56%). SiO_2-coated magnetic graphene oxide modified with a pyrrole-thiophene copolymer showed a maximum adsorption capacity for Cu(II), Pb(II), Zn(II), Cr(III) and Cd(II) in aqueous solution corresponding 201, 230, 125, 98 and 80 mg g^{-1}, respectively.[474] High-temperature hydrothermally prepared polypyrrole-derived N-doped carbon nanotubes decorated with fish scale-like MoS_2 nanosheets showed a significantly much higher removal capacity for Pb(II) (q_m: 381.87 mg g^{-1}) in waste water.[475] Based

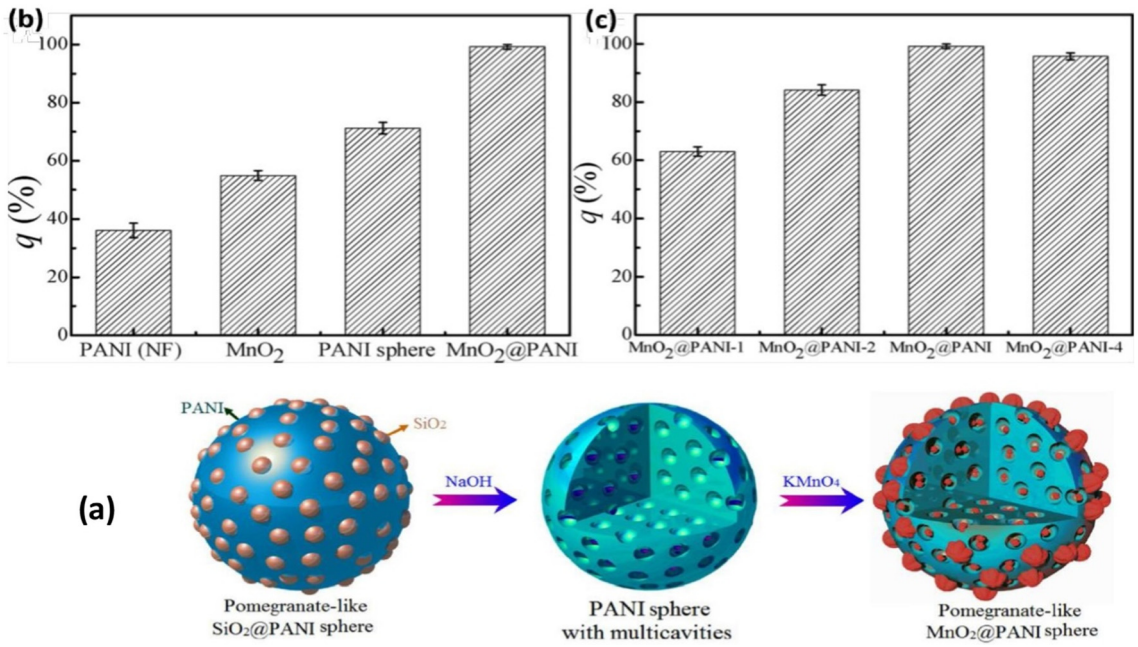

Fig. 27 (a) Schematic representation of the preparation of pomegranate-like MnO_2@PANI sub-microspheres, (b) removal ratios of Pb(II) ions with PANI(NF), MnO_2, PANI sphere and MnO_2@PANI as adsorbent, (c) removal ratios of Pb(II) ions with MnO_2@PANI-1, to MnO_2@PANI-2, MnO_2@PANI and MnO_2@PANI-4 as adsorbent. Adsorption conditions: [Pb(II)] = 60 mg L^{-1}, [adsorbent] = 0.5 g L^{-1}, pH = 5.0 ± 0.1, T = 25 °C, 12 h.[468] Reproduced with permission from Elsevier.

on XPS studies, the following possible mechanism for the adsorption of Pb(II) on the C-Ppy@MoS_2 has been proposed:

$$Mo(IV) + 2H^+ + 4e^- + 4H_2O\ (aq) \rightarrow 5H_2\ (g) + MoO_4^{2-}(VI)$$

$$MoO_4^{2-}(VI) + Pb^{2+} + S \rightarrow PbMoO_{4-x}S_x\ (s)$$

It is believed that the protons produced in the above reaction may have a driving effect on the adsorption process. The unique structure of the fish scale-like MoS_2 nanosheets on the C-PPy nanotubes accounts for the adsorption of Pb(II).

5.2.3 Other metal ions. Dutta *et al.*[476] fabricated hollow polyaniline microsphere (PNHM)/Fe_3O_4-40 (Fe_3O_4 content: 40 wt%) magnetic nanocomposites. Subsequent investigations, shown in Fig. 28(a–d) and adsorption studies revealed about 98–99% removal of As(III) and As(V) from the contaminated water in the presence of PNHM/Fe_3O_4-40 and followed pseudo-second-order kinetics and Freundlich isotherm. The maximum adsorption capacity for As(III) and As(V) corresponded to 28.27 and 83.08 mg g^{-1}, respectively. The adsorption of arsenic species on the surface of PNHM/Fe_3O_4-40 could be attributed to the formation of a monodentate–mononuclear/bidentate–binuclear As–Fe surface complex. The probable schematic representation of the arsenic adsorption mechanism in aqueous solution was deduced based on X-ray photoelectron spectroscopy analysis and is displayed in Fig. 29. The reusability studies of the PNMH/Fe_3O_4-40 demonstrated ~83% removal efficiency of As(III) in the third adsorption cycle, and was found to be much higher than many other reported adsorbents. The Fe_3O_4-40 composite was also found to be a very effective adsorbent in the removal of arsenic from naturally contaminated groundwater samples.

Further studies have shown an increase in the adsorption of As(III) and As(V) on the surface of PNHM/Fe_3O_4-40 on increasing the temperature from 293 K to 313 K.[477] In another study, Fe_3O_4/PANI was prepared by the chemical polymerization method.[478] SEM studies confirmed the formation of PANI on the surface of Fe_3O_4 grains. This core–shell structure of Fe_3O_4/5%PANI exhibited the highest arsenic adsorption ability at pH 7 and 300 K. According to Muhammad *et al.*,[479] the Fe_3O_4/PANI core–shell composite can be applied as an effective adsorbent for the removal of hexavalent chromium and divalent nickel from water. Polyaniline/Fe^0 (ref. 480) and iron-functionalized polythiophene (PTh@Fe)[481] were also reported as excellent adsorbents for the removal of arsenic from aqueous solutions. In addition, heavy metals from aqueous solution have also been removed by polyaniline coated on sawdust,[482] Fe_3O_4-embedded poly(thiophene),[483] PAN/PANI-Nylon,[484] 2-aminopyridine functionalized magnetic core–shell Fe_3O_4@Polypyrrole composite,[485] and Fe_3O_4/SiO_2/PANI-SDBS nanocomposite.[486] Fe_3O_4@PPy core–shell functio-

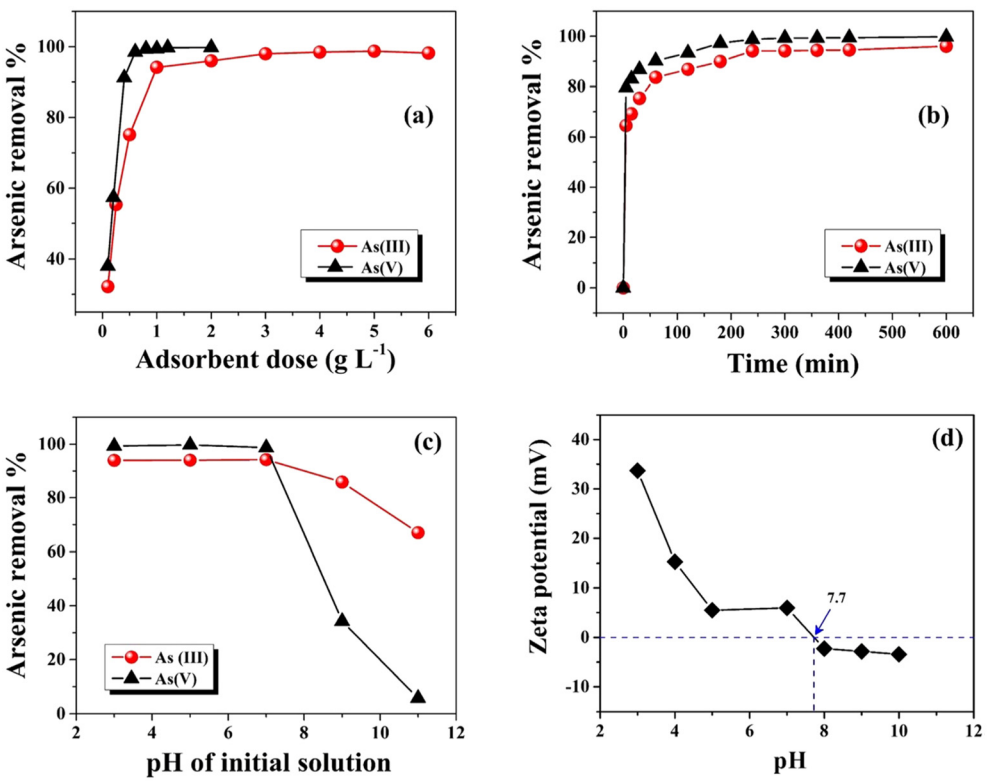

Fig. 28 (a) Effect of adsorbent dose (Experimental conditions: C_0: 1000 μg L^{-1}; pH~7; contact time: 240 min; T: 300 ± 3 K), (b) effect of contact time (Experimental conditions: adsorbent dose: 1 g L^{-1}; C_0: 1000 μg L^{-1}; pH ~7; T: 300 ± 3 K), (c) influence of initial solutions pH (Experimental conditions: adsorbent dose: 1 g L^{-1}; C_0: 1000 μg L^{-1}; contact time: 240 min; T: 300 ± 3 K) on As(III) and As(V) removal efficiency using PNHM/Fe_3O_4-40, (d) ζ-potential of PNMH/Fe_3O_4-40 under various pH conditions.[476] Reproduced with permission from Nature Publication.

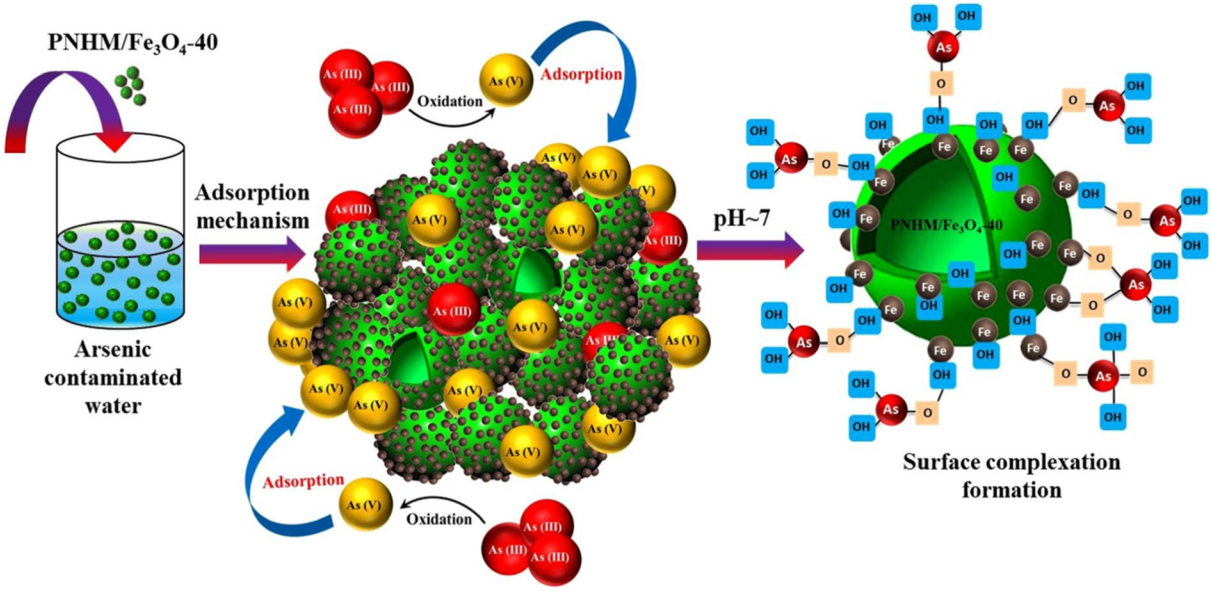

Fig. 29 Schematic representation of arsenic adsorption mechanism in aqueous solution.[476] Reproduced with permission from Nature Publication.

nalized with tetrakis (4-carboxyphenyl) porphyrin (TCCP) prepared in multiple steps displayed 100% efficiency for Hg(II) removal in water.[487] Investigations have also been reported on the adsorptive removal of Hg^{2+} by polyaniline/attapulgite.[488] Ren *et al.*[489] prepared Fe_3O_4@Polypyrrole@Sodium dodecyl sulfate core@shell composite and observed the selective removal of Mn(VII) and other dyestuffs from wastewater (Table 3).

5.3. Removal of dyes

These dyes are primarily used by the leather, paint, varnish, pharmaceutical, textile, printing, pulp and paper, food and several other industries.[60–64] Fig. 30 depicts the sources and pathways of various dye pollutants in water bodies.[88] However, the discharge of these highly toxic, carcinogenic and non-biodegradable toxic dyes from these sources, including their inappropriate disposal on agricultural land without suitable treatment, even in extremely small amounts, is dangerous to aquatic life, microorganism, and human health.[61] The details have already been described about the classification, examples, applications, solubility in water, and ecotoxicological effects of dyes on living organisms.[88] Therefore, the issue of toxic dyes present in wastewater remains a major challenge to existing conventional water treatment systems. As a consequence, the environmental remediation of the presence of these water-soluble dyes in wastewater is mandatory before they are released into water bodies, to avoid negative effects. In view of this, the adsorption process, among the different available technologies, is considered as one of the most studied.

In this regard, polyaniline has been reported as one of most studied and cost-effective adsorbents in the decontamination processes of wastewater treatment, owing to its easy synthesis with a possibility of doping, exhibiting environmental stability, mechanical flexibility and good physicochemical properties and the presence of amine and imine groups.[64,489] However, conventional PANI powder has a low surface area that limits its ability to adsorb dye. In this regard, hollow and core–shell-structured conducting polymers, especially polyaniline, have been used for the effective adsorption of dyes owing to their high surface area and other properties.

From this perspective, hollow-structure polyaniline is more advantageous for the removal of dye due to its high surface area and porous structure. In addition, core–shell-structured polyaniline also offers several advantages that include enhanced adsorption capacity, improved selectivity, better stability, and achieving increased surface area and the ability to incorporate different materials for specific interactions with the dye molecule.[64,68] Accordingly, the adsorption performance of hollow conducting polymers, hollow conducting polymer composites and conducting polymer-based core–shell composites has been reviewed below for the removal of different dyes from water.[490–550]

5.3.1 Rhodamine

5.3.1.1 Hollow ICPs. Wu *et al.*[491] used a functionalized polystyrene sphere as the template to fabricate hollow spherical polyaniline (average dia: 300 nm, shell thickness: 100 nm) and observed its high adsorption capacity for RhB (61.75 mg g^{-1}). According to Chen *et al.*[492] hollow polyaniline helical nanobelts have been prepared through the generation of hollow oligoaniline helical nanobelts acting as sacrificial templates during the chemical oxidation method. It was inferred that the presence of the large number of adsorption sites comprising several amino and imino groups in hollow PANI helical nanobelts facilitated the effective adsorption of rhodamine 6G.

5.3.1.2 Binary core–shell composites. Investigations have also been made on the removal of rhodamine B dye in

Table 3 Performance data of hollow ICPs, hollow ICP nanocomposites and ICP based core–shell adsorbents in removal of heavy metal ions in water medium

Metal ions	Adsorbent used	Water type	Preparative method	Experimental conditions on removal of metal ions	q_m (mg g^{-1})	Removal isotherm fitted to	Kinetics data fitted to (k)	Ref.
Cr(VI)	Hollow PANI micro/nano sphere	Waste water	Monomer polymerization in alk solution with Triton X-100 as soft templates	Cr(VI): 1.2 m mol L^{-1} (20 mL), dosage: 10 mg, pH 3.0, q_e (time): ~79 mg g^{-1} (180 min)	127.88	Langmuir	Pseudo sec. order	417
Cr(VI)	Amino acid-doped PANI nanotubes	Aqueous solutions	*In situ* chemical polymerization	Temp.: 25 °C Cr(VI): 30 mg L^{-1} (10 mL), dosage: 0.25 g, pH: 7, removal (time): ~100% (120 min)	60	Langmuir	Pseudo sec. order	419
Cr(VI)	Bamboo-like PPy nanotubes	Aqueous solution	Reactive-template vapor phase polymerization method	Cr(VI): 1.95 mmol L^{-1} (20 mL), dosage: 3 mg, pH: 3, adsorption capacity (time): ~9 mmol g^{-1} (1400 min)	9.281 mmol g^{-1}	Langmuir	Pseudo sec. order (0.0031 g $mmol^{-1}$ min^{-1})	420
Cr(VI)	Core–shell polyaniline/polystyrene	Aqueous solutions	Microemulsion polymer of polystyrene followed by *in situ* polymer of aniline monomer	Temp.: 20 °C Cr(VI): 100 mg L^{-1} (50 mL), dosage: 250 mg, pH: 2, removal (time): ~95% (30 min)	19	Temkin	Pseudo sec. order (k: 6.27 × 10^{-3} mg L^{-1} min^{-1})	421
Cr(VI)	Polyacrylonitrile/polyaniline core/shell nanofiber mat	Aqueous solution	*Via* electrospinning followed by *in situ* polymerization	Temp.: 25 °C, Cr(VI): 207 mg L^{-1} (30 mL), dosage: 100 mg, pH: 2, q_t (time): 53.4 mg g^{-1} (12 h)	71.28	Langmuir	Pseudo sec. order (k: 7.20 × 10^{-3} g mg^{-1} min^{-1})	422
Cr(VI)	Sulfonated poly(arylene ether nitrile)/polypyrrole core/shell	Aqueous solution	Electrospinning technique followed by *in situ* polymerization	Temp.: RT, Cr(VI): 50 ppm (50 mL), dosage: 20 mg, pH: 2, removal (time): 56.5% (4 h)	165.3	Langmuir	Pseudo-second order (k: 6.9 × 10^{-4} g mg^{-1} min^{-1})	423
Cr(VI)	Ag-P/PPy core–shell	Water	*In situ* chemical oxidative polymerization	Temp.: RT, Cr(VI): 50 mg L^{-1} (50 mL), dosage: 0.05 g, pH: 2, removal (time): 99.4% (55 min)	138.5	Temkin and Redlich Peterson	Pseudo-second order	424
Cr(VI)C	Polypyrrole-wrapped oxidized MWCNTs	Aqueous solution	*In situ* chemical polymerization	Temp.: 25 °C Cr(VI): 200 mg L^{-1} (50 mL), dosage: 0.5 g L^{-1}, pH: 2, removal (time): 100% (300 min)	294	Langmuir	Pseudo sec. order (k: 0.0028 g mg^{-1} min^{-1})	425
Cr(VI)	PPy-coated Halloysite nanotube (HNT) clay	Deionized water	*In situ* polymerization of pyrrole in the dispersion of HNTs	Temp.: 25 °C, Cr(VI): 100 mg L^{-1} (50 mL), dosage: 1.5 g L^{-1}, pH: 2.0, removal (time); ~100% (24 h)	149.25	Langmuir	Pseudo sec. order (k: 0.019 g mg^{-1} min^{-1})	427
Cr(VI)	Core–shell Fe_3O_4/PANI microspheres	Water	Interfacial polymerization	Temp.: RT, Cr(VI): 100 mg g^{-1} (60 mL), dosage: 0.1 g ^{1}, pH: 2, removal (time); ~86% (180 min)	200	Langmuir isotherm	Pseudo sec. order	428
Cr(VI)	Fe_3O_4/PPy nanotubes	Aqueous solution	One-pot process	Temp.: 25 °C, Cr(VI): 20 mg L^{-1} (50 mL), dosage: 0.01 g, pH:1, removal (time); 94.62% (24 h)	451.45	Langmuir	Pseudo sec. order	429
Cr(VI)	Fe_3O_4-coated PPy	Aqueous solution	*In situ* polymerization of pyrrole monomer	Temp.: 25 °C, Cr(VI): 200 mg L^{-1} (50 mL), dosage: 2 g L^{-1}, pH: 2, removal (time); 100% (24 h)	169.5	Langmuir	Pseudo-sec. order (k: 0.037 g mg^{-1} min^{-1}) for [Cr(VI)]: 150 mg L^{-1}	430
Cr(VI)	Fe_3O_4@ arginine-functionalized PPy	Deionised water	*In situ* polymerization	Temp.: 25 °C. Cr(VI): 200 mg L^{-1} (50 mL), dosage: 0.05 g, pH: 2, removal (time); ~100% (1 h)	322.58	Langmuir	Pseudo sec. order (k: 6.67 × 10^{-3} g mg^{-1} min^{-1})	431

Table 3 *(Contd.)*

Metal ions	Adsorbent used	Water type	Preparative method	Experimental conditions on removal of metal ions	q_m (mg g^{-1})	Removal isotherm fitted to	Kinetics data fitted to (k)	Ref.
Cr(VI)	PPy/γ-Fe_2O_3	Aqueous media	Emulsion polymerization	Temp.: RT, Cr(VI): 2.5 mg L^{-1} (10 mL), dosage: 2 mg, pH: 2, removal (time); ~100% (1 h)	208.8	Langmuir	Pseudo sec. order (k: 2.0 × 10^{-2} g mg^{-1} min^{-1})	432
Cr(VI)	PANI/γ-Fe_2O_3	Aqueous media	Emulsion polymerization	Temp.: RT, Cr(VI): 2.5 mg L^{-1} (10 mL), dosage: 2 mg, pH: 2, removal (time); ~100% (1 h)	195.7	Langmuir	Pseudo sec. order (k: 7.5 × 10^{-4} g mg^{-1} min^{-1})	432
Cr(VI)	PPy-modified corncob-core sponge	Aqueous solution	Solution polymerization	Temp.: 25 °C, Cr(VI): 100 mg L^{-1}, dosage: 3 g L^{-1}, pH: 3.5, removal, (time);~100% (180 min)	84.7	Langmuir	Pseudo sec. order (k: 0.0023 g mg^{-1} min^{-1}): [Cr (VI)]: 50 mg L^{-1}	434
Cr(VI)	MnO_2-coated polyaniline nanofibers	Aqueous solution	*In situ* oxidative polymerization	Temp.: 298 K, Cr(VI): 10 mg L^{-1} (50 mL), dosage: 10 mg, pH: 1, removal (time); ~96% (60 min)	158.2	Freundlich	Pseudo-sec. order (k: 0.0751 g mg^{-1} min^{-1})	436
Cr(VI)	PPy/hollow mesoporous silica	Aqueous solution	*In situ* polymerization	Temp.: 25 °C, Cr(VI): 400 mg L^{-1} (25 mL), dosage: 80 mg, pH: 2, removal (time);~100% (24 h)	322	Langmuir	Quasi-second-order	437
Cr(VI)	Polyacrylonitrile/PPy core/shell nanofiber mat	Aqueous solution	Electrospinning followed by *in situ* polymerization of pyrrole monomer	Temp.: 25 °C Cr(VI): 200 ppm (30 mL), dosage: 0.20 g, pH: 2, removal (time); 84.5% (12 h)	61.80	Langmuir	Pseudo sec. order (k: 1.77 × 10^{-3} g mg^{-1} min^{-1})	439
Cr(VI)	L-Cystine-doped glucose carbon sphere @PPy	Water	*In situ* growth method	Temp.: RT, Cr(VI): 100 mg L^{-1} (100 mL), dosage: 0.050 g, pH: 1, adsorption capacity, q_e (time); 209.18 mg g^{-1}, (24 h)	108.41	Langmuir	Pseudo sec. order (k: 0.0014 g mg^{-1} min^{-1})	440
Cr(VI)	PANI@Nano hollow carbon sphere	Wastewater	*In situ* polymerization method	Temp.: 298 K, Cr(VI): 100 mg L^{-1} (25 mL), dosage: 10 mg, pH: 1, removal (time);100% (300 min)	250	Langmuir	Pseudo sec. order (k: 0.284 × 10^{-3} g mg^{-1} min^{-1})	441
Cr(VI)	PPy/attapulgite core–shell	Aqueous solutions	*In situ* polymerization on the surface of attapulgite	Temp.: 298 K Cr(VI): 50 mg L^{-1} (100 mL), dosage: 0.2 g, pH: 3, removal (time): 99.27% (10 min)	48.45	Langmuir	Pseudo sec. order (k: 1069 × 10^{-5} mg^{-1} s^{-1})	442
Cr(VI)	Cu slag@PANI	Aqueous solution	*In situ* polymerization	Temp.: 303 K Cr(VI): 300 mg L^{-1} (20 mL), dosage: 0.01 g, pH: 2, absorption capacity (time): 357.68 mg g^{-1} (24 h)	343.23 (303 K)	Langmuir	Pseudo sec. order (k: 0.00409 g mg^{-1} min^{-1})	443
Cr(VI)	PANI nanotubes@$Ni(OH)_2$	Aqueous solution	By depositing $Ni(OH)_2$ on 2-naphthalene sulfonic acid-doped PANI nano-tubes surface	Temp.: 25 °C, Cr(VI): 100 mg L^{-1} (50 mL), dosage: 0.03–0.05 g (50 mL), pH: 4.0, removal (time): ~100% (24 h)	625 (25 °C)	Langmuir	Pseudo-sec. order (k: 0.03008 g mg^{-1} min^{-1})	444
Cr(VI)	PPy@5% $MgFe_2O_4$	Water and wastewater	Oxidation method	Temp.: 25 °C., Cr(VI): 100 mg L^{-1} (10 mL), dosage: 1 g L^{-1}, pH: 3–6, removal (time): ~93 mg g^{-1} (600 min)	138.6	Langmuir	Pseudo sec order (0.00 21 g mg-1 min^{-1})	445
Cr(VI)	PANI@Almond shell	Aqueous solutions	*In situ* chemical polymerization	Temp.: 298 K, Cr(VI): 50 mg L^{-1}, dosage: 0.5 g L^{-1}, pH: 7, removal (time): 95.86% (120 min)	335.25	Freundlich	Pseudo sec. order (k: 0.0273 mg g^{-1} min^{-1})	447

Table 3 *(Contd.)*

Metal ions	Adsorbent used	Water type	Preparative method	Experimental conditions on removal of metal ions	q_m (mg g^{-1})	Removal isotherm fitted to	Kinetics data fitted to (k)	Ref.
Cr(VI)	PPy–PANI-coated rice husk ash	Aqueous solutions	*In situ* chemical polymerization	Temp.: RT, Cr(VI): 50 mg L^{-1} (100 mL), dosage: 0.8 g L^{-1}, pH: 2, removal (time): ~98% (300 min)	769.15	Freundlich	Pseudo sec. order (k: 0.009 mg g^{-1} min^{-1})	448
Cr(VI)	Graphene/SiO_2@PPy	Deionized water	*In situ* polymerization	Temp.: 298 K, Cr(VI): 100 mg L^{-1} (250 mL), dosage: 100 mg, pH: 2, q_e (time): ~240 mg g^{-1} (5000 min)	429.2	Langmuir	Pseudo sec. order (k: 1.852×10^{-5} min^{-1})	449
Cr(VI)	PPy/Fe_3O_4/chitosan	Water	Co-precipitation followed by *in situ* polymerization	Temp.: 25 °C, Cr(VI): 100 mg L^{-1} (50 mL), dosage: 100 mg, pH: 2, q (time): ~84% (40 min)	105	Langmuir	—	450
Cr(VI)	PMMA/rice husk/PPy membrane	Water	Electrospinning and chemical polymerization	Temp.: 283 K, Cr(VI):10 mg L^{-1}, dosage (membrane): 0.02, mx0.02 m (wt: 0.6 mg), pH: 2.0, removal (time): ~95% (24 h)	363.63	Langmuir	Pseudo sec. order (k: 49.90 mg g^{-1} min^{-1})	451
Cr(VI)	PS/PANI/Fe_3O_4	Water	Simultaneous chem. oxidation polymerization and precipitation	Temp.: 303 K, Cr(VI): 5 mg L^{-1} (30 mL), dosage: 0.05 g, pH: 2.0, efficiency (time): 100% (120 min)	23.753	Freundlich	Pseudo sec. order	452
Cr(VI)	PANI/wood sawdust/PEG	Water	Oxidation polymerization	Temp.: RT, Cr(VI): 50 ppm (50 mL), dosage: 40 g L^{-1}, pH: 5, removal (time): ~98% (30 min)	3.2	Langmuir	—	453
Cr(VI)	γ-Fe_3O_4/chitosan/PPy	Aqueous media.	Coprecipitation method + *in situ* polymerization	Temp.: RT, Cr(VI): 10 mg L^{-1} (10 mL), dosage: 2 mg, pH: 2, removal (time): 100% (720 min)	301.2	Freundlich	Pseudo sec. order (k: 7.12×10^{-5} min^{-1})	455
Cr(VI)	PANI/jute fiber	Deionized water	*In situ* polymerization	Temp.: 25 °C, Cr(VI): 100 mg L^{-1} (200 mL), dosage: 1.0 g, pH: 2, removal (time): 98% (120 min)	50	Langmuir	Pseudo sec order (k: 0.0023 mg g^{-1} min^{-1})	471
Pb(II)	Amino acid-doped PANI nanotubes	Aqueous solutions	*In situ* chemical polymerization	Temp.: 25 °C [Pb(II):]:30 mg L^{-1} (10 mL), dosage:0.25 g, pH: 7, removal (time): ~68% (120 min)	—	—	—	419
Pb(II)	Hollow polyaniline nanosphere	Deionized water	Chemical polymerization	Temp.: 30 °C, Pb(II): 20 mg L^{-1} (25 mL), dosage: 20 mg, pH: 7, absorptivity (time): 97% (24 h)	1589	Freundlich	—	456
Pb(II)	Fe_3O_4/@Py yolk–shell	Water	Multi step	Pb(II): 1 mg L^{-1} (100 mL), dosage:15 mg, pH: 6, removal (time): ~96% (30 min)	65.093	Langmuir, Freundlich	Pseudo sec. order (k: 0.004 g mg^{-1} h^{-1})	458
Pb(II)	PTh coated on PS	Deionized water	Chemical oxidative polymerization	Temp.: RT, Pb(II): 100 mg L^{-1} (25 mL), dosage: 0.25 mg, pH: 2, removal (time): ~85% (30 min)	—	—	—	460

Table 3 *(Contd.)*

Metal ions	Adsorbent used	Water type	Preparative method	Experimental conditions on removal of metal ions	q_m (mg g^{-1})	Removal isotherm fitted to	Kinetics data fitted to (k)	Ref.
Pb(II)	PTh coated on PVC	Deionized water	Chem. oxi. polymerization	Temp.: RT, Pb(II): 100 mg L^{-1} (25 mL), dosage: 0.25 mg, pH: 2, removal (time): ~85% (30 min)	—	—	—	460
Pb(II)	PANI/Fe_3O_4	Wastewater	*In situ* polymerization	Temp.: 25 °C, Pb(II): 50 ppm (100 mL), dosage: 3 mg, pH: 9, removal (time): 93% (60 min)	114.9	Langmuir	Pseudo sec. order (k: 0.0074 g g^{-1} min^{-1})	462
Pb(II)	$CoFe_2O_4$@PANI	Water	Aniline polymerization	Temp.: 25 °C, Pb(II): 17 mg L^{-1} (50 mL), dosage: 1 g, pH: 7, removal (time): 98% (120 min)	23.31	Langmuir	Quasi first order	463
Pb(II)	PPy-coated ZnO-NiO	Wastewater	Chemical polymerization	Temp.: 298 K, Pb(II): 100 mg L^{-1} (100 mL), dosage: 25 mg, pH: 5, removal (time): 98.7% (240 min)	436.48	Langmuir	Pseudo sec. order (k: 0.00013 mg g^{-1} min^{-1})	464
Pb(II)	PANI nanotubes/Ni^0	Aqueous solution	Immobilisation	Temp.: 25 °C, Pb(II): 100 mg L^{-1} (20 mL), dosage: 0.5 g L^{-1}, pH: 5.1, removal (time): ~90% (24 h)	414.6	Langmuir	Pseudo sec. order (k: 0.00798 mg g^{-1} min^{-1})	465
Pb(II)	MnO_2@PANI	Water	Oxidation polymerization	Temp.: 25 °C, Pb(II): 60 mg L^{-1} (20 mL), dosage: 0.5 g L^{-1}, pH: 5, removal (time): ~98% (12 h)	309.6	Langmuir	Pseudo sec. order (k: 17.52 g mg^{-1} min^{-1})	468
Pb(II)	PTP/polyvinylpyrolidine (PVP)/sulfonic acid/Cu	Aqueous solution	*In situ* co-polymerization	Temp.: 298 K, Pb(II): 30 mg L^{-1} (10 mL), dosage: 3.0 g L^{-1}, pH: 7, removal (time): ~28 mg g^{-1} (180 min)	111.11	Langmuir	Pseudo sec. order (k: 3.62 × 10^{-4} g g^{-1} min^{-1})	469
Pb(II)	PPy/Fe_3O_4/seaweeds	Aqueous solution	*In situ* chemical oxidative polymerization	Temp.: 40 °C, Pb(II): 100 mg L^{-1} (50 mL), dosage: 10 mg, pH: 5, removal (time): 97.25% (20 min)	333.33	Langmuir	Pseudo sec. order (k: 0.005535 g mg^{-1} min^{-1})	470
Pb(II)	Carbon–PPy@MoS_2	Wastewater	Template method involving five steps	Temp.: 25 °C, Pb(II): 54.26 ppm (100 mL), dosage: 50 mg, removal (time): 100% (10 min)	381.87	Langmuir	Pseudo sec order (k: 1.75 × 10^{-4} g mg^{-1} min^{-1})	475
Pb(II)	Fe_3O_4/SiO_2/PANI-SDBS	Wastewater	Polymerization of aniline	Temp.: 30 °C. Pb(II): 15 mg L^{-1} (50 mL). dosage: 30 mg, pH: 7.0, removal (time): 94.1% (120 min)	72.20	Freundlich model	Pseudo sec. order	486
As(V)	γ-Fe_2O_3@PANI	Deionized water	*In situ* polymerization	Temp.: 298 K, As(V): 20 mg L^{-1} (100 mL), adsorbent: 0.5 g L^{-1}, pH: 5, q_e (time): 0.354 mg g^{-1} (5 h)	37.61	Langmuir	Pseudo sec. order (k: 1.733 g $mmol^{-1}$ min^{-1})	457
As(III)	Hollow PANI microsphere-Fe_3O_4 (Fe_3O_4: 40 wt%)	Water	Multiple steps	Temp.: 300 K, As(III): 1000 mg L^{-1} (100 mL), dosage: 5 g L^{-1}, pH:7, removal (time): 98% (240 min)	28.27	Freundlich	Pseudo sec order (k: 0.363 g mg^{-1} min^{-1})	476

Table 3 *(Contd.)*

Metal ions	Adsorbent used	Water type	Preparative method	Experimental conditions on removal of metal ions	q_m (mg g^{-1})	Removal isotherm fitted to	Kinetics data fitted to (k)	Ref.
As(v)	Hollow polyaniline microsphere/Fe_3O_4 (Fe_3O_4: 40 wt%)	Water	Multiple steps	Temp.: 300 K, As(v): 1000 mg L^{-1} (100 mL), dosage: 2 g L^{-1}, pH:7, removal (time): 100% (240 min)	83.078	Freundlich	Pseudo sec order (k: 0.733 g mg^{-1} min^{-1})	476
As(v)	PANI/Fe^0	Aqueous solutions	Polyaniline nanofiber in polymerization media + $NaBH_4$	Temp.: RT, As(v): 1 mg L^{-1} (20 mL), dosage: 1 mg L^{-1}, pH: 7, removal (time): 100% (60 min) (24 h)	227.3	Langmuir isotherm	Pseudo sec. order (k: 0.01343–0.01714 g mg^{-1} min^{-1})	480
As(III)	PANI/Fe^0	Aqueous solutions	Polyaniline nanofiber in polymerization media + $NaBH_4$	Temp.: RT, As(III): 1 mg L^{-1} (20 mL), dosage: 1 g L^{-1}, pH: 7, removal (time): 100% (60 min)	232.5	Langmuir isotherm	Pseudo sec. order (k: 0.0332 g mg^{-1} min^{-1})	480
Cd(II)	PANI/jute fiber	Deionized water	*In situ* polymerization	Temp.: 25 °C, Cd(II): 100 mg L^{-1} (200 mL) (750 mL), dosage: 1.0 g, pH: 5, removal (time): 99% (120 min)	140	Langmuir	Pseudo sec. order (k: 0.0039 mg g^{-1} min^{-1})	471
Cd(II)	PANI-coated sawdust	Wastewater	Mixing method	Temp.: 20.5 °C, Cd(II): 40 mg L^{-1} (750 mL), dosage: 0.75 g, pH: 6, q_e (time): ~500 mg g^{-1} (35 min)	430	Freundlich	Pseudo sec. order	482
Cd(II)	Fe_3O_4/SiO_2/PANI-SDBS	Waste water	Polymerization of aniline	Temp.: 30 °C, Cd(II): 15 mg L^{-1} (50 mL), dosage: 30 mg, pH: 7.0, removal (time): 77.47% (120 min)	67.84	Freundlich model	Pseudo sec. order	486
Mn(VII)	Functionalized-Fe_3O_4@PPy	Aqueous solution	*In situ* polymerization of pyrrole monomer on Fe_3O_4	Temp.: 20 °C, Mn(VII): 150 mg L^{-1} (50 mL), dosage: 20 mg, pH: 2, contact time: ~90% (240 min)	781.25	Freundlich	Pseudo sec. order (k: 4.8 × 10^{-4} g mg^{-1} min^{-1})	485
Mn(VII)	Core@Shell Fe_3O_4@Polypyrrole@Sodium Dodecyl Sulphate	Complex wastewater	Hydrothermal + *in situ* polymerization methods	Temp.: 20 °C, Mn(VII): 60 mg L^{-1} (50 mL), dosage: 10 mg, pH: 7, removal (time): ~93.14% (60 min)	175.75	Langmuir	Pseudo sec. order (k: 2.93 × 10^{-5} g mg^{-1} min^{-1})	489
Cu(II)	PPy/γ-Fe_2O_3	Aqueous media	Emulsion polymerization	Temp.: RT, Cu(II): 2.5 mg L^{-1} (10 mL), dosage: 2 mg, pH: 2, q_e (time): ~165 mg g^{-1} (2 h)	170	Langmuir	Pseudo sec. order (k: 4.7 × 10^{-2} g mg^{-1} min^{-1})	432
Cu(II)	PANI/γ-Fe_2O_3	Aqueous media	Emulsion polymerization	Temp.: RT, Cu(II) 2.5 mg L^{-1} (10 mL), dosage: 2 mg, pH: 2, q_e (time): ~165 mg g^{-1} (2 h)	106.8	Langmuir	Pseudo sec. order (k: 6.1 × 10^{-3} g mg^{-1} min^{-1})	432
Cu(II)	Fe_3O_4@PPy yolk–shell	Water	Multistep	Cu(II): 1 mg L^{-1} (100 mL), dosage:15 mg, pH:6, removal (time): ~95% (30 min)	25.179	Langmuir, Freundlich	Pseudo sec. order (k: 0.035 g mg^{-1} h^{-1})	458
Ni(II)	Amino acid-doped PANI nanotubes	Aqueous solutions	*In situ* chemical polymerization	Temp.: 25 °C Ni(II):30 mg L^{-1} (10 mL), dosage:0.25 g, pH: 7, removal (time): ~68% (120 min)	—	—	—	419

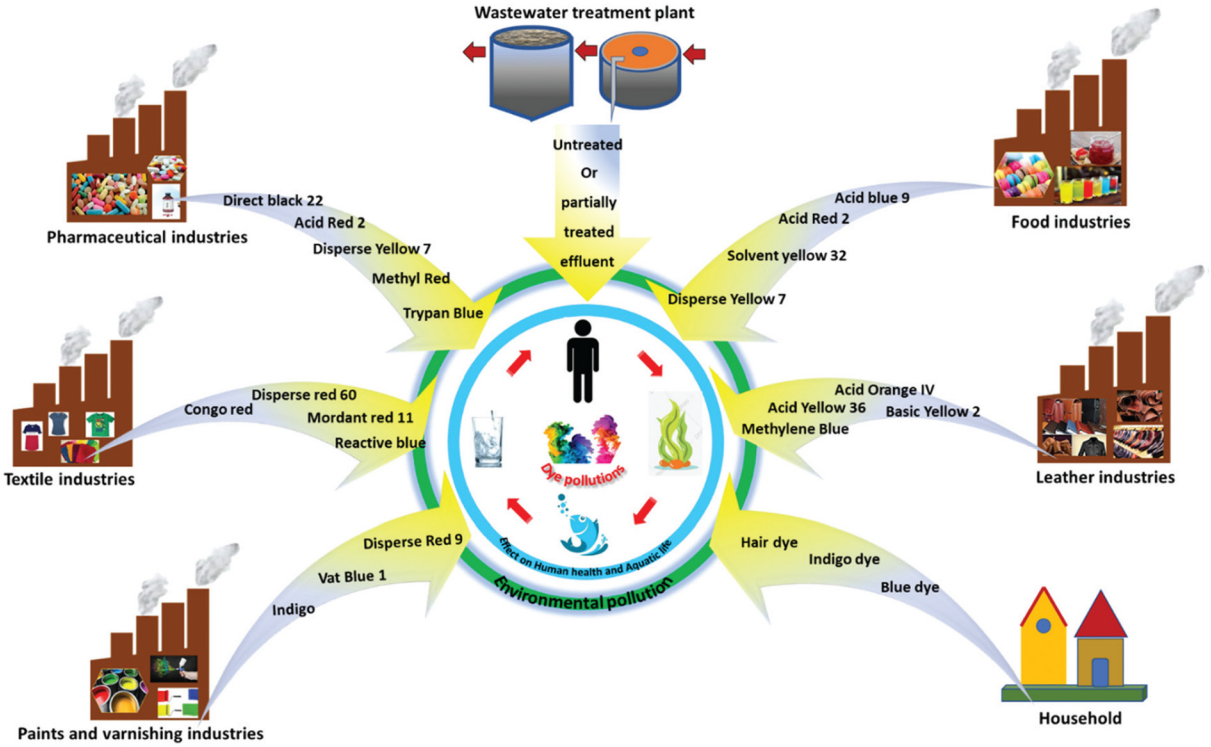

Fig. 30 Sources and pathways of dyes in the environment.[88] Reproduced with permission from RSC.

aqueous solutions by using polyaniline coated on filter papers,[493] PANI/Sawdust,[494] and PANI@Carbonized tea waste material.[495] Rachna *et al.*[496] studied the removal of RHB dye using PANI@Zn ferrite and observed maximum removal at pH 2. The adsorbent was also found to be effective even after desorption. Thermodynamics studies indicated the adsorption process to be spontaneous and exothermic in nature. Dhanavel *et al.*[497] prepared α-MoO_3/polyaniline by the chemical oxidative polymerization method. Furthermore, these findings showed the maximum adsorption capacity of 36.36 mg g^{-1} and 76.22 mg g^{-1} corresponding to RhB and CR dyes, respectively. Ovando-Medina *et al.*[498] coated polypyrrole (dia: 200–300 nm) on coffee grounds waste (CGD) by *in situ* pyrrole polymerization using potassium persulfate as oxidant. Subsequent studies have shown that the removal of the RhB dye from aqueous solution is favoured by basic pH due to its adsorption on CGD/PPy. It was also noted that the adsorption isotherm followed the Redlich–Peterson and Langmuir models with q_m of 50.59 mg g^{-1}.

5.3.1.3 Ternary core–shell composites. Ren *et al.*[499] used Fe_3O_4@polypyrrole@4-vinylpyridine composites for the removal of rhodamine B and some other dyes (methylene blue, malachite green, alizarin red). The investigations on the adsorption kinetics and isotherm studies of rhodamine B fitted well with the pseudo-second-order model and Langmuir model (q_m: 58.72 g mg^{-1}), respectively. The removal of RhB after five adsorption–desorption cycles of rhodamine B was found to be to 97.87%. According to the proposed mechanism, the adsorption of different dyes on the ternary composite could be related to the synergistic effect of electrostatic interaction, hydrogen-bonding interaction, and π–π interaction. Thermodynamic studies indicated spontaneous endothermic behavior for all four dyes. Xu *et al.*[500] used polyaniline/attapulgite-supported nanoscale Fe^0 to study the removal property and degradation mechanism for rhodamine B, in addition to alizarin yellow R, methyl red, chrome black T, methyl orange and methylene blue. Their findings indicated relatively better removal performance of the composite adsorbent for azo dyes compared with non-azo dyes. Polyaniline-modified magnetic nanocomposites coated with dicationic ionic liquid was used to remove rhodamine B from a water sample.[501] The overall findings indicated best fitting of the kinetic data and adsorption studies to the pseudo-second order and Temkin's models, respectively.

In another study, the maximum adsorption capacity values of rhodamine B, methylene blue, malachite green, and crystalline violet present on Fe_3O_4@polypyrrole@2-acrylamido-2-methyl-1-propanesulfonic acid composite in aqueous solution were found to be 215.054 mg g^{-1}, 183.486 mg g^{-1}, 144.718 mg g^{-1} and 194.175 mg g^{-1}, respectively.[502] The trilaminar composite maintained a removal efficiency exceeding 95% after going through 5 cycles. The kinetic, adsorption isotherm and thermodynamic studies indicated pseudo-second-order, Langmuir model and an endothermic spontaneous adsorption process, respectively. In addition, a mechanism has also been proposed on the adsorption of dyes by Fe_3O_4@PPy@AMPS

composite based on the electrostatic interactions between dyes and adsorbent, formation of hydrogen bonding involving O (in AMPS) and H (dyes), π–π interactions between the benzene rings (AMPS) and in dye including the hydrophobic interactions. Sayed *et al.*[503] prepared a PANI/C hybrid by an *in situ* chemical oxidation method under ultrasonic vibration. Scanning electron microscopy of the composite revealed the PANI network formation of intersecting nanorods. They also reported that the uptake of rhodamine B by the free form of the employed polyaniline took place due to hydrogen bonding, electrostatic interactions, and pi–pi interaction.

Varghese *et al.*[504] prepared a PEG-capped PANI/TiO_2/CuO composite by *in situ* chemical oxidative polymerization to study its adsorption performance in the removal of rhodamine B and other organic dyes in water. TEM studies of the trilaminar composite confirmed the incorporation of TiO_2/CuO into the tubular-shaped fibrous network of PANI. The adsorption efficiency of MB, MG, CR, RhB, and CV on PANI/TiO_2/CuO after 120 minutes corresponded to the removal efficiency of 98%, 67.7%, 95.1%, 64.4%, and 97.3%, respectively (Fig. 31(a)). The effect of a variety of materials on the adsorption of RhB dye has also been studied and the corresponding findings are displayed in Fig. 31(b). These findings revealed the superior removal performance by PANI/TiO_2/CuO (PTC) (89.7%) compared with PANI, (64.9%) TiO_2 (63.9%), CuO (44.3%), PANI/TiO_2 (PT): (72.9%), PANI/CuO (PC): 60.4%, and TiO_2/CuO (TC): 52.7% in 240 min due to its more negative zeta potential value. Fig. 31(c) shows the effect of adsorbent (PANI/

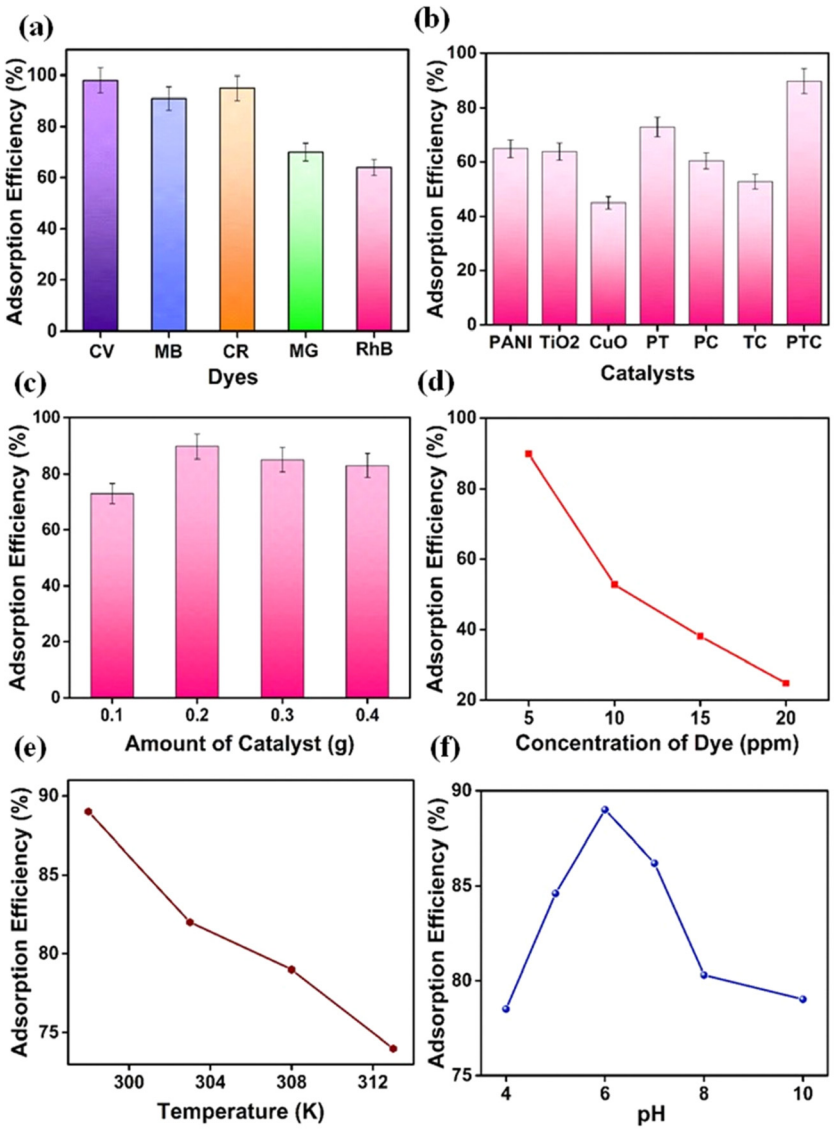

Fig. 31 (a) Adsorption efficiency of various dyes using PANI/TiO_2/CuO at 120 min, (b) efficiency of RhB using different catalysts at 240 min, (c) effect of amount of adsorbent on RhB adsorption using PANI/TiO_2/CuO for 120 min, (d) RhB adsorption at different dye concentrations using PANI/TiO_2/CuO for 240 min, (e) effect of RhB adsorption using PANI/TiO_2/CuO at different temperatures, and (f) effect of pH on the adsorption of RhB using PANI/TiO_2/CuO.[504] Reproduced with permission from Elsevier.

TiO_2/CuO) amounts on the adsorption of RhB for 120 min. According to this, the maximum adsorption efficiency was inevitable at 0.2 g of adsorbent. The variation of initial dye concentration in Fig. 31(d) indicated the maximum removal efficiency of 89.7% (adsorbent: 0.2 g, dye: 5 mg L^{-1}). The temperature dependence of the adsorption studies in Fig. 31(e) showed the removal efficiency decreasing from 89.7% (25 °C) to 78% (50 °C). The dependence of the pH, displayed in Fig. 31(f), showed the removal efficiency of RhB increasing from 78.5% to 89.7% on increasing pH from 4 to 6. Furthermore, the adsorption process followed the Langmuir adsorption isotherm (q_m: 3.53 mg g^{-1}) and pseudo-second-order kinetics. Fig. 32 shows the effect of pH on the adsorption efficiency of PANI/TiO_2/CuO.

5.3.2 Congo red

5.3.2.1 Hollow ICPs. A natural amino acid-doped polyaniline hollow tubular morphology[419] and hollow spherical polyaniline shell[491] exhibited a removal capacity for Congo red from aqueous solution corresponding to 955.6 mg·g^{-1} and 60 mg g^{-1}, respectively. Benhaddad *et al.*[505] synthesized hollow sea urchin-shaped polypyrrole in acidic medium using nanostructured MnO_2 powder acting as oxidizing agent and sacrificial template. Subsequently, they studied its comparative performance in the adsorption of Congo red and methylene blue in aqueous solutions. These studies indicated that adsorption and removal of Congo red and methylene blue was favoured under acidic and basic pH conditions, respectively. The adsorption followed Langmuir isotherm and pseudo-second-order kinetics for both the dyes. Mondal *et al.*[506] prepared a network of polyaniline nanotubes by *in situ* polymerization of aniline in the presence of ammonium persulfate and different aromatic carboxylic acids acting as a dopant (referred to as B4CA). Subsequent investigations on its application in wastewater treatment led to the following maximum adsorption capacity order for CR and other dyes: indigo carmine (300 mg g^{-1}) ≥ Eriochrome Black T (288 mg g^{-1}) > methyl orange (285 mg g^{-1}) > Congo red (194 mg g^{-1}) > *N*,*N*′-bis(4-benzosulfonic acid)-perylene-3,4,9,10-tetracarboxylbisimide (192 mg g^{-1}). It may be noted that the adsorption of the dye is guided here by the electrostatic interaction between dye molecules and the PANI surface.

5.3.2.2 Binary core–shell composites. PANI@ZnO nanocomposites were synthesized by the oxidation chemical process and its time-dependent performance evaluated for the adsorption of Congo red from aqueous solution, keeping pH: 5.0, C_0: 150 mg L^{-1}, and adsorbent dose: 10 mg at 298 K.[507] These findings suggested 81.37% removal of CR at 60 min. The kinetic model and isotherm data fitted well with the pseudo-second-order model (k: 0.0004 g mg^{-1} min^{-1}) and Langmuir (q_m: 76.92 mg g^{-1}), respectively. The regeneration efficiency of PANI@ZnO was found to be adequate even after five repeated cycles. Tanweer *et al.*[508] prepared 3D-polyaniline/activated silica gel by *in situ* polymerization and used it as potential adsorbent in the successful removal of Congo red, brilliant green, crystal violet, and methyl orange. In another approach, hollow electrospun Polypyrrole@Cellulose fibrous membrane was prepared by electrospinning followed by a dip-coating approach, and achieved 99.4% rejection of anionic Congo red.[509]

Teng *et al.*[510] observed 89.62% removal of CR from aqueous solution on PANI-coated Fe_3O_4 nanoparticles (PANI/Fe_3O_4: 70/30). These studies also indicated slightly enhanced dye removal by PANI/Fe_3O_4 compared with PANI alone. The adsorption of CR on the PANI/Fe_3O_4 adsorbent could be ascribed to the possible bond formation between the –OH functional group (Fe_3O_4) and CR, electrostatic interactions between the $-NH^+$ of PANI (emeraldine salt form) and anionic sulfonic group of CR dye, and hydrogen bonding interaction between CR and the PANI/Fe_3O_4 surface. The regeneration studies showed 77.4% removal retained after the fifth cycle of adsorption–desorption. Singh *et al.*[511] confirmed the coverage of *in situ*-prepared PANI over the zinc titanate surface by FESEM. This showed dramatically enhanced Congo red adsorption (q_m: 64.51 mg g^{-1}) compared with that of PANI and zinc titanate.

5.3.2.3 Ternary core–shell composites. Recently, several works have been reported on ternary core–shell composites comprising Fe_3O_4 as a magnetic material. In one such work, Fe_3O_4/polypyrrole/carbon black nanocomposite fabricated by encapsulating Fe_3O_4 nanoparticles in PPy/Carbon black exhibited 96.9% removal of Congo red under given experimental conditions.[512] The findings matched well with the Langmuir

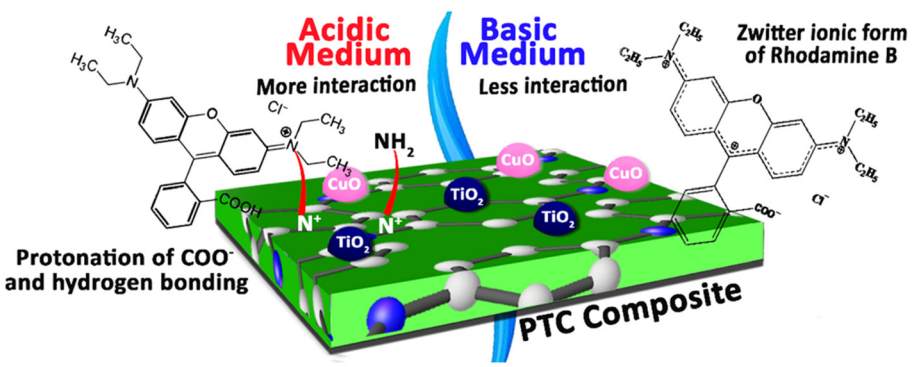

Fig. 32 The effect of pH on the adsorption efficiency of PANI/TiO_2/CuO.[504] Reproduced with permission from ACS.

isotherm (q_m: 500 mg g^{-1}) and pseudo-second order kinetics. Dutta *et al.*[513] fabricated polyaniline hollow microsphere (PNHM)/MnO_2/Fe_3O_4 composites by *in situ* deposition of MnO_2 and Fe_3O_4 nanoparticles on the surface of PNHM. Subsequently, they used it as adsorbent to study the removal of methyl green and Congo red in water. In view of this, the effect of pH on MG and CR dye removal efficiency (inset: change of wavelength of the dye solutions at different solution pH) are presented in Fig. 33(a and b), respectively. In addition, the variation of the zeta potential of PNHM/MnO_2/Fe_3O_4 with the variation of pH, the effect of adsorbent dose, contact time, and initial dye concentration on MG and CR dye removal efficiency are, respectively, described in Fig. 33(c–f). It is noted that the ternary composite showed 98% and 88% adsorption efficiency in the removal of CR and MG under optimum conditions. The adsorption mechanism of MG and CR dye removal on the surface of PNHM/MnO_2/Fe_3O_4 at pH ~6.75 is schematically displayed in Fig. 34. This has been explained on the basis of electrostatic interaction, ion exchange and the formation of covalent bonds.

A PANI@ZnO-SiO_2 hybrid material displayed good adsorption efficacy for CR (83.82 mg g^{-1}) and MB (71.19 mg g^{-1}) in aqueous solution.[514] According to Weng *et al.*,[515] ultrathin Mg silicate nanosheets were grown on Fe_3O_4@PPy and subsequently used as adsorbent to remove Congo red from aqueous solution. These findings revealed the applicability of the Langmuir isotherm model with maximum monolayer adsorption capacities of 540.5 mg^{-1} and kinetic data fitting to the pseudo-second-order model (k: 0.9030 g mg^{-1} min^{-1}). Adsorptive removal of CR on L-cysteine/rGO/PANI nanocomposite was done at room temperature to find out the optimum conditions.[516] These findings indicated the data fitted well with the Langmuir model (q_m: 56.57 mg g^{-1}) and kinetics validating pseudo-second-order. Furthermore, the

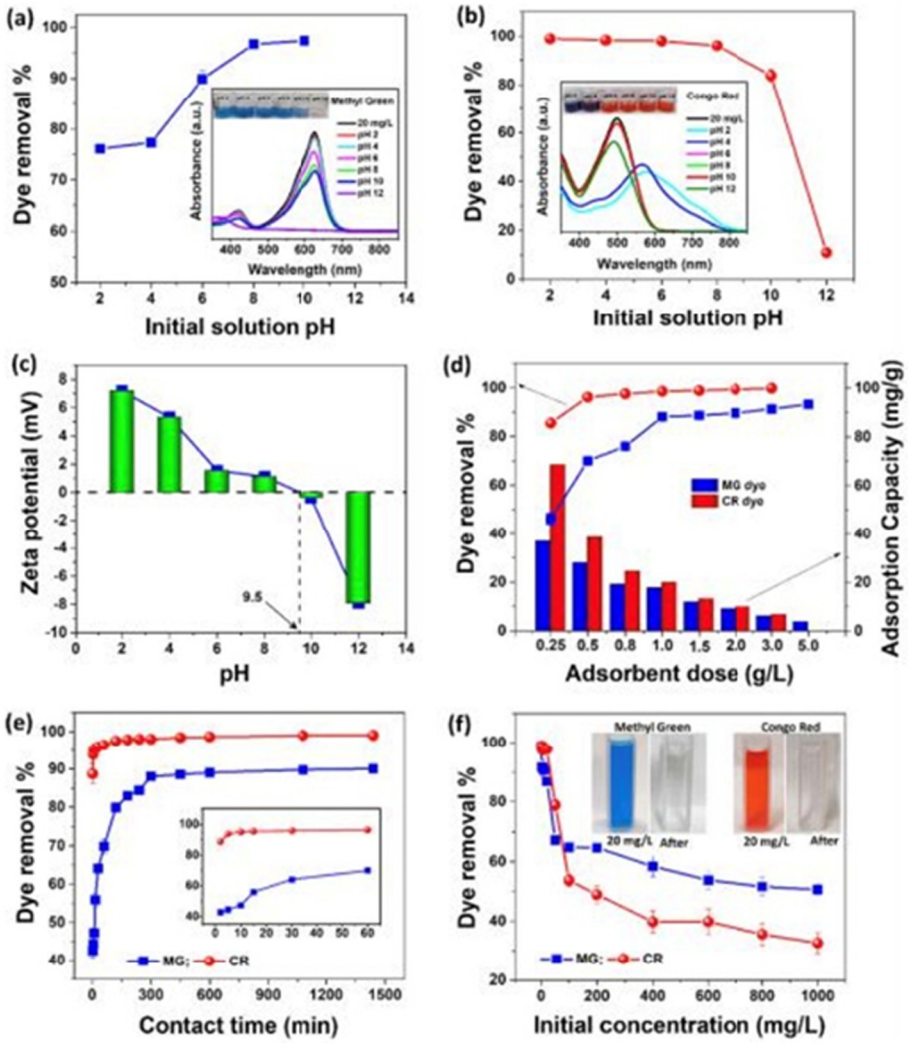

Fig. 33 Effect of pH on (a) MG and (b) CR dye removal efficiency (inset: change of wavelength of the dye solutions at different solution pH); (c) zeta potential of PNHM/MnO_2/Fe_3O_4 with the variation of pH, effect of (d) adsorbent dose, (e) contact time and (f) initial dye concentration on MG and CR dye removal efficiency.[513] Reproduced with permission from ACS.

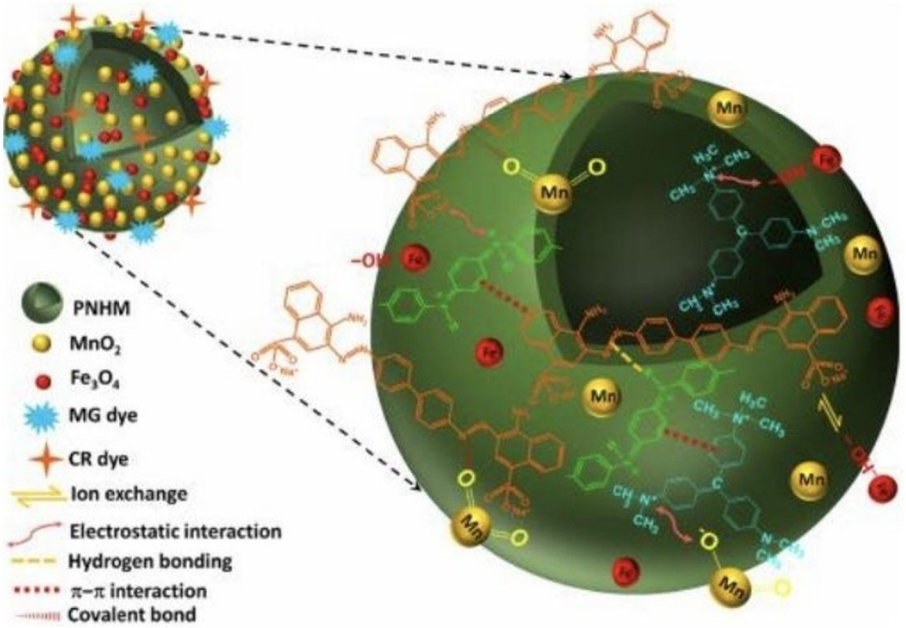

Fig. 34 Schematic representation of plausible adsorption mechanism of MG and CR dye on the surface of PNHM/MnO_2/Fe_3O_4 at pH ~6.75.[513] Reproduced with permission from ACS.

adsorption process was found, guided *via* intra-particle diffusion and thermodynamic studies that indicated the adsorption process of CR was endothermic and spontaneous.

5.3.3 Methylene blue

5.3.3.1 Hollow ICPs. Contamination by toxic, carcinogenic, and non-biodegradable methylene blue in water remains a threat to human health as well as environmental safety and needs urgent attention.[517] Ayad *et al.*[518] observed the adsorption capacity of PANI nanotubes to be about 8 times higher compared with PANI powder. In addition, the adsorption data of MB best fitted with the Langmuir isotherm (monolayer saturation capacity: 9.21 mg g^{-1}) and followed pseudo-second-order kinetics (k: 0.03595 g mg^{-1} min^{-1}). In another study, polyaniline hollow nanotubes (external dia: 50–60 nm, internal dia: 5–10 nm) have been *in situ* synthesized by using acid green crystal as structure-directing agent as well as template, and were used in the adsorption of methylene blue from aqueous media.[519] The experimental data supported fitting of a pseudo-first-order kinetic model (k: 0.001 mon^{-1}) and maximum monolayer of 69.4 mg g^{-1}. Amer *et al.*[520] reported the acid-free synthesis of polyaniline nanotubes *via* the aniline oxidation using ammonium peroxydisulfate as an oxidant in the presence of methyl orange as a structure-guiding agent in the dual removal of MB and AG dyes from aqueous solution. The kinetic studies confirmed the second-order model, while, adsorption data fitted well to the Langmuir isotherm. Furthermore, the calculated values of the maximum monolayer capacity for MB and AG were found to 91.1 and 58 mg g^{-1}, respectively.

5.3.3.2 Binary core–shell composites. PPy@MoS_2 hollow microtubes prepared through the combination of multiple steps successfully removed CR and MB from aqueous solution, with kinetic data fitting well the pseudo-second order.[521] Furthermore, the adsorption process followed the Langmuir model and Freundlich model for MB (q_m: 121.3 mg g^{-1}) and CR (q_m: 598.7 mg g^{-1}). The observed performance of dye removal was ascribed to its 1D hierarchical hollow structure and the synergistic effect between the MoS_2 nanoflakes and PPy coating. Ayad *et al.*[522] observed complete adsorption of methylene blue displayed by the polyaniline nanotubes base/silica composite (0.05 g) in 10 min corresponding to the 0.95 mg L^{-1} initial concentration of the dye. According to their findings, rate of adsorption increased in the following order: PANI NTs base/silica composite > PANI NTs base > conventional PANI base/silica composite > conventional PANI base. The experimental data were applied to study the kinetics (pseudo-first order, pseudo-second order) and the intraparticle diffusion models. Furthermore, MB adsorption data fitted best with the Langmuir isotherm. PANI partially covering the TiO_2 hydrate in water (pH 3–11) exhibited a high maximum adsorption capacity (458.10 mg g^{-1}).[523] Further investigations have shown its 99% regeneration capability achieved after 10 cycles. It was suggested that the adsorption performance of MB onto PANI/TIO_2 is guided by hydrogen bonding and electrostatic interaction on amino sites, π–π stacking, a hydrophobic effect on the benzene ring site and a synergistic effect.

El-Sharkaway *et al.*[524] synthesized a transparent layered and wrinkled wavy structure of GO covered with PANI and used it subsequently in the preparation of PANI-RGO, and used this to study the adsorption ability for MB in water. The kinetic studies of the PANI/GO and PANI/RGO indicated pseudo-first-order kinetics and the adsorption data best suited the Langmuir model. The estimated maximum dye adsorption capacity values of MB on PANI/GO and PANI/RGO adsorbents were found to be 14.2 and 19.2 mg g^{-1}, respectively. These

findings affirmed PANI/RGO to be more effective compared with PANI/GO for the removal of MB. Ayad *et al.*[525] prepared a coating of polypyrrole on a cotton textile by *in situ* oxidative polymerization of pyrrole monomer and subsequently used this as adsorbent of methylene blue in alkaline solutions. The adsorption process followed the Freundlich isotherm model and the adsorption kinetics fitted well with pseudo-second order. They also extended their work on the removal of Acid Green 25 in acidic medium and observed some affinity.

5.3.3.3 Ternary core–shell composites. Fe_3O_4@Polypyrrole@Sulfamic acid composite prepared by the hydrothermal method and *in situ* polymerization has been evaluated for its performance in the adsorption of MB and other dyes (MG, CV, and RhB).[526] The adsorption kinetics and adsorption isotherms of all the dyes were found to fit with pseudo-second-order and Langmuir adsorption isotherm, respectively. The thermodynamic study of the adsorption process indicated a spontaneous heat absorption behavior. Wang *et al.*[527] fabricated a core–shell Fe_3O_4@Polypyrrole@Sodium dodecyl benzene sulfonate (SDBS) composite following the combination of different methods and studied the effect of different parameters on the adsorption of MB and MG from aqueous solutions. These findings indicated kinetics and adsorption following the pseudo-second order and Langmuir isotherm (q_m^{MB}: 124.07 mg g^{-1}, q_m^{MG}: 73.10 mg g^{-1}), respectively. Furthermore, the cycling stability of the adsorbent was also assessed by carrying out an adsorption–desorption experiment for five cycles. These findings have shown the remarkable removal efficiencies of MB (80%) and MG (90%) following the five desorption–adsorption cycles. The excellent adsorption performance of dye on the ternary core–shell composite was assigned to the synergistic effect of the electrostatic interactions, hydrogen bonding, and π-π interactions mediated by PPy and SDBS.

Polypyrrole/GO@Fe_3O_4 has been prepared by a one-step method and used as magnetic adsorbent in the removal of methylene blue dye from aqueous solution (pH: 8).[528] This adsorbent exhibited an adsorption capacity of 323.2 mg g^{-1} for MB. A super-paramagnetic architecture comprising Fe_3O_4@PPy@RGO ternary nano-adsorbents was fabricated to remove methylene from wastewater.[529] The choice of Fe_3O_4 hollow spheres, polypyrrole layers and graphene sheets was guided by the role they play in contributing towards the abundant hydrophilic groups, protecting hollow spheres from acid corrosion/surface oxidation and in enhancing the removal performance of Fe_3O_4@PPy. HRTEM studies of Fe_3O_4@PPy@RGO established the formation of a ternary nano-architecture comprising wrapping of Fe_3O_4@PPy by RGO sheets. Fig. 35(a) shows Fe_3O_4@PPy@RGO exhibiting a superior removal efficiency for MB compared with Fe_3O_4 and Fe_3O_4@PPy in neutral solution (pH: 7). Furthermore, Fe_3O_4@PPy@RGO retained about 96% removal efficiency after five cycles of the adsorption–desorption process Fig. 35(b). In addition, the removal efficiency of these adsorbents in acidic solution (pH: 2) and alkaline solution (pH 10) are also displayed in Fig. 35(c and d), respectively. Graphene-modified magnetic polypyrrole[530] and Fe_3O_4/polypyrrole/phytic acid[531] also efficiently removed methylene blue from aqueous solution.

5.3.4 Methyl orange. Methyl orange (MO) is ably used in the textile, food, paper, and cosmetics industries, and for several other purposes.[532] However, its release into industrial effluents deteriorates the water quality with a hazardous impact on public health, affecting the human eye and causing skin irritation, nausea, diarrhea and respiratory tract irritation. The high water solubility, and high stability towards heat and temperature of MO makes the removal of this dye from aqueous solution not exciting.[533]

5.3.4.1 Hollow ICPs and their composites. Very limited research has been reported on the removal of methyl orange using hollow spheres and one-dimensional ICPs as adsorbents. According to Zhao *et al.*,[419] amino acid-doped polyaniline nanotubes exhibited the following order towards the adsorption capacity of different dyes: Congo red (112.0 mg g^{-1}) > orange yellow (69.2 mg g^{-1}) ≥ indigo carmine (66.8 mg g^{-1}) > methyl orange (54.8 mg g^{-1}) > crystalline violet (50.0 mg g^{-1}). Yildirim *et al.*[534] carried out the removal of methyl orange using a polyaniline nanotube-filled sodium alginate bio-composite to study the effect of adsorbent dose, pH, time, and concentration of MO. Based on the applicability of the Langmuir isotherm, maximum adsorption capacity (q_m) was found to be 370.4 mg g^{-1} at 25 °C under optimum conditions.

5.3.4.2 Binary and ternary core–shell composites. TEM studies of a PANI-MWCNTs (4 wt%) composite prepared by *in situ* oxidative polymerization showed spherical PANI covering the tubular structure of MWCNT nonuniformly.[535] The adsorption studies of methyl orange using PANI-MWCNTs as adsorbent agreed with the second-order kinetics (k: 5.265 × 10^{-4} g mg^{-1} min^{-1} at 30 °C) and Langmuir equilibrium model (q_m: 149.25 mg g^{-1}). Polyaniline (skin)/polyamide 6 (core) composite fiber prepared *via* a facile *in situ* oxidation polymerization was tested for the removal of methyl orange.[536] These findings revealed the adsorption/desorption kinetics and isotherms following the pseudo-second-order and Langmuir models (q_m: 58.7 mg g^{-1}), respectively. A waterborne poly vinyl pyrrolidone-stabilized polyaniline core (dia: 85–90 nm)–shell (dia: 20–22 nm) composite also effectively removed MO in aqueous solution.[537]

Zhang *et al.*[538] fabricated halloysite nanotubes/polypyrrole nanocomposites by *in situ* polymerization of pyrrole monomer in the presence of HNTs. Subsequently, its adsorption efficiency was evaluated in the removal of methyl orange as a function of adsorbent dose, contact time, initial concentration MO, and temperature on the adsorption efficiency. The adsorption kinetics fitted the pseudo-second-order and adsorption isotherms validated by Langmuir (q_m: 2 146 mg g^{-1}) and Freundlich models. The thermodynamic investigations pointed to an adsorption process of methyl orange onto HNTs/PPy that was spontaneous and exothermic. Furthermore, regeneration experiments have shown the reusability of HNTs/PPy nanocomposites at least three times in removing methyl orange in aqueous solution.

Yao *et al.*[539] prepared core–shell Fe_3O_4@C@polyaniline composite microspheres as a separable adsorbent for the

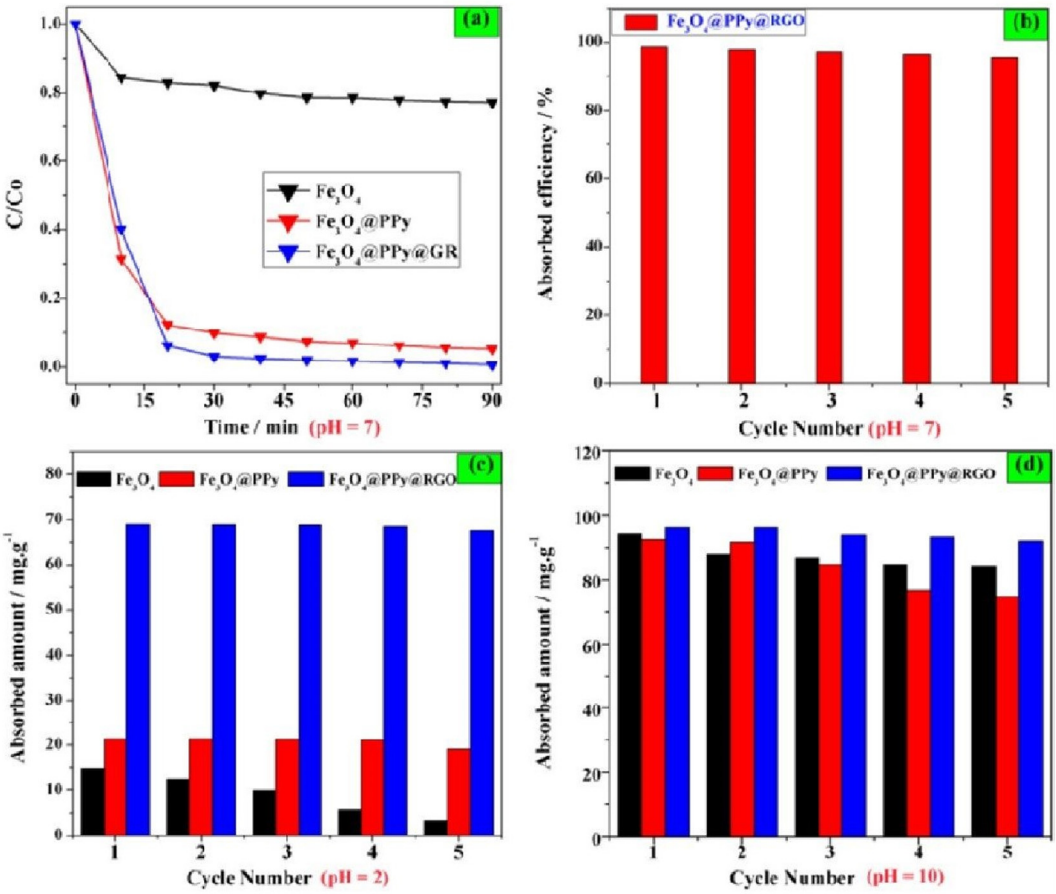

Fig. 35 (a) Removal efficiency of magnetic adsorbents in neutral solution (pH 7); (b) removal efficiency of Fe_3O_4@PPy@RGO in five cycles, neutral solution (pH 7); (c) removal efficiency of magnetic adsorbents in acidic solution (pH 2) and (d) alkaline solution (pH 10).[529] Reproduced with permission from Elsevier.

removal of MO dye from aqueous solution. The TEM images of the product confirmed the core–shell structure of the Fe_3O_4@C@PANi composite microspheres. The adsorption isotherms and kinetics data supported the Langmuir and pseudo-second-order models, respectively. The trilaminar core–shell composite also exhibited excellent adsorption capability (q_m: 120.2 mg g^{-1}), and retained excellent adsorption capability (~81%) after five adsorption–desorption cycles.

5.3.5 Other dyes. In addition, several studies have also been reported using different core–shell adsorbents comprising conducting polymers (in the removal of several other dyes), such as: polymethylmethacrylate/rice husk ash/polypyrrole (E102, IC),[451] magnetic Fe_3O_4@Polypyrrole@Sodium dodecyl sulfate (MG, AR1),[489] magnetic core–shell Fe_3O_4@Polypyrrole@4-vinylpyridine (AR, MG),[499] Polyaniline/attapulgite-supported nanoscale zero-valent iron (AYR, MO, methyl red, chrome black T),[500] Magnetite@Polypyrrole@2-acrylamido-2-methyl-1-propanesulfonic acid microspheres (MG, CV),[502] 3D polyaniline/activated silica gel (BG,CV, MO),[508] Hollow polyaniline microsphere/MnO_2/Fe_3O_4 (MG),[513] Polyaniline hollow nanotubes (AG),[519,520] Fe_3O_4@Polypyrrole@Sodium dodecyl benzene sulfonate (MG),[527] Fe_3O_4/polypyrrole/phytic acid (CV),[531] Polyaniline@TiO_2 and Polyaniline@SiO_2 (CV, R6G,BB,CV),[540] graphene/Fe_3O_4/polyaniline (MG,AR1),[541] carbon nanotube/polyaniline (MG),[542] Fe_3O_4@RGO@PANI (MG),[543] wheat straw-core hydrogel spheres with polypyrrole nanotubes (EY),[544] polypyrrole/$Mn_{0.8}Zn_{0.2}Fe_2O_4$/graphite oxide (AR1),[545] polyaniline coating chitosan-graphene oxide-functionalized carbon nanotube (AR1, BG),[546] polythiophene/ZnO/MWCNTs and polythiophene/ZnO/ox-MWCNTs (BG),[547] and Fe_3O_4@PDA@PANI (TTZ, SY).[548]

Table 4 presents the removal of the various dyes in aqueous solution based on hollow intrinsically conducting polymers, nanocomposites comprising hollow intrinsically conducting polymers and core–shell based ICP nanocomposites as adsorbents.

5.4. Supercapacitor applications of hollow ICPs

Supercapacitors are considered as energy storage devices, storing and releasing energy through the movement of ions within the electrolyte.[549,550] Furthermore, carbonaceous materials, conducting polymers, and transition metal oxides have attracted much attention as electrode material in this application. A comparison of their merit/demerits is highlighted in Table 5. These supercapacitors are regarded as more

Table 4 Performance of hollow ICPs, hollow ICP nanocomposites and ICP based core–shell structured materials as adsorbents in the removal of various dye in water medium[a]

Dye	Adsorbent	Water type	Preparative method	Experimental conditions and findings	q_m (mg g^{-1})	Removal isotherm fitted to	Kinetics data fitted to	Ref.
CR	Amino acid-doped PANI nanotubes	Aqueous solutions	*In situ* chemical polymerization	Temp.: 25 °C CR:30 mg L^{-1} (10 mL), dosage:0.25 g, pH: 7, removal (time): ~110 mg g^{-1} (90 min)	112	Langmuir	Pseudo first-order	419
OG	PANI@Almond shell	Aqueous solutions	*In situ* chemical polymerization	Temp.: 298 K, OG: 50 mg L^{-1}, dosage: 0.5 g L^{-1}, pH: 5, removal (time): 94.69% (120 min)	190.98	Freundlich	Pseudo sec. order (k: 0.0008 mg g^{-1} $min^{-}1$)	447
MO	PPy/Fe_3O_4/chitosan	Water	Co-precipitation and *in situ* polymerization	Temp.: 25 °C, MO: ~100 mg L^{-1} (50 mL), adsorbent: 100 mg, pH: 3, removal efficiency (time): 67 mg g^{-1} (40 min)	95	Langmuir	—	450
IC	PMMA/rice husk/PPy membrane	Water	Electrospinning and chemical polymerization	Temp.: 283 K, IC: 30 mg L^{-1}, dosage (membrane): 0.02m × 0.02 m (wt: 0.6 mg), pH:2.0, q_e (time): 142.9 mg g^{-1} (70 min)	144.93	Langmuir	Pseudo sec. order (k: 0.002 g mg^{-1} min^{-1})	451
E102	PMMA/rice husk/PPy membrane	Water	Electrospinning and chemical polymerization	Temp.: 283 K, TZ:60 mg L^{-1}, dosage (membrane): 0.02 m × 0.02 m^2 (wt: 0.6 mg), pH: 2.0, q_e (time): 165.7 mg g^{-1} (60 min)	171.23	Langmuir	Pseudo sec. order (k: 0.002 min^{-1})	451
RhB	Fe_3O_4@PPy@Sodium dodecyl sulphate	Complex wastewater	Combination of a hydrothermal method *in situ* polymerization	Temp.: 20 °C, RhB:40 mg L^{-1} (50 mL), adsorbent: 10 mg, pH: 7, removal (time): 94.83% (7 h)	127.55	Langmuir	Pseudo sec. order (k: 3.027 × 10^{-3} g mg^{-1} min^{-1})	489
CR	Fe_3O_4@PPy@Sodium dodecyl sulphate	Complex wastewater	Combination of hydrothermal method and *in situ* polymerization	Temp.: 20 °C, CR:40 mg L^{-1} (50 mL), adsorbent: 10 mg, pH: 7, removal (time): 96.45% (7 h)	101.63	Langmuir	Pseudo sec. order (k: 2.75 × 10^{-4} g mg^{-1} min^{-1})	489
MB	Fe_3O_4@PPy@Sodium dodecyl sulphate	Complex wastewater	Combination of a hydrothermal method *in situ* polymerization	Temp.: 20 °C, MB:40 mg L^{-1} (50 mL), adsorbent: 10 mg, pH: 7, removal (time): 93.27% (400 min)	135.50	Langmuir	Pseudo sec. order (k: 1.71 × 10^{-4} g mg^{-1} min^{-1})	489
MG	Fe_3O_4@PPy@Sodium dodecyl sulphate	Complex wastewater	Three-step process	Temp.: 20 °C, MG:40 mg L^{-1} (50 mL), adsorbent: 10 mg, pH: 7, removal (time): 96.03% (7 h)	182.82	Langmuir	Pseudo sec. order (k: 8.93 × 10^{-4} g mg^{-1} min^{-1})	489
AR1	Fe_3O_4@PPy@Sodium dodecyl sulphate	Complex wastewater	Combination of a hydrothermal method *in situ* polymerization	Temp.: 20 °C, AR1:40 mg L^{-1} (50 mL), adsorbent: 10 mg, pH: 2, removal (time): 92.99% (7 h)	181.16	Langmuir	Pseudo sec. order (k: 2.66 × 10^{-4} g mg^{-1} min^{-1})	489
RhB	Hollow spherical PANI	Aqueous solution	*In situ* polymerization on functionalized polystyrene template	RhB: 100 mg L^{-1} (50 mL), adsorbent: 5 mg, q_e (time): 61.75 mg g^{-1} (72 h)	61.75	—	—	491
CR	Hollow spherical PANI	Aqueous solution	Chemical polymerization	CR: 5 mg (50 mL), Adsorbent: 100 mg L^{-1}, q_e (time): 46.91 (72 h)	46.91	—	—	491
Rh6G	Hollow PANI helical nanobelts	Aqueous solution	Chemical oxidation of aniline	Temp.: RT, Rh6G: 50 mg (100 mL), adsorbent: 479 mg L^{-1}, removal (time): ~249 mg L^{-1} (120 min)	0.42 mg mg^{-1}	Langmuir	Pseudo sec. order (k: 1.28 mg mg^{-1} min^{-1})	492
RhB	Coating of PANI onto carbonized tea waste	Aqueous solutions	Coating of polyaniline onto carbonized tea waste material	Temp.: 30 °C, RhB: 50 mg L^{-1} (100 mL), adsorbent: 100 mg, pH: 8.0, removal (min): 95.21% (60 min)	34.93	Langmuir	Pseudo-second-order (k: 0.0035 g mg^{-1} min^{-1})	495

Table 4 *(Contd.)*

Dye	Adsorbent	Water type	Preparative method	Experimental conditions and findings	q_m (mg g^{-1})	Removal isotherm fitted to	Kinetics data fitted to	Ref.
RhB	α-MoO_3/PANI	Water	Chemical oxidative polymerization using camphor sulfonic acid as dopant	Temp.: 20 °C, RhB: 2.1 × 10^{-5} mol L^{-1} (50 mL), adsorbent: 50 mg, pH:3, Removal (time): 91% (60 min)	36.36	Langmuir	—	497
CR	α-MoO_3/PANI	Water	Chemical oxidative polymerization using camphor-10 sulfonic acid as dopant	Temp.: 15 °C, CR: 1.5 × 10^{-5} mol L^{-1} (1000 mL), adsorbent: 50 mg, pH: 5, removal (time): 94.6 (60 min)	76.22	Langmuir	—	497
RhB	PPy/coffee grounds waste	Aqueous solution	Pyrrole polymerization	Temp.: 15 °C, RhB: 200 mg L^{-1} (150 mL), adsorbent: 125 mg, pH: 9, removal (time): 32 mg g^{-1} (80 min)	50.597	Redlich–Peterson and Langmuir	—	498
RhB	Fe_3O_4@PPy@4-Vinylpyridine	Wastewater	Multiple steps	Temp.: 20 °C, RhB: 50 mg L^{-1} (30 mL), adsorbent: 10 mg, pH = 7, removal (time): ~97% (500 min)	58.72	Langmuir	Pseudo sec. order (k: 9.728 × 10^{-4} g mg^{-1} min^{-1})	499
MB	Fe_3O_4@PPy@4 vinylpyridine	Wastewater	Multiple steps	Temp.: 20 °C, MB: 50 mg L^{-1} (30 mL), adsorbent: 10 mg, pH = 7, removal (time): ~100% (500 min)	85.98	Langmuir	Pseudo sec. order (k: 3.704 × 10^{-3} g mg^{-1} min^{-1})	499
MG	Fe_3O_4@PPy@4-vinylpyridine	Wastewater	Multiple steps	Temp.: 20 °C, MG: 50 mg L^{-1} (30 mL), adsorbent: 10 mg pH = 7, removal (time): ~98% (600 min)	36.114	Langmuir	Pseudo sec. order	499
AR	Fe_3O_4@PPy@4-vinylpyridine	Wastewater	Multiple steps	Temp.: 20 °C, AR: 200 mg L^{-1} (30 mL), adsorbent: 10 mg pH = 7, removal (time): ~90% (600 min)	55.90	Freundlich	Pseudo sec. order (k: 2.270 × 10^{-4} g mg^{-1} min^{-1})	499
MB	PANI/attapulgite-supported nanoscale zero-valent Fe	Aqueous solution	Liquid-phase chemical reduction method	Temp.: 298 K., MB: 60 mg L^{-1} (50 mL), adsorbent: 0.05 g, pH: 11, removal (time): 30% (30 minutes)	23	Langmuir	—	500
AYR	PANI/attapulgite-supported nanoscale zero-valent Fe	Aqueous solution	Liquid-phase chemical reduction method	Temp.: 298 K, AYR: 60 mg L^{-1} (50 mL), adsorbent: 0.05 g, pH:3, removal (time): 99.56% (10 min)	72	Langmuir	—	500
RhB	Polyaniline magnetic nanoparticles/dicationic ionic liquid	Tap/industrial and lake water	Coating aniline and dicationic ionic liquids on magnetic nanoparticle	Temp.: 298 K, RhB:10 mg g^{-1} (10 mL), adsorbent: 20 mg, pH: 1, removal (time); ~94% (60 min)	109.90	Temkin	Pseudo sec. order (k: 0.4172 g mg^{-1} min^{-1})	501
RhB	Magnetite@PPy@2-acrylamido-2-methyl-1-propanesulfonic acid microspheres	Aqueous solutions	Two-step process	Temp.: 293 K., RhB: 60 mg L^{-1}, adsorbent: 7 mg, pH: 7, removal (time): >90% (300 min)	215.054	Langmuir	Pseudo sec. order (k: 2.441 × 10^{-3} g mg^{-1} min^{-1})	502
MB	Magnetite@PPy@2-acrylamido-2-methyl-1-propanesulfonic acid microspheres	Aqueous solutions	Two-step process	Temp.: 293 K. MB: 50 mg L^{-1}, adsorbent: 7 mg, pH: 7, removal (time): ~100% (240 min)	183.486	Langmuir	Pseudo sec. order	502
CV	Magnetite@PPy@2-acrylamido-2-methyl-1-propanesulfonic acid microspheres	Aqueous solutions	Two-step process	Temp.: 293 K, CV: 50 mg L^{-1}, adsorbent: 7 mg, pH: 7, removal (time): ~100% (300 min)	194.175	Langmuir	Pseudo sec. order (k: 3.156 × 10^{-3} g mg^{-1} min^{-1})	502
RhB	PEG capped PANI/TiO_2/CuO	Water	*In situ* polymerization of aniline in the presence of TiO_2/CuO	Temp.: 300 K. RhB: 5 mg L^{-1} (50 mL), adsorbent: 0.2 g, pH: 6, removal (time): 89.7% (240 min)	3.53	Langmuir	Pseudo sec. order (k: 0.809 g. mg^{-1} min^{-1})	504
CR	PANI@ZnO	Deionized water	*In situ* oxidation chemical process	Temp.: 298 K, CR: 150 mg L^{-1} (25 mL), adsorbent: 10 mg, pH: 5, Removal (time):~70% (60 min)	76.92	Langmuir	Pseudo sec. order (0.0004 g mg^{-1} min^{-1})	507

Table 4 *(Contd.)*

Dye	Adsorbent	Water type	Preparative method	Experimental conditions and findings	q_m (mg g^{-1})	Removal isotherm fitted to	Kinetics data fitted to	Ref.
MO	3D PANI@Activated SiO_2 gel	Aqueous solution	*In situ* polymerization	Temp.: 298.15 K, MO: 50 mg L^{-1} (30 mL), adsorbent: 0.25 g, pH: 3, removal efficiency (time): ~100% (200 min)	161.29	Langmuir	Pseudo sec. order 0.036 g mg^{-1} min^{-1}	508
BG	3D PANI@Activated SiO_2 gel	Aqueous solution	*In situ* polymerization	Temp.: 298.15 K. BG: 50 mg L^{-1} (30 mL), adsorbent: 0.025 g, pH: 8, removal (time): 100% (200 min)	136.98	Langmuir	Pseudo sec. order (k: 1.34 g mg^{-1} min^{-1})	508
CR	PANI-$ZnTiO_3$	Aqueous solutions	Polymerization of aniline in the suspensions of ZTO	Temp.: RT, CR:50–150 ppm (100 mL), adsorbent: 200 mg, pH: natural pH, removal (time): 90% (15 min)	64.51	Langmuir	Pseudo sec. order (k: 0.000509 g s^{-1} mg^{-1})	511
CR	Fe_3O_4/PPy/carbon black	Aqueous solution	Encapsulating Fe_3O_4 nanoparticles in PPy/carbon black	CR: 120 mg L^{-1} (40 mL), adsorbent: 0.5 g L^{-1}, pH: 7, removal (time): 95% (240 min)	500	Langmuir	Pseudo sec. order (k: 0.007 × 10^{-2} g mg^{-1} min^{-1})	512
MB	Fe_3O_4/PPy/carbon black	Aqueous solution	Encapsulating Fe_3O_4 nanoparticles in PPy/carbon black	MB: 40 mg L^{-1} (40 mL), adsorbent: 0.5 g L^{-1}, pH: 7, removal (time): 95.9% (120 min)	90.9	Langmuir	Pseudo sec. order (k: 0.14 × 10^{-2} g.mg^{-1} min^{-1})	512
CR	PANI microsphere/MnO_2/Fe_3O_4	Aqueous solution	*In situ* deposition	Temp.: 303 ± 3 K, CR: 20 mg L^{-1}, adsorbent: 1 g L^{-1}, pH: ~6.75, removal (time): 98% (1500 min)	599.49	Elovich	Pseudo sec. order (k: 0.25 g mg^{-1} min^{-1})	513
MG	PANI microsphere/MnO_2/Fe_3O_4	Aqueous solution	*In situ* deposition	Temp.: 303 ± 3 K, MG: 20 mg L^{-1}, adsorbent: 1 g L^{-1}, pH: ~6.75, removal (time): 88% (1500 min)	1142.13	Freundlich	Pseudo sec. order (k: 0.012 g mg^{-1} min^{-1})	513
CR	L-Cysteine/rGO/PANI	Aqueous solution	rGO + 0.1M L-cysteine solution + aniline monomer + APS	Temp.: RT, CR: 30 mg L^{-1} (10 mL), adsorbent: 0.025 g, pH: neutral, removal (time): 98% (10 min)	56.57	Langmuir	Pseudo sec. order	516
MB	Polyaniline nanotubes	Aqueous solutions	*In situ* polymerization	Temp.: 25 °C, MB: 3.1 mg L^{-1} (100 mL), adsorbent: 0.05 g, pH: q_e/time: ~0.6 mg g^{-1} (150 min)	9.21	Langmuir	Pseudo sec. order (k: 0.03595 g mg^{-1} min^{-1})	518
MB	Polyaniline hollow nanotubes	*In situ* synthesis	*In situ* polymerization	Temp.: RT, MB: 6.2 mg L^{-1} (100 mL), Adsorbent: 10 mg, pH: 11, Removal/time: ~92% (600 min)	69.4	Langmuir	Pseudo sec. order (k: 0.001 g mg^{-1} min^{-1})	519
AG	PANI hollow nanotubes	Aqueous media	Using acid green as a structure-directing agent and soft template	Temp.: 298 K, AG:6.1 mg L^{-1} (100 mL), adsorbent: 10 mg, pH: 3.0, removal (time): 52% (6 h)	57.8	Langmuir	Pseudo sec. order (k: 8.9 × 10^{-4} g mg^{-1} min^{-1})	519
MB	Polyaniline nanotubes	Aqueous medium	Aniline oxidation in the presence of methyl orange	Temp.: 298 K, MB = 8.8 mg L^{-1} (0.1 L), adsorbent: 20 mg, pH: 9, removal (time): > 90% (300 min)	91.1	Langmuir	Pseudo sec. order (k: 0.00117 g mg^{-1} min^{-1})	520
AG	PANI nanotubes	Aqueous medium	Green approach *via* the aniline, oxidation	Temp.: 25 °C, AG: 20 mgL^{-1} (100 ml), adsorbent: 8 mg L^{-1}, pH: 3, removal (time): 67% (320 min)	58	Langmuir	Pseudo sec.-order (k: 0.002 g mg^{-1} min^{-1})	520
CR	PPy@MoS_2 hollow microtubes	Aqueous medium	Hydrothermal process, *in situ* polymerization and sulfidation	Temp.: RT, CR: 60 mg L^{-1} (5 mL), adsorbent: 50 mg L^{-1}, pH: neutral, removal (time): 84,14% (120 min)	598.7	Freundlich	Pseudo sec. order (k: 0.0030 g mg^{-1} min^{-1})	521
MB	PPy@MoS_2 hollow microtubes	Aqueous medium	Hydrothermal process and *in situ* polymerization and sulfidation	Temp.: RT, MB:150 mg L^{-1} (5 mL), adsorbent: 50 mg L^{-1}, pH: neutral, removal (time): 41.1% (120 min)	121.3	Langmuir	Pseudo sec. order (k: 0.0003 g mg^{-1} min^{-1})	521

Table 4 *(Contd.)*

Dye	Adsorbent	Water type	Preparative method	Experimental conditions and findings	q_m (mg g^{-1})	Removal isotherm fitted to	Kinetics data fitted to	Ref.
MB	PANI nanotubes base/silica	Distilled water	*In situ* polymerization	Temp.: 25 °C, MB: 0.95 mg L^{-1} (100 mL), adsorbent: 0.05 g, removal (time): 100% (10 min)	10.31	Langmuir	Pseudo sec. order (k: 0.09 g mg^{-1} min^{-1})	522
MB	PANI/TiO_2 hydrate	Distilled water	One-pot chemical oxidative polymerization	Temp.: 298 K, MB:100–200 mg L^{-1} (10 mL), adsorbent: 2 g L^{-1}, pH: 3–11, removal (time): ~100% (12 h)	458.10	Freundlich model	Pseudo sec. order (k: 0.0009 g mg^{-1} min^{-1})	523
MB	PPy-coated cotton textile	Aqueous solution	*In situ* oxidative polymerization of cotton textiles	Temp.: 25 °C, MB: 3.9 mg L^{-1} (50 mL), adsorbent: 0.05 g, pH: 7, removal (time): 96% (24 h)	6.83	Freundlich	Pseudo sec. order (k: 0.083 g mg^{-1} min^{-1})	525
MB	Fe_3O_4@PPy@SDBS	Aqueous solutions	Through hydrothermal, *in situ* polymerization, and surface modification	Temp.: 20 °C, MB: 20–30 mg L^{-1} (30 mL), adsorbent: 10 mg, pH: 7, removal (time): ~97% (500 min)	124.07	Langmuir	Pseudo sec. order (1.213×10^{-3} g mg^{-1} min^{-1})	527
MG	Fe_3O_4@PPy@SDBS	Aqueous solutions	Through hydrothermal, *in situ* polymerization, and surface modification	Temp.: 20 °C, MG: 20 mg L^{-1} (30 mL), adsorbent: 8 mg, pH: 7, removal (time): ~96% (500 min)	73.10	Langmuir	Pseudo sec. order (1.445×10^{-3} g mg^{-1} min^{-1})	527
MB	PPy/GO@Fe_3O_4	Aqueous solutions	One step	Temp.: RT, MB: 100 mg L^{-1} (40 mL), adsorbent: 10 mg, pH: 8, removal (time): ~80% (140 min)	323.2	Langmuir	Pseudo second, order (k: 0.00172 g mg^{-1} min^{-1})	528
MB	Fe_3O_4@PPy/RGO	Aqueous solutions	Chemical route	Temp.: 30 °C. MB:100 mg L^{-1} (30 mL), adsorbent: 0.333 g L^{-1}, pH: natural, removal (time): ~95% (60 min)	270.3	Langmuir isotherm	Pseudo-second-order (k: 0.0154 g mg^{-1} min^{-1})	530
MB	Fe_3O_4/polypyrrole/phytic acid	Water	*In situ* polymerization	Temp.: 35 °C, MB: 100 ppm (50 mL), adsorbent: 80 mg, pH: 10, removal (time): ~86.4% (120 min)	153.84	Langmuir	Pseudo sec. order (k: 0.001 g mg^{-1} min^{-1})	531
CV	Fe_3O_4/polypyrrole/phytic acid	Water	*In situ* polymerization	Temp.: 35 °C, CV: 100 ppm (50 mL), adsorbent: 80 mg, pH: 10, removal (time): ~85% (120 min)	181.82	Langmuir	Pseudo sec. order (k: 0.001 g mg^{-1} min^{-1})	531
MO	PANI nanotube-filled sodium alginate	Distilled water	Mixing of PANI nanotubes in water + $CaCl_2$	Temp.: 35 °C, MO: 20 mg L^{-1} (50 mL), adsorbent: 0.05 g, pH: 2, removal (time): ~76% (90 min)	370.4	Langmuir	Pseudo sec. order (k: 0.001 g mg^{-1} min^{-1})	534
MO	PANI-MWCNT	Water	*In situ* oxidative polymerization	Temp.: 30 °C, MO: 30 mgL^{-1} (100 ml), adsorbent: 8 mg L^{-1}, pH: neutral, removal (time): ~94% (60 min)	149.25	Langmuir	Pseudo sec. order (k: 5.265×10^{-4} g mg^{-1} min^{-1})	535
MO	PANI (skin)/polyamide 6 (core)	Aqueous solution	*In situ* oxidation polymerization	Temp.: 298 K, MO:10 ppm, adsorbent: 0.03g, pH: 6, removal (time): 58.7 mg g^{-1} (120 min)	58.7	Langmuir	Pseudo sec. order	536
MO	Waterborne poly vinyl pyrrolidone-stabilized PANI core–shell	Tap water	Waterborne PVP-stabilized PANI core–shell	Temp.: 28 °C, MO: 32.73 mg L^{-1} (20 ml), adsorbent: 5 mg, pH 7.02, removal (time): 100% (15 min)	—	Langmuir	—	537

Table 4 *(Contd.)*

Dye	Adsorbent	Water type	Preparative method	Experimental conditions and findings	q_m (mg g^{-1})	Removal isotherm fitted to	Kinetics data fitted to	Ref.
MO	Halloysite nanotubes/PPy	Aqueous solution	*In situ* polymerization	Temp.: 25 °C, MO: 90 mg L^{-1} (50 mL), adsorbent: 0.15 g, pH: natural, removal (time): 98.6% (120 min)	214.6	Langmuir and Freundlich	Pseudo sec. order (k: 0.0037 g mg^{-1} min^{-1})	538
RB	PANI@TiO_2	Deionized water	Sonochemical method	Temp.: 28 °C. RB: 100 mg L^{-1} (100 mL), adsorbent: 50 mg, pH: 6.7, q_t (time): ~80 mg g^{-1} (120 min)	—	Langmuir and Freundlich	First order (k: 0.007 min^{-1}), pseudo sec. order (k: 0.00008 g mg^{-1} $min^{-1/2}$)	540
RB	PANI@SiO_2	Deionized water	Sonochemical method	Temp.: 28 °C. RB: 100 mg L^{-1} (100 mL), adsorbent: 50 mg, pH: 6, q_t (time): ~30 mg g^{-1} (120 min)	—	Langmuir and Freundlich	First order (k: 0.024 min^{-1}), pseudo sec. order (k: 0.00029 g mg^{-1} $min^{-1/2}$)	540
R6G	PANI@TiO_2	Deionized water	Sonochemical method	Temp.: 28 °C. R6G: 50 mg L^{-1} (100 mL), adsorbent: 5 mg, pH: 6.7, q_t (time): ~90 mg g^{-1} (120 min)	94	Langmuir and Freundlich	First order (k: 0.023 min^{-1}), pseudo sec. order (k: 0.00 069 g mg^{-1} $min^{-1/2}$)	540
R6G	PANI@SiO_2	Deionized water	Sonochemical method	Temp.: 28 °C. R6G: 5 mg L^{-1} (100 mL), adsorbent: 5 mg, pH: 6.7, q_t (time): ~60 mg g^{-1} (120 min)	61	Langmuir and Freundlich	First order (k: 0.011 min^{-1}), pseudo sec. order (k: 0.00 006 g mg^{-1} $min^{-1/2}$)	540
CR	PANI@TiO_2	Deionized water	Sonochemical method	Temp.: 28 °C. CR: 100 mg L^{-1} (100 mL), adsorbent: 5 mg, pH: 6.7, q_t (time): ~93 mg g^{-1} (120 min)	93	Langmuir and Freundlich	First order (k: 0.020 min^{-1}), pseud sec. order (k: 0.00048 g mg^{-1} $min^{-1/2}$)	540
CR	PANI@SiO_2	Deionized water	Sonochemical method	Temp.: 28 °C. CR: 100 mg L^{-1} (100 mL), adsorbent: 5 mg, pH: 6.7, q_t (time): ~70 mg g^{-1} (120 min)	71	Langmuir and Freundlich	First order (k: 0.0253 min^{-1}), pseudo sec. order (k: 0.00034 g mg^{-1} $min^{-1/2}$)	540
MB	PANI@TiO_2	Deionized water	Sonochemical method	Temp.: 28 °C. MB: 100 mg L^{-1} (100 mL), adsorbent: 50 mg, pH: 6.7, q_t (time): ~90 mg g^{-1} (120 min)	89	Langmuir and Freundlich	Pseudo first order (k: 0.024 min^{-1}), pseudo sec. order (k: 0.00050 g mg^{-1} $min^{-1/2}$)	540
MB	PANI@SiO_2	Deionized water	Sonochemical method	Temp.: 28 °C, MB: 50 mg L^{-1} (100 mL), adsorbent: 50 mg, pH: 6.7, q_t (time): ~73 mg g^{-1} (120 min)	74	Langmuir and Freundlich	First order (k: 0.037 min^{-1}), pseudo sec. order (k: 0.00056 g mg^{-1} $min^{-1/2}$)	540
EB	PANI@TiO_2	Deionized water	Sonochemical method	Temp.: 28 °C. EB: 100 mg L^{-1} (100 mL), adsorbent: 5 mg, pH: 6.7, q_t (time) ~55 mg g^{-1} (120 min)	—	Langmuir and Freundlich	First order (k: 0.008 min^{-1}) pseudo sec. order (k: 0.00011 g mg^{-1} $min^{-1/2}$)	540
EB	PANI@SiO_2	Deionized water	Sonochemical method	Temp.: 28 °C. EB: 100 mg L^{-1} (100 mL), adsorbent: 5 mg, pH: 6.7, q_t (time) ~55 mg g^{-1} (120 min)	—	Langmuir and Freundlich	First order (k: 0.013 min^{-1}) pseudo sec. order (k: 0.00012 g mg^{-1} $min^{-1/2}$)	540
BB	PANI@TiO_2	Deionized water	Sonochemical method	Temp.: 28 °C. BB: 100 mg L^{-1} (100 mL), adsorbent: 5 mg, pH: 6.7, q_t (time):~42 mg g^{-1} (120 min)	—	Langmuir and Freundlich	Pseudo first order (k: 0.011 min^{-1}), pseudo sec. order (k: 0.00013 g mg^{-1} $min^{-1/2}$)	540

Table 4 *(Contd.)*

Dye	Adsorbent	Water type	Preparative method	Experimental conditions and findings	q_m (mg g^{-1})	Removal isotherm fitted to	Kinetics data fitted to	Ref.
BB	PANI@SiO_2	Deionized water	Sonochemical method	Temp.: 28 °C. BB: 100 mg L^{-1} (100 mL), adsorbent: 5 mg, pH: 6.7, q_t (time): ~42 mg g^{-1} (120 min)	86	Langmuir and Freundlich	Pseudo first order (k: 0.038 min^{-1}), pseudo sec. order (k: 0.00060 g mg^{-1} $min^{-1/2}$)	540
MG	Graphene/Fe_3O_4/PANI	Aqueous solutions	Multiple steps	Temp.: 25 °C, MG: 16 mg L^{-1} (50 mL), adsorbent: 30 mg, pH: 6.5, removal (after cycle 1): 97.72%	196.10	Langmuir	Pseudo sec. order (k: 0.0022 g mg^{-1} min^{-1})	541
AR1	Graphene/Fe_3O_4/PANI	Aqueous solutions	Multiple steps	Temp.: 25 °C, AR1: 16 mg L^{-1} (50 mL), adsorbent: 30 mg, pH: 6.5, removal efficiency (after cycle 1): 97.013%	150.27	Langmuir	Pseudo sec. order (k: 0.0021 g mg^{-1} min^{-1})	541
MG	CNT/PANI	Aqueous solution	Static interfacial polymerization technique	Temp.: 20 °C, MG: 8–12 mg L^{-1} (100 mL), adsorbent: 0.1 g, pH: 7, removal (time): ~95% (120 min)	15.45	Langmuir	Pseudo sec- order (k: 5.0 × 10^{-3} mg g^{-1} $min^{-0.5}$)	542
AR1	PPy/$Mn_{0.8}Zn_{0.2}Fe_2O_4$/GO (PMG50)	Wastewater	*In situ* Py polymerization	Temp.: 298 K, AR1:10 mg L^{-1} (10 mL), adsorbent: 100 mg, pH: 2, removal (time): 98.8% (120 min)	—	—	Pseudo sec. order (0.320 g mg^{-1} min^{-1})	545
BG	Cross-linked PANI/chitosan-graphene oxide-oxidized SWCNT	Aqueous solution	Chemical oxidative copolymerization	Temp.: 22 °C, BG: 5 mg L^{-1} (25 mL), adsorbent: 12.5 mg, pH 6, removal efficiency (time): ~98.4% % (120 min)	21.27	—	Pseudo-second-order (k: 9.2 × 10^{-4} mg g^{-1} min-$^{0.5}$)	546
AR1	Cross-linked PANI/chitosan-graphene oxide-oxidized SWCNT	Aqueous solution	Chemical oxidative copolymerization	Temp.: 22 °C, AR1: 20 mg L^{-1} (25 mL), adsorbent: 12.5 mg, pH 2, removal efficiency (time): 99.7% (120 min)	90.91	—	Pseudo-second-order (k: 3.4 × 10^{-4} mg g^{-1} $min^{-0.5}$)	546
BG	Core–shell polythiophene/ZnO/MWCNTs	Aqueous solutions	*In situ* chemical polymerization (two-way method)	Temp.: 25 °C. BG: 5 mg L^{-1} (20 mL), adsorbent: 30 mg, pH: 6, removal efficiency (time): 94% (90 min)	8.3	—	Pseudo second-order (k: 1.9 × 10–3 mg g^{-1} min^{-1})	547

[a] q_m: maximum adsorption capacity. AG: acid green, AR: acid red, AR1: acid red 1, AYR: alizarin yellow R, BB: brilliant blue, BG: brilliant green, CR: Congo red, CV: crystal violet, E102 (tartrazine: TTz), EB: Evans blue, EY: eosin Y, OG: orange green, IC: indigo carmine, MG: malachite green, MO: methyl orange, MB: methylene blue, MR: methyl red, OG: orange green, Rh: rhodamine, RhB: rhodamine B, Rh6B: rhodamine 6B. Rh6G: rhodamine 6G, SY: sunset yellow.

Table 5 Merits and demerits of different electrode materials.[7] Reproduced with permission from Elsevier

Materials	Advantages	Disadvantages
Carbonaceous materials	High specific surface area	Low energy density
	High electrical conductivity Inexpensive Eco-friendly High electrochemical stability	Poor cyclability
Conducting polymers	High specific capacitance	Low conductivity
	Tunable electrical conductivity Unique solution processability High flexibility Easy fabrication	Poor electrochemical stability
Transition metal oxide	High specific capacitance	Low conductivity
	Wide potential window	Poor electrochemical stability
	High energy density	

promising candidates for having very high-power density, long cycling stability and excellent durability. The supercapacitors can be classified into electrical double-layer capacitors (EDLCs), pseudocapacitors (PCs), and hybrid supercapacitors, as schematically based on the mechanism involved in energy storage (Fig. 36).[551] EDLCs are non-faradaic supercapacitors or ultracapacitors involving the storage of the charge taking place in the electrical double layer formed at the electrode/electrolyte interface without any changes in the chemical properties of the electrode materials. In the case of PC, charge is stored electrochemically through highly reversible redox reactions at the electrode–electrolyte interface, and they offer more power and charge density compared with EDLCs. A hybrid supercapacitor, on the other hand, is a combination of an EDLC and a pseudocapacitor and allows for both faradaic and non-faradaic charge storage.

In this regard, intrinsically conducting polymers are favoured in supercapacitor applications due to their simple synthesis, tunable conductivity, large surface area, high flexibility, and pseudocapacitive properties.[7] These features enable them to store and release energy quickly, thereby making conducting polymers an ideal candidate for high-power applications. The superior electrochemical performance of these ICPs is greatly guided by their morphology. In view of this, hollow-structured material electrodes can be better alternatives by offering higher specific surface area to facilitate the large electrode/electrolyte interface favorable for the fast transport of charges and ions as well as act as the ion reservoir to benefit the accumulation of ions. Therefore, ICPs are considered as promising electrode materials due to their low production cost and their ability to possess redox pseudocapacitance and double-layer capacitance. However, the application of ICPs is limited due to their inferior stability; therefore, ICP is combined with other active materials to overcome this intrinsic disadvantage. Accordingly, the performance of ICP for hollow-structured ICPs, their composites and core–shell-based materials is discussed below.

5.4.1 Hollow ICP microspheres. Tan *et al.*[552] prepared hollow polyaniline microspheres using sulfonated polystyrene microspheres as template. The electrochemical investigations of hollow polyaniline predicted an increase in the specific capacitance of hollow polyaniline microspheres with the feed ratio of aniline (ANI) to sulfonated polystyrene (SPS), referred to as $r_{ANI/SPS}$, and attained a maximum value of 421 F g^{-1} corresponding to $r_{ANI/SPS}$ of 1.0. The cycle life performance of the hollow polyaniline microspheres electrode was tested for 500 cycles (10 mA cm^{-2}). It decreased for the first 200 cycles, most likely due to the swelling and shrinking of PANI, and finally remained more or less unaltered. In another study, an interfacial polymerization method was used to synthesize hollow polyaniline nano-capsule with holes in the wall in the absence of any template.[553] According to TEM studies, PANI nano-particles formed nano-rods, with uniform hollow capsule-like structures comprising the holes on the wall

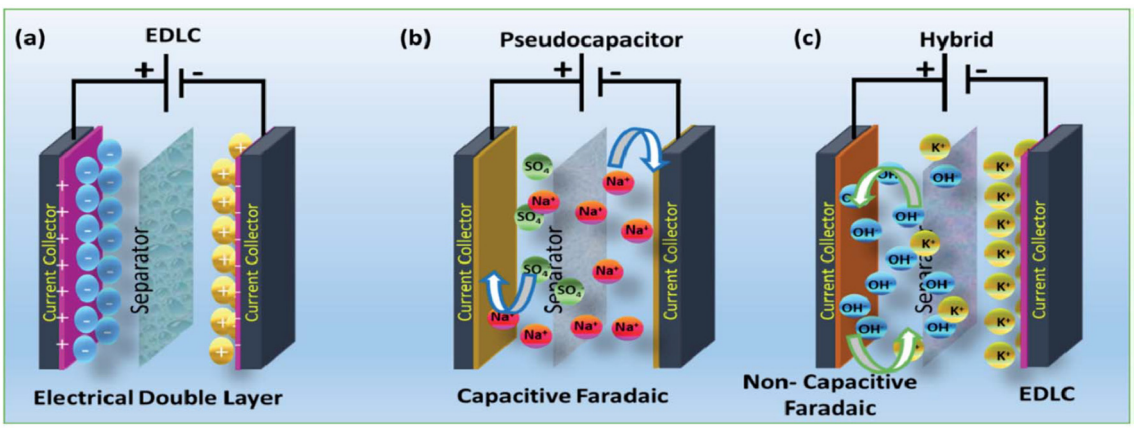

Fig. 36 Charge storage mechanism of supercapacitors, (a) EDLCs, (b) pseudocapacitors and (c) hybrid supercapacitors.[551] Reproduced with permission from RSC.

(capsule). The PANI nano-capsule electrode displayed high specific capacitance of 502 F g^{-1} (at the current density of 5 mA cm^{-2}) and excellent cycling stability. The electrochemical performance of the capsule-like PANI electrode was attributed to the conductivity and hollow nanostructure that accounted for rapid electrolyte transport and shortened ion diffusion paths within the active materials.

Polyaniline hollow microspheres (dia: 410 nm, thickness: 72 nm) doped by (poly(2-acrylamido-2-methylpropane sulfonic acid)) (PAMPS) synthesized by a self-assembly method have shown excellent promise in the field of supercapacitors.[554] Li *et al.*[555] fabricated Ce^{3+}-doped polyaniline hollow microspheres by a self-assembly method; it exhibited a high specific capacitance of 248.2 F g^{-1} (1 mA cm^{-2}) due to its enhanced conductivity compared with PANI (201.6 F g^{-1}). In another approach, hollow PANI nanospheres prepared by *in situ* chemical oxidative polymerization of aniline in the presence of uniform poly(methyl methacrylate-butyl methacrylate-methacrylic acid) latex microspheres (self-sacrificial template) demonstrated specific capacitance (485.5 F g^{-1} at 1 A g^{-1}) and performance after 500 cycles (69%).[556]

Polypyrrole hollow nanospheres prepared using polystyrene (PS) as a template that was subsequently removed by dissolving it in DMF displayed high specific capacitances (350 F g^{-1} at 1 A g^{-1}).[557] The corresponding symmetric supercapacitor has shown the maximum energy density of 40 Wh kg^{-1} at a power density of 490 W kg^{-1}. Electrochemical studies were also performed on hollow polypyrrole films prepared by depositing polypyrrole on a 3D colloidal crystal template.[558] According to Li *et al.*,[559] hollow capsular polypyrrole nanofibers with porous capsule acted as a flexible, binder-free, self-supported supercapacitor electrode exhibiting specific capacitance of 203 F g^{-1} at 2 mV s^{-1} and excellent capacitance retention (>90% after 11 000 charge–discharge cycles @10 A g^{-1}). This was attributed to the availability of enough free space in the capsular walls of the hollow PPy film to facilitate the volume variation during doping/de-doping. Zhang *et al.*[244] synthesized PEDOT hollow nanospheres by expulsion of SiO_2 from the SiO_2@PEDOT nanospheres by dissolving it hydrofluoric acid. The PEDOT hollow sphere film fabricated in this manner showed a high specific capacitance (121.6 F g^{-1}) at the current density of 0.5 A g^{-1} and sustained 65.7% of its initial specific capacitance at a current density of 8.0 A g^{-1}.

5.4.2 Nanotubes of ICPs. According to Cui *et al.*,[100] a dual-colloid interface co-assembly approach for the synthesis of hollow mesoporous conducting polymers (mPPy-nb-4) delivered specific capacitance of 225 F g^{-1} (1 mV s^{-1}) and also offered a power density of 343 mW cm^{-3} at an energy density of 0.2 mWh cm^{-3}. In another study, Chen *et al.*[492] prepared hollow polyaniline helical nanobelts by using a synthetic template (oligomers) following *in situ* chemical oxidation of aniline. They observed specific capacitance up to 688 F g^{-1} (scan rate: 5 mV s^{-1}) and 81.6% retention (1000 cycles). Subsequent studies on the fabricated symmetric supercapacitor showed energy density and power density of.14.37 Wh kg^{-1} and 500 W kg^{-1}, respectively. Fan *et al.*[560] synthesized polyaniline nanotubes using natural tubular halloysite as a hard template and subsequently subjected it to carbon coating by a hydrothermal method (Fig. 37(a)). The electrochemical performance of this electrode material indicated high specific capacitance (654 F g^{-1} at 1 A g^{-1}), and excellent electrochemical stability with capacitance retentions (~87% after 10 000 cycles). This suggested that the carbon-coated PANI electrode acted as a constraint layer to prevent the tubular-structured PANI from expanding outward during the charge–discharge process. ZnO nanorod arrays (sacrificial templates) were used to fabricate polyaniline nanotube arrays and their electrochemical polymerization was studied for supercapacitor applications (Fig. 37(b)).[561] Jyothibasu and Lee[562] fabricated polypyrrole tubes using curcumin (template), as schematically shown in Fig. 37(c) and combined it with functionalized carbon nanotubes (f-CNTs) to form freestanding electrodes (referred to as PPyC3T2/f-CNT). It showed excellent areal capacitance of 11 830.4 mF cm^{-2} at a current density of 2 mA cm^{-2} in a thick freestanding PPyC3T2/f-CNT-electrode at a high mass loading of 30 mg cm^{-2}. Furthermore, a symmetric supercapacitor assembled by using the PPyC3T2/f-CNT displayed an areal capacitance, cycling stability, high energy density and maximum power density of 2732 mF cm^{-2} at 2 mA cm^{-2}, 118.18% retention after 12 500 cycles, 242.84 μW h cm^{-2} and 129.35 mW cm^{-2}, respectively.

Hollow PANI nanotubes (inner dia: 80 nm, outer dia: 180 nm) prepared *via* one-step polymerization attained specific capacitance of 436 F g^{-1} (0.5 A g^{-1}) in H_2SO_4 (1 mol L^{-1}) solution with good cycling stability (89.2%: 500 cycles at a current density of 0.5 A g^{-1}).[563] Crystalline tetragonal hollow polyaniline nanotubes prepared by using methyl orange as self-degrading template showed a specific capacitance of 590 ± 36 F g^{-1} at a scan rate of 5 mV s^{-1}.[564] The assembled symmetrical device exhibited maximum energy density and power density of 14.56 Wh kg^{-1} and 250 W kg^{-1}, respectively. Ahn *et al.*[565] prepared PPy hollow nanoparticles with controlled diameters through surfactant-templated chemical oxidation polymerization (Fig. 37(d)). The specific capacitance of PPy hollow nanoparticles (326 F g^{-1}) fabricated in this manner was found to be approximately twice as large as that of solid PPy nanospheres. High-performance supercapacitor performance has also been displayed by PANI nanofibers, nanotubes, and nanospheres,[566] and hollow polyaniline nanofibers fabricated by electrospinning.[312] Hryniewicz and Vidotti[567] for the first time electrodeposited PEDOT nanotubes onto stainless steel mesh electrodes in the presence of methyl orange template and observed enhanced supercapacitive and electrocatalytic properties. Wan *et al.*[568] observed high specific capacitance (290 F g^{-1} at 1 A g^{-1}) and outstanding cyclic stability (capacitance retention: 83% even after 1000 cycles) for the polyaniline hollow nanofibers supercapacitor electrode exhibiting 3D porous network architecture.

5.4.3 Hollow ICP nanocomposites. Zhang *et al.*[569] prepared hollow polypyrrole/cellulose hydrogels to study their performance as a flexible supercapacitor. The assembled symmetrical supercapacitor device delivered high specific capacitance (255

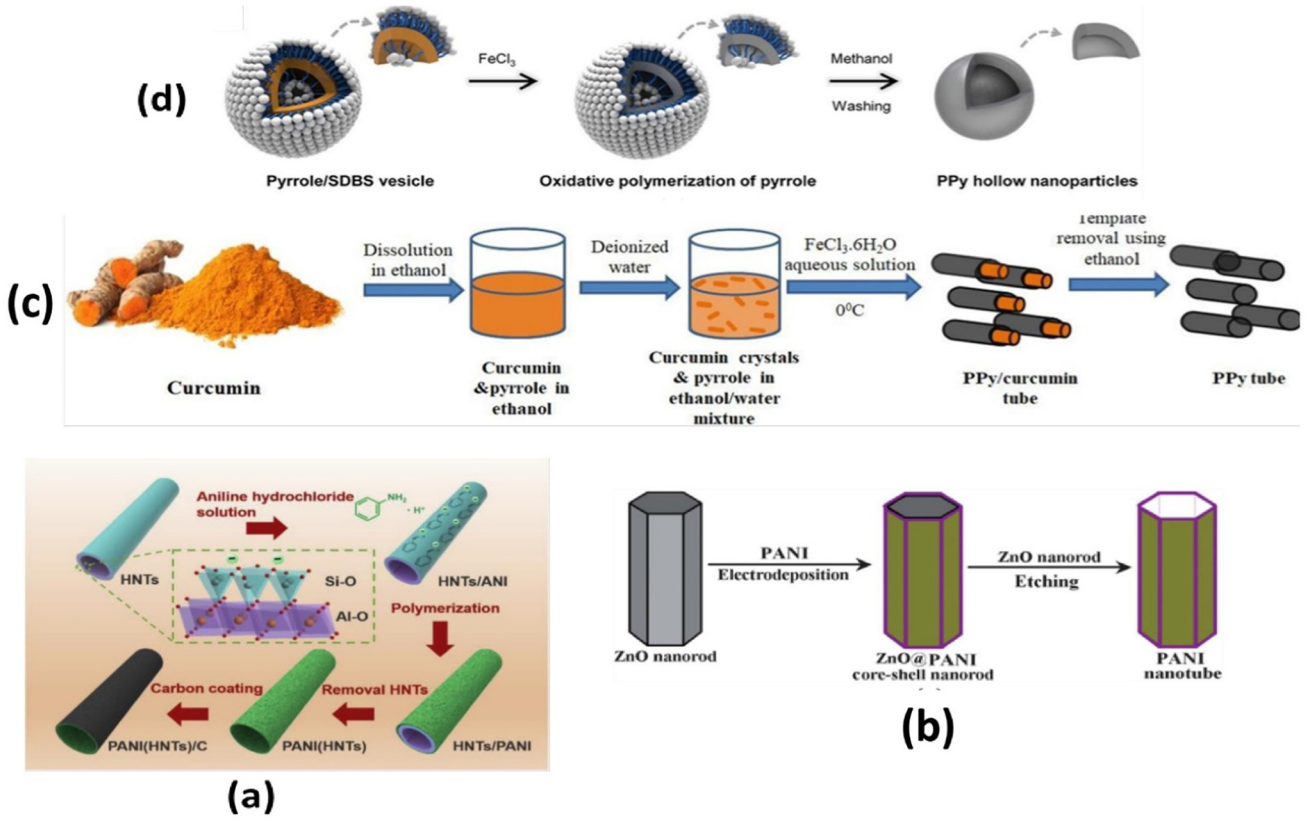

Fig. 37 (a) Schematic presentation on the preparation procedure of PANI(HNTs) and PANI(HNT)s/C.[560] Reproduced with permission from Elsevier. (b) The illustration for the formation of PANI nanotubes *via* a sacrificial ZnO nanorods template route.[561] Reproduced with permission from RSC. (c) Schematic representation of the preparation of polypyrrole tubes using curcumin as template.[562] Reproduced with permission from RSC. (d) Schematic diagram of the synthesis of PPy hollow nanospheres.[565] Reproduced with permission from RSC.

F g^{-1} at 0.25 A g^{-1}), good rate capability (77% capacitance retention at 30 A g^{-1}), cycling stability (80% after 10 000 cycles at 10 A g^{-1}) and energy density (20.4 Wh kg^{-1}) at a power density of 194 W kg^{-1}. Wang and others[570] investigated the electrochemical performance of mesoporous MnO_2/polyaniline composite with a unique morphology of hierarchical hollow submicron spheres synthesized by an interfacial approach. Electrochemical studies revealed its superior electrochemical properties, as indicated by its specific capacitance (262 F g^{-1}) and higher capacitance retention (93% of its initial capacitance after 800 cycles) owing to its microstructure and polyaniline/MnO_2 coexisting together.

3D hollow balls of graphene–polyaniline hybrids were prepared through the self-assembly of graphene oxide and PMMA followed by the polymerization of polyaniline, and demonstrated high specific capacitance and good cycling stability.[571] Luo *et al.*[572] used layer-by-layer assembly for the preparation of a graphene–polyaniline hollow microsphere for supercapacitor application. It displayed excellent specific capacitance (381 F g^{-1}: 4.0 A g^{-1}) and good cycling stability (83% after 1000 cycles) in 1 M H_2SO_4 solution due to a synergistic effect. The hierarchical Ti_3C_2/PANI nanotubes have shown excellent specific capacitance performance (596 F g^{-1} at 0.1 A g^{-1}) with 94.7% retention after 5000 cycles (at 1 A g^{-1}).[573] Furthermore, a symmetric supercapacitor device based on this showed excellent performance (energy density: 25.6 Wh kg^{-1} at 153.2 W kg^{-1}, power density: 1610.8 W kg^{-1} at 13.2 Wh kg^{-1}, capacitance retention 81.1% after 4000 cycles).

Devi and Kumar[574] prepared nanocomposites of reduced graphene oxide/polyaniline nanotubes in the presence as well as the absence of irradiated high energetic ions and performed electrochemical investigations as a supercapacitor. They observed the relatively enhanced specific capacitance (482 F g^{-1} at 0.5 A g^{-1}) and cycling stability (92%) compared with the unirradiated nanocomposite. This was ascribed to the increased surface energy and porosity as a result of irradiation. Yang *et al.*[575] tested the electrochemical performance of a polypyrrole hollow nanosphere intercalated graphene-based flexible supercapacitor and observed its area specific capacitance and capacitance retention of 381.54 mF cm^{-2} (at 2 mA cm^{-2}) and 93.94% after 1000 cycles, respectively. Graphene–polypyrrole hollow sphere,[576] hollow polypyrrole nanosphere embedded in N-doped graphene layers,[577] 3D-arrayed polyaniline hollow nanospheres encaging RuO_2 nanoparticles,[578] polyaniline hollow fibers decorated by graphene,[579] graphene–polypyrrole nanotubes,[580] 3D metal–organic frameworks with conductive polypyrrole tubes,[581] and hollow PPy nanospheres decorated on the CNT[582] have been synthesized and also used

as electrode materials for electrochemical supercapacitor applications.

5.4.4 Core–shell-based ICP nanocomposites

5.4.4.1 Binary core–shell nanocomposites. Tian *et al.*[583] wrapped polyaniline nanowires on polypyrrole hollow nanotubes by the chemical method and observed a high specific capacitance (~765 F g^{-1} at a scan rate of 10 mV s^{-1}) and the capacitance loss of ~13.7% after 1000 charging/discharging cycles. This performance was explained on the basis of the synergistic effect of PANI and PPy. Core–shell polyaniline-functionalized carbon quantum dots exhibited high specific capacity of 264.6 F g^{-1} (2.5 A g^{-1}) and high stability indicated by 5000 charge–discharge cycles.[584] The sea urchin-like polyaniline grown on the surface of polypyrrole by dilute solution polymerization (referred to as PPy@PANI) displayed a core–shell structure, according to Fig. 38(a).[585] The variation of the specific capacitance *versus* the scan rate is displayed in Fig. 38(b). According to this, the specific capacitance of PPy@PANI corresponds to 510 F g^{-1} (scan rate: 10 mV s^{-1}) compared with the PPy (87 F g^{-1}) electrode and the pure PANI (256 F g^{-1}) electrodes. PPy@PANI also showed good cycling stability as evident from 12.4% loss of specific capacitance after 1000 charge/discharge, as seen in Fig. 38(c). This electrochemical performance of the PPy@PANI electrode has been ascribed to the synergistic effect between the core PPy and shell PANI layer.

Li *et al.*[586] fabricated hollow microsphere (MS) and microtubes (MT) of PPy using polystyrene microspheres and methyl orange as hard and soft templates, respectively. Subsequently, they prepared composites of MS and MT with poly(1,5-diaminoanthraquinone) (referred as PDAAQ) and observed the following order for specific capacitance at a current density of 1 A g^{-1}:

PPy@PDAAQ MTs (533 F g^{-1}) > PPy@PDAAQ MSs (471 F g^{-1}) > PDAAQ, (348 F g^{-1}) >PPy MTs (322 F g^{-1}) > PPy (MSs 235 F g^{-1}).

The hollow morphology of PPy could account for the observed high specific capacitance of PPy@PDAAQ MTs.

The specific capacitance retention after 10 000 cycles followed the following trend:

PDAAQ (146.0%) > PPy@PDAAQ MTs (107.4%), PPy@PDAAQ MSs (98.0%), PPy MTs (43.6%), and PPy MSs (27.3%).

Fan *et al.*[587] prepared a core–shell hybrid comprising PS@PANI, polyaniline hollow spheres (PANI-HS)@GO and PANI-HS@ ERGO (electrochemically reduced graphene oxide) according to the procedure as illustrated in Fig. 39(a). The morphology and structure of the PANI-HS36@GO (36: shell

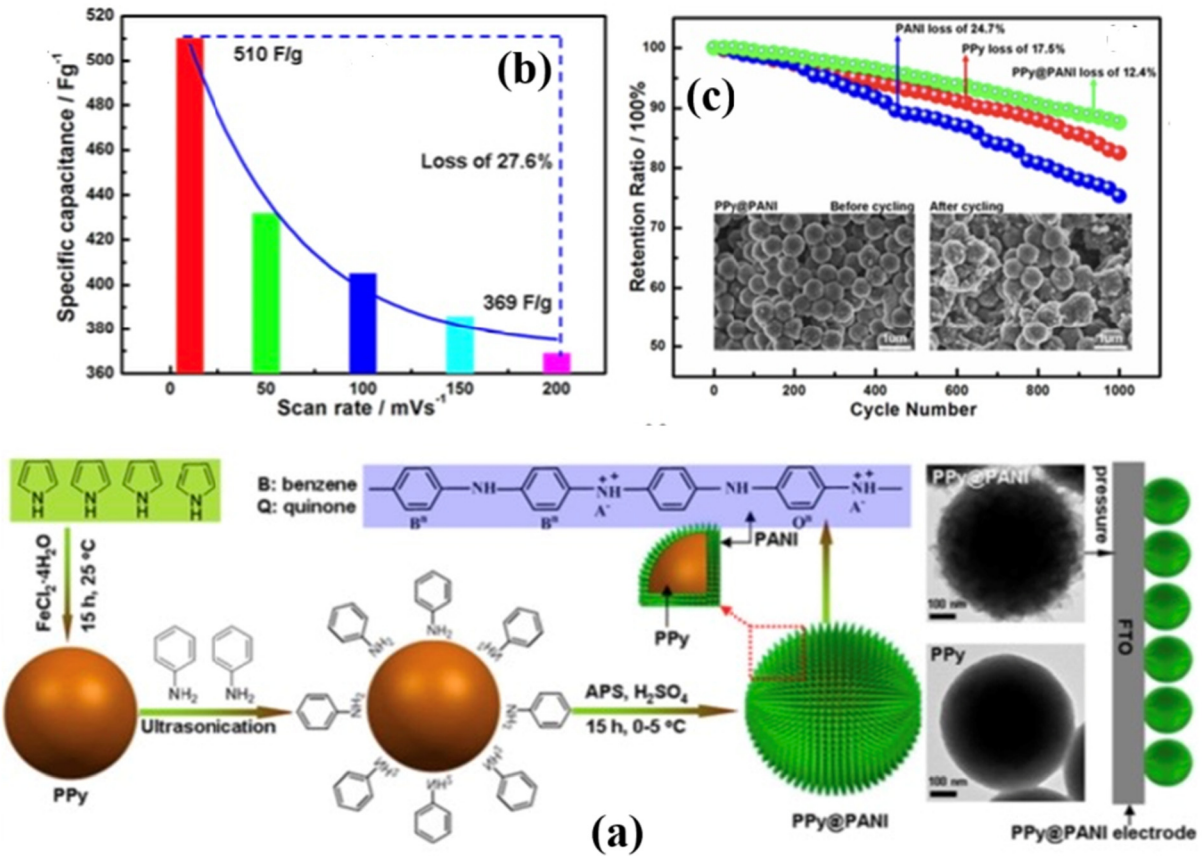

Fig. 38 (a) Schematic diagram for the synthesis of core–shell PPy@PANI nanospheres. (b) SC values' plot of the scan rates and (c) charge/discharge cycling of the core–shell PPy@PANI-0.008, individual PPy, and the PANI electrode carried out at 5 A g^{-1} in H_2SO_4 aqueous electrolyte (1 M). The insert is the SEM images of the core–shell@PANI-0.008 before and after 1000 cycles.[585] Reproduced with permission from ACS.

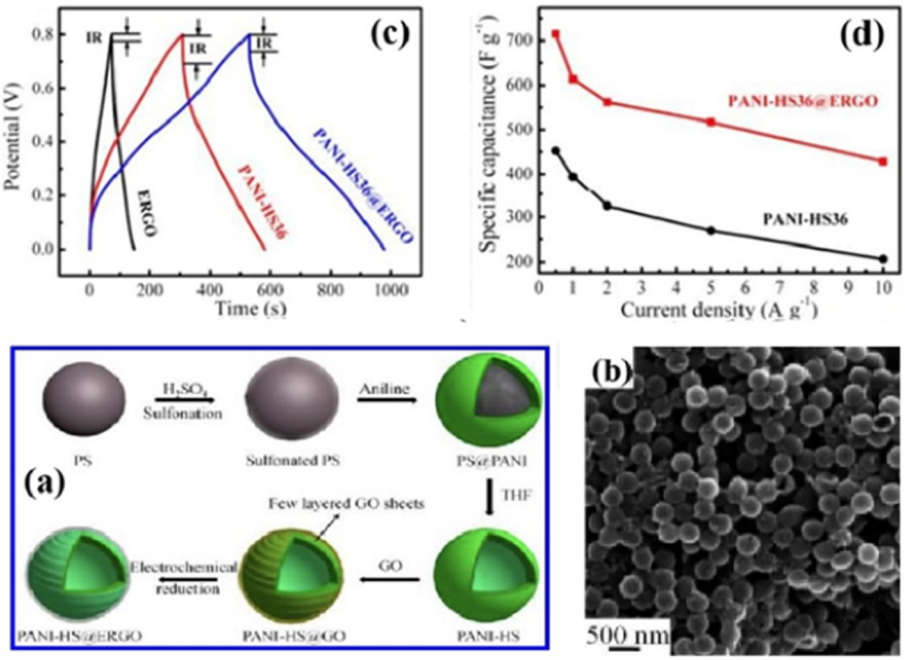

Fig. 39 (a) Schematic illustration on the preparation of PANI-HS36@ERGO hybrids (36 here refers to shell thickness in nm), (b) SEM images of PANI-HS36@GO hybrids, (c) galvanostatic charge–discharge curves of ERGO, PANIHS36, and PANI-HS36@ERGO hybrids within a potential window of 0–0.80 V at a current density of 1 A g^{-1} (modified), and (d) plots of specific capacitance for PANI-HS36 and PANI-HS36@ERGO hybrids at various current densities (modified).[587] Figure reproduced with permission from ACS.

thickness of PANI-HS) hybrid was studied by SEM and is displayed in Fig. 39(b). The PANI-HS36@ERGO hybrid indicated its significantly high specific capacitance corresponding to 614 F g^{-1} at 1 A g^{-1} current density (Fig. 39(c)) and maintained 90% after 500 charging/discharging cycles at a current density of 1 A g^{-1} (Fig. 39(d)) due the synergistic effect.

Du *et al.*[588] used MnO_2 nanotubes as the reactive template for the preparation of PANI nanotubes using an *in situ* polymerization process, that exhibited excellent specific capacitance (455.7 F g^{-1} at 0.5 A g^{-1}), rate capability of 63.2% even up to 30 A g^{-1}. However, it showed poor cycling stability due to the swelling and shrinking of PANI during intercalating/deintercalating. Therefore, they fabricated hierarchical carbon layer-encapsulated PANI nanotubes by a hydrothermal method and observed its superior performance compared with the PANI nanotubes. In addition, the assembled symmetric supercapacitors based on this delivered high energy density (42.32 Wh kg^{-1}) and power density (16.44 kW kg^{-1}) and had good cycling stability. Mini and Devendrappa[589] prepared a core/shell polyaniline/NiO nanocomposite and studied its electrochemical performance as an electrode in supercapacitor applications. These findings revealed its specific capacitance, energy density, power density and coulombic efficiency corresponding to 362 F g^{-1} (1 A g^{-1}), 50.2 Wh kg^{-1}, 0.50 kW kg^{-1} and 99% (at 4 Ag^{-1}), respectively. The enhanced specific capacitance performance was ascribed to the nanosized effect of NiO and the synergic effect between NiO and PANI.

Polypyrrole nanosphere (dia: ~70 nm)/graphene oxide synthesized *via in situ* surface-initiated polymerization exhibited specific capacitance of 370 F g^{-1}@0.5 A g^{-1}, and capacitance retention of 91.2% even after 4000 cycles owing to the core–shell structure and synergistic effect.[590] Qi *et al.*[591] reported the preparation of core–shell-structured tubular graphene nanoflake-coated polypyrrole nanotubes and observed its large capacitance, high capacitance retention and stable cycling performance. The energy density and cycling stability of the symmetric supercapacitor device based on this correspond to 11.4 μWh cm^{-2} at 720 μW cm^{-2} and over 80% capacitance retention after 5000 cycles, respectively.

In recent years, there has been considerable interest in studying the capacitive properties of MoS_2 for its application in supercapacitors.[592–597] However, despite many advantages, the aggregation, poor electrical conductivity and specific capacitance of MoS_2 limit its practical application in energy storage electrode materials.[592] As a result, MoS_2 is combined with conducting polymers to overcome this problem. In view of this, Chen *et al.*[593] prepared urchin-like MoS_2@PANI (MoS_2: 25 wt%) by a hydrothermal method and observed its maximum capacitance of 645 F g^{-1} at 0.5 A g^{-1} due to the synergistic effect. In addition, excellent cycling stability (89% capacitance retention) was observed after 2000 cycles at a current density of 10 A g^{-1}.

Zhang *et al.*[594] fabricated core/shell microspheres comprising hollow MoS_2/PANI-5 (5 represents the mass ratio of aniline to hollow MoS_2 microspheres). The electrochemical studies of this electrode material displayed the specific capacitance of 633 F g^{-1} @0.5 A g^{-1} and retention of the capacitance up to 86.0% after 1000 cycles at 10 A g^{-1}, benefitting from polyani-

line confined firmly on the microspheres of MoS_2. In addition, in the MoS_2/PANI-5 composite the energy density could deliver 31.7 W h kg^{-1} at the power density of 0.3 kW kg^{-1}.

A template-assisted method was employed to synthesize the MoS_2/PANI (mass ratio = 1 : 2) hollow microsphere and used as a promising electrode for a supercapacitor.[595] SEM images clearly established the coating of PANI on the surface of the hollow structure of MoS_2 microspheres (dia: ~2 μm). The specific capacitance was found to be 299 F g^{-1} at a scan rate: 10 A g^{-1} and was attributed to the synergistic effect of MoS_2 core and PANI coating shell. MoS_2/PANI microsphere electrode materials also delivered excellent cycling stability, as evident from its retention of 84.3% after 8000 cycles. The investigations also indicated the energy density reaching 23.1 Wh kg^{-1} at a power density of 8320 W kg^{-1}. The specific capacitances of the fabricated symmetric supercapacitor based on MoS_2/PANI microspheres electrodes corresponded to 231, 139, 97, 79 F g^{-1} at the current density of 0.2 A g^{-1}. Furthermore, the assembled symmetric supercapacitor also exhibited high cycling stability (80.4% after 5000 cycles at 1 A g^{-1}). These findings highlighted the potential application of MoS_2/PANI hollow microspheres for supercapacitors.

Ansari *et al.* reported[596] the formation of a mechanically exfoliated MoS_2 sheet coupled with polyaniline. TEM studies of the product indicated PANI was coated on the MoS_2 sheet and displayed the specific capacitance of 510.12 F g^{-1} at a current of 1 A g^{-1} due to the synergistic effect and interfacial interaction. The hierarchical PEDOT@MoS_2 showed high specific capacitance (2540 mF cm^{-2} at 1 mA cm^{-2}) and excellent capacitance retention (98.5%) after 5000 cycles at a high current density of 100 mA cm^{-2}.[597] This was ascribed to the hierarchical core/shell structure of the electrode material and the synergic effect. In addition, the assembled asymmetric supercapacitor delivered a high energy density (937 Wh m^{-2}) at 6500 W m^{-2} and excellent cycling stability with capacitance retention of 100% (5000 cycles).

According to Liang *et al.*,[598] V_2O_5@PPy displayed high conductivities and the synergic effect accounted for the specific capacitance of 307 F g^{-1} and good cycling life (82% capacity retention up to 1000 cycles). Such performance of V_2O_5@PPy benefited from the enhanced conductivity, synergistic effect, and the stability of the composite. The symmetric V_2O_5/PPy device exhibited a maximum energy density of 37 Wh Kg^{-1} at a power density of 161 W kg^{-1}. In addition, polyaniline-carbon nanotube core–shell,[599] pistil-like $MnCo_2O_{4.5}$@PANI,[600] and high-performance electrodes for supercapacitors.[601] Ni ferrite@Polypyrrole,[602] core/sheath structured ultralong MnO_x/PPy nanowires,[603] and CuS@PANI[604] also displayed superior performance as electrodes in supercapacitor applications. The performance of MWCNT coated with PANI (core dia: ~80–150 nm) has also been evaluated for supercapacitor application.[605] The findings showed maximum specific capacitance (552.11 F g^{-1} at 4 mA cm^{-2}) for PANi/MWCNT (10 wt%) in 1 M H_2SO_4.

Xia *et al.*[606] prepared a core–shell PANI/CNTs nanostructured hybrid by chemical vapor and electrochemical deposition methods according to Fig. 40. Subsequent findings based on galvanostatic charge/discharge (GCD) curves of CNTs and PANI/CNTs with and without the addition of 0.02 M Fe^{3+}/Fe^{2+} are displayed in Fig. 41(a). It was inferred that discharge time was extended on the addition of the Fe^{3+}/Fe^{2+} redox couple. The following order for discharge time was observed: PANI/CNTs (0.02 M Fe^{3+}/Fe^{2+}) > PNI/CNTs > CNT (0.02 M Fe^{3+}/Fe^{2+}) > CNTs. GCD curves of PANI/CNTs at different current density in 1 M H_2SO_4 in Fig. 41(b) confirmed the ideal capacitive mechanism of the core–shell hybrid. GCD curves of PANI/CNTs in 1 M H_2SO_4/0.02 M Fe^{3+}/Fe^{2+} electrolyte at different current densities are displayed in Fig. 41(c). These findings affirmed a non-ideal triangular pattern corresponding to the redox reaction behavior of the Fe^{3+}/Fe^{2+} redox couple. The specific capacitance curves of PANI/CNTs at different current densities in Fig. 41(d) showed improvement in the specific capacitance of PANI/CNTs (1005 F g^{-1}) on adding 0.02 M Fe^{3+}/Fe^{2+} (1547 F g^{-1}) at 2 A g^{-1} in 1 M H_2SO_4. This superior performance was attributed to the synergistic effect originating from the contribution of the Fe^{3+}/Fe^{2+} redox couple and the PANI/CNTs core–shell structure. In addition, the specific capacitance of the assembled symmetric architecture device was calculated and found to be 412 F g^{-1} at 0.5 A g^{-1}. In addition, the energy density (22.9 Wh kg^{-1}) at a power density of 700.1 W kg^{-1} and the capacitance retention of 97% (2000 charge–discharge cycles) was reached using PVA/H_2SO_4/Fe^{3+}/Fe^{2+} gel as redox electrolyte. These findings supported the role played by the core–shell PANI/CNT hybrid electrode and Fe^{3+}/Fe^{2+} redox additive electrolyte in achieving this enhanced electrochemical performance.

An enhanced electrochemical performance has been reported for the hierarchical $NiCo_2S_4$@PANI core–shell nanowires grown on a carbon filter.[607] The specific capacitance of the electrode fabricated in this manner showed enhanced areal capacitance of 4.74 F cm^{-2} (1823 F g^{-1}) at 2 mA cm^{-2}

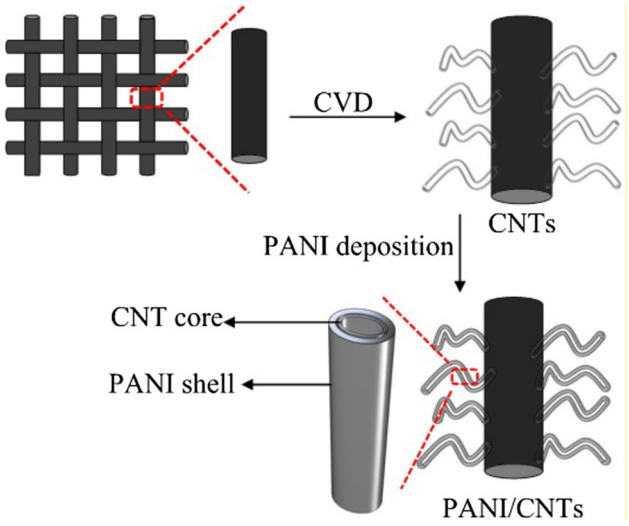

Fig. 40 Illustrations of the fabrication process for PANI/CNTs on carbon cloth (CC).[606] Reproduced with permission from Springer.

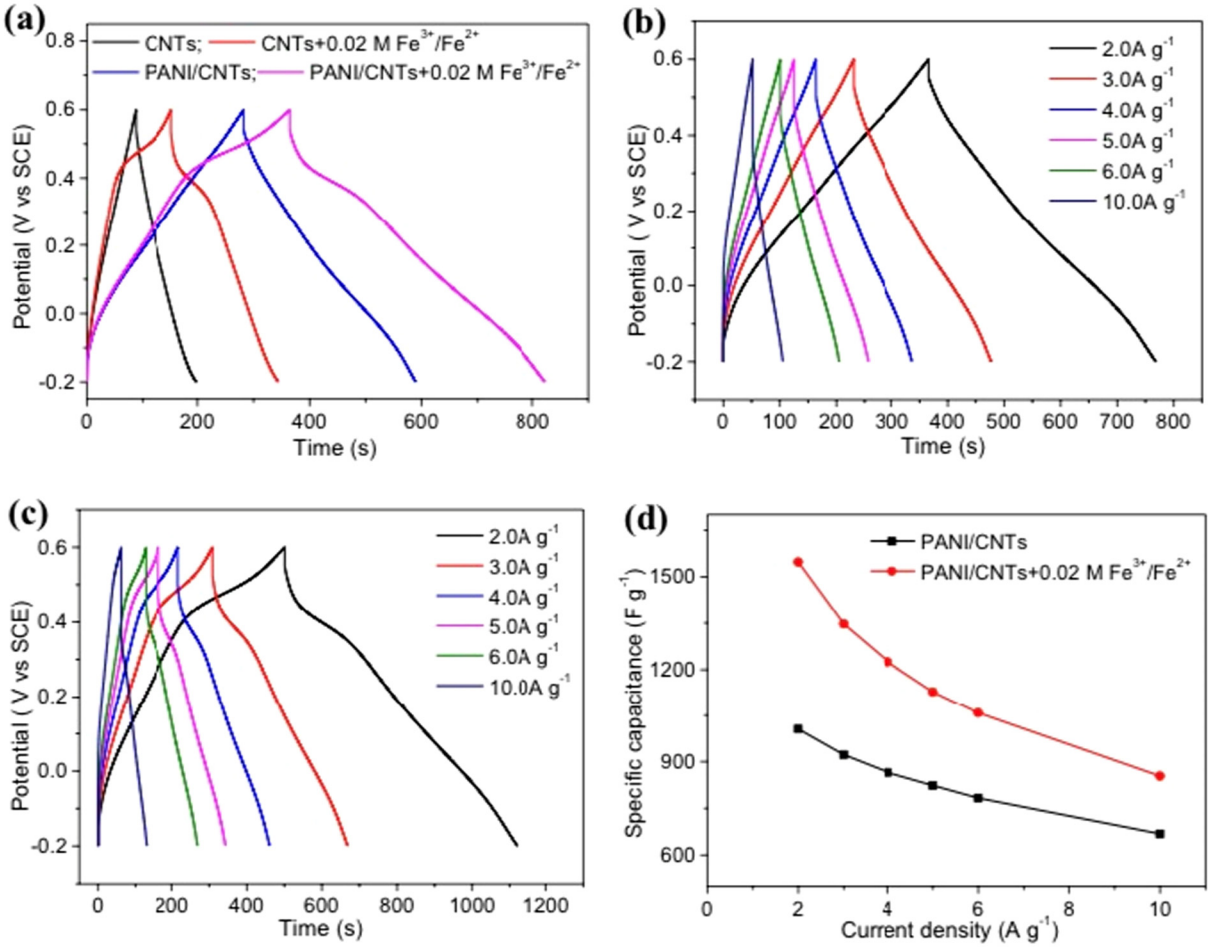

Fig. 41 (a) GCD curves of CNTs and PANI/CNTs at 1.5 mA cm^{-2} in 1 M H_2SO_4 with and without the addition of 0.02 M Fe^{3+}/Fe^{2+}. (b) GCD curves of PANI/CNTs testing in 1 M H_2SO_4 electrolyte at different current densities. (c) GCD curves of PANI/CNTs testing in 1 M H_2SO_4/0.02 M Fe^{3+}/Fe^{2+} electrolyte at different current densities. (d) Specific capacitance curves of PANI/CNTs at different current densities.[606] Reproduced with permission from Springer.

and a capacitive retention of 86.2% (5000 cycles) compared with $NiCo_2S_4$/CF due to the availability of the more electrochemically active sites and faster ionic diffusion. The excellent cycling stability of $NiCo_2S_4$@PANI/CF was suggested to be induced by the presence of the PANI shell. The assembled asymmetric supercapacitor (positive electrode: $NiCo_2S_4$@PANI/CF, negative electrode: graphene/CF) delivered a high energy density of 64.92 Wh kg^{-1} at a power density of 276.23 W kg^{-1}. This was found to be significantly higher compared with the asymmetric and symmetric supercapacitors based on $NiCo_2S_4$ and was ascribed to the core/shell heterostructure of $NiCo_2S_4$@PANI/CF.

Pan *et al.*[608] displayed more surface capacitive contribution and enhanced electrochemical performance benefiting from the unique heterostructure in $NiCo_2O$@Polyaniline nanotubes anchored on carbon. Their finding showed a specific capacitance of 720.5 C g^{-1} at 1 A g^{-1}, found to be much better than that of $NiCo_2O_4$. In addition, cycling performance and coulombic efficiency was also investigated for the $NiCo_2O_4$@PANI electrode. These findings showed the sample retaining 99.64% of its initial gravimetric capacity following 10 000 cycles with 100% coulombic efficiency due to the high efficiency of rapid electron transfer for charge storage and delivery. They also suggested that unique coaxial structure of $NiCo_2O_4$@Polyaniline increases the interface area of the electrode/electrolyte and facilitates a shorter diffusion path for ions and electrons.

Mu *et al.*[609] used polystyrene sulfonate microspheres as a template to fabricate graphene/polyaniline hybrid hollow microspheres in two steps involving the layer-by layer assembly technique followed by *in situ* oxidative chemical polymerization. Subsequent studies have indicated a specific capacitance of graphene/polyaniline hybrid hollow microspheres of ~633 F g^{-1} in a 1.0 M H_2SO_4 electrolyte as well as excellent cycling stability (with 92%) of its original specific capacitance, in all probability due to the synergistic effect. Alternatively, the contribution of the unique structure facilitating the reduced transport lengths for both mass and charge transport also cannot be ruled out. The energy density has also been calcu-

lated and found to be 382.97 Wh kg^{-1} at a current density of 10 mA cm^{-2}.

In another study, the hierarchical polyaniline/NiCo-layered double hydroxide (PANI/NiCo-LDH) core–shell composite nanofiber network was prepared by a two-step strategy (*in situ* oxidative polymerization and electrochemical deposition) on carbon cloth.[610] The choice of a LDH nanosheet shell grown on the PANI network in this work was guided by the role it plays in facilitating ion and electron transport and also in relieving the strain change of the electrode during redox reaction. The electrode fabricated in this manner delivered a specific capacitance of 1845 F g^{-1} at 0.5 A g^{-1} and excellent cycling stability (82% after 5000 cycles at 10.0 A g^{-1}), benefiting from rapid electron transport and ion diffusion. In addition, the assembled asymmetric device (positive electrode: PANI/NiCo-LDH, negative electrode: activated carbon) displayed excellent energy density (46.0 Wh kg^{-1}) at a power density of 351.6 W kg^{-1} and good cycling performance. Polyaniline/graphene nanosheets,[611] $Co(OH)_2$–polyaniline,[612] polyaniline/$NiCo_2S_4$,[613] carbon nanotube@polypyrrole core–shell,[614,615] and a Janus-type α-Fe_2O_3/PEDOT nanoparticles core/shell[616] also functioned as high-performance supercapacitive electrode materials.

5.4.4.2 Ternary and quaternary core–shell ICP nanocomposites. Vellakkat and Hundekkal[617] reported the formation of a chitosan-mediated synthesis of core/double shell ternary polyaniline/chitosan/cobalt oxide nano composite for their application as a high energy storage electrode material in supercapacitors. In another study, *in situ* chemically prepared polyaniline film-wrapped Ag-decorated MnO_2 nanorod (PANI/Ag@MnO_2) showed a specific capacitance of 1028.66 F g^{-1} at a current density of 1 A g^{-1} synergistically.[618] Furthermore, the assembled asymmetric supercapacitor (PANI/Ag@MnO_2//AC) device in 1 M H_2SO_4 displayed high energy density (49.77 Wh kg^{-1}) at a power density of 1599.75 W kg^{-1}. According to Iqbal *et al.*,[619] a ternary composite comprising porous Polyaniline@CNT-MnO_2 nanorods prepared by a hydrothermal method and *in situ* oxidative polymerization of aniline in 0.1 M KOH electrolyte achieved specific capacity, cycle life, energy density and power density of 143.26 C g^{-1}at 3 mV s^{-1}, 119% (3500 cycles) at 0.3 A g^{-1}, 27.17 Wh kg^{-1} and 298 W kg^{-1}, respectively. MWCNT@MnO_2@PPy supercapacitor electrodes attained specific capacitance of 272.7 F g^{-1} and reasonable cycling performance.[620] Ho *et al.*[621] synthesized a PPy/multilayer graphene-wrapped copper nanoparticles (MLG-Cu NPs) composite by a two-step process on a flexible carbon cloth substrate. This displayed excellent specific capacitance performance (845.38 F g^{-1}) at the current density of 1 A g^{-1}.

Moreno *et al.*[622] recorded the cyclic voltammetry (CV) of vertically aligned ZnO@CuS@PEDOT core@shell nanorod arrays decorated with MnO_2 nanoparticles at different scan rates in 1 M $LiClO_4$ aqueous electrolyte. The appearance of a more-or-less quasi-rectangular with symmetric shape of CV indicated the fast reversible reaction and an ideal capacitor-type behaviour. Furthermore, ZnO@CuS@PEDOT exhibited excellent electrochemical performance, as evident from its high specific areal capacitance of 19.85 mF cm^{-2}, good rate capability and cycling stability. This promising capacitive behavior was attributed to the unique hierarchical core–shell hybrid nanorod configuration and synergistic effects. A core@shell hollow Bi_2O_{3-x}@Carbon fiber@PEDOT electrode fabricated through a multistep process exhibited specific capacitance of 460 F g^{-1} (1 A g^{-1}) and reasonably good cycling stability.[623] It was also noted that energy density, power density and remarkable cycling performance in the assembled symmetric supercapacitor corresponded to 16.4 Wh kg^{-1}, 500.34 W kg^{-1} and 99% capacitance retention after 8500 cycles.

The coaxial core–sheath shaped supercapacitor based on polypyrrole-functionalized graphene/carbon nanotubes hollow fibers exhibited ultrahigh length specific capacitance and energy density.[624] According to Ghosh *et al.*,[625] an asymmetric supercapacitor comprising 3-D urchin shaped coaxial MnO_2@PANI composite and a self-assembled 3-D pillared graphene foam exhibited an energy density of 37 Wh kg^{-1} at a power density of 386 W kg^{-1} and stable cycling performance. In another report, graphene carbon sphere@PANI@RGO composites reached specific capacitance of 446.19 F g^{-1} (scan rate: 5 mV s^{-1}) in 1 M H_2SO_4 solution with 93.4% capacitance retentions after 1000 cycles.[626] Wang *et al.*[627] prepared a core–shell MoS_2/PPy/PANI ternary hybrid with a 'pizza-like' nanostructure. It achieved a high specific capacitance (1273 F g^{-1} at 0.5 A g^{-1}) with good cycling performance (83% after 3000 charge/discharge cycles). This was ascribed to the synergistic effect, improved electrical conductivity and enhanced electrolyte/electrode interaction. Recently, Liu *et al.*[628] synthesized poly(3,4-propylenedioxythiophene)-OH/CoNi-SeS@Hollow carbon sphere *via* a sulfurization/selenization ion exchange method and *in situ* oxidation, and showed excellent electrochemical performance (mass specific capacity: 775.1 C g^{-1} at 1 A g^{-1}). The assembled asymmetric supercapacitor device possessed a good energy density (84.8 Wh kg^{-1}) and excellent power density (8000 W kg^{-1}), and the capacity retention rate of 82.85% at 4 A g^{-1} (after 20 000 cycles). It was suggested that a synergistic effect of the conductive polymer, the hollow structure, and modified electronic structure contributed to achieving the better capacitance performance.

Polypyrrole-coated low-crystallinity Fe_2O_3 supported on carbon cloth,[321] graphene/polyaniline/MnO_2,[322] GO/α-MnO_2/PANI,[323] $(CoCrFeMnNi)_3O_4$@CC-PPy,[324] $LaMnO_3$@CC-PPy,[325] PPy/black phosphorus oxide/CNT,[326] PANI/GO/$CuFe_2O_4$[629] and PANI-coated CuO–ZnO–MnO[630] have also been investigated as electrodes for their supercapacitor performance.

Table 6 shows the electrochemical performance of various supercapacitors fabricated based on polyaniline electroactive material.

6. Future scope and perspectives

Conducting polymers, in spite of promising cost-effectiveness and tunable properties, have certain limitations such as lower conductivity compared with metals, and poor mechanical

Table 6 Preparative methods and electrochemical performance of hollow ICPs, hollow ICP composites and ICP-core–shell materials in supercapacitor applications

Electrode material	Method of preparation	Electrolyte	Specific capacitance (current density)	Cycling stability	Energy density (ED)	Power density (PD)	Ref.
$Ppy_{1\%}/DBSA_{2\%}/NiO_{97\%}$-GS	Electrodeposition at 4 mA cm^{-2} for 10 min	0.1 M $LiClO_4$	679 at 1 A g^{-1}	83.9% (1000 cycle) at 1 A g^{-1}	94.4 Wh kg^{-1}	94.4 W kg^{-1}	154
MnO_2@PPy	Hard template (PS) method.	1 M Na_2SO_4	295 F g^{-1} at of 1 A g^{-1}	100% (20 000 cycles) 10 A g^{-1}	42 Wh kg^{-1}	1100 W kg^{-1}	239
Core–shell nanorod arrays with PANI deposited into $NiCo_2O_4$	Electrochemical polymerization	1 M H_2SO_4	901 F g^{-1} at1 A g^{-1}	91% (3000 cycles) at 10 A g^{-1}	81.77 Wh kg^{-1} at a PD of 399.3 W kg^{-1}	—	320
D-Fe_2O_3@PPy/CC	Chemical reduction and electrodeposition methods	1 M Na_2SO	640 F g^{-1} at 1 mA cm-1	79.3% of its (10 mA cm-2) after 5000 cycles	—	—	321
$(CoCrFeMnNi)_3O_4$@CC-PPy	Two-step electrodeposition	2 M H_2SO_4	791 F g^{-1} at 0.5 A g^{-1}	63% (5000 cycles) at 10 A g^{-1}	49.2 Wh kg^{-1} (PD: 800 W kg^{-1})	—	324
$LaMnO_3$@CC-PPy	Two-step electrodeposition		862 F g^{-1} at 1 A g^{-1}	66% (3000 cycles) at 10 A g^{-1}	73 Wh k^{-1}	—	325
Hollow polyaniline helical nanobelts	By chemical oxidation of aniline	—	688 F g^{-1} at 5 mV s^{-1}	81.6% (1000 cycles)	14.37 Wh kg^{-1} at PD of 500 W kg^{-1}	—	492
Hollow polyaniline microspheres	*In situ* chemical oxidative polymerization with SPS spheres as the template	1 M H_2SO_4	421 F g^{-1}	45% (500 cycles) at 10 mA cm^{-2}	—	—	552
Hollow polyaniline nanocapsules	Interfacial polymerization method	1 M H_2SO_4	502 F g^{-1} at 5 mA cm^{-2}	83.1% (1000 cycles) at 10 mA cm^{-2}	—	—	553
Ce^{3+}-doped polyaniline hollow microspheres	Self-assembly method	H_2SO_4	248.2 F g^{-1} at 1 mA cm^{-2}	41.6% (5000 cycles) at 5 mA cm^{-2}	—	—	555
Hollow polyaniline nanospheres	Self-sacrificial templates and emulsion polymerization	1 M HCl	485.5 F g^{-1} at 1 A g^{-1}	69% (500 cycles) at 5 A g^{-1}	—	—	556
Polypyrrole hollow nanospheres	Hard template method	1 M H_2SO_4	350 at 1A g^{-1}	—	40 Wh kg^{-1}	490 W kg^{-1}	557
Hollow polypyrrole films	Electrochemical oxidative polymerization of pyrrole		~300 F g^{-1} at 3 A g^{-1}	No decrease in capacitance (1000)	—	—	558
Hollow capsular polypyrrole nanofiber	Vapor-phase polymerization	1 M H_2SO_4	203 F g^{-1} at 2 mV sec^{-1}	>90% (11 000 cycles) at 10 A g^{-1}	—	—	559
Nanotubular-polyaniline	Using natural tubular halloysite as hard template	1 M H_2SO_4	654 F g^{-1} at 1 A g^{-1}	120% (until 2000 cycles) and 87% (10 000) at 100 mV s^{-1}	—	—	560
Polyaniline nanotube arrays	Electrochemical polymerization using ZnO nanorod arrays as sacrificial templates	1 M H_2SO_4	675 F g^{-1} at 50 mV sec^{-1}	Decrease in ~30% of Csp value (100) at 50 mV s^{-1}	—	—	561
Polyaniline nanotubes (inner dia: 80 nm, outer dia: 180 nm)	One-step polymerization and acrylic acid in aqueous solution	1 mol L^{-1} H_2SO_4	436 F g^{-1} at 0.5 A g^{-1}	89.2% (500 cycles) at 0.5 A g^{-1}	—	—	563
Crystalline tetragonal hollow PANI nanotubes	MO (self-sacrificial template) in acidic solutions to facilitate the growth of PANI nanotubes	1 mol L^{-1} H_2SO_4	~590 ± 36 1 F g^{-1} at 5 mV s^{-1}	Capacitance loss of 49.6% (1000 cycles) at 10 A g^{-1}	14.56 Wh kg^{-1} at PD of 250 W kg^{-1}	—	564
PPy hollow nanoparticles	Surfactant-templated chemical oxidation polymerization	1 M Na_2SO_4	326 F g^{-1} at A g^{-1}	86% (10 000 cycles)	—	—	565
Hollow polyaniline nanofiber	Chemical oxidation polymerization	1 M H_2SO_4	290 F g^{-1} at 1 A g^{-1}	83% (1000 cycles) at 3 A g^{-1}	—	—	568
MnO_2/polyaniline hollow sphere	Interfacial synthesis	0.5 M Na_2SO_4	262 F g^{-1} at 1.5 mA cm^{-1}	93% (800 cycles) at 9 mA cm^{-1}	—	—	570
3D-hollow balls of graphene-polyaniline	Self-assembly method	1 M H_2SO_4	331 F g^{-1} at 1 A g^{-1}	14% loss of capacitance (500 cycles) at 1 A g^{-1}	—	—	571

Table 6 *(Contd.)*

Electrode material	Method of preparation	Electrolyte	Specific capacitance (current density)	Cycling stability	Energy density (ED)	Power density (PD)	Ref.
3D-graphene–polyaniline hybrid hollow spheres	Layer-by-layer assembly	1 M H_2SO_4	381 F g^{-1} at 4.0 A g^{-1}	83% (1000 cycles) at 0.5A g^{-1}	—	—	572
Hollow polyaniline nanotubes supported on Ti_3C_2 MXene	By exfoliating Ti_3C_2 followed by *in situ* polymerization	1 M H_2SO_4	596.6 F g^{-1} at 0.1 A g^{-1}	94.7% (5000 cycles) at 1 A g^{-1}	25.6 Wh kg^{-1} at PD of 153.2 W kg^{-1}	1610 Wkg^{-1} at ED of 13.2 Wh kg^{-1}	573
RGO/polyaniline nanotubes	*In situ* reduction	1 M-H_2SO_4	Unirradiated: 448 F g^{-1} at 0.5 A g^{-1}	Unirradiated: 89% (1000)	Unirradiated: 30.52 Wh kg^{-1}	Unirradiated: 174.96 W kg^{-1}	574
RGO/polyaniline nanotubes	*In situ* reduction	1 M-H_2SO_4	Irradiated: 482 F g^{-1} at 0.5 A g^{-1}	Irradiated: 92% (1000 cycles)	Irradiated: 32.81 Wh kg^{-1}	Irradiated: 174.98 W kg^{-1}	574
Graphene–polypyrrole hollow sphere	Pickering emulsion polymerization	1 M H_2SO_4	238 F g^{-1} at 1 A g^{-1}	90.7% (1500 cycles) at 1 A g^{-1}	—	—	576
N-doped graphene (NG)/hollow PPy	Hollow PPy nanospheres prepared by using a sacrificial template and embedded in NG layers	1 M HCl	575 F g^{-1} at a current density of 1 A g^{-1}	90.1 (500 cycles) at 1 A $g^{-1.}$	47.92 Wh kg^{-1} at 1 A g^{-1}	—	577
Polyaniline hollow nanospheres encaging RuO_2 nanoparticles	Polymerizing aniline monomers on 3D-arrayed PS nanospheres	1.0 M aqueous $HClO_4$	1570 F g^{-1} at 10 mV s^{-1}	77.6% (1000 cycles) at 10 mV s^{-1}	—	—	578
Polyaniline hollow fibers (PANI-HF)	*In situ* polymerization of aniline in the presence of electrospun PAN nanofibers	1 M H_2SO_4	425 F g^{-1} at 20 mV s^{-1}	72% (500 cycles) at 100 mV s^{-1}	—	—	579
PANI-hollow fiber decorated by RGO	Self-assembling of GO sheets on PANI-HF followed by electrochemical reduction of GO	1 M H_2SO_4	449 F g^{-1} at 20 mV s^{-1}	91% (500 cycles) at 100 mV s^{-1}	—	—	579
Graphene–polypyrrole nanotube	Multi steps	2 M H_2SO_4 aqueous solution	324 F g^{-1} at 1.5 A g^{-1}	88% (200 cycles) at 1.5 A g^{-1}	—	—	580
MOF-PPy tubes (mass ratio % of PPy : 28)	Dispersion and mixing method	1 M Na_2SO_4	554.4 F g^{-1} at 0.5 A g^{-1}	90.7% (10 000 cycles) at 20 A g^{-1}	0.0113 mW h cm^{-2} with PD of 0.12 mW cm^{-2}	—	581
Hollow PPy nanospheres decorated on CNTs	*Via in situ* chem. oxid. emulsion interfacial polymerization	1.0 M aqueous $NaNO_3$	33.9 F g^{-1} at 20 mV s^{-1}	71% (500 cycles)	—	—	582
Polyaniline nanowires wrapped on the polypyrrole nanotubes	Chemical synthesis method	1 M H_2SO_4	765 F g^{-1} at a scan rate of 10 mV s^{-1}	86.3% (1000 cycles) at 10 mV s^{-1}	—	—	583
Core–shell polyaniline-functionalized carbon quantum dots (CQDs)	*Via* adsorption of CQDs on PANI to be produced PANI	1 M H_2SO_4	264.6 F g^{-1} at 2.5 A g^{-1}	High stability (5000 cycles)	—	—	584
PPy@PANI nanosphere	By dilute solution polymerization	H_2SO_4	510 F g^{-1} at 10 mV s^{-1}	87.6% (1000 cycles) at 5 A g^{-1}	—	—	585
Polypyrrole@poly(1,5-diaminoanthraquinone)	Dispersion and sonication	1.0 M H_2SO_4	533 F g^{-1} at 1 A g^{-1}	107.4% (10 000 cycles) at 100 mV s^{-1} .	7.5 Wh kg^{-1} (at a PD of 96.1 W kg^{-1})	1124.9 W kg^{-1} (at ED of 4.0 Wh kg^{-1})	586
Graphene-wrapped polyaniline hollow spheres	Solution-based coassembly process	1 M H_2SO_4	614 F g^{-1} at 1 A g^{-1}	90% (500 cycles) 1 A g^{-1}	—	—	587
Carbon layer-encapsulated polyaniline nanotubes	*In situ* polymerization + hydrothermal method	1 M H_2SO_4	410.5 F g^{-1} at 1 A g^{-1}	63% (2000 cycles)	42.32 Wh kg^{-1}	16.44 kW kg^{-1}	588
Polyaniline/nickel oxide core/shell	*In situ* polymerization in the presence of NiO nanoparticles	1 M H_2SO_4	372 F g^{-1} at 20 mV s^{-1}	—	50.2 Wh Kg^{-1} at 1 Ag^{-1}	0.50 kW Kg^{-1} at 1 Ag^{-1}	589
Core–shell nanospherical polypyrrole/graphene oxide	*In situ* surface-initiated polymerization method	1.0 M H_2SO_4	370 F g^{-1} at 0.5 A g^{-1}	91.2% (4000 cycles)	—	—	590

Table 6 *(Contd.)*

Electrode material	Method of preparation	Electrolyte	Specific capacitance (current density)	Cycling stability	Energy density (ED)	Power density (PD)	Ref.
MoS_2@PANI (wt% of MoS_2 in: 71.2% for sample react 24 h)	Chemical polymerization	0.5 M H_2SO_4	669 F g^{-1} at 1 A g^{-1}	91% (4000 cycles) at 10 A g^{-1}	106 Wh kg^{-1} at a power density of 106 kW kg^{-1}	—	592
MoS_2@Polyaniline (with 25 wt% MoS_2)	One-pot hydrothermal method, energy density was 25.7 Wh kg	1 M H_2SO_4	645 F g^{-1} at 0.5 A g^{-1}	89% (2000 cycles) at 10 A g^{-1}	25.7 Wh kg^{-1} at PD of 779.9 W kg^{-1}	—	593
Hollow MoS_2/PANI core/shell microsphere	*In situ* oxidative polymerization	1 M H_2SO_4	633 F g^{-1} at 0.5 A g^{-1}	86.0% (1000 cycles) at 10 A g^{-1}	31.7 W h kg^{-1} at 0.3 kW kg^{-1}	—	594
MoS_2/polyaniline hollow microsphere	Template-assisted method	1 M H_2SO_4	364 F g^{-1} at a scan rate of 5 mV s^{-1}	84.3% (8000 cycles) at 10 A g^{-1}	32 Wh kg^{-1} at PD of 320 W kg^{-1}	—	595
Mechanically exfoliated MoS_2 sheet coupled with polyaniline	*In situ* chemical oxidative polymerization	KOH	510.12 F g^{-1} at 1 A g^{-1}	~80% (2500 cycles)	—	—	596
PEDOT@MoS_2	Electrochemical co-deposition of EDOT and MoS_2	1 M H $_2SO_4$	2540 mF cm^{-2} at 1 mA cm^{-2}	98.5% (5000 cycles) at 100 mA cm^{-2}	937 Wh m^{-2} at PD of 6500 W m^{-2}	—	597
V_2O_5@Polypyrrole (V_2O_5 Sol : Pyrrole : SDBS = 40 ml : 0.1 ml : 20 mg)	Sol–gel with *in situ* polymerization method	1 M Na_2SO_4	307 F g^{-1} at 1 A g^{-1}	~60% (2000 cycles) at 3 A g^{-1}	37 Wh Kg^{-1} at PD of 161 W kg^{-1}	—	598
3D core–shell pistil-like $MnCo_2O_4$/polyaniline	Electrochemical deposition polymerization	2 M KOH	1098 F g^{-1} at 1 A g^{-1}	83.2% (5000 cycles) at 10 A g^{-1}	—	—	600
Nickel ferrite/polypyrrole core–shell	*In situ* chemical oxidation containing sodium dodecyl sulfate	0.1 N H_2SO_4	721.66 F g^{-1} at 1 A g^{-1}	No significant change (1–1000 cycles)	51.95 Wh kg^{-1}	6.18 kW kg^{-1}	602
Core/sheath-structured ultralong MnO_x/polypyrrole nanowires	*In situ* polymerization	1.0 M Na_2SO_4	1091.4 F g^{-1} at 1 A g^{-1}	97.4% (10 000 cycles) at 10 A g^{-1}	144 Wh kg^{-1} at PD of 1100 W kg^{-1}	—	603
CuS@Polyaniline microspheres	Chemical oxidative polymerization	Li_2SO_4	308.1 F g^{-1} at 0.5 A g^{-1}	71.6% (1000 cycles) at 1 A g^{-1}	——	—	604
Polyaniline/CNT core–shell	Chemical vapor deposition and electrochemical deposition	1 M H_2SO_4 electrolyte	823 F g^{-1} at 5.0 A g^{-1}	—	22.9 Wh kg^{-1} at PD of 700.1 W kg^{-1}	—	606
Hierarchical $NiCo_2S_4$@Polyaniline grown on carbon fiber	Hydrothermal method and potentiostatic deposition	6 M KOH	1823 F g^{-1} at 2 mA cm^{-2}	86.2% (5000 cycles)	64.92 Wh kg^{-1} at PD of 276.23 W kg^{-1}	—	607
$NiCo_2O_4$@PANI nanotubes anchored on C	Electrodeposition method	—	720.5 C g^{-1} at 1 A g^{-1}	99.64% (10 000 cycles)	—	—	608
Graphene/polyaniline hybrid hollow microspheres	Combination of layer-by layer assembly and *in situ* chemical oxidative polymerization	1.0 M H_2SO_4	633 F g^{-1} at 10 mA cm^{-2}	92% (1000 cycles) at at 80 mV s^{-1}	382.97 Wh kg^{-1} at 10 mA cm^{-2}	—	609
PANI/NiCo-LDH core–shell composite	Electrochemical deposition method	2.0 M KOH	1845 F g^{-1} at 0.5 A g^{-1}	82% (5000 cycles) at 0.5 A g^{-1}	46.0 Wh kg^{-1} at PD of 351.6 W kg^{-1}	—	610
Graphene nanosheets coating with polyaniline	*In situ* polymerization	6 M KOH	261.4 F g^{-1} at 100 mA g^{-1}	Capacitance decreased to 161.2 F g^{-1} after 500 cycles at 0.1 A g^{-1}	—	—	611
Polyaniline-coated $NiCo_2S_4$	Chemical oxidative polymerization	PVA-KOH gel	1879 F g^{-1} at 1 A g^{-1}	91.1% (2000 cycles) at 8 A g^{-1}	54.06 Wh kg^{-1} at PD of 0.79 kW kg^{-1}	27.1 Kw kg^{-1} at ED of 15.9 Wh kg^{-1}	613
Hierarchical core/shell Janus-type a-Fe_2O_3/PEDOT	Multistep process	PVA–H_2SO_4 Hydrogel	252.8 F g^{-1} at 0.1 A g^{-1}	92% (1000) at 0.6 A g^{-1}	136.3 Wh kg^{-1}	10 526 W kg^{-1}	616
Core/double shell PANI/chitosan/cobalt oxide	*In situ* chemical oxidation method	1 M H_2SO_4	1253 F g^{-1} at 5 mV s^{-1}	91% (5000) at of 1 A g^{-1}	95.42 Wh kg^{-1} at 1 A g^{-1}	1549 W kg^{-1} at 3 A g^{-1}	617
Polyaniline-Ag-MnO_2 nanorod	Two-step process	2 M KOH	1028.6 F g^{-1} at 1 A g^{-1}	93.7% (5000 cycles) at 10 A g^{-1}	49.77 Wh kg^{-1}	1599.75 W kg^{-1}	618

Table 6 *(Contd.)*

Electrode material	Method of preparation	Electrolyte	Specific capacitance (current density)	Cycling stability	Energy density (ED)	Power density (PD)	Ref.
Polyaniline@CNTs–MnO_2	Hydrothermal and *in situ* oxidative polymerization of aniline	0.1 M KOH	143.26 C g^{-1} at 3 mV s^{-1}	119% (3500 cycles) at 3.0 A g^{-1}	27.17 Wh kg^{-1} at 0.3 A g^{-1}	298.00 W kg^{-1} at 0.3 A g^{-1}	619
MWCNTs@MnO_2@Polypyrrole	Multiple steps	—	272.7 F g^{-1}	60% after 300 cycles	—	—	620
ZnO NRs@CuS@PEDOT@MnO_2	Multiple steps	1 M $LiClO_4$	19.85 mF cm^{-2} at 5 mV s^{-1}	18% loss of initial value (1500) at 100 mV s^{-1}	—	—	622
Hollow Bi_2O_3@Carbon fibre@PEDOT	Electrospinning technique using stabilization, pyrolyzation and polymerization	PVA-KOH g	460 F g^{-1} at 1 A g^{-1}	93.6% (10 000 cycles) at 2 A g^{-1}	16.4 Wh kg^{-1}	500.34 W kg^{-1}	623
Hierarchical graphene/polyaniline hollow microsphere	Multiple steps	1 M H_2SO_4	446.19 F g^{-1} at 5 mV s^{-1}	93.4% (1000 cycles) at 2 A g^{-1}, 8.7% (5000 cycles) at 2 A g^{-1}	—	—	626
"Pizza-like" MoS_2/polypyrrole/polyaniline architecture	Multistep process	0.5 m H_2SO_4	1273 F^{-1} g at 0.5 A g^{-1}	~83% (3000 cycles) at 2 A g^{-1}	—	—	627

strength, processability, solubility and environmental stability remain the key issues to be addressed in their high-demand applications.[1,2] These challenges are very critical to future ongoing research in order to harness the full potential of conducting polymers in different applications. Furthermore, advancements through innovative synthesis methods including new materials compositions and material design are likely to play key roles in developing scalable and cost-effective hollow conducting polymers, their nanocomposites and core–shell materials with significantly enhanced performance in their applications in electrical/environmental remediation and energy storage devices. Recently, research is also emerging on the electrodeposition technique as a promising approach for developing effective electrode materials in supercapacitor applications.[154,321–325] In this regard, the unique insight gained by focusing exclusively on hollow and core–shell morphologies in the present review article across the three distinct applications (EMI shielding, adsorption, supercapacitors) complements the existing literature.

Electromagnetic interference creates electronic pollution that is very harmful to human health and the functioning of electronic devices and remains a critical challenge for researchers.[9] The practical application of electromagnetic interference/microwave absorption materials is limited by complex synthetic procedures and expensive raw materials. In this regard, lightweight hollow ICPs and their binary and ternary composites and core–shell structured materials are reported in trapping/absorbing electromagnetic waves to enhance dielectric loss, multiple internal reflection, and scattering of EM waves.[9] However, challenges require researchers to develop thermally and mechanically stable hollow-structured ICPs, their composites, and core–shell-based materials with superior electrical conductivity, dielectric/magnetic, and corrosion-resistance properties, for applicability to a wide range of frequencies and absorption bandwidth.[54] The conducting blends with simultaneously enhanced mechanical properties could also be interesting for future applications in EMI shielding and microwave absorption.[388]

The removal of heavy metals and organic dyes in wastewater remains a critical challenge for researchers.[84,88] In this regard, polyaniline and polypyrrole have attracted considerable attention as promising adsorbents in the separation of dyes and metal ions from wastewater. In view of this, hollow conducting polymers[60–64] and core–shell materials[66,67] hold great promise in the adsorptive removal of metal ions from wastewater due to their enhanced surface area, tunability, and potential for synergistic effects.[88] Challenges exist in developing low-cost, high-performing adsorbents with significantly enhanced activity and long-term stability for the separation of the mixture of individual dyes, metal ions, dye/metal ions and other types of pollutants present in wastewater. Furthermore, regeneration of the spent adsorbents is still challenging and needs more attention in developing cost-effective regeneration methods for their reusability with high economic viability and environmental sustainability.[631] Furthermore, safe disposal or reuse of spent/exhausted adsorbents also needs to be considered.

Hollow ICPs have emerged as a promising electrode material in supercapacitor applications. Their larger surface area and shorter ion diffusion path facilitate faster charging and discharging.[72,73] However, the future scope of hollow conducting polymers as an electrode material is limited due to their poor structural stability, which results in lower cyclability and capacity retention of the assembled supercapacitor.[632] This problem can be mitigated by fabricating nanocomposites by integrating different components, such as carbonaceous, metal oxides, metal chalcogenides, and MXene base materials through an inexpensive and facile synthesis approach. Attention is also focused on achieving enhanced mechanical stability of hollow ICPs to prevent degradation during repeated charging and discharging cycles. In addition, the fabrication of hollow copolymers of ICPs remains another area not well addressed so far.[633] In addition, core–shell nanostructured electrode materials fabricated by the coating of ICPs on a conducting core have been very promising due to the short ion transport pathways and abundant active sites. Recently, the electrodeposition method has also received more attention, though there exist several challenges in real-world applications.

Future research also needs to be focused on the development of new cost-effective synthetic core–shell methods. This can be realized by utilizing naturally driven green and sustainable biomass,[634] plant waste,[635] marine bio-waste,[636] marine plastic waste,[637] biomass waste,[638–642] cotton,[643] fly ash of coal waste[644] and agricultural by-products[645] as a source of carbon in realizing the fabrication of conducting polymer-coated core–shell materials across the three distinct application fields.

7. Summary and conclusion

The hollow conducting polymers (such as hollow microspheres, nanotubes, *etc.*) have attracted great attention for their wide and multifaceted applications guided by their properties. In this regard polyaniline and, to some extent polypyrrole, have received much attention owing to good processability, excellent environmental stability, and unique properties, such as controllable internal structures, low density, high surface areas, permeability including surfaces and interfaces, properties controllable by oxidation and protonation states, and their ability to exist in a number of intrinsic redox states. In view of this, the present article has dealt with the general methods reported on the preparation of conducting polymers and fabrication of hollow (PANI < PPy, PTh and PEDOT) structures and their mechanism. This was followed by a review of the synthetic strategies for the fabrication of their hollow morphologies, such as nanotubes, nanocapsules, nano and microspheres *etc.* by utilizing hard templates (Al_2O_3, SiO_2, polystyrene *etc.*), soft templates, sacrificial templates and template-free methods. The article further describes the formation of nanocomposites comprising hollow and core–shell structures of ICPs and their applications in the protection of the environment and harnessing of energy. The choice of hollow morphology of conducting polymers is considered a novel approach for the trapping of microwave radiation through enhanced internal reflection, and their remarkable performance has been reviewed. In addition, a review of hollow-structured conducting polymers has demonstrated their great structural advantages as efficient adsorbents in the removal of toxic metal ions and dyes present in waste water. The review finally concludes with future perspectives on hollow and core–shell ICPs for their application as microwave absorbers, adsorbents and electrode materials in the absorption of electromagnetic waves and removal of metals ions/dyes in wastewater. It is also anticipated that the present review will provide a significant inspiration to researchers working on hollow and core–shell ICP for their application several other fields.

Conflicts of interest

There are no conflict of interests to declare.

Data availability

No primary research results, software or code have been included and no new data were generated or analysed as part of this review.

Acknowledgements

The author, formerly a Professor in the Department of Chemistry at the Indian Institute of Technology (IIT) Kharagpur, remains very appreciative for making this effort possible and gratefully acknowledge. Author also thanks to his former research scholars Dr Ritwick Panigrahi, Dr. Kunal Manna, Dr Soumi Dutta and Dr Rakesh Manna for their valuable contributions in this field. Thanks are also extended to Professor Ashok Kumar Gupta, Dr Brahma Gupta, Mr Akash Rawat, Mr Adarsh Singh, Department of Civil Engneering, IIT Kharagpur, Dr. Tapas Kuila, Senior Principal Scientist and Mr Anjan Chakraorty, CSIR-Central Mechanical Engineering Research Institute, Durgapur, India for their assistance at various stages of preparing this article.

References

1 A. Varghese, K. R. P. Sunajadevi and D. Pinheiro, *Energy Adv.*, 2025, **4**, 743.
2 S. K. Srivastava, *Nanostructured Materials for Environmental Applications*, ed. S. Balakumar, V. Keller and M. V. Shankar, Springer, 2021, pp. 167–215.
3 M. B. Hasan, M. M. Parvez, A. Y. Abir and M. F. Ahmad, *Heliyon*, 2015, **11**, e42375.
4 H. H. Al-Refai, A. A. Ganash and M. A. Hussein, *Mater. Today Commun.*, 2021, **26**, 101935.

5 M. A. H. Bayan, F. A. Taromi, M. Lanzi and F. Pierini, *Sci. Rep.*, 2021, **11**, 21144.
6 H. Zhang, X. Wang, H. Ma and M. Xue, *Adv. Energy Sustainable Res.*, 2021, **2**, 2100088.
7 E. Dhandapani, S. Thangarasu, S. Ramesh, K. Ramesh, R. Vasudevan and N. Duraisamy, *J. Energy Storage*, 2022, **52**, 104937.
8 X. Gao, Y. Bao, Z. Chen, J. Lu, T. Su, L. Zhang and J. Ouyang, *Adv. Electron. Mater.*, 2023, **9**, 2300082.
9 S. K. Srivastava and K. Manna, *J. Mater. Chem. A*, 2022, **10**, 7431–7496.
10 C. Van Le and H. Yoon, *Int. J. Mol. Sci.*, 2024, **25**, 1564.
11 H. Kazim, M. Sabri, A. AlOthman and M. Tawalbeh, *Nano-Struct. Nano-Objects*, 2024, **40**, 101371.
12 T. Nezakati, A. Seifalian, A. Tan and A. M. Seifalian, *Chem. Rev.*, 2018, **118**, 6766–6843.
13 A. Puiggalí-Jou, L. J. del Valle and C. Alemán, *J. Controlled Release*, 2019, **309**, 244–264.
14 S. K. Srivastava, *RSC Appl. Interfaces*, 2024, **1**, 340–429.
15 J. Kumari, A. Singh, A. Rawat, S. K. Srivastava, A. K. Gupta and R.SC. Sustain, Submitted, 2025.
16 M. S. Tamboli, A. A. Gupta, H. S. Avchat, S. S. Bhosale and D. S. Shrikant, *Webology*, 2020, **17**, 761–771.
17 M. Ayad, G. El-Hefnawy and S. Zaghlol, *Chem. Eng. J.*, 2013, **217**, 460–465.
18 M. Aleahmad, H. G. Taleghani and H. Eisazadeh, *Asian J. Chem.*, 2010, **22**, 7353–7360.
19 Y. Gao, Z.-H. Kang, X. Li, X.-J. Cui and J. Gong, *CrystEngComm*, 2011, **13**, 3370–3372.
20 E. Saracino, S. Zuppolini, V. Guarino, V. Benfenati, A. Borriello, R. Zamboni and L. Ambrosio, *RSC Adv.*, 2021, **11**, 11347–11355.
21 K. Huang, Y. Zhang, Y. Long, J. Yuan, D. Han, Z. Wang, L. Niu and Z. Chen, *Chem. – Eur. J.*, 2006, **12**, 5314–5319.
22 M. M. Sk and C. Y. Yue, *J. Mater. Chem. A*, 2014, **2**, 2830.
23 S. Virji, J. X. Huang, R. B. Kaner and B. H. Weiller, *Nano Lett.*, 2004, **4**, 491–496.
24 E. Song and J.-W. Choi, *Nanomaterials*, 2013, **3**, 498–523.
25 G. Li, H. Peng, Y. Wang, Y. Qin, Z. Cui and Z. Zhang, *Macromol. Rapid Commun.*, 2004, **25**, 1611–1614.
26 J. Jang, J. Bae and K. Lee, *Polymer*, 2005, **46**, 3677–3684.
27 X.-G. Li, A. Li and M.-R. Huang, *Chem. – Eur. J.*, 2008, **14**, 10309–10317.
28 H. Wang and Y. Lu, *Synth. Met.*, 2012, **162**, 1369–1374.
29 Q. Zhang, W. Li, X. Liu, J. Ma, Y. Gu, R. Liu and J. Luo, *ACS Appl. Mater. Interfaces*, 2024, **16**, 1461–1473.
30 D. Zhang, X. Fan, X. Hao and G. Dong, *Ind. Eng. Chem. Res.*, 2019, **58**, 1906–1913.
31 H. Wang, Y. Liu, L. Kong, S. Yin, X. Shen and S. Premlatha, *Colloids Surf., A*, 2023, **665**, 131234.
32 M. Shi, Y. Zhang, M. Bai and B. Li, *Synth. Met.*, 2017, **233**, 74–78.
33 C. Yu, J. Zhai, X. Gao, M. Wan, L. Jiang, T. Li and Z. Li, *J. Phys. Chem. B*, 2004, **108**, 4586–4589.
34 B. Butoi, A. Groza, P. Dinca, A. Balan and V. Barna, *Polymers*, 2017, **9**, 732.
35 S. J. T. Rezaei, Y. Bide and M. R. Nabid, *Synth. Met.*, 2011, **161**, 1414–1419.
36 G. M. Neelgund and A. Oki, *Polym. Int.*, 2011, **60**, 1291–1295.
37 H.-W. Park, T. Kim, J. Huh, M. Kang, J. E. Lee and H. Yoon, *ACS Nano*, 2012, **6**, 7624–7633.
38 K. Namsheer, V. B. Reneesha and C. S. Rout, Synthesis and Morphology of Conducting Polymers, ACS Symposium Series, 2023, Vol. 1438, Ch. 2, pp. 9–27, DOI: 10.1021/bk-2023-1438.ch002.
39 L. Yu, X. Y. Yu and X. W. Lou, *Adv. Mater.*, 2018, **30**, 1800939.
40 L. Yu, H. Hu, H. B. Wu and X. W. Lou, *Adv. Mater.*, 2017, **29**, 1604563.
41 X. Wang, J. Feng, Y. Bai, Q. Zhang and Y. Yin, *Chem. Rev.*, 2016, **116**, 10983–11060.
42 P. Liu and L. Zhang, *Crit. Rev. Solid State Mater. Sci.*, 2009, **34**, 75–87.
43 Y. Xue, S. Chen, J. Yu, B. R. Bunes, Z. Xue, J. Xu, B. Lu and L. Zang, *J. Mater. Chem. C*, 2020, **8**, 10136–10159.
44 I. Hussain, S. Sahoo, M. S. Sayed, M. Ahmad, M. S. Javed, C. Lamiel, Y. Li, J.-J. Shim, X. Ma and K. Zhang, *Coord. Chem. Rev.*, 2022, **458**, 214429.
45 X. W.. Lou, L. A. Archer and Z. Yang, *Adv. Mater.*, 2008, **20**, 3987–4019.
46 K. An and T. Hyeon, *Nano Today*, 2009, **4**, 359–373.
47 M. Zhu, Y. Cheng, Q. Luo, M. El-khateeb and Q. Zhang, *Mater. Chem. Front.*, 2021, **5**, 2552–2587.
48 L. Yang, H. Xu, G. He and H. Chen, *Dalton Trans.*, 2022, **51**, 13559–13572.
49 J. Qi, X. Lai, J. Wang, H. Tang, H. Ren, Y. Yang, Q. Jin, L. Zhang, R. Yu, G. Ma, Z. Su, H. X. Zhao and D. Wang, *Chem. Soc. Rev.*, 2015, **44**, 6749–6773.
50 K. Zhang, K. Song and K. Clays, *Nanophotonics*, 2018, **7**, 693–671.
51 X. Zhu, J. Tang, H. Huang, T. Lin, B. Luo and L. Wang, *Sci. Bull.*, 2020, **65**, 496–512.
52 A. Venkataraman, E. V. Amadi, Y. Chen and C. Papadopoulos, *Nanoscale Res. Lett.*, 2019, **14**, 220.
53 G. Ma, Z. Wen, J. Jin, Y. Lu, X. Wu, M. Wu and C. Chen, *J. Mater. Chem. A*, 2014, **2**, 10350–10354.
54 C. Kuila, A. Maji, N. C. Murmu, T. Kuila and S. K. Srivastava, *Carbon*, 2023, **210**, 118075.
55 R. Manna, K. Ghosh and S. K. Srivastava, *Langmuir*, 2021, **37**, 7430–7441.
56 R. Manna and S. K. Srivastava, *ACS Omega*, 2021, **6**, 9164–9175.
57 D. Xu, M. Zhang, C. Wang, Z. Shen, M. Wang, J. Zhang, Z. Han, L. Li, X. Xiong and P. Chen, *Polymer*, 2025, **317**, 127900.
58 K. Manna and S. K. Srivastava, *J. Phys. Chem. C*, 2018, **122**, 19913–19920.
59 S. Kumari, J. Dalal, A. Kumar, R. Pal, R. Chahal and A. Ohlan, *RSC Adv.*, 2024, **14**, 662–676.
60 S. Senguttuvan, P. Senthilkumar, V. Janaki and S. Kamala-Kannan, *Chemosphere*, 2021, **267**, 129201.

61 E. N. Zare, A. Motahari and M. Sillanpää, *Environ. Res.*, 2018, **162**, 173–195.
62 P. Rana, B. Kaur, K. Poonia, V. Soni, P. Singh, S. Thakur, C.-W. Huang, V.-H. Nguyen and P. Raizada, *Inorg. Chem. Commun.*, 2025, **172**, 11365.
63 A. Taghizadeh, M. Taghizadeh, M. Jouyandeh, M. K. Yazdi, P. Zarrintaj, M. R. Saeb, E. C. Lima and V. K. Gupta, *J. Mol. Liq.*, 2020, **312**, 113447.
64 S. Dutta, *Fabrication od sustainable nano adsorbents in removal of toxic pollutants from contaminated water*, Ph. D Thesis, Indian Institute of Technology, Kharagpur, 2022.
65 X. Y. Lai, J. E. Halpert and D. Wang, *Energy Environ. Sci.*, 2012, **5**, 5604–5618.
66 C. F. Jones, L. Resina, F. C. Ferreira, P. Sanjuan-Alberte and T. Esteves, *J. Phys. Chem. C*, 2024, **128**, 11083–11100.
67 Y. Bhattacharjee and S. Bose, *ACS Appl. Nano Mater.*, 2021, **4**, 949–972.
68 M. K. Goswami, A. Srivastava, R. K. Dohare, A. K. Tiwari and A. Srivastav, *Environ. Sci. Pollut. Res.*, 2023, **30**, 73031–73060.
69 L. Wang, X. Li, X. Shi, M. Huang, X. Li, Q. Zeng and R. Che, *Nanoscale*, 2021, **13**, 2136.
70 L. Liu, S. Liu, L. Zhao, G. Su, X. Liu, H. Peng, J. Xue and A. Tang, *J. Mol. Liq.*, 2020, **313**, 113593.
71 A. Muhammad, A.-U. H. Ali Shah, S. Bilal and G. Rahman, *Materials*, 2019, **12**, 1764.
72 C. Xia, W. Chen, X. Wang, M. N. Hedhili, N. Wei and H. N. Alshareef, *Adv. Energy Mater.*, 2015, 1401805.
73 D. Khalafallah, D. E. E. Refaay, X. Gu, A. M. A. Henaish and Q. Zhang, *Energy Storage Mater.*, 2025, **78**, 104284.
74 N. Maruthi, M. Faisal and N. Raghavendra, *Synth. Met.*, 2021, **272**, 116664.
75 B. G. Soares, G. M. O. Barra and T. Indrusiak, *J. Compos. Sci.*, 2021, **5**, 173.
76 M. Zahid, R. Anum, S. Siddique, H. M. F. Shakir and Z. A. Rehan, *J. Thermoplast. Compos. Mater.*, 2021, **36**, 1717–1761.
77 X. Su, Y. Liu, Z. Liao, Y. Bi, M. Ma, Y. Chen, Y. Ma, F. Wan and K. L. Chung, *Synth. Met.*, 2022, **291**, 117190.
78 N. Biçer, I. T. Çelik and I. A. Kariper, *J. Ind. Text.*, 2022, **51**, 36S–64S.
79 A. Kausar and I. Ahmad, *J. Compos. Sci.*, 2023, **7**, 240.
80 J. Wang, Q. Sun, J. Li, Y. Guo, W. Tian, Y. Liu, B. Wu, L. Deng, N. Mahmood and X. Jian, *Mater. Today Phys.*, 2023, **31**, 100981.
81 H. Hajjaoui, A. Soufi, W. Boumya, M. Abdennouri and N. Barka, *J. Compos. Sci.*, 2021, **5**, 233.
82 A. Samadi, M. Xie, J. Li, H. Shon, C. Zheng and S. Zhao, *Chem. Eng. J.*, 2021, **418**, 129425.
83 S. Jadoun, J. P. Fuentes, B. F. merUrbano and J. Yáñez, *J. Environ. Chem. Eng.*, 2023, **11**, 109226.
84 A. Samadi, Z. Wang, S. Wang, S. K. Nataraj, L. Kong and S. Zhao, *Chem. Eng. J.*, 2023, **478**, 147506.
85 M. M. Talukder, M. M. R. Khan and M. K. Amin, *S. Afr. J. Chem. Eng.*, 2023, **44**, 276–282.
86 A.-N. Chowdhury, S. R. Jesmeen and M. M. Hossain, *Polym. Adv. Technol.*, 2004, **15**, 633–638.
87 A. Nasar and F. Mashkoor, *Environ. Sci. Pollut. Res. Int.*, 2019, **26**, 5333–5356.
88 S. Dutta, B. Gupta, S. K. Srivastava and A. K. Gupta, *Mater. Adv.*, 2021, **2**, 4497–4531.
89 R. Rehman, A. Raza, F. Yasmeen, A. Dar, Z. T. Al-thagaf and Z. Meraf, *Adsorpt. Sci. Technol.*, 2022, 7047832, DOI: 10.1155/2022/7047832.
90 J. Stejskal, *Polymers*, 2022, **14**, 4243.
91 K. M. Z. Hasan, N. A. Khan, M. Yoon and S. H. Jhung, *J. Ind. Eng., Chem.*, 2025, **152**, 330–339.
92 Y. Han and L. Dai, *Macromol. Chem. Phys.*, 2019, 1800355, DOI: 10.1002/macp.201800355.
93 L. Fu, Q. Qu, R. Holze, V. V. Kondratiev and Y. Wu, *J. Mater. Chem. A*, 2019, **7**, 14937–14970.
94 M. I. Ul Hoque and R. Holze, *Polymers*, 2023, **15**, 730.
95 S. Ahmed, A. Ahmed, D. B. Basha, S. Hussain, I. Uddin and M. A. Gondal, *Synth. Met.*, 2023, **295**, 117326.
96 M. G. Tadesse, A. S. Ahmmed and J. F. Lübben, *J. Compos. Sci.*, 2024, **8**, 53.
97 V. J. V. Vinayak, K. Deshmukh, V. R. K. Murthy and S. K. K. Pasha, *J. Energy Storage*, 2024, **100**, 113551.
98 O. B. Okafor, A. P. I. Popoola, O. M. Popoola and S. O. Adeosun, *Next Mater.*, 2025, **6**, 100389.
99 E. N. Zare, P. Makvandi, B. Ashtari, F. Rossi, A. Motahari and G. Perale, *J. Med. Chem.*, 2019, **63**, 1–22.
100 J. Cui, F.-F. Xing, H. Luo, J.-Q. Qin, Y. Li, Y. Zhong, F. Wei, J. Fu, C. Jing, J. Cheng, Z.-S. Wu and S. Liu, *J. Energy Chem.*, 2021, **62**, 145–152.
101 K. Z. Mousaabadi, A. A. Ensafi, R. Fazel-Zarandi and A. Vahabi, *J. Iran. Chem. Soc.*, 2024, **21**, 1769–1794.
102 T.-H. Le, Y. Kim and H. Yoon, *Polymers*, 2017, **9**, 150.
103 A. G. MacDiarmid, R. J. Mammone, R. B. Kaner, S. J. Porter, R. Pethig, A. J. Heeger; and D. R. Rosseinsky, *Philos. Trans. R. Soc., A*, 1985, **314**, 3–15.
104 J. V. Yakhmi, V. Saxena and D. K. Aswal, *Functional Materials Preparation, Processing and Applications*, Elsevier, 2012, pp. 61–110, DOI: 10.1016/B978-0-12-385142-0.00002-7.
105 A. K. Bakhshi, *Bull. Mater. Sci.*, 1995, **18**, 469–495.
106 P. C. Maity, M.Tech. Thesis, Indian Institute of Technology, Hyderabad, 2016. https://raiithold.iith.ac.in/2718/1/MS14METCH11003.pdf.
107 C.-C. Hung and T.-C. Wen, *J. Taiwan Inst. Chem. Eng.*, 2011, **42**, 371–376.
108 S. Qian, H. A. Lin, Q. Pan, S. Zhang, Y. Zhang, Z. Geng, Q. Wu, Y. He and B. Zhu, *Bioact. Mater.*, 2023, **26**, 24–51.
109 H. Tang, H. Cai, H. Zhao, Z. Liu, R. Tan and F. Huang, *CCS Chem.*, 2023, **5**, 2534–2544.
110 G. G. Wallace, G. M. Spinks, L. A. P. Kane-Maguire and P. R. Teasdale, *Conductive. Electroactive Polymers*, 3rd edn, CRC Press, 2008.
111 S. Goswami, S. Nandy, E. Fortunato and R. Martins, *J. Solid State Chem.*, 2023, **317**, 123679.

112 K. Namsheer and C. S. Rout, *RSC Adv.*, 2021, **11**, 5659–5697.
113 B. Qiu, J. Wang, Z. Li, X. Wang and X. Li, *Polymers*, 2020, **12**, 310.
114 S. P. Armes and J. F. Miller, *Synth. Met.*, 1988, **22**, 385–393.
115 J. Stejskal, A. Riede, D. Hlavatá, J. Prokeš, M. Helmstedt and P. Holler, *Synth. Met.*, 1998, **96**, 55–61.
116 R. Manna, *Functionalized Graphene Based Nanocomposites as Flexible Dielectric Materials and Microwave Absorber*, Ph. D Thesis, Indian Institute of Technology, Kharagpur, 2021.
117 J. Yang, Y. Ding, G. Chen and C. Li, *Eur. Polym. J*, 2007, **43**, 3337–3343.
118 S. Budi, Yusmaniar, A. Juliana, U. Cahyana, A. Purwanto, A. Imaduddin and E. Handoko, *IOP Conf. Ser.:J. Phys.: Conf. Ser.*, 2018, **983**, 012162, DOI: 10.1088/1742-6596/983/1/012162.
119 A. H. Majeed, L. A. Mohammed, O. G. Hammoodi, S. Sehgal, M. A. Alheety, K. K. Saxena, S. A. Dadoosh, I. K. Mohammed, M. M. Jasim and N. U. Salmaan, *Int. J. Polym. Sci.*, 2022, 9047554, DOI: 10.1155/2022/9047554.
120 J. Mahmood, N. Arsalani, S. Naghash-Hamed, Z. Hanif and K. E. Geckeler, *Sci. Rep.*, 2024, **14**, 11653.
121 J. C. Thieblemont, M. F. Planche, C. Petrescu, J. M. Bouvier and G. Bidan, *Synth. Met.*, 1993, **59**, 81–96.
122 Y. Sood, K. Singh, H. Mudila, P. E. Lokhande, L. Singh, D. Kumar, A. Kumar, N. M. Mubarak and M. H. Dehghani, *Heliyon*, 2024, **10**, e33643.
123 M. Omastová, J. Pionteck and M. Trchová, *Synth. Met.*, 2003, **135–136**, 437–438.
124 Y. Kudoh, *Synth. Met.*, 1996, **79**, 17–22.
125 Y. Kudoh, K. Akami and Y. Matsuya, *Synth. Met.*, 1998, **95**, 191–196.
126 A. Yussuf, M. Al-Saleh, S. Al-Enezi and G. Abraham, *Int. J. Polym. Sci.*, 2018, 4191747, DOI: 10.1155/2018/4191747.
127 Y. Tan and K. Ghandi, *Synth. Met.*, 2013, **175**, 183–191.
128 A. Kausaite-Minkstimiene, V. Mazeiko, A. Ramanaviciene and A. Ramanavicius, *Colloids Surf., A*, 2015, **483**, 224–231.
129 V. Bocchi, L. Chierici, G. P. Gardini and R. Mondelli, *Tetrahedron*, 1970, **26**, 4073–4082.
130 T. V. Vernitskaya and O. N. Efimov, *Russ. Chem. Rev.*, 1997, **66**, 443–457.
131 A. F. Diaz and J. Bargon, *Handbook of Conducting Polymers*, Marcel Dekker, NewYork, 1986.
132 T. P. Kaloni, P. K. Giesbrecht, G. Schreckenbach and M. S. Freund, *Chem. Mater.*, 2017, **29**(24), 10248–10283.
133 D. Thanasamy, D. Jesuraj, S. K. K. Kannan and V. Avadhanam, *Polymer*, 2019, **175**, 32–40.
134 M. Jaymand, M. Hatamzadeh and Y. Omidi, *Prog. Polym. Sci.*, 2015, **47**, 26–69.
135 S. Das, D. P. Chatterjee, R. Ghosh and A. K. Nandi, *RSC Adv.*, 2015, **5**, 20160.
136 S. Nie, Z. Li, Y. Yao and Y. Jin, *Front. Chem.*, 2021, **9**, 803509.
137 G. Heywang and F. Jonas, *Adv. Mater.*, 1992, **4**, 116–118, DOI: 10.1002/adma.19920040213.
138 Y. Jiang, T. Liu and Y. Zhou, *Adv. Funct. Mater.*, 2020, 2006213.
139 R. Corradi and S. Armes, *Synth. Met.*, 1997, **84**, 453–454.
140 N. Paradee and A. Sirivat, *Polym. Int.*, 2014, **63**, 106–113.
141 S. G. Im, D. Kusters, W. Choi, S. H. Baxamusa, M. C. M. Van de Sanden and K. K. Gleason, *ACS Nano*, 2008, **2**, 1959–1967.
142 D. Bhattacharyya, R. M. Howden, D. C. Borrelli and K. K. Gleason, *J. Polym. Sci., Part B: Polym. Phys.*, 2012, **50**, 1329–1351.
143 Y.-H. Ha, N. Nikolov, S. K. Pollack, J. Mastrangelo, B. D. Martin and R. Shashidhar, *Adv. Funct. Mater.*, 2004, **15**, 615–622.
144 M. A. Ali, H. Kim, C. Lee, H. Nam and J. Lee, *Synth. Met.*, 2011, **161**, 1347–1352.
145 J. M. Bone and J. L. Jenkins, *J. Chem. Educ.*, 2023, **100**(10), 4062–4071.
146 S. A. Kumar, S. Sahoo, G. K. Laxminarayana and C. S. Rout, *Small*, 2024, **20**, 2402087.
147 J. Liao, S. Wu, Z. Yin, S. Huang, C. Ning, G. Tan and P. K. Chu, *ACS Appl. Mater. Interfaces*, 2014, **6**, 10946–10951.
148 S. A. Campbell, Y. Li, S. Breakspear, F. C. Walsh and J. R. Smith, *Trans. IMF*, 2007, **85**, 237–244.
149 X. Luo and X. T. Cui, *Acta Biomater.*, 2011, **7**, 441–446.
150 J. Tietje-Girault, C. Ponce de Leó and F. C. Walsh, *Surf. Coat. Technol.*, 2007, **201**, 6025–6034.
151 J. Li, L. Zhao and P. Liu, *Langmuir*, 2023, **39**(40), 14297–14307.
152 K. K. Shiu, F.-Y. Song and K.-W. Lau, *J. Electroanal. Chem.*, 1999, **476**, 109–117.
153 S. S. Shah, M. A. Aziz, A.-R. Al-Betar and W. Mahfoz, *Arabian J. Chem.*, 2022, **15**, 104058.
154 J. E. Nady, A. Shokry, M. Khalil, S. Ebrahim, A. M. Elshaer and M. Anas, *Sci. Rep.*, 2022, 3611, DOI: 10.1038/s41598-022-07483-y.
155 K. M. Cheung, D. Bloor and G. C. Stevens, *J. Mater. Sci.*, 1990, **25**, 3814–3837.
156 R. Menon and A. K. Mukherjee, *Encycl. Nanosci. Nanotechnol.*, 2004, **8**, 715–729.
157 S. V. J. Siti, A. Ulianas and S. Aini, *J. Phys.:Conf. Ser.*, 2021, **1788**(1), 012004, DOI: 10.1088/1742-6596/1788/1/012004.
158 X. Gong, L. Dai, A. W. H. Mau and H. J. Griesser, *J. Polym. Sci., Part A: Polym. Chem.*, 1998, **36**, 633–643.
159 T. Yamamoto, *J. Organomet. Chem.*, 2002, **653**, 195–199.
160 M. Mueller, M. Fabretto, D. Evans, P. Hojati-Talemi, C. Gruber and P. Murphy, *Polymer*, 2012, **53**, 2146–2151.
161 R. Brooke, P. Cottis, P. Talemi, M. Fabretto, P. Murphy and D. Evans, *Prog. Mater. Sci.*, 2017, **86**, 127–146.
162 S. P. Armes, *Synth. Met.*, 1987, **20**, 365–371.
163 Y. Cao, A. Andreatta, A. J. Heeger and P. Smith, *Polymer*, 1989, **30**, 2305–2311.
164 Y. Li and J. Yang, *J. Appl. Polym. Sci.*, 1997, **65**, 2739–2744.
165 S. Sinha, S. Bhadra and D. Khastgir, *J. Appl. Polym. Sci.*, 2009, **112**, 3135–3140.

166 T. Yonehara, K. Komaba and H. Goto, *Polymers*, 2020, **12**, 375.
167 C. A. Ferreira, S. Aeiyach, M. Delamar and P. C. Lacaze, *J. Electroanal. Chem.*, 1990, **284**, 351–369.
168 G. Ciric-Marjanovic, M. Trchova and J. Stejskal, *J. Raman Spectrosc.*, 2008, **39**, 1375–1387.
169 A. Kaur, B. Bajaj, A. Kaushik, A. Saini and D. Sud, *Mater. Sci. Eng. B*, 2022, **286**, 116005.
170 S. Zhang, B. Cheng, Z. Jia, Z. Zhao, X. Jin, Z. Zhao and G. Wu, *Adv. Compos. Hybrid Mater.*, 2022, **5**, 1658–1698.
171 Y. Xie, D. Kocaefe, C. Chen and Y. Kocaefe, *J. Nanomater.*, 2016, 2302595, DOI: 10.1155/2016/2302595.
172 Q. Zhang, W. Wang, J. Goebl and Y. Yin, *Nano Today*, 2009, **4**, 494–507.
173 Y. Bao, C. Shi, T. Wang, X. Li and J. Ma, *Microporous Mesoporous Mater.*, 2016, **227**, 121–136.
174 A.-G. Schiopu, D. M. Iordache, M. Oproescu, L. M. Cursaru and A.-M. Iota, *Crystals*, 2024, **14**, 899.
175 R. R. Poolakkandy and M. M. Menamparambath, *Nanoscale Adv.*, 2020, **2**, 5015–5045.
176 Y. Boyjoo, M. Wang, V. K. Pareek, J. Liu and M. Jaroniec, *Chem. Soc. Rev.*, 2016, **45**, 6013–6047.
177 T. He, D. Chen, X. Jiao, Y. Xu and Y. Gu, *Langmuir*, 2004, **20**, 8404–8408.
178 T. Cheng, Y. Xiang, X. He, J. Pang, W. Zhu, L. Luo, Y. Cao and R. Pei, *J. Mater. Chem. B*, 2025, **13**, 4739–4769.
179 A. Bai, C.-C. Hu, Y.-F. Yang and C.-C. Lin, *Electrochim. Acta*, 2008, **53**, 2258–2264.
180 C. Mijangos and J. Martin, *Polymers*, 2023, **15**, 525.
181 S. Xiong, Q. Wang and H. Xia, *Mater. Res. Bull.*, 2004, 1569–1580.
182 B. H. Kim, D. H. Park, J. Joo, S. G. Yu and S. H. Lee, *Synth. Met.*, 2005, **150**, 279–284.
183 L. Liu, C. Zhao, Y. Zhao, N. Jia, Q. Zhou, M. Yan and Z. Jiang, *Eur. Polym. J.*, 2005, **41**, 2117–2121.
184 F.-L. Cheng, M.-L. Zhang and H. Wang, *Sensors*, 2005, **5**, 245–249.
185 N. Esman and J.-P. Lellouche, *Polym. Chem.*, 2010, **1**, 158–160.
186 J. Jang and J. H. Oh, *ChemComm*, 2004, 882–883.
187 S. Chuanyu and W. Yu, *Optoelectron. Adv. Mater., Rapid Commun.*, 2012, **6**, 1037–1040.
188 S. Das, A. Kumar and K. S. Narayan, *Phys. Rev. Mater.*, 2022, **6**, 025602.
189 R. Liu, S. I. Cho and S. B. Lee, *Nanotechnology*, 2008, **19**, 215710.
190 P. P. Pednekar, S. C. Godiyal, K. R. Jadhav and V. J. Kadam, Chapter 23 - Mesoporous silica nanoparticles: a promising multifunctional drug delivery system, *Micro Nano Technol*, ed. A. Ficai and A. M. B. T.-N. for C. T. Grumezescu, Elsevier, 2017, pp. 593–621.
191 G. D. Fu, J. P. Zhao, Y. M. Sun, E. T. Kang and K. G. Neoh, *Macromolecules*, 2007, **40**, 2271–2275.
192 Y. Hao, L. Song and Y. Zhang, *Prog. Org. Coat.*, 2022, **168**, 106912.
193 Y. Li, Y. Chang, M. Jin, Y. Liu and G. Han, *J. Appl. Polym. Sci.*, 2012, **126**, 1316–1321.
194 W. Wang, L. Lu, T. Chen and M. Rao, *J. Appl. Polym. Sci.*, 2012, **126**, 974–979.
195 J. Ge, L.-H. Rong, X. Cheng, Y. Tang, D. J. Pochan, E. B. Caldona and R. C. Advincula, *Macromolecules*, 2025, **58**, 3289–3297.
196 M. N. Gorsd, M. N. Blanco and L. R. Pizzio, *Procedia Mater. Sci.*, 2012, **1**, 432–438.
197 A. B. D. Nandiyanto, A. Suhendi, T. Ogi, R. Umemotoa and K. Okuyama, *Chem. Eng. J.*, 2014, **256**, 421–430.
198 Y.-C. Kuo, S.-S. Wang, K.-C. Chang, H. Chen and J. Thermoplast, *Compos. Mater.*, 2013, **28**, 1091–1109.
199 S.-J. Ding, C.-L. Zhang, M. Yang, X.-Z. Qu, Y.-F. Lu and Z.-Z. Yang, *Polymer*, 2006, **47**, 8360–8366.
200 M.-Y. Bai, Y.-J. Cheng, S. A. Wickline and Y. Xia, *Small*, 2009, **5**, 1747–1752.
201 Y. Yang, Y. Chu, F. Yang and Y. Zhang, *Mater. Chem. Phys.*, 2005, **92**, 164–171.
202 Z. Niu, Z. Yang, Z. Hu, Y. Lu and C. C. Han, *Adv. Funct. Mater.*, 2003, **13**, 949–954.
203 R. Panigrahi and S. K. Srivastava, *Mater. Res. Bull.*, 2015, **64**, 33–41.
204 R. Panigrahi and S. K. Srivastava, *Sci. Rep.*, 2015, **5**, 7638.
205 M. Saraf, A. Deep and A. Sharma, Conference:EMSI-2014, University of Delhi. DOI: 10.13140/2.1.4400.0009.
206 C. Mangeney, S. Bousalem, C. Connan, M.-J. Vaulay, S. Bernard and M. M. Chehimi, *Langmuir*, 2006, **22**, 10163–10169.
207 X. Shi, A. L. Briseno, R. J. Sanedrin and F. Zhou, *Macromolecules*, 2003, **36**, 4093–4098.
208 C. Sun and D. Sheng, *Chem. Lett.*, 2011, **40**, 153–155.
209 B. H. Sung, Y. G. Ko and U. S. Choi, *Colloids Surf., A*, 2007, **292**, 217–223.
210 X. Feng, C. Mao, G. Yang, W. Hou and J.-J. Zhu, *Langmuir*, 2006, **22**, 4384–4389.
211 Y. Gao, F. Wang, J. Gong, Z. Su and L. Qu, *J. Nanosci. Nanotechnol.*, 2008, **8**, 5972–5976.
212 L. Zhang and P. Liu, *Mater. Lett.*, 2010, **64**, 1755–1757.
213 S. Zuo, W. Liu, C. Yao, X. Li, Y. Kong, X. Liu, H. Mao and Y. Li, *Chem. Eng. J.*, 2013, **228**, 1092–1097.
214 Y. Gao, X. Li, J. Gong, B. Fan, Z. Su and L. Qu, *J. Phys. Chem. C*, 2008, **112**, 8215–8222.
215 C.-L. Zhu, S.-W. Chou, S.-F. He, W.-N. Liao and C.-C. Chen, *Nanotechnology*, 2007, **18**, 275604.
216 Z. Zhang, J. Deng, J. Sui, L. Yu, M. Wan and Y. Wei, *Macromol. Chem. Phys.*, 2006, **207**, 763–769.
217 Z. Zhang, J. Sui, L. Zhang, M. Wan, Y. Wei and L. Yu, *Adv. Mater.*, 2005, **17**, 2854–2857.
218 G. Li, Y. Li, Y. Li, H. Peng and K. Chen, *Macromolecules*, 2011, **44**, 9319–9323.
219 W. Liu, A. L. Cholli, R. Nagarajan, J. Kumar, S. t Tripathy, F. F. Bruno and L. Samuelson, *J. Am. Chem. Soc.*, 1999, **121**, 11345–11355.
220 S.-R. Yun, G.-O. Kim, C. W. Lee, N.-J. Jo, Y. Kang and K.-S. Ryu, *J. Nanomater.*, 2012, 894539, DOI: 10.1155/2012/894539.

221 A. Madani, B. Nessark, R. Brayner, H. Elaissari, M. Jouini, C. Mangeney and M. M. Chehimi, *Polymer*, 2010, **51**, 2825–2835.
222 C. H. Chang, P. S. Son, J.-A. Yoon and S.-H. Choi, *J. Nanomater.*, 2010, 168025, DOI: 10.1155/2010/168025.
223 S. Li, M. Zhou, Y. Zhang, X. Zhang and L. Ding, *J. Macromol. Sci., Part A:Pure Appl. Chem.*, 2018, **55**, 98–105.
224 K. Manna, *Fabrication of Carbonaceous/Magnetic Nanomaterial filled Polymer Nanocomposites in Electromagnetic Interference Shielding Applications*, Ph. D Thesis, Indian Institute of Technology Kharagpur, 2020.
225 J. Zhang, T. Qiu, S. Ren, H. Yuan, L. He and X. Li, *Mater. Chem. Phys.*, 2012, **134**, 1072–1078.
226 T.-L. Hsieh, P.-S. Hung, C.-J. Wang, Y.-S. Chou and P. W. Wu, *SN Appl. Sci.*, 2019, **1**, 319.
227 S. M. Marinakos, D. A. Shultz and D. L. Feldheim, *Adv. Mater.*, 1999, **11**, 34–37.
228 F. Yin, D. Wang, Z. Zhang, C. Zhang and Y. Zhang, *Mater. Lett.*, 2017, **207**, 225–229.
229 D. Su, J. Zhang, S. Dou and G. Wang, *ChemComm*, 2015, **51**, 16092–16095.
230 C. H. Chang, P. S. Son, J.-A. Yoon and S.-H. Choi, *J. Nanomater.*, 2010, 168025, DOI: 10.1155/2010/168025.
231 L. Qu and G. Shi, *J. Polym. Sci., Part A: Polym. Chem.*, 2004, **42**, 3170–3177.
232 J. Huang, B. Quan, M. Liu, Z. Wei and L. Jiang, *Macromol. Rapid Commun.*, 2008, **29**, 1335–1340.
233 L. Piraux, V.-A. Antohe, E. Ferain and D. Lahem, *RSC Adv.*, 2016, **6**, 21808–21813.
234 A. Kros, R. J. M. Nolte and N. A. J. M. Sommerdijk, *Adv. Mater.*, 2002, **14**, 1779–1782.
235 X. Lixin, L. Guangye, L. Jingfu and S. Mengtao, *Kinet. Catal.*, 2011, **52**, 716–722.
236 D. P. Dubal, Z. Caban-Huertas, R. Holze and P. Gomez-Romero, *Electrochim. Acta*, 2016, **191**, 346–354.
237 X. Zhang and S. K. Manohar, *J. Am. Chem. Soc.*, 2005, **127**, 14156–14157.
238 L. Benhaddad, M.-C. Bernard, C. Deslouis, L. Makhloufi, B. Messaoudi, A. Pailleret and H. Takenouti, *Synth. Met.*, 2013, **175**, 192–199.
239 C. Wang, Z. Liu, Q. Wang, J. Guo, Q. Zhao and Y. Lu, *J. Electroanal. Chem.*, 2021, **901**, 115780.
240 J. Zhao, Z. Li, J. Wang, Q. Li and X. Wang, *J. Mater. Chem. A*, 2015, **3**, 15124–15132.
241 J. Wu, Y. Liu and L. Bao, *Chem. Lett.*, 2015, **44**, 557–559.
242 T. Yao, T. Cui, X. Fang, J. Yu, F. Cui and J. Wu, *Chem. Eng. J.*, 2013, **225**, 230–236.
243 J. Rehmen, T. Pathirana, L. Garcia-Quintana, R. Kerr, P. C. Howlett, K. Zuber, C. Pozo-Gonzalo and D. R. Evans, *ACS Appl. Nano Mater.*, 2020, **3**, 3820–3828.
244 S. Zhang, J. Ren, Y. Zhang, H. Peng, S. Chen, F. Yang and Y. Cao, *Org. Electron.*, 2020, **77**, 105497.
245 S.-C. Luo, H.-H. Yu, A. C. A. Wan, Y. Han and J. Y. Ying, *Small*, 2008, **4**, 2051–2058.
246 X. Zhang, D. Xin, Z. Yu, J. Sun, Q. Li, X. He, Z. Liu and Z. Lei, *J. Colloid Interface Sci.*, 2025, **677**, 472–481.
247 C.-W. Kung, Y.-H. Cheng, H.-W. Chen, R. Vittal and K.-C. Ho, *J. Mater. Chem. A*, 2013, 10693–10702.
248 Y.-H. Cheng, C.-W. Kung, L.-Y. Chou, R. Vittal and K.-C. Ho, *Sens. Actuators, B*, 2014, **192**, 762–768.
249 M. Wan, *Adv. Mater.*, 2008, **20**, 2926–2932.
250 F.-L. Li and H.-J. Zhang, *Materials*, 2017, **10**, 995.
251 L. Pan, H. Qiu, C. Dou, Y. Li, L. Pu, J. Xu and Y. Shi, *Int. J. Mol. Sci.*, 2010, **11**, 2636–2657.
252 Z. Zhang, T. Sun, M. Shao and Y. Zhu, in *Functional Nanomaterials: Synthesis, Properties, and Applications*, ed. W.-Y. Wong and Q. Dong, Wiley, Ch. 8, 2022, pp. 303–336. DOI: 10.1002/9783527828562.ch8.
253 A. Ali, R. Jamal and T. Abdiryim, *RSC Adv.*, 2021, **11**, 33425–33430.
254 Z. Zhang, Z. Wei and M. Wan, *Macromolecules*, 2002, **35**, 5937–5942.
255 E. N. Konyushenko, M. Trchová, J. Stejskal and I. Sapurina, *Chem. Pap.*, 2010, **64**, 56–64, DOI: 10.2478/s11696-009-0101-z.
256 J. Han, J. Dai, C. Zhou and R. Guo, *Polym. Chem.*, 2013, **4**, 313–321.
257 G. H. Lim and H. J. Choi, *J. Ind. Eng. Chem.*, 2017, **47**, 51–55.
258 L. Zhang, Y. Long, Z. Chen and M. Wan, *Adv. Funct. Mater.*, 2004, **14**, 693–698.
259 Z. Zhang, M. Wan and Y. Wei, *Adv. Funct. Mater.*, 2006, **16**, 1100–1104.
260 L. Zhang, H. Peng, Z. D. Zujovic, P. A. Kilmartin and J. Travas-Sejdic, *Macromol. Chem. Phys.*, 2007, **208**, 1210–1217.
261 U. Rana, K. Chakrabarti and S. Malik, *J. Mater. Chem.*, 2012, **22**, 15665–15671.
262 J. Huang and M. Wan, *J. Polym. Sci., Part A: Polym. Chem.*, 1999, **37**, 1277–1284.
263 J. Wu, Y. Li and W. Feng, *Synth. Met.*, 2007, **157**, 1013–1018.
264 X. Wu, Y. Wang, Y. Xiao, Y. Han, T. Li and Y. Ma, *Synth. Met.*, 2022, **291**, 117212.
265 Y. Long, Z. Chen, N. Wang, Y. Ma, Z. Zhang, L. Zhang and M. Wan, *Appl. Phys. Lett.*, 2003, **83**, 1863–1865.
266 L. Zhang, H. Peng, J. Sui, P. A. Kilmartin and J. Travas-Sejdic, *Curr. Appl. Phys.*, 2008, **8**, 312–315.
267 W. Wu, D. Pan, Y. Li, G. Zhao, L. Jing and S. Chen, *Electrochim. Acta*, 2015, **152**, 126–134.
268 J. Mu, G. Ma, H. Peng, J. Li, K. Sun and Z. Lei, *J. Power Sources*, 2013, **242**, 797–802.
269 L. Zhang and M. Wan, *Thin Solid Films*, 2005, **477**, 24–31.
270 R. Panigrahi and S. K. Srivastava, *RSC Adv.*, 2013, **3**, 7808–7815.
271 Z. Zhang, Z. Wei, L. Zhang and M. Wan, *Acta Mater.*, 2005, **53**, 1373–1379.
272 Q. Sun and Y. Deng, *Mater. Lett.*, 2008, **62**, 1831–1834.
273 H. Qiu and M. Wan, *Macromolecules*, 2001, **34**, 675–677.
274 H. Xia, D. Cheng, P. Lam and H. S. O. Chan, *Nanotechnology*, 2006, **17**, 3957–3961.
275 Y. Li, Z. Li and F. Zheng, *Mater. Lett.*, 2015, **148**, 34–36.

276 K. Huang, X.-H. Meng and M. Wan, *J. Appl. Polym. Sci.*, 2006, **100**, 3050–3054.
277 Y. Zhu, D. Hu, M. X. Wan, L. Jiang and Y. Wei, *Adv. Mater.*, 2007, **19**, 2092–2096.
278 L. Zhang and M. Wan, *Adv. Funct. Mater.*, 2003, **13**, 815–820.
279 W. Liang, S. Rhodes, J. Zheng, X. Wang and J. Fang, *ACS Appl. Mater. Interfaces*, 2018, **10**, 37426–37433.
280 M. Liu, C. Luo, R. Huang, H. Peng, Y. Wang and J. Travas-Sejdic, *Int. J. Polym. Mater. Polym. Biomater.*, 2014, **63**, 602–608.
281 L. Zhang, H. Ping, J. Sui, C. Soellar, P. A. Kilmartin and J. Travas-Sejdic, *J. Phys. Chem. C*, 2009, **113**, 9128–9134.
282 N. P. Tavandashti, M. Ghorbani and A. Shojaei, *Polym. Int.*, 2015, **64**, 88–95.
283 H. Ding, J. Shen, M. Wan and Z. Chen, *Macromol. Chem. Phys.*, 2008, **209**, 864–871.
284 C. Zhou, J. Han, G. Song and R. Guo, *J. Polym. Sci., Part A: Polym. Chem.*, 2008, **46**, 3563–3572.
285 R. Yuan, H. Wang, T. Ji, L. Mu, L. Chen, Y. Zhu and J. Zhu, *J. Mater. Chem. A*, 2015, **3**, 19299–19303.
286 L. Ren, K. Li and X. Chen, *Polym. Bull.*, 2009, **63**, 15–21.
287 S. Pang, W. Chen, Z. Yang, Z. Liu, X. Fan and D. Fang, *Polymers*, 2017, **9**, 510.
288 K. P. D. Orellana and M. E. Roberts, Meet. Abstr., 2014, **MA2014-01**, 266. https://iopscience.iop.org/issue/2151-2043/MA2014-01/2.
289 S. Wang, Q. Lu, Y. K. Kwon and H. J. Choi, *J. Mol. Liq.*, 2025, **437**, 128554.
290 N.-R. Chiou, L. J. Lee and A. J. Epstein, *Chem Mater.*, 2007, **19**, 3589–3591.
291 Y.-S. Zhang, W.-H. Xu, W.-T. Yao and S.-H. Yu, *J. Phys. Chem. C*, 2009, **113**, 8588–8594.
292 H. Zhang, Y. Li, X. Wang, J. Li and F. Wang, *Polymer*, 2011, **52**, 4246–4252.
293 Z. Wei and M. Wan, *Adv. Mater.*, 2002, **14**, 1314–1317.
294 C. Gao, M. Ai, X. Li and Z. Xu, *J. Polym. Sci., Part A: Polym. Chem.*, 2011, **49**, 2173–2182.
295 Y. Zhu, G. Ren, M. Wan and L. Jiang, *Macromol. Chem. Phys.*, 2009, **210**, 2046–2051.
296 P. Liu, Y. Zhu, J. Torres, S. H. Lee and M. Yun, *J. Polym. Sci., Part A: Polym. Chem.*, 2017, **55**, 3973–3979.
297 B. Sim and H. J. Choi, *RSC Adv.*, 2015, **5**, 11905.
298 A. Tajima, Y. Ogawa, K. Nakabayashi and M. Atobe, Proceedings of the Annual Meeting of the Japan Society of Sonochemistry, 2015, 24, Session ID P10, Pages 39–40, 2017. DOI: 10.20577/pamjss.24.0_39.
299 D. P. Bhattarai, A. P. Tiwari, B. Maharjan, B. Tumurbaatar, C. H. Park and C. S. Kim, *J. Colloid Interface Sci.*, 2019, **534**, 447–458.
300 X. Yang, Z. Zhu, T. Dai and Y. Lu, *Macromol. Rapid Commun.*, 2005, **26**, 1736–1740.
301 J. Wang, Y. Xu, F. Yan, J. Zhu and J. Wang, *J. Power Sources*, 2011, **196**, 2373–2379.
302 Y. Xia, M. Wei and Y. Lu, *Synth. Met.*, 2009, **159**, 372–376.
303 Y. Bian, C. Yang, Q. Gu, X. Zhu, Y. Wang and X. Zhang, *J. Polym. Sci., Part A:Polym. Chem.*, 2019, **57**, 1550–1555.
304 X. Zhang, J.-S. Lee, G. S. Lee, D.-K. Cha, M. J. Kim, D. J. Yang and S. K. Manohar, *Macromolecules*, 2005, **39**, 470–472.
305 Z. Guo, Y. Qiao, H. Liu, C. Ding, Y. Zhu, M. Wan and L. Jiang, *J. Mater. Chem.*, 2012, **22**, 17153–17158.
306 A. Ali, R. Jamal, T. Abdiryim and X. Huang, *J. Electroanal. Chem.*, 2017, **787**, 110–117.
307 J. Lee, S.-B. Cho, K. C. Dimitrov, Y. Lee and D.-Y. Khang, *Eur. Polym. J.*, 2024, **206**, 112771.
308 X. Ni, X. Hu, S. Zhou, C. Sun, X. Bai and P. Chen, *Polym. Adv. Technol.*, 2011, **22**, 532–537.
309 J. Sui, L. Zhang, J. Travas-Sejdic and P. A. Kilmartin, *Macromol. Symp.*, 2010, **290**, 107–114.
310 M. Acosta, M. D. Santiago and J. A. Irvin, *Materials*, 2022, **15**, 8820.
311 X. Karagiorgis, S. Sandhu, P. J. Skabara and R. Dahiya, *Polym. Int.*, 2025, DOI: 10.1002/pi.70026.
312 Y.-E. Miao, W. Fan, D. Chen and T. Liu, *ACS Appl. Mater. Interfaces*, 2013, **5**, 4423–4428.
313 Z.-Q. Feng, J. Wu, W. Cho, M. K. Leach, E. W. Franz, Y. I. Naim, Z.-Z. Gu, J. M. Corey and D. C. Martin, *Polymers*, 2013, **54**, 702–708.
314 M. Zhu, J. Tang, W. Wei and S. Li, *Mater. Chem. Front.*, 2020, **4**, 1105–1149.
315 M.-Y. Bai and Y. Xia, *Macromol. Rapid Commun.*, 2010, **31**, 1863–1868.
316 C. Niu, B. Zou, Y. Wang, L. Chen, H. Zheng and S. Zhou, *Chem. Commun.*, 2015, **51**, 5009–5012.
317 H. Gu, J. Huang, N. Li, H. Yang, G. Chen, C. Dong, C. Gong and H. Guan, *J. Mater. Sci. Technol.*, 2023, **146**, 145–153.
318 H. Lv, Q. Pan, Y. Song, X.-X. Liu and T. Liu, *Nano-Micro Lett.*, 2020, **12**, 118.
319 Z. Chen, X. Zhao, R. Lu, R. Hong and X. Yang, *Synth. Met.*, 2023, **296**, 117378.
320 N. Jabeen, Q. Xia, M. Yang and H. Xia, *ACS Appl. Mater. Interfaces*, 2016, **8**, 6093–6100.
321 C. Wu, Z. Pei, M. Lv, D. Huang, Y. Wang and S. Yuan, *Molecules*, 2023, **28**, 434.
322 A. Xu, Y. Yu, W. Li, Y. Zhang, S. Ye, Z. Zhao and Y. Qin, *Electrochim. Acta*, 2022, **435**, 141378.
323 D. Liu, L. Zhou, Y. Liu, C. Xia, J. Ouyang and A. A. Adesina, *J. Environ. Chem. Eng.*, 2025, **12**, 113450.
324 X. Hu, Y. Duan, Z. Hao, Z. Meng, B. Wang, Z. Kang, S. Liu and H. Tian, *J. Alloys Compd.*, 2024, **1009**, 176851.
325 X. Sun, Z. Hao, F. Zeng, J. Xu, H. Nan, Z. Meng, J. Yang, W. Shi, Y. Zeng, X. Hu and H. Tian, *J. Colloid Interface Sci.*, 2022, **610**, 601–609.
326 Z. Lv, Y. Tang, Z. Zhu, J. Wei, W. Li, H. Xia, Y. Jiang, Z. Liu, Y. Luo, X. Ge, Y. Zhang, R. Wang, W. Zhang, X. J. Loh and X. Chen, *Adv. Mater.*, 2018, **13**, 1805468.
327 F. Fauzi, Y. Di, D. M. Morales and R. K. Bose, *ACS Appl. Energy Mater.*, 2025, **8**, 4656–4668.
328 P. Yin, D. Lan, C. Lu, Z. Jia, A. Feng, P. Liu, X. Shi, H. Guo, G. Wu and J. Wang, *J. Mater. Sci. Technol.*, 2025, **204**, 204–223.

329 Y. Li, G. Chen, Q. Li, G. Qiu and X. Liu, *J. Alloys Compd.*, 2011, **509**, 4104–4107.
330 C. Cui, Y. Du, T. Li, X. Zheng, X. Wang, X. Han and P. Xu, *J. Phys. Chem. B*, 2012, **116**, 9523–9531.
331 L. Wang, J. Zhu, H. Yang, F. Wang, Y. Qin, T. Zhao and P. Zhang, *J. Alloys Compd.*, 2015, **634**, 232–238.
332 Z. Wan, H. Ma, S. Hou, Y. Wang, J. Ho and H. Ge, *J. Mater. Sci.: Mater. Electron.*, 2021, **32**, 10991–11003.
333 S. Chhetri and T. Kuila, *RSC Appl. Polym.*, 2024, **2**, 507–533.
334 S. K. Srivastava and V. Mittal, *Hybrid Nanomaterials: Developments in Energy, Environments and Polymer Nanocomposites*, ed. S. K. Srivastava and V. Mittal, Scrivener-Wiley, 2017, pp. 241–320.
335 R. Che, J. Gu, J. Kong, W. Lu, Y. Huang, H. Lv, X. Liu, X. i. Qi, G. Wu and H. Wu, *Cell Rep. Phys. Sci.*, 2025, **6**, 102502.
336 P. Saini, V. Choudhary, N. Vijayan and R. K. Kotnala, *J. Phys. Chem. C*, 2012, **116**, 13403–13412.
337 Y. Yang, J. Zhang, W. Zou, S. Wu, F. Wu, A. Xie and Z. Wei, *Macromol. Rapid Commun.*, 2018, **39**, 1700591.
338 C. Xu, F. Wu, A. Xie, L. Duan, Z. Yang, Y. Xia, M. Sun and Z. Xiong, *Ind. Eng. Chem. Res.*, 2020, **59**, 7604–7610.
339 R. Guo, L. Wu, J. Shi, F. Wu and A. Xie, *Synth. Met.*, 2022, **290**, 117161.
340 M. Wan, J. Li and S. Li, *Polym. Adv. Technol.*, 2001, **12**, 651–657.
341 R. Moučka, M. Sedlačík, H. Kasparyan, J. Prokeš, M. Trchová, F. Hassouna and D. Kopecký, *Int. J. Mol. Sci.*, 2020, **21**, 8814.
342 Y. Sun, G. Guo, B. Yang, M. He, Y. Tian, J. C. Cheng and Y. Liu, *J. Mater. Res.*, 2012, **27**, 457–462.
343 X. Yang, B. Fan, X. Wang, X. Tang, J. Wang, G. Tong, X. Wang and W. Tian, *J. Environ. Chem. Eng.*, 2021, **9**, 105672.
344 S. K. Singh, M. J. Akhtar and K. K. Kar, *Ind. Eng. Chem. Res.*, 2020, **59**, 9076–9084.
345 H. Wang, K. Zhang and Y. Zhu, *J. Mater. Sci.: Mater. Electron.*, 2024, **35**, 1063.
346 Q. Chu, W. Tao, H. Lin, M. Ma, S. Chen, Y. Shi, H. He and X. Wang, *Ind. Crops Prod.*, 2023, **194**, 116299.
347 C. Yang, H. Li, D. Xiong and Z. Cao, *React. Funct. Polym.*, 2009, **69**, 137–144.
348 J. Guo, Y. Sun, X. Li, S. Xi, M. M. Ibrahim, H. Qiu, G. A. M. Mersal, Z. M. El-Bahy, V. Murugadoss, W. Abdul, F. Zhou, J. Ren, Z. Guo and J. Zhu, *Compos. Sci. Technol.*, 2024, **258**, 110917.
349 A. Elhassan, X. Lv, I. Abdalla, J. Yu, Z. Li and B. Ding, *Polymers*, 2024, **16**, 1160.
350 P. Tang, J. Du, M. Li, X. Zhao, H. Ren, X. Zhang, G. Wu and X. Wang, *ACS Appl. Nano Mater.*, 2024, **7**, 10325–10337.
351 D. Promlok, W. Wichaita, S. Phongtamrug, C. Kaewsaneha, P. Sreearunothai, T. Suteewong and P. Tangboriboonrat, *Prog. Org. Coat.*, 2024, **186**, 108002.
352 Y.-F. Zhu, Q.-Q. Ni, Y.-Q. Fu and T. Natsuki, *J. Nanopart. Res.*, 2013, **15**, 1988.
353 J. Hou, L. Zhang, H. Qiu, W. Duan, X. Wang, X. Wan and X. Du, *J. Mater. Sci.:Mater. Electron.*, 2017, **28**, 9279–9288.
354 Y.-F. Zhu, L. Zhang, T. Natsuki, Y.-Q. Fu and Q.-Q. Ni, *Synth. Met.*, 2012, **162**, 337–343.
355 P. Tang, M. Li, J. Du, Y. Gong, X. Zhang, G. Wu and X. Wang, *Appl. Surf. Sci.*, 2024, **649**, 159183.
356 B. Zhang, Y. Du, P. Zhang, H. Zhao, L. Kang, X. Han and P. Xu, *J. Appl. Polym. Sci.*, 2013, **130**, 1909–1916.
357 W. Zhou, X. Hu, X. Bai, S. Zhou, C. Sun, J. Yan and P. Chen, *ACS Appl. Mater. Interfaces*, 2011, **3**, 3839–3845.
358 Y. Sun, F. Xiao, X. Liu, C. Feng and C. Jin, *RSC Adv.*, 2013, **3**, 22554–22559.
359 Z. Wu, D. Tan, K. Tian, W. Hu, J. Wang, M. Su and L. Li, *J. Phys. Chem. C*, 2017, **121**, 15784–15792.
360 M. Qiao, X. Lei, Y. Ma, L. Tian, K. H. Su and Q. Zhang, *Ind. Eng. Chem. Res.*, 2016, **55**, 6263–6275.
361 M. Wang, Y. Lin, Y. Liu and H. Yang, *J. Mater. Sci. Mater. Electron.*, 2019, **30**, 14344–14354.
362 S. H. Hosseini, A. Moghimi and M. Moloudi, *Mater. Sci. Semicond. Process.*, 2014, **24**, 272–277.
363 C. Dong, D. Li, H. Wang, B. Cai, Y. Xin, H. Peng, Y. Zhao, N. Wang, Z. Cui and G. Wang, *Carbon*, 2023, **215**, 118459.
364 S. Kumari, J. Dalal, A. Kumar and A. Ohlan, *Adv. Eng. Mater. A*, 2022, **24**, 2200635.
365 J. Li, H. Ji, Y. Xu, J. Zhang and Y. Yan, *J. Mater. Res. Technol.*, 2020, **9**, 762–772.
366 X. Li, L. Yu, W. Zhao, Y. Shi, L. Yu, Y. Dong, Y. Zhu, Y. Fu, X. Liu and F. Fu, *Chem. Eng. J.*, 2020, **379**, 122393.
367 L. Gai, Y. Zhao, G. Song, Q. An, Z. Xiao, S. Zhai and Z. Li, *Composites, Part A*, 2020, **136**, 105965.
368 C. Tian, Y. Du, P. Xu, R. Qiang, Y. Wang, D. Ding, J. Xue, J. Ma, H. Zhao and X. Han, *ACS Appl. Mater. Interfaces*, 2015, **7**, 20090–20099.
369 Q. Shang, H. Feng, J. Liu, Q. Lian, Z. Feng, N. Chen, J. Qiu and H. Wu, *J. Colloid Interface Sci.*, 2021, **584**, 80–91.
370 L. Yu, Y. Zhu and Y. Fu, *Appl. Surf. Sci.*, 2018, **427**, 451–457.
371 Y.-Y. Wang, W.-J. Sun, H. Lin, P.-P. Gao, J.-F. Gao, K. Dai, D.-X. Yan and Z.-M. Li, *Composites, Part B*, 2020, **199**, 108309.
372 J. Liu, Z. Wang, S. Rehman and H. Bi, *RSC Adv.*, 2017, **7**, 53104–53110.
373 A. Ohlan, K. Singh, A. Chandra and S. K. Dhawan, *ACS Appl. Mater. Interfaces*, 2010, **2**, 927–933.
374 Y. Zhang, M. Qiu, Y. Yu, B. Y. Wen and L. Cheng, *ACS Appl. Mater. Interfaces*, 2016, **9**, 809–818.
375 P. Saini, V. Choudhary, B. P. Singh, R. B. Mathur and S. K. Dhawan, *Mater. Chem. Phys.*, 2009, **113**, 919–926.
376 X. Tian, F. Meng, F. Meng, X. Chen, Y. Guo, Y. Wang, W. Zhu and Z. Zhou, *ACS Appl. Mater. Interfaces*, 2017, **9**, 15711–15718.
377 M. Zhang, X. Qian, Q. Zeng, Y. Zhang, H. Cao and R. Che, *Carbon*, 2021, **175**, 499–508.
378 F. Liu, J. Sui, G. I. N. Waterhouse, W. Zhou, X. Jiang, Z. Zhang and L. Yu, *J. Mater. Sci.*, 2022, **57**, 7570–7586.

379 J. Shu, L. Wang, Y. Dai, A. Chen, X. Wang and Z. Deng, *J. Alloys Compd.*, 2024, **1001**, 175030.
380 L. Yang, M. Liu, G. Liang, X. Xiong, W. You, H. Cheng and R. Che, *J. Mater. Chem. C*, 2024, **12**, 15501–15509.
381 B. Zhang, J. Wang, J. Peng, J. Sun, X. Su, Y. Zou and Y. Zhou, *J. Mater. Sci.: Mater. Electron.*, 2019, **30**, 9785–9797.
382 C. Ge, X. Zhang, J. Liu, F. Jin, J. Liu and H. Bi, *Appl. Surf. Sci.*, 2016, **378**, 49–56.
383 K. Manna and S. K. Srivastava, *ACS Sustainable Chem. Eng.*, 2017, **5**, 10710–10721.
384 K. Manna and S. K. Srivastava, *Langmuir*, 2020, **36**, 4519–4531.
385 S. Ji, C. Li, Z. Zhang, X. Jiang and L. Yu, *Synth. Met.*, 2018, **239**, 59–65.
386 L. Meng, J. Li, X. Li, Z. Wang and W. Zhou, *J. Alloys Compd.*, 2023, **966**, 171528.
387 D. Han, N. Xiao, H. Hu, B. Liu, G. Song and H. Yan, *RSC Adv.*, 2015, **5**, 97944–97950.
388 R. Panigrahi, S. K. Srivastava and J. Pionteck, *Rubber Chem. Technol.*, 2018, **91**, 97–119.
389 H. Yang, A. Wang, X. Feng, H. Dong, T. Zhuang, J. Sui, S. Zhao and C. Sun, *Polymers*, 2023, **15**, 1866.
390 C. Li, Y. Zhang, S. Ji, X. Jiang, Z. Zhang and L. Yu, *J. Mater. Sci.*, 2018, **53**, 5270–5286.
391 X. Liu, S. W. Or, C. M. Leung and S. L. Ho, *J. Appl. Phys.*, 2014, **115**, 17A507.
392 Y. Wang, X. Wu, W. Zhang, C. Luo, J. Li, Q. Wang and Q. Wang, *Mater. Chem. Phys.*, 2018, **209**, 23–30.
393 J. Ding, L. Wang, Y. Zhao, L. Xing, X. Yu, G. Chen, J. Zhang and R. Che, *Small*, 2019, **15**, 1902885.
394 J. Zhang and X. Wang, *J. Mater. Sci.: Mater. Electron.*, 2018, **29**, 1592–1599.
395 M. Zhang, L. Zhao, W. Zhao, T. Wang, L. Yuan, Y. Guo, Y. Xie, T. Cheng, A. Meng and Z. Li, *Nano Res.*, 2023, **16**, 3558–3569.
396 Y. Wang, X. Wu, W. Zhang and S. Huang, *Synth. Met.*, 2015, **210**, 165–170.
397 X. Liu, X. Zhao, J. Yan, Y. Huang, T. Li and P. Liu, *Carbon*, 2021, **178**, 273–284.
398 H. Wang, S. Feng, M. Sun, X. Li, C. Wang, Z. Lin, M. Ma, T. Li and Y. Ma, *J. Colloid Interface Sci.*, 2024, **658**, 889–902.
399 A. P. Singh, M. Mishra, P. Sambyal, B. K. Gupta, B. P. Singh, A. Chandra and S. K. Dhawan, *J. Mater. Chem. A*, 2014, **2**, 3581–3593.
400 L. Wang, Y. Huang, C. Li, J. Chen and X. Sun, *Synth. Met.*, 2014, **198**, 300–307.
401 J. Zhao, J. Lin, J. Xiao and H. Fan, *RSC Adv.*, 2015, **5**, 19345–19352.
402 D. Zhang, J. Cheng, X. Yang, B. Zhao and M. Cao, *J. Mater. Sci.*, 2014, **49**, 7221–7230.
403 Z. He, Y. Fang, X. Wang and H. Pang, *Synth. Met.*, 2011, **161**, 420–425.
404 T. Liu, N. Liu, S. Zhai, S. Gao, Z. Xiao, Q. An and D. Yang, *J. Alloys Compd.*, 2019, **779**, 831–843.
405 V. Shukla, *J. Mater. Sci.*, 2020, **55**, 2826–2835.
406 T. K. Gupta, B. P. Singh, R. h B. Mathur and S. R. Dhakate, *Nanoscale*, 2014, **6**, 842–851.
407 P. B. Liu, Y. Huang and X. Sun, *ACS Appl. Mater. Interfaces*, 2013, **5**, 12355–12360.
408 S.-S. Afzali, S. H. Hekmatara, J. Seyed-Yazdi and S. M. B. M. Hosseini, *Sci. Rep.*, 2022, **12**, 9590.
409 Y. Wang, X. Wu, W. Zhang, C. Luo, J. Li and Q. Wang, *Synth. Met.*, 2017, **231**, 7–14.
410 P. Liu, Y. Huang, Y. Yang, J. Yan and X. Zhang, *J. Alloys Compd.*, 2016, **662**, 63–68.
411 D. Lakherwal, *International Journal of Environmental Research and Development*, 2014, **4**, 41–48.
412 N. Rama Jyothi, Heavy Metal Sources and Their Effects on Human Health, in *Heavy Metals - Their Environmental Impacts and Mitigation*, ed. M. K. Nazal and H. Zhao, IntechOpen, 2021, Ch. 2, DOI: 10.5772/intechopen.95370.
413 M. Chigondo, B. Nyamunda, M. Maposa and F. Chigondo, *Water Sci. Technol.*, 2022, **85**, 1600–1619.
414 M. I. Khan, M. K. Almesfer, A. Elkhaleefa, I. Shigidi, M. Z. Shamim, I. H. Ali and M. Rehan, *Polymers*, 2021, **13**, 3810.
415 A. Olad and R. Nabavi, *J. Hazard. Mater.*, 2007, **147**, 845–851.
416 H. Chang, Q. Meng, D. Liu, Y. Wu, Z. Yang, B. Sun, F. Liu and Y. Liu, *J. Appl. Polym. Sci.*, 2022, **139**, e52822.
417 H. Wu, Q. Wang, G. T. Fei, S. H. Xu, X. Guo and L. D. Zhang, *Nanoscale Res. Lett.*, 2018, **13**, 401.
418 X. Guo, G. T. Fei, H. Su and L. D. Zhang, *J. Phys. Chem. C*, 2011, **115**, 1608–1613.
419 Z. Zhao, Y. Yang, L. Xu, Z. Qiu, Z. Wang, Y. Luo and K. Du, *J. Chem.*, 2022, 2041512, DOI: 10.1155/2022/2041512.
420 S. Li, X. Lu, X. Li, Y. Xue, C. Zhang, J. Lei and C. Wang, *J. Colloid Interface Sci.*, 2012, **378**, 30–35.
421 M. S. Lashkenari, B. Davodi, M. Ghorbani and H. Eisazadeh, *High Perform. Polym.*, 2012, **24**, 345–355.
422 J. Wang, K. Pan, E. P. Giannelis and B. Cao, *RSC Adv.*, 2013, **3**, 8978–8987.
423 Y. Zhan, X. Wan, S. He and Y. He, *J. Chem. Technol. Biotechnol.*, 2018, **93**, 1432–1442.
424 A. H. Bhat and T. N. Chisti, *J. Chem. Eng.*, 2023, **11**, 110664.
425 M. Bhaumik, S. Agarwal, V. K. Gupta and A. Maity, *J. Colloid Interface Sci.*, 2016, **470**, 257–267.
426 B. Qiu, C. Xu, D. Sun, H. Yi, J. Guo, X. Zhang, H. Qu, M. Guerrero, X. Wang, N. Noel, Z. Luo, Z. Guo and S. Wei, *ACS Sustainable Chem. Eng.*, 2014, **2**, 2070–2080.
427 N. Ballav, H. J. Choi, S. B. Mishra and A. Maity, *Appl. Clay Sci.*, 2014, **102**, 60–70.
428 X. Han, L. Gai, H. Jiang, L. Zhao, H. Liu and W. Zhang, *Synth. Met.*, 2013, **171**, 1–6.
429 W. Zhang, Y. Wang, Y. Fei, Y. Wang, Z. Zhang, M. Kou, Q. Feng, S. Wang and X. Du, *Adv. Mater. Sci. Eng.*, 2021, 7068003, DOI: 10.1155/2021/7068003.
430 M. Bhaumik, A. Maity, V. V. Srinivasu and M. S. Onyango, *J. Hazard. Mater.*, 2011, **190**, 381–390.

431 M. Chigondo, H. K. Paumo, M. Bhaumik, K. Pillay and A. Maity, *J. Mol. Liq.*, 2019, **275**, 778–791.
432 A. E. Chávez-Guajardo, J. C. Medina-Llamas, L. Maqueira, C. A. S. Andrade, K. G. B. Alves and C. P. de Melo, *Chem. Eng. J.*, 2015, **281**, 826–836.
433 A. M. Muliwa, T. Y. Leswifi, M. S. Onyango and A. Maity, *Sep. Purif. Technol.*, 2016, **158**, 250–258.
434 J. Zhang, H. Chen, Z. Chen, J. He, W. Shi, D. Liu, H. Chi, F. Cui and W. Wang, *RSC Adv.*, 2016, **6**, 59292–59298.
435 T. Wen, Q. Fan, X. Tan, Y. Chen, C. Chen, A. Xu and X. Wang, *Polym. Chem.*, 2016, **7**, 785–794.
436 K. V. Brungesh, B. M. Nagabhushana, M. N. K. Harish and R. H. Krishna, *J. Environ. Anal. Toxicol.*, 2017, **7**, 1000442.
437 L. Du, P. Gao, Y. Liu, T. Minami and C. Yu, *Nanomaterials*, 2020, **10**, 686.
438 S. Sahu, U. K. Sahu and R. K. Patel, *J. Chem. Eng. Data*, 2019, **64**, 1294–1304.
439 J. Wang, K. Pan, Q. He and B. Cao, *J. Hazard. Mater.*, 2013, **244–245**, 121–129.
440 Y. Li, I. Peng, J. Guo and Z. Chen, *Langmuir*, 2020, **36**, 11508–11516.
441 F. Wang, Y. Zhang, Q. Fang, Z. Li, Y. Lai and H. Yang, *Chemosphere*, 2021, **263**, 128109.
442 Y. Chen, H. Xu, S. Wang and L. Kang, *RSC Adv.*, 2014, **4**, 17805–17811.
443 Y. Wu, H. Li, Z. Zhao, X. Yi, D. Deng, L. Zheng, X. Luo, Y. Cai, W. Luo and M. Zhang, *J. Alloys Compd.*, 2021, **851**, 156741.
444 M. Bhaumik, V. K. Gupta and A. Maity, *J. Environ. Chem. Eng.*, 2018, **6**, 2514–2527.
445 P. Karthikeyan, S. S. Elanchezhiyan, S. Meenakshi and C. M. Park, *J. Hazard. Mater.*, 2021, **408**, 124892.
446 S. Li, X. Lu, Y. Xue, J. Lei, T. Zheng and C. Wang, *PLoS One*, 2012, **7**, e43328.
447 A. Hsini, A. Essekri, N. Aarab, M. Laabd, A. A. Addi, R. Lakhmiri and A. Albourine, *Environ. Sci. Pollut. Res. Int.*, 2020, **27**, 15245–15258.
448 S. Dutta, S. K. Srivastava and A. K. Gupta, *Mater. Adv.*, 2021, **2**, 2431–2443.
449 W. Fang, X. Jiang, H. Luo and J. Geng, *Chemosphere*, 2018, **197**, 594–602.
450 N. S. Alsaiari, A. Amari, K. M. Katubi, F. M. Alzahrani, F. B. Rebah and M. A. Tahoon, *Processes*, 2021, **9**, 576.
451 H. D. da Rocha, E. S. Reis, G. P. Ratkovski, R. J. da Silva, F. D. S. Gorza, G. C. Pedro and C. P. de Melo, *J. Taiwan Inst. Chem. Eng.*, 2020, **110**, 8–20.
452 M. K. Debnath, M. A. Rahman, H. Minami, M. M. Rahman, M. A. Alam, M. K. Sharafat, M. K. Hossain and H. Ahmad, *J. Appl. Polym. Sci.*, 2019, **136**, 47524.
453 M. R. Samani and D. Toghraie, *J. Environ. Health Sci. Eng.*, 2019, **17**, 53–62.
454 W. Yao, T. Ni, S. Chen, H. Li and Y. Lu, *Compos. Sci. Technol.*, 2014, **99**, 15–22.
455 E. da S. Reis, F. D. S. Gorza, G. da C. Pedro, B. G. Maciel, R. J. da Silva, G. P. Ratkovski and C. P. de Melo, *J. Environ. Chem. Eng.*, 2021, **9**, 104893.
456 J. Han, P. Fang, J. Dai and R. Guo, *Langmuir*, 2012, **28**, 6468–6475.
457 Y. Zhang, D.-B. Jiang, Y. Wang, T. C. Zhang, G. Xiang, Y.-X. Zhang and S. Yuan, *Ind. Eng. Chem. Res.*, 2020, **59**, 7554–7563.
458 A. Mehdinia, R. Niroumand and A. Jabbari, *Int. J. Environ. Sci. Technol.*, 2020, **17**, 2721–2730.
459 N. Wang, J. Feng, W. Yan, L. Zhang, Y. Liu and R. Mu, *Front. Environ. Sci. Eng.*, 2022, **16**, 105.
460 Z. Vatani and H. Eisazadeh, *Polym. Plast. Technol.*, 2013, **52**, 1621–1625.
461 J. Chen, R. Dong, S. Chen, D. Tang, X. Lou, C. Ye, T. Qiu and W. Yan, *J. Cleaner Prod.*, 2022, **338**, 130536.
462 A. S. Rad, *J. Water Wastewater*, 2020, **31**, 169–183.
463 P. Shakhsari, P. A. Azar, F. Z. Hargalani and M. H. Givianrad, *IOSRJEN*, 2021, **11**, 06–15.
464 L. I. A. Ali, H. F. Alesary, H. K. Ismail, W. H. Hassan, A. A. Kareem and B. K. Nile, *J. Water Process Eng.*, 2024, **64**, 105589.
465 M. Bhaumik, A. Maity and H. G. Brink, *Chem. Eng. J.*, 2021, **417**, 127910.
466 F. Wang, L. Huang, J. Li, L. Lin, Z. Liu and Z. Dong, *Polym. Chem.*, 2014, **5**, 4332–4338.
467 E. N. Zare, M. M. Lakouraj and A. Ramezani, *New J. Chem.*, 2016, **40**, 2521–2529.
468 C. Cui, X. Sun, C. Zhou, Y. Liu, H. Xiong, Y. Li and J. Han, *Colloids Surf., A*, 2021, **616**, 126336.
469 M. Karegar and M. M. Khodaei, *J. Appl. Polym. Sci.*, 2022, **139**, 51489.
470 G. Sarojini, S. Venkateshbabu and M. Rajasimman, *Chemosphere*, 2021, **278**, 130400.
471 Q. Huang, D. Hu, M. Chen, C. Bao and X. Jin, *J. Mol. Liq.*, 2019, **285**, 288–298.
472 J. Chen, J. Zhu, N. Wang, J. Feng and W. Yan, *Chem. Eng. J.*, 2019, **360**, 1486–1497.
473 P. Sun, W. Zhang, B. Zou, X. Wang, L. Zhou, Z. Ye and Q. Zhao, *Appl. Clay Sci.*, 2021, **209**, 106151.
474 K. Molaei, H. Bagheri, A. A. Asgharinezhad, H. Ebrahimzadeh and M. Shamsipur, *Talanta*, 2017, **167**, 607–616.
475 H. Zhang, X. Ding, S. Wang, Y. Huang, X.-F. Zeng, S. Maganti, Q. Jiang, M. Huang, Z. Guo and D. Cao, *Eng. Sci.*, 2022, **18**, 320–328.
476 S. Dutta, K. Manna, S. K. Srivastava, A. K. Gupta and M. K. Yadav, *Sci. Rep.*, 2020, **10**, 4982.
477 S. Dutta, A. K. Gupta, S. K. Srivastava and M. K. Yadav, Arsenic in the Environment: Bridging Science to Practice for Sustainable Development As2021, Proceedings of the 8th International Congress and Exhibition, 2021, The Netherlands, CRC Press.
478 V. Q. Trung, N. T. H. Trang, T. M. Thi, K. Vorayuth, N. M. Nghia and M. A. Tuan, *Mater. Trans.*, 2018, **59**, 1095–1100.
479 A. Muhammad, A. u. H. A. Shah and S. Bilal, *Appl. Sci.*, 2020, **10**, 2882.

480 M. Bhaumik, C. Noubactep, V. K. Gupta, R. I. McCrindle and A. Maity, *Chem. Eng. J.*, 2015, **271**, 135–146.
481 R. Chetia, S. Devi, N. Shukla, A. Hazarika, S. Bordoloi, B. Pokhrel, B. K. Saikia, A. Gogoi and S. Konwer, *ACS Omega*, 2024, **9**, 37012–37024.
482 M. S. Mansour, M. E. Ossman and H. A. Farag, *Desalination*, 2011, **272**, 301–305.
483 Y. Sadeghipour, F. Mojoudi and G. Behbudi, *Adv. Appl. NanoBio-Technol.*, 2020, **1**, 20–27.
484 A. Almasian, M. Giahi, G. C. Fard, S. A. Dehdast and L. Maleknia, *Chem. Eng. J.*, 2018, **351**, 1166–1178.
485 M. Zheng, Y. Wei, J. Ren, B. Dai, W. Luo, M. Ma, T. Li and Y. Ma, *Sep. Purif. Technol.*, 2021, **277**, 119455.
486 M. M. Youssif and M. Wojnicki, *Materials*, 2025, **18**, 2083.
487 J. Shokraiyan, M. Asadi, V. Jahed, T. Sahraeian and M. Rabbani, *Desalin. Water Treat.*, 2021, **231**, 244–253.
488 H. Cui, Y. Qian, Q. Li, Q. Zhang and J. Zhai, *Chem. Eng. J.*, 2012, **211–212**, 216–223.
489 J. Ren, C. Wang, H. Zhang, X. Liu, T. Yang, W. Zheng, T. Li and Y. Ma, *Langmuir*, 2023, **39**, 10098–10111.
490 W. Wang, Y. Lv, H. Liu and Z. Cao, *Sep. Purif. Technol.*, 2024, **330**, 125265.
491 Y. Wu, H. Chang, J. Peng, Y. Liu, B. Sun, Z. Yang, S. Gao and F. Liu, *Polym. Bull.*, 2023, **80**, 3675–3688.
492 S. Chen, D. Xu, L. Chen, Y. Zhang, C. Hu, L. Zhang and J. Chen, *ACS Appl. Polym. Mater.*, 2023, **5**, 10303–10314.
493 S. Majumdar, U. Saikia and D. Mahanta, *J. Chem. Eng. Data*, 2015, **60**, 3382–3391.
494 M. H. Fekri, M. B. Keivani, M. R. Mehr and B. Akbari-adergani, *J. Mazandaran Univ. Med. Sci.*, 2019, **29**, 166–179.
495 P. L. Meena, J. K. Saini, A. K. Surela, K. Poswal and L. K. Chhachhia, *Biomass Convers. Biorefin.*, 2024, **14**, 1711–1730.
496 K. Rachna, A. Agarwal and N. B. Singh, *Environ. Nanotechnol. Monit. Manage.*, 2018, **9**, 154–163.
497 S. Dhanavel, E. A. K. Nivethaa, K. Dhanapal, V. K. Gupta, V. Narayanan and A. Stephen, *RSC Adv.*, 2016, **6**, 28871–28886.
498 V. M. Ovando-Medina, N. E. Dávila-Guzmán, N. V. Pérez-Aguilar, H. Martínez-Gutiérrez, I. D. Antonio-Carmona, S. Y. Martínez-Amador and A. Dector, *Iran. Polym. J.*, 2018, **27**, 171–181.
499 J. Ren, C. Wang, J. Ding, T. Li and Y. Ma, *ACS Appl. Polym. Mater.*, 2022, **4**, 9449–9462.
500 H. Xu, Y. Zhang, Y. Cheng, W. Tian, Z. Zhao and J. Tang, *Adsorpt. Sci. Technol.*, 2019, **37**, 217–235.
501 M. S. Shahriman, N. N. M. Zain, S. Mohamad, N. S. A. Manan, S. M. Yaman, S. Asmand and M. Raoov, *RSC Adv.*, 2018, **8**, 33180–33192.
502 C. Wang, B. Liang, H. Gao, T. Yang, T. Li, Y. Ma, H. M. Abo-Dief, G. Roymahapatra, J. Zhang, K. M. Abualnaja, Z. M. El-Bahy and Z. Guo, *Colloids Surf., A*, 2024, **700**, 134659.
503 M. A. Sayed, A. Mohamed, S. A. Ahmed, A. M. El-Sherbeeny, W. A. Zoubi and M. R. Abukhadra, *ACS Omega*, 2023, **8**, 47210–47223.
504 A. Varghese, S. Devi and K. R. D. Pinheiro, *Mater. Today Commun.*, 2023, **35**, 105739.
505 L. Benhaddad, N. Belhouchat, A. Gueddouri, M. L. Hammache and H. Saighi, *Russ. J. Gen. Chem.*, 2023, **93**, 2378–2392.
506 S. Mondal, U. Rana, P. Das and S. Malik, *ACS Appl. Polym. Mater.*, 2019, **1**, 1624–1633.
507 I. Toumi, H. Djelad, F. Chouli and A. Benyoucef, *J. Inorg. Organomet. Polym. Mater.*, 2021, **32**, 112–121.
508 M. S. Tanweer, Z. Iqbal and M. Alam, *Langmuir*, 2022, **38**, 8837–8853.
509 C. Ao, B. Zhang, L. Yuan, J. Li, D. Wu, R. Xu and B. Pan, *J. Membr. Sci.*, 2024, **708**, 123020.
510 X. P. Teng, M. Y. K. Bryan, P. V. Chai and J. Y. Law, *Mater. Today Proc.*, 2021, **46**, 1875–1881.
511 S. Singh, S. Perween and A. Ranjan, *J. Environ. Chem. Eng.*, 2021, **9**, 105149.
512 H. Ali and A. M. Ismail, *J. Polym. Environ.*, 2023, **31**, 976–998.
513 S. Dutta, S. K. Srivastava, B. Gupta and A. K. Gupta, *ACS Appl. Mater. Interfaces*, 2021, **13**, 54324–54338.
514 I. Benchikh, S. Lahreche, Y. Benmimoun and A. Benyoucef, *Res. Square*, preprint, 2022, DOI: 10.21203/rs.3.rs-1479466/v1.
515 Y. Weng, Z. Jin, S. Xie and M. Zhang, *Colloids Surf., A*, 2024, **681**, 132745.
516 S. Razzaq, M. Akhtar, S. Zulfiqar, S. Zafar, I. Shakir, P. O. Agboola, S. Haider and M. F. Warsi, *J. Taibah Univ. Sci.*, 2021, **15**, 50–62.
517 I. Khan, K. Saeed, I. Zekker, B. Zhang, A. H. Hendi, A. Ahmad, S. Ahmad, N. Zada, H. Ahmad, L. A. Shah, *et al.*, *Water*, 2022, **14**, 242.
518 M. M. Ayad and A. A. El-Nasr, *J. Phys. Chem. C*, 2010, **114**, 14377–14383.
519 W. A. Amer, M. M. Omran, A. F. Rehab and M. M. Ayad, *RSC Adv.*, 2018, **8**, 22536–22545.
520 W. A. Amer, M. M. Omran and M. M. Ayad, *Colloids Surf., A*, 2019, **562**, 203–212.
521 Y. Zhang, S. He, Y. Zhang, Y. Feng, Z. Pan and M. Zhang, *Colloids Surf., A*, 2022, **632**, 127765.
522 M. M. Ayad, A. Abu El-Nasr and J. Stejskal, *J. Ind. Eng. Chem.*, 2012, **18**, 1964–1969.
523 N. Wang, J. Chen, J. Wang, J. Feng and W. Yan, *Powder Technol.*, 2019, **347**, 93–102.
524 E. A. El-Sharkaway, R. M. Kamel, I. M. El-Sherbiny, S. S. Gharib, E. A. El-Sharkaway, R. M. Kamel, I. M. El-Sherbiny and S. S. Gharib, *Environ. Technol.*, 2019, **41**, 2854–2862.
525 M. M. Ayad, W. A. Amer, S. Zaghlol, I. M. Minisy, P. Bober and J. Stejskal, *Chem. Pap.*, 2018, **72**, 1605–1618.
526 Y. Wang, *J. Appl. Organomet. Chem.*, 2025, **39**, e7977.
527 C. Wang, B. Zhang, X. Sun, Y. Zhang, W. Li, T. Yang, Y. Ma, Z. Sun and T. Li, *Sep. Purif. Technol.*, 2024, **329**, 125140.
528 A. A. Nezhad, M. Alimoradi and M. Ramezani, *Mater. Res. Express*, 2018, **5**, 025508.

529 W. Zhang, L. Hao, Y. Wang, Q. Lin, C. Lu and Z. Xu, *J. Environ. Chem. Eng.*, 2016, **4**, 882–890.
530 L. Bai, Z. Li, Y. Zhang, T. Wang, R. Lu, W. Zhou, H. Gao and S. Zhang, *Chem. Eng. J.*, 2015, **279**, 757–766.
531 N. Mohanty, S. Behera and B. N. Patra, *Ind. Eng. Chem. Res.*, 2025, **64**, 2274–2282.
532 K. O. Iwuozor, J. O. Ighalo, E. C. Emenike, L. A. Ogunfowora and C. A. Igwegbe, *Curr. Res. Green Sustainable Chem.*, 2021, **4**, 100179.
533 S. Radoor, J. Karayil, A. Jayakumar, J. Parameswaranpillai and S. Siengchin, *Colloids Surf., A*, 2021, **611**, 125852.
534 S. Yildirim, B. Isik and V. Ugraskan, *Mater. Chem. Phys.*, 2023, **307**, 128083.
535 S. Pete, R. A. Kattil and L. Thomas, *Diam. Relat. Mater.*, 2021, **117**, 108455.
536 Y. Xia, T. Li, J. Chen and C. Cai, *Synth. Met.*, 2013, **175**, 163–169.
537 A. R. Prasad and A. Joseph, *RSC Adv.*, 2017, **7**, 20960.
538 M. Zhang, L. Chang and Z. Yu, *Desalin. Water Treat.*, 2018, **110**, 209–218.
539 W. Yao, C. Shen and Y. Lu, *Compos. Sci. Technol.*, 2013, **87**, 8–13.
540 M. Maruthapandi, L. Eswaran, J. H. T. Luong and A. Gedanken, *Ultrason. Sonochem.*, 2020, **62**, 104864.
541 N. Sadegh, H. Haddadi, F. Sadegh and A. Asfaram, *Polyhedron*, 2024, **248**, 116671.
542 Y. Zeng, L. Zhao, W. Wu, G. Lu, F. Xu, Y. Tong, W. Liu and J. Du, *J. Appl. Polym. Sci.*, 2013, **127**, 2475–2482.
543 Z. Tang, M. Ai and J. Peng, *J. Comput. Theor. Nanosci.*, 2017, **14**, 1965–1969.
544 F. Huang, X. Tian, W. Wei, X. Xu, J. Li, Y. Guo and Z. Zhou, *J. Cleaner Prod.*, 2022, **344**, 131100.
545 M. A. Gabal, E. A. Al-Harthy, Y. M. Al Angari, M. Abdel Salam, A. Awad, A. A. Al-Juaid and A. Saeed, *Catalysts*, 2022, **12**, 1624.
546 H. K. Alzahrani and D. F. Katowah, *Nanocomposites*, 2023, **9**, 183–202.
547 S. A. Alqarni, *Nanocomposites*, 2022, **8**, 47–63.
548 Z. Miri, S. Elhami, V. Zare-Shahabadi and H. J. Jahromi, *Spectrochim. Acta, Part A*, 2021, **262**, 120130.
549 P. Roy and S. K. Srivastava, *Nanomaterials for Electrochemical Energy Storage Devices*, Scrivener Publishing, 2020.
550 S. Raj, S. K. Srivastava, P. Kar and P. Roy, *RSC Adv.*, 2016, **6**, 95760–95767.
551 N. Swain, B. Saravanakumar, M. Kundu, L. Schmidt-Mende and A. Ramadoss, *J. Mater. Chem. A*, 2021, **9**, 25286–25324.
552 Y.-T. Tan, F. Ran, L.-R. Wang, L.-B. Kong and L. Kang, *J. Appl. Polym. Sci.*, 2012, **127**, 1544–1549.
553 W. Yang, Z. Gao, N. Song, Y. Zhang, Y. Yang and J. Wang, *J. Power Sources*, 2014, **272**, 915–921.
554 Z. Li, Y. Shen and Y. Li, *J. Electrochem. Soc.*, 2018, **165**, G75–G79.
555 Z. Li, J. Hu, Y. Li and J. Liu, *ChemistrySelect*, 2018, **3**, 6737–6742.
556 Z. Wang, H. Qiang, C. Zhang, Z. Zhu, M. Chen, C. Chen and D. Zhang, *J. Polym. Res.*, 2018, **25**, 129.
557 R. Hong, X. Zhao, R. Lu, M. You, X. Chen and X. Yang, *Molecules*, 2024, **29**, 2331.
558 M. S. Kim, J. H. Moon, P. J. Yoo and J. H. Park, *J. Electrochem. Soc.*, 2012, **159**, A1052–A1056.
559 Z. Li, J. Cai, P. Cizek, H. Niu, Y. Du and T. Lin, *J. Mater. Chem. A*, 2015, **3**, 16162–16167.
560 P. Fan, S. Wang, H. Liu, L. Liao, G. Lv and L. Mei, *Electrochim. Acta*, 2020, **331**, 135259.
561 Z.-L. Wang, R. Guo, G.-R. Li, H.-L. Lu, Z.-Q. Liu, F.-M. Xiao, M. Zhang and Y.-X. Tong, *J. Mater. Chem.*, 2012, **22**, 2401–2404.
562 J. P. Jyothibasu and R.-H. Lee, *J. Mater. Chem. A*, 2020, **8**, 3186–3202.
563 H.-H. Huang, Y.-H. Wu, M.-Z. Wang and X.-W. Ge, *Chin. J. Chem. Phys.*, 2018, **31**, 827–832.
564 D. Xu, A. Chen, Q. Sheng, G. Hu, L. Chen, Y. Zhang, S. Chen and C. Hu, *J. Power Sources*, 2025, **638**, 236627.
565 K.-J. Ahn, Y. Lee, H. Choi, M.-S. Kim, K. Im, S. Noh and H. Yoon, *Sci. Rep.*, 2015, **5**, 14097, DOI: 10.1038/srep14097.
566 S. Xiong, Y. Zhang, Y. Wang, B. Wu, J. Chu, X. Wang, R. Zhang, M. Gong, Z. Li and Z. Chen, *High Perform. Polym.*, 2019, **32**, 600–608.
567 B. M. Hryniewicz and M. Vidotti, *ACS Appl. Nano Mater.*, 2018, **1**, 3913–3924.
568 Y. Wang, X. Wu, Y. Xiao, Y. Han, T. Li and Y. Ma, *Synth. Met.*, 2023, **299**, 117483.
569 X. Zhang, J. Zhao, T. Xia, Q. Li, C. Ao, Q. Wang, W. Zhang, C. Lu and Y. Deng, *Energy Storage Mater.*, 2020, **31**, 135–145.
570 J.-G. Wang, Y. Yang, Z.-H. Huang and F. Kang, *J. Power Sources*, 2012, **204**, 236–243.
571 N. B. Trung, T. V. Tam, H. R. Kim, S. H. Hur, E. J. Kim and W. M. Choi, *Chem. Eng. J.*, 2014, **255**, 89–96.
572 J. Luo, Q. Ma, H. Gu, Y. Zheng and X. Liu, *Electrochim. Acta*, 2015, **173**, 184–192.
573 W. Wu, C. Wang, C. Zhao, D. Wei, J. Zhu and Y. Xu, *J. Colloid Interface Sci.*, 2020, **580**, 601–613.
574 M. Devi and A. Kumar, *Polym. Compos.*, 2020, **41**, 653–667.
575 Y. Yang, P. Zhu, L. Zhang, T. Li, Q. Wang, R. Sum and C. Wong, 19th International Conference on Electronic Packaging Technology (ICEPT), Shanghai, China, 2018, pp. 270–274, DOI: 10.1109/ICEPT.2018.8480452.
576 S. Wu, J. Tian, X. Yin and W. Wu, *Nano*, 2019, **14**, 1950056.
577 Z. Wang, C. Zhang, C. Xu, Z. Zhu and C. Chen, *Ionics*, 2016, **23**, 147–156.
578 H. Kwon, D. Hong, I. Ryu and S. Yim, *ACS Appl. Mater. Interfaces*, 2017, **9**, 7412–7423.
579 F. A. Tabar, F. Sharif and S. Mazinani, *Polymer*, 2018, **154**, 80–89.
580 J. Liu, J. An, Y. Ma, M. Li and R. Ma, *J. Electrochem. Soc.*, 2012, **159**, A828–A833.

581 X. Xu, J. Tang, H. Qian, S. Hou, Y. Bando, Md. S. A. Hossain, L. Pan and Y. Yamauchi, *ACS Appl. Mater. Interfaces*, 2017, **9**, 38737–38744.
582 P. Liu, X. Wang and H. Li, *Synth. Met.*, 2014, **189**, 173–176.
583 D. Tian, H. Cheng, Q. Li, C. Song, D. Wu, X. Zhao, S. Hu, S. Chen and C. Hu, *Electrochim. Acta*, 2021, **398**, 139328.
584 K. Kakaei, S. Khodadoost, M. Gholipour and N. Shouraei, *J. Phys. Chem. Solids*, 2021, **148**, 109753.
585 S. Chen, H. Cheng, D. Tian, Q. Li, M. Zhong, J. Chen, C. Hu and H. Ji, *ACS Appl. Energy Mater.*, 2021, **4**, 3701–3711.
586 J. Li, X. Li, W. Wei, D. Wang and P. Liu, *Electrochim. Acta*, 2021, **395**, 139193.
587 W. Fan, C. Zhang, W. W. Tjiu, K. P. Pramoda, C. He and T. Liu, *ACS Appl. Mater. Interfaces*, 2013, **5**, 3382–3391.
588 P. Du, W. Wei, D. Liu, H. Kang and P. Liu, *Chem. Eng. J.*, 2018, **335**, 373–383.
589 V. Mini and H. Devendrappa, *Mater. Today Proc.*, 2018, **5**, 23148–23155.
590 W. Wu, L. Yang, S. Chen, Y. Shao, L. Jing, G. Zhao and H. Wei, *RSC Adv.*, 2015, **5**, 91645–91653.
591 K. Qi, R. Hou, S. Zaman, B. Y. Xia and H. Duan, *J. Mater. Chem. A*, 2018, **6**, 3913–3918.
592 J. Zhu, W. Sun, D. Yang, Y. Zhang, H. H. Hoon, H. Zhang and Q. Yan, *Small*, 2015, **11**, 4123–4129.
593 Q. Chen, F. Xie, G. Wang, K. Ge, H. Ren, M. Yan, Q. Wang and H. Bi, *Ionics*, 2021, **27**, 4083–4096.
594 X. Zhang, L. Ma, M. Gan, G. Fu, M. Jin and Y. Zhai, *Appl. Surf. Sci.*, 2018, **460**, 48–57.
595 S. Zhang, X. Song, S. Liu, F. Sun, G. Liu and Z. Tan, *Electrochim. Acta*, 2019, **312**, 1–10.
596 S. A. Ansari, H. Fouad, S. G. Ansari, M. P. Sk and M. H. Cho, *J. Colloid Interface Sci.*, 2017, **504**, 276–282.
597 Y. Cai, L. Xu, H. Kang, W. Zhou, J. Xu, X. Duan, X. Lu and Q. Xu, *Electrochim. Acta*, 2021, **370**, 137791.
598 Y. Liang, Z. Wei, X. Zhang and R. Wang, *ES Energy Environ.*, 2022, **18**, 101–110.
599 D. Thanasamy, D. Jesuraj, V. Avadhanam, K. Chinnadurai, S. Kumar and K. Kannan, *J. Energy Storage*, 2022, **53**, 105087.
600 Z. Li, Y. Sui, J. Qi, F. Wei, Y. He, Q. Meng, Y. Ren, X. Zhang, Z. Zhan and Z. Sun, *Compos. Interfaces*, 2019, **27**, 631–644.
601 I. Chakraborty, N. Chakrabarty, A. Senapati and A. K. Chakraborty, *J. Phys. Chem. C*, 2018, **122**, 27180–27190.
602 S. S. Scindia, R. B. Kamble and J. A. Kher, *AIP Adv.*, 2019, **9**, 055218.
603 J. Fu, Y. Zhang, H. Zhao, R. Jiang and R. Zhang, *J. Colloid Interface Sci.*, 2020, **559**, 39–44.
604 C. Chen, Q. Zhang and C. Peng, *Polym. Polym. Compos.*, 2017, **25**, 483–488.
605 A. Imani and G. Farzi, *J. Mater. Sci.: Mater. Electron.*, 2015, **26**, 7438–7444.
606 C. Xia, M. Leng, W. Tao, Q. Wang, Y. Gao and Q. Zhang, *J. Mater. Sci.: Mater. Electron.*, 2019, **30**, 4427–4436.
607 X. Liu, Z. Wu and Y. Yin, *Chem. Eng. J.*, 2017, **323**, 330–339.
608 C. Pan, Z. Liu, W. Li, Y. Zhuang, Q. Wang and S. Chen, *J. Phys. Chem. C*, 2019, **123**, 25549–25558.
609 B. Mu, W. Zhang and A. Wang, *J. Nanopart. Res.*, 2014, **16**, 2432.
610 X. Ge, Y. He, T. Plachy, N. Kazantseva, P. Saha and Q. Cheng, *Nanomaterials*, 2019, **9**, 527.
611 X. Li, H. Song, Y. Zhang, H. Wang, K. Du, H. Li, Y. Yuan and J. Huang, *Int. J. Electrochem. Sci.*, 2012, **7**, 5163–5171.
612 J. H. Shendkar, M. Zate, K. Tehare, V. V. Jadhav, R. S. Mane, M. Naushad, J. M. Yun and K. H. Kim, *Mater. Chem. Phys.*, 2016, **180**, 226–236.
613 X. He, Q. Liu, J. Liu, R. Li, H. Zhang, R. Chen and J. Wang, *Chem. Eng. J.*, 2017, **325**, 134–143.
614 P. Li, E. Shi, Y. Yang, Y. Shang, Q. Peng, S. Wu, J. Wei, K. Wang, H. Zhu, Q. Yuan, A. Cao and D. Wu, *Nano Res.*, 2014, **7**, 209–218.
615 Y. Yesi, I. Shown, A. Ganguly, T. T. Ngo, L.-C. Chen and K.-H. Chen, *ChemSusChem*, 2016, **9**, 370–378.
616 J. W. Park, W. Na and J. Jang, *J. Mater. Chem. A*, 2016, **4**, 8263–8271.
617 M. Vellakkat and D. Hundekkal, *Mater. Res. Express*, 2016, **3**, 015502.
618 M. B. Poudel, M. Shin and H. J. Kim, *Int. J. Hydrogen Energy*, 2021, **46**, 474–485.
619 J. Iqbal, M. O. Ansari, A. Numan, S. Wageh, A. Al-Ghamdi, M. G. Alam, P. Kumar, R. Jafer, S. Bashir and A. H. Rajpar, *Polymers*, 2020, **12**, 2918.
620 A. H. P. de Oliveira, M. L. F. Nascimento and H. P. de Oliveira, *Mater. Res.*, 2016, **19**, 1080–1087.
621 H.-Y. Ho, H.-I. Chu, Y.-J. Huang, D.-S. Tsai and C.-P. Lee, *Nanotechnology*, 2023, **34**, 125401.
622 J. Rodríguez-Moreno, E. Navarrete-Astorga, E. A. Dalchiele, R. Schrebler, J. R. Ramos-Barrado and F. Martín, *Chem. Commun.*, 2014, **50**, 5652–5655.
623 Y. Huang, J. Wang, X. Ju, S. Zhang and X. Sun, *J. Energy Storage*, 2023, **72**, 108460.
624 R. Li, P. Song, Z. Ji, H. Zhou, Y. Xue, L. Kong and X. Shen, *Appl. Surf. Sci.*, 2024, **649**, 159188.
625 K. Ghosh, C. Y. Yue, M. M. Sk and R. K. Jena, *ACS Appl. Mater. Interfaces*, 2017, **9**, 15350–15363.
626 L. Liu, Y. Wang, Q. Meng and B. Cao, *J. Mater. Sci.*, 2017, **52**, 7969–7983.
627 K. Wang, L. Li, Y. Liu, C. Zhang and T. Liu, *Adv. Mater. Interfaces*, 2016, **3**, 1600665.
628 Y. Liu, X. Wang, T. Abdiryim, R. Jamal, A. Abdurexit, F. Xu, N. Fan, K. Song and H. Yang, *J. Energy Storage*, 2024, **94**, 112530.
629 M. Wang, Y. Lin, Y. Liu and H. Yang, *J. Mater. Sci. Mater. Electron.*, 2019, **30**, 14344–14354.

630 N. Boutaleb, G. M. Al-Senani, S. D. Al-Qahtani, A. Benyoucef and B. D. Alkoudsi, *Colloids Surf., A*, 2025, **718**, 136867.
631 A. V. Baskar, N. Bolan, S. A. Hoang, P. Sooriyakumar, M. Kumar, L. Singh, T. Jasemizad, L. P. Padhye, G. Singh, A. Vinu, B. Sarkar, M. B. Kirkham, J. Rinklebe, S. Wang, H. Wang, R. Balasubramanian and K. H. M. Siddique, *Total Environ.*, 2022, **822**, 153555.
632 O. B. Okafor, A. P. I. Popoola, O. M. Popoola, U. O. Uyor and V. E. Ogbonna, *Polym. Bull.*, 2024, **81**, 189–246.
633 N. Singh and U. Riaz, *Polym. Bull.*, 2022, **79**, 10377–10408.
634 S. Rawat, R. K. Mishra and T. Bhaskzar, *Chemisphere*, 2022, **2**, 131961.
635 G. Jiang, R. A. Senthil, Y. Sun, T. R. Kumar and J. Pan, *J. Power Sources*, 2022, **520**, 230886.
636 A. T. S. C. Brandão, S. State, R. Costa, P. Potorac, J. A. Vazquez, J. Valcarcel, A. F. Silva, L. Anicai, M. Enachescu and C. M. Pereira, *ACS Omega*, 2023, **8**, 18782–18798.
637 D. Tashima, T. Kashio, T. Eguchi, S. Kumagai, T. Tsubota and J. D. W. Madden, *Mater. Lett.*, 2023, **18**, 100193.
638 P. Manasa, S. Sambasivam and F. Ran, *J. Energy Storage*, 2022, **54**, 105290.
639 K. Mensah-Darkwa, C. Zequine, P. K. Kahol and R. K. Gupta, *Sustainability*, 2019, **11**, 414.
640 X. Zhu, Y. Zeng, X. Zhao, D. Liu, W. Lei and S. Lu, *EcoEnergy*, 2025, **3**, e70000, DOI: 10.1002/ece2.70000.
641 B. R. Holla, M. Kanthraj, Vaishali, Namitha and K. A. Vishnumurthy, *J. Ind. Chem. Soc.*, 2025, **102**, 101948.
642 P. H. Patil and S. A. Jadhav, *RSC Appl. Interfaces*, 2024, **1**, 624.
643 N. V. Challagulla, M. Vijayakumar, D. S. Rohita, G. Elsa, A. B. Sankar, T. N. A. Rao and M. Karthik, *Energy Technol.*, 2020, **8**, 2000417.
644 S. N. Karri, S. P. Ega, V. Perupogu and P. Srinivasan, *ChemistrySelect*, 2021, **6**, 2576–2589.
645 S. Rajput, V. Tyagi, Sonika, R. Nayak and S. K. Verma, *Energy Technol.*, 2025, **13**, 2401977.